FINAL REPORT

"The Effects of Magnetic Nozzle Configurations on Plasma Thrusters"

Prepared by

Professor P.J. Turchi
Department of Aerospace Engineering,
Applied Mechanics and Aviation
The Ohio State University
2036 Neil Avenue, 328 Bolz Hall
Columbus, Ohio 43210-1276

Sponsored by

National Aeronautics and Space Administration
Lewis Research Center
21000 Brookpark Road
Cleveland, Ohio 44135

Technical Officer

M.A. Mantenieks
On-Board Propulsion Branch
NASA Lewis Research Laboratory

OSURF Project Nos. : 720331 and 723221
Master Project: 766488
Start Date: 05 Dec 1987
End Date: 31 Dec 1995

Grant / Contract No. : NAG3-843
Sponsor ID No. : 30030104

FINAL REPORT Grant No. NAS 3 - 843

ABSTRACT

Over the course of eight years, The Ohio State University has performed research in support of electric propulsion development efforts at the NASA Lewis Research Center, Cleveland, OH. This research has been largely devoted to plasma propulsion systems including magnetoplasmadynamic (MPD) thrusters with externally-applied, solenoidal magnetic fields, hollow cathodes, and pulsed plasma microthrusters (PPTs). Both experimental and theoretical work has been performed, as documented in four master's theses, two doctoral dissertations, and numerous technical papers. The present document is the final report for the grant period 5 December 1987 to 31 December 1995, and summarizes all activities. Detailed discussions of each area of activity are provided in appendices: Appendix I - Experimental studies of magnetic nozzle effects on plasma thrusters; Appendix II - Numerical modeling of applied-field MPD thrusters; Appendix III - Theoretical and experimental studies of hollow cathodes; and Appendix IV - Theoretical, numerical and experimental studies of pulsed plasma thrusters. Especially notable results include the efficacy of using a solenoidal magnetic field downstream of a plasma thruster to collimate the exhaust flow, the development of a new understanding of applied-field MPD thrusters (based on experimentally-validated results from state-of-the art, numerical simulation) leading to predictions of improved performance, an experimentally-validated, first-principles model for orificed, hollow-cathode behavior, and the first time-dependent, two-dimensional calculations of ablation-fed, pulsed plasma thrusters.

FINAL REPORT Grant No. NAS 3 - 843

TABLE OF CONTENTS

FINAL REPORT Grant No. NAS 3 - 843

INTRODUCTION

Research on plasma thrusters has been performed at The Ohio State University over several years in support of efforts at the NASA Lewis Research Center. These efforts have ranged from steady-state, applied-field MPD thrusters to various forms of pulsed plasma thruster. The corresponding research at Ohio State included early work on magnetic nozzle flows, initiated by Professor T.M. York, and later efforts by Professor P.J. Turchi on plasma flow diagnosis, hollow cathodes, modeling of MPD thrusters and development of advanced pulsed plasma thrusters. Numerical simulation of MPD thrusters, using the MACH2 code, has been compared with experimental results, especially the extensive data base developed at NASA LeRC on steady-state, applied-field MPD thrusters at the 100 kW-level. When the focus of near term NASA efforts shifted to much lower average-power systems, attention was directed to pulsed and quasi-steady, plasma thrusters in self-field and applied-field arrangements. One arrangement is the so-called pulsed plasma microthruster (PPT) that operates in self-field mode. The discharge accelerates mass generated by ablating the insulator between the thruster's electrodes. This device has been used successfully for many years for satellite station-keeping and there is now interest in extending its capabilities to higher energy missions. Such extension requires improvement of system components and better understanding of PPT operation. The Ohio State effort in support of these improvements included development of numerical techniques to model PPT behavior, examination of new propellant and circuit arrangements for PPTs, and assistance in creation of a new experimental facility at NASA LeRC for studies of such arrangements.

PROGRESS

Experimental Studies of Magnetic Nozzles:

The initial efforts under the grant were based experimentally on a quarter-scale version of the self-field, quasi-steady MPD thruster usually referred to as the Princeton benchmark thruster. Scaling of current and mass-flow in the quarter-scale device at Ohio State was specified in a manner that preserved the electromagnetic force-density in the thruster and the mass flow-rate per unit area. Scaling considerations and details of the experimental set-up are discussed in Ref. 1, which is also included for convenience in Appendix I.

Although no attempt was made to maintain the magnetic Reynolds number or other such dimensionless parameters in scaling down from the benchmark thruster, the quarter-scale device nevertheless provided an adequate source of high speed plasma for experiments evaluating some effects of solenoidal magnetic fields applied downstream of the thruster exit. The results of studies of so-called "magnetic nozzle" effects are discussed in the paper of Appendix I, and four master's degree theses [2 - 5] previously transmitted to NASA LeRC under separate cover. The principal result of these efforts was recognition of the utility of solenoidal fields applied downstream of the thruster for collimation of the exhaust flow. At the modest values of magnetic Reynolds number for the present experiments, however, magnetic flux is well-diffused into the exhaust flow, so action of the applied-field (as a conventional, solid-wall, nozzle) to convert internal energy to directed exhaust energy by expansion is not expected nor exhibited experimentally. Indeed, spectroscopic study [4] suggests that the exhaust flow is driven toward sonic conditions (presumably in the course of collimation by the converging portion of the solenoidal magnetic field).

Numerical Modeling of Applied-field MPD Thrusters:

Theoretical studies of applied-field MPD thrusters were undertaken to support the experimental program at NASA LeRC. In these experiments, the MPD thruster operates in steady-state, and the externally-applied, solenoidal magnetic field has its maximum value within the thrust chamber and diverges to lower values downstream. The expectation has been in such devices that interaction of the (radial) discharge current with the axially-directed magnetic field in the thrust chamber would impart rotational energy to the plasma flow which is then converted to kinetic energy in the exhaust by flow expansion in the diverging magnetic-nozzle. Such behavior is extremely complex to follow in detail, and depends critically on the interactions of several competing processes in the discharge flow. Numerical modeling is, therefore, required at a level that will properly include all the relevant physical phenomena. Ohio State performed this modeling by adapting an existing code, MACH2, that had been developed for the US Air Force, originally by Mission Research Corp., Albuquerque, NM. The development and modifications of MACH2 performed by Ohio State under the present grant are summarized in Table I. Details of the Ohio State efforts are described in Refs. 6 and 7, included for convenience in Appendix II, and in a doctoral thesis [8] previously transmitted to NASA LeRC under separate cover.

By means of MACH2, examination of the details of the flow field within the thruster has yielded important new insights into thruster operation and performance. In particular, the inclusion of viscosity for the partially-ionized, two-temperature plasma has proven to be critical for understanding the behavior of applied-field MPD thrusters. For example, basic theory indicates that the back EMF across the rotating plasma flow in the thrust chamber scales as the product of azimuthal speed and applied-field. If inertia is the only counter to the electromagnetic torque in the plasma, the azimuthal speed should increase linearly with field at constant mass flow rate and discharge current. This implies that the voltage should scale as the square of the applied-field. Experiments, however, show a linear increase of voltage with applied-field. A limiting value of azimuthal speed has been postulated, possibly related to Alfven critical speed in some unspecified manner. The MACH2 simulations demonstrate that the azimuthal speed is indeed limited, but by viscous drag forces within the thrust chamber that increase with the electromagnetic torque.

TABLE I

Summary of modifications of the MACH2 code by Ohio State for the Applied-field MPD Problem

-- Added means for calculating in-plane (B_r, B_z) magnetic field in steady-state. Procedure uses Biot-Savart Law to solve for magnetic fields on computational boundaries due to azimuthally-directed plasma currents (in addition to external solenoids). Solution relaxes to steady-state consistent with these fields. (Without this procedure, the magnetic field boundary conditions are not well-posed in steady-state.)

-- Modified stress tensor to include real viscous effects due to velocity shear, (thereby converting code from Euler to Navier-Stokes formulation).

-- Developed viscosity coefficient for partially-ionized gas (e.g., argon) for use with modified stress tensor. Also developed associated thermal conductivity coefficient.

-- Established edits for thruster quantities, (e.g., thrust).

As the plasma spins up because of the electromagnetic torque on the incoming mass flow, it is pressed against the inside of the anode surface by centrifugal force. A brake is thus applied more forcefully as higher torque attempts to increase the rotational speed. Furthermore, the viscosity increases with increased ion temperature in the rotationally-pressurized, frictionally-limited flow. This increase of viscosity is contrary to the behavior of a partially-ionized gas with equal electron and ion temperatures. The present modeling, however, allows the electron temperature to be lower than the ion temperature, so the ionization level and effective ion charge-number for collisions do not increase with ion temperature. The characteristic viscosity of the rotating plasma in the thrust chamber appears to increase with the product of discharge current and applied-field, resulting in a maximum value for the rotational speed (at the exit plane) that becomes constant as this product increases.

In addition to providing a new visualization of applied-field MPD thruster behavior, the MACH2 modeling also reasonably captures both the magnitudes and trends of plasma voltage, thrust and exhaust speed measured in the NASA LeRC experiments. The associated flow fields may then be subjected to credible examination to understand areas for possible improvement of thruster performance. Such examination, for example, indicates that the plasma is anomalously resistive in many regions. This condition tends to limit the Hall parameter to much lower values than would occur classically. Azimuthal currents in the plasma are relatively weak compared to the current (ampere-turns) of the applied-field coil, so the flux of the in-plane field is fully distributed in the plasma as it exits the thrust chamber. The plasma is able to separate from the flux in the exhaust plume because the magnetic Reynolds number is much less than unity. Thus, eddy-current drag on the exhaust flow is relatively low. Indeed, the low magnetic Reynolds number and full penetration of flux in the flow tend to defeat significant, positive contribution from a magnetic nozzle effect. Decreasing the flux coupling to the plasma within the chamber by lowering the plasma density to increase the electron Hall parameter may not succeed, if anomalous resistivity effects increase at the same time. A separate, downstream coil, with flux not coupled to the plasma flow from the thrust chamber, however, could provide a useful magnetic nozzle arrangement. To be effective, the magnetic Reynolds number of the exhaust flow must be significantly increased. This requirement, however, may correspond to higher power operation than permitted by mission constraints.

If the interaction of the exhaust flow with a downstream magnetic nozzle can be improved, energy deposited in plasma rotation could be extracted for directed kinetic energy. It would then be useful to alleviate the viscous limitation on azimuthal speed. In the present arrangement, centrifugal forces in the plasma are balanced by pressure gradients that are supported by the inside surface of the anode. This forces close contact of the high speed plasma with the non-moving solid, so drag increases. If the plasma could be supported magnetically, then the effective drag might be reduced. The basic approach consists of increasing the azimuthal Hall current, so the radially-inward electromagnetic force balances the centrifugal force in the plasma. To the extent that this balance is created, however, it is unstable (Rayleigh-Taylor, Kelvin-Helmholtz). There might be some regime in which benefits are obtained without significant growth of perturbations.

Success with MACH2 simulations (Appendix II) and subsequent analytical modeling of steady-state, applied-field MPD thrusters at NASA LeRC encouraged design of an improved electrode-geometry for future experiments with quasi-steady, applied-field MPD thrusters at low average-power levels. The new design, which has been transmitted to NASA LeRC under separate cover, seeks to improve thrust efficiency by operating at proportions and propellant flow predicted to achieve optimum performance. Based on the limited expectation of converting rotational-energy to kinetic energy of axial flow by magnetic means, it was also suggested that a solid-wall nozzle could be used to expand the rotating flow. The trade-off here, of course, is one of viscous drag and loss of material from the solid-wall nozzle vs the gain over simply allowing the rotational energy to be lost.

Hollow Cathode Studies:

Part of the support of the program at NASA LeRC on MPD thrusters involved consideration of cathode performance. In particular, the possibility of operating a hollow cathode in an MPD thruster was seen as one approach to improving thruster performance and lifetime. Such cathodes had been used in earlier applied-field MPD thrusters [9], and are used in several other areas of space technology (e.g., ion engine sources, plasma contactors). An Ohio State graduate student had already been started on a doctoral dissertation for theoretical study of hollow cathodes, so work was expanded to include experiments at NASA LeRC.

The studies of hollow cathode behavior performed under this grant were completed in terms of scaling relations for the design and operation of orificed hollow cathodes. This work is discussed in detail in a doctoral dissertation [10], transmitted to NASA LeRC under separate cover, and in three papers [11 - 13], included in Appendix III for convenience. The theoretical model indicates a tendency for the hollow cathode to operate too efficiently, in the sense that higher currents permit very low cathode fall voltages. This is a manifestation of the increase in energy production in the plasma column by resistive heating at higher current. Resistive heating scales as the square of the current, while the loss of energy from the hollow cathode scales as the product of current and plasma volume divided by the orifice area. Operation at higher current therefore does not require as much contribution by the cathode fall to pay for losses. As the cathode fall decreases, back-streaming of plasma electrons to the cathode surface increases. More thermionic emission by the cathode surface is needed to obtain the net current flow. This increased emission, however, heats the plasma column further, causing a lower fall voltage and even higher back-streaming. There is minimum cathode fall below which the no solution is possible. This implies a maximum current-to-diameter ratio. The calculated value for this ratio is consistent with empirical evidence from hollow cathode tests over the last few decades.

In a related paper [14], also in Appendix III, the results of scaling relationships are used to devise a low power plasma thruster based on hollow cathode discharges. It appears that frozen-flow losses may preclude high efficiency in a thruster based on a single hollow cathode discharge. Scaling of particle density inversely with orifice size at fixed current-to-diameter ratio, however, suggests that combined operation of multiple hollow cathodes can provide a sufficiently collisional overall flow to permit efficient thruster performance at low power.

Pulsed Plasma Thrusters:

As the prospect of megawatt-level, average-power in space receded into an indefinite future, interest returned to pulsed plasma thrusters. These thrusters might service missions for which the average power is less than the kilowatt-levels now satisfied by steady-state arcjets, or that require higher values of specific impulse than arcjets can provide. For several decades, plasma thrusters have been operated at megawatt levels in short pulses, either as single-shot, laboratory models or repetitively on actual space missions. The former category include devices in which the current pulse is maintained at nearly constant levels for times longer than required for the discharge and flow field to achieve *quasi-steady* operation. The latter category comprises the various forms of pulsed plasma microthruster, usually abbreviated as

PPT. These devices utilize an arc discharge to ablate a solid slab of insulating material between the thruster electrodes. The propellant mass obtained in this way is then accelerated by interaction of the arc discharge with its self-magnetic field. Typically, the current waveform is a damped, sinusoid, similar to that of an LRC-circuit. Ablation-fed thrusters have also been operated in quasi-steady fashion simply by changing the circuitry to supply constant current.

Efforts on pulsed plasma thrusters by Ohio State under this grant comprised both theoretical and experimental activities. Theoretical studies included zero-dimensional modeling of circuits and plasmas, and the development of computational tools for two-dimensional, unsteady analyses of ablation-fed thrusters. Experimental work ranged from developing new thruster and circuit concepts to testing the behavior of multi-material propellant slabs in the LES 8/9 PPT. Some effort was also expended to provide diagnostics and EMI-shielding for pulsed plasma thruster experiments at NASA LeRC.

<u>Theoretical efforts</u>: Although pulsed plasma thrusters have been studied experimentally for many years, the level of theoretical attention has been rather rudimentary. Various simple models based on plasma slug or snow-plow dynamics have been used to calculate basic plasma motion and circuit behavior. In the case of pulsed or static, gas pre-fills, the initial condition of the plasma (temperature, density, thickness) is assumed and subsequent dynamics are calculated. This approach is used by both simple models based on ordinary differential equations, and also by sophisticated MHD codes. As long as the later behavior of the plasma is reasonably insensitive to the assumed initial conditions, such calculations can be useful. In the case of pulsed, ablation-fed thrusters, however, the initial interactions between the discharge and the solid surface will determine the amount of material ablated into the vacuum and the subsequent dynamics of this material. The behavior of the initial plasma created by ablating the surface may represent the entire operation of the thruster, if no additional material is ablated. Further ablation, however, can cause thruster operation to change from acceleration of a dynamic plasma discharge to quasi-steady ablation and plasma acceleration in an arc that remains adjacent to the insulator surface. The latter arrangement closely resembles the burning of solid-propellant, with electrical energy taking the place of chemical energy in providing heat to ablate the solid surface.

Simple zero-dimensional codes were written for LRC-circuits or lumped-element, pulse-forming lines providing current to a dynamic plasma discharge load. These codes are useful in examining the effect of current waveform on performance of thrusters operating as plasma-slug accelerators. For thrusters based on quasi-steady ablation of the insulator, analytical models [15] indicate that the mass flow rate and the electromagnetic thrust both scale as the square of the current, so performance simply depends on the impedance of the quasi-steady, ablation-arc at the insulator surface relative to the impedance of the power source. The specific impulse would tend to be constant.

The general situation includes a plasma discharge that initially follows the electrically-conducting plasma, but then changes to a stationary distribution near the ablating insulator. Detailed understanding of this behavior requires a rather sophisticated calculational capability. Part of this capability must include a model for ablation of the solid insulator due to heat conduction and radiation from the plasma discharge. With assistance from the USAF Phillips Laboratory, Albuquerque, NM, the MACH2 code was modified to include the effects of heat conduction (in addition to plasma radiation) in a new model for the surface ablation. This model was used to simulate for the first time the behavior of a PPT (LES - 6), including calculation of impulse-bit and ablated mass per shot [15].

While these calculations were reasonable close to experimental results, there was still concern that the non-monotonic variation of heat flux with time was an important factor, especially in regard to the late-time evaporation of material as the surface cooled after completion of the oscillating current-pulse. Efforts most recently [16] have, therefore, focused on improving the ablation model in MACH2 to include non-monotonic heating of the propellant surface. This improvement is necessary in order to allow the surface temperature to decrease faster than the interior temperature after the main electrical pulse. The ablation rate is a strong function of surface temperature, so late-time contribution to the total mass ablated per shot depends critically on the rate at which the surface cools. Appendix IV includes the first two papers to apply MACH2 for modeling PPT behavior.

Experimental Efforts: There are several areas of interest in attempting to improve the performance of pulsed plasma thrusters. In such attempts, it is important to retain or incorporate features that allowed earlier pulsed plasma thrusters to gain acceptance for mission application. These features may include propellant feed in the form of a spring-advanced, solid slab, switching of the main power pulse by ignition of a surface arc on the propellant itself, and low mass for the total propulsion unit.

The possibility of improving the PPT's specific impulse by using lower molecular weight propellants points toward insulating materials that have high amounts of hydrogen instead of fluorine, for example, polyethylene vs Teflon. Earlier tests with polyethylene, however, indicated that the insulator surface would develop black layers of electrically-conducting carbon after repeated arc discharges. In contrast, Teflon surfaces would stay white and insulating. It has been suggested in the present effort that the high voltage hold-off properties of the propellant surface could be retained by interleaving Teflon layers with layers of more hydrogenic plastic. The layers would parallel electrical potential surfaces, so that even if carbon developed on the non-Teflon portions, sufficient voltage hold-off would be provided by the Teflon portions. This new arrangement is described in detail in Ref. 17, (included in Appendix IV).

Several tests of this concept were made using the LES 8/9 PPT at NASA LeRC. The propellant slab on one side of the thruster was modified to accept a set of alternating Teflon and polyethylene layers. These layers were held in a Teflon carriage, so the material next to the electrodes remained the same as in usual PPT operation to preserve possible vacuum-plastic-metal, triple-point interactions. Tens of thousands of discharges were fired successfully without premature breakdown. Inspection of the surface, however, indicated a growth of carbon deposits on the exposed polyethylene surfaces. It is not clear at this time whether the observed deposits had reached a steady level or would continue to accumulate with additional discharges. It had been anticipated that the lower melting point of polyethylene vs Teflon would correlate with faster recession of the polyethylene surface. Instead, the experiments suggest that the carbon deposits may protect the polyethylene from ablating. More work needs to be done with both polyethylene and other hydrogen-rich plastics to examine the long term behavior of the carbon deposits. The evolution of solid carbon-deposits may depend on slight differences in surface temperature relative to transition temperatures for surface decomposition and evaporation as monomers vs polymers. Experiments with polyethylene/Teflon combinations, substituted for pure Teflon in a LES 8/9 thruster, suggested such differences (based on comparison of thermal diffusivities).

New Power-Circuitry: A separate approach to improving PPT performance involves matching the power source to the plasma accelerator load. For steady-state devices such matching is accomplished by equating the power supply and thruster impedances. Pulsed systems, however, do not necessarily have well-defined impedances for either the pulsed electrical source or the thruster load. A special case is a uniform pulseline driving a quasi-steady ablation-arc. The line has an impedance $Z_L = (L / C)^{1/2}$, where L and C are, respectively, the inductance and capacitance per unit length of line. For high magnetic Reynolds number flow, the arc impedance is constant at approximately $Z_a = \mu uh/w$, where h and w are the height and width of the discharge and u is a characteristic flow speed, scaled by Alfven critical speed.

Other pulsed circuits may have characteristic impedance values, but depend on matching the time-variation of the current pulse with the time-varying requirements of the dynamic plasma discharge. For example, an LRC-circuit has a characteristic impedance $0.5\ (L / C)^{1/2}$, where L and C are the inductor and capacitor values. The impedance of a dynamic plasma discharge is $L'u(t)$, where the rate of change of inductance with time is the product of the inductance gradient, L', and the instantaneous speed, $u(t)$, of the plasma slug carrying the discharge current. The plasma speed increases with time, so the impedance increases during the time power is delivered from the current source. Experience with similar circuits and electromagnetically-accelerated, changing-inductance loads indicates that the efficiency of conversion of stored energy into kinetic energy can attain values of 30 - 50 %.

Initial plans anticipated that examination of the effects of current waveform on PPT performance could be performed using a pulse-forming network (PFN). A survey of candidate capacitors for the PFN, however, indicated that, at the voltages (~ 1-3 kV) and total energies (< 100 J) appropriate to PPTs for near term application, values of stored-energy per unit mass and discharge current are too low to permit a multi-element

PFN. Problems also existed in terms of high values of parasitic inductance and low tolerance for voltage reversal.

Other circuit and power system arrangements were considered with the intent of providing a reasonably constant vs oscillatory current waveform to the PPT. These arrangements included inductive storage and switching, and also special, rotating machinery. The basic problem remained that while various approaches permitted very high values of stored-energy per unit mass (> 100 kJ/kg) such values are practical only at very high energies (> 1 MJ). Capacitive energy storage remains the proper choice at lower energies for high current discharges. To achieve adequate stored-energy per unit mass, however, the charging voltage is much higher than the voltage needed across the PPT discharge (~ 1000 vs 100 V).

A new circuit arrangement was devised to allow capacitive energy storage at high voltage to couple efficiently to the PPT discharge. This circuit is described in detail in Ref. 18, which is included in Appendix IV for convenience. Briefly, a single capacitor delivers its energy to an inductor, which is then "crowbarred" by the PPT. Energy transfer from the capacitor to the inductive store is very efficient. The inductance value is chosen to obtain the desired discharge current given the charging-voltage needed for high energy density in the capacitor. For example, an available 10 µf capacitor stores 50 J at 3.2 kV and would provide a peak current of 10 kA to an inductor store of 1 µh in about 5 µsec. This same inductive store would be drained of its energy by a discharge impedance of 10 mΩ in a characteristic time of 100 µsec. Energy transfer from an inductive store to a resistive or increasing-inductance load is also an efficient process.

The actual behavior of the new circuit is somewhat more complicated than the sequence of separate events for charging and discharging an inductive store. For example, there is a reversal of voltage on the capacitor. This reversal, however, is relatively small (< 15 % of initial voltage), and is much less than the repeated reversals experienced by the capacitor in the oscillatory discharges of present PPTs.

A variation on the use of the PPT with the new inductive circuit is also described in Ref 18, and consists of arranging the plasma flow geometry and system timing to achieve quasi-steady operation. Such operation could allow factor of 3 - 5 improvement in both efficiency and specific impulse over present PPT systems.

CONCLUDING REMARKS

The research activities sponsored under the present grant covered a broad range of topics of interest to plasma propulsion. The original directions of research involved the use of solenoidal magnetic fields to improve plasma thruster performance. Two different types of arrangement were investigated, a quasi-steady MPD thruster followed by a solenoidal field, and a steady-state MPD thruster with the solenoidal field at maximum value within the thrust chamber. In both arrangements, the important physical phenomenon determining the usefulness of a "magnetic nozzle" is the separation of magnetic flux and the plasma flow. For the case of a solenoidal field placed downstream of a plasma thruster (with magnetic flux from the external solenoid largely excluded from the thrust chamber), the exhaust flow first encounters converging magnetic field lines, which tend to collimate the diverging flow from the thrust chamber. Such convergence of a supersonic flow, however, also drives it toward a sonic condition. Meanwhile, magnetic flux of the solenoidal field diffuses into the plasma. Both this resistive diffusion and the flow convergence tend to increase the plasma temperature, thereby transferring energy to internal states of the plasma (and also to radiation).

Subsequent expansion of the plasma flow as the solenoidal magnetic field-lines diverge allows a portion of the internal energy of the plasma to be returned to directed kinetic-energy. Diffusion of magnetic flux out of the plasma must also occur. The resistive heating associated with such diffusion requires the loss of energy from the plasma flow. Thus, the magnetic nozzle shares the problems of solid-wall nozzles in regard to loss of flow energy and momentum. The usual viscous boundary-layer of conventional nozzles is replaced by the magnetic-diffusion skin-depth. The performance of a conventional nozzle suffers as the (viscous) Reynolds number becomes small, and that of a magnetic nozzle similarly decreases with lower magnetic Reynolds number. For typical MPD thrusters (with specific-impulse values < few 1000 sec), minimum diameters for the exhaust flow should be tens of centimeters to operate a magnetic nozzle without substantial loss due to magnetic diffusion. Such dimensions will usually demand high power in the exhaust flow, which will imply pulsed (or quasi-steady) operation if the mission power is less than several megawatts.

The case of the applied-field MPD thruster, in which the maximum of the solenoidal field occurs inside the thrust chamber has similar difficulties in using the solenoidal field as a magnetic nozzle. Unless azimuthal Hall currents generated in the thrust chamber are sufficient to create axial magnetic fields that counter the applied field over most of the cross-section of the plasma flow, magnetic flux from the external coil will be largely diffused throughout the plasma. Extraction of this flux from the plasma exhaust results in the same loss of flow energy previously discussed. The diverging field acts as a magnetic brake, not a nozzle. In order to accomplish a magnetic nozzle, the plasma flow must be *borne* on the field lines, not *born* on them.

The application of insights gained in our research on MPD thrusters with applied magnetic fields will have to await new initiatives to develop such devices. Similarly, our success in achieving a first-principles model that allows design and scaling of orificed hollow-cathodes will become important only when empirical data, gathered over a few decades is no longer adequate to guide the design of new devices. The potential for developing a hollow cathode at levels and dimensions appropriate for plasma thrusters, including arcjets and MPD thrusters is clearly available using our model. The use of this model in such work remains a future possibility.

The most recent work on pulsed plasma microthrusters offers the opportunity to design new arrangements and operating modes for a device that has proven itself over two decades of application in space. Such design activity appears to be increasing for the near future, as spacecraft missions at modest power call for the kind of robust simplicity that permitted early entry of PPTs into the inventory of practical space thrusters. Work at Ohio State, under a new grant sponsored by NASA Lewis Research Center, is therefore proceeding and will be the subject of future reports and papers. This work includes the operation of a benchmark PPT arrangement [19], the design of which began under the present grant.

REFERENCES

1. T. M. York, C. Zakrzwski, G. Soulas, "Diagnostics and Performance of a Low-Power MPD Thruster with Applied Magnetic Nozzle", J. Propulsion and Power 9, 553 (1993).

2. C. Zakrzwski, "Experimental Investigation of a 1/4-Scale Magnetoplasmadynamic Thruster Without and With Applied Magnetic Nozzle Fields", MS Thesis, Department of Aeronautical and Astronautical Engineering, The Ohio State University. June, 1990.

3. G. C. Soulas, "Applied Magnetic Field Nozzle Effects on a Scaled Magnetoplasmadynamic Thruster", MS Thesis, Department of Aeronautical and Astronautical Engineering, The Ohio State University. April, 1991.

4. "Qualitative Spectroscopic Study of Magnetic Nozzle Flow", with T. Umeki, AIAA Preprint 92-3161 (1992).

5. H. Kamhawi, "Variable Applied Magnetic Nozzle Effects in a Magnetoplasmadynamic Thruster", MS Thesis, Department of Aeronautical and Astronautical Engineering, The Ohio State University. December, 1993.

6. P.G. Mikellides, P.J. Turchi and N.F. Roderick, "Analysis of Applied-Field Plasma Thrusters Using the MACH2 Code", 30th AIAA/SAE/ASME/ASEE Joint Propulsion Conference, Indianapolis, IN, (June 27 - 29, 1994). AIAA Preprint 94-3338.

7. P.G. Mikellides, P.J. Turchi and N.F. Roderick, "Theoretical Model for Applied-Field MPD Thrusters", 31st AIAA/ASME/SAE/ASEE Joint Propulsion Conference, 10 - 12 July 1995, San Diego, CA. AIAA Preprint 95-2676.

8. P.G. Mikellides, "A Theoretical Investigation of Magnetoplasmadynamic Thrusters", PhD. dissertation, Department of Aeronautical and Astronautical Engineering, The Ohio State University. December, 1994.

9. D.B. Fradkin, "Analysis of Acceleration Mechanisms and Performance of an Applied Field MPD Arcjet", PhD. dissertation, Princeton University Department of Aerospace and Mechanical Sciences Report 1088-T (1973).

10. A. Salhi, "Theoretical and Experimental Studies of Orificed Hollow Cathode Discharges", PhD. dissertation, Department of Aeronautical and Astronautical Engineering, The Ohio State University. December, 1993.

11. A. Salhi and P.J. Turchi, "Theoretical Modeling of Orificed Hollow Cathode Discharges", submitted to Journal of Propulsion and Power, September 1994.

12. A. Salhi, P.J. Turchi and R.M. Myers, "Experimental Investigation of a Hollow Cathode Discharge", ibid.

13. A. Salhi and P.J. Turchi, "Scaling Relations for Design and Operation of Orificed-Hollow Cathodes", 30th AIAA/SAE/ASME/ASEE Joint Propulsion Conference, Indianapolis, IN, (June 27 - 29, 1994). AIAA Preprint 94-3133.

14. P.J. Turchi and A. Salhi,"Low Power Plasma Thruster Based on a Hollow Cathode Discharge", ibid. AIAA Preprint 94-3126.

15. P.G. Mikellides and P.J. Turchi,"Modeling of Ablation-Fed Pulsed Plasma Thrusters", 31st AIAA/ASME/SAE/ASEE Joint Propulsion Conference, 10 - 12 July 1995, San Diego, CA. AIAA Preprint 95-2915.

16. P.G. Mikellides and P.J. Turchi, "Modeling of Late-Time Ablation in Teflon Pulsed-Plasma-Thrusters", 32nd AIAA/ASME/SAE/ASEE Joint Propulsion Conference,1 - 3 July 1996, Lake Buena Vista, FL. AIAA Preprint 96-2733.

17. R.J. Leiweke, P.J. Turchi, H.Kamhawi, R.M. Myers, "Experiments with Multi-MaterialPropellants in Ablation-Fed Pulsed Plasma Thrusters", 31st AIAA/ASME/SAE/ASEE Joint Propulsion Conference, 10 - 12 July 1995, San Diego, CA. AIAA Preprint 95-2916.

18. P.J. Turchi, R.J. Leiweke and H. Kamhawi, "Design of an Inductively-Driven Pulsed Plasma Thruster," 32nd AIAA/ASME/SAE/ASEE Joint Propulsion Conference,1 - 3 July 1996, Lake Buena Vista, FL. AIAA Preprint 96-2731.

19. H. Kamhawi, P.J. Turchi, R.J. Leiweke and R.M. Myers, "Design and Operation of a Laboratory Bench-Mark PPT", ibid. AIAA Preprint 96-2732.

FINAL REPORT Grant No. NAS 3 - 843

APPENDIX I

EXPERIMENTAL STUDIES OF MAGNETIC NOZZLE EFFECTS ON PLASMA THRUSTERS

T. M. York, C. Zakrzwski, G. Soulas, "Diagnostics and Performance of a Low-Power MPD Thruster with Applied Magnetic Nozzle", J. Propulsion and Power 9, 553 (1993)

JOURNAL OF PROPULSION AND POWER
Vol. 9, No. 4, July–Aug. 1993

Diagnostics and Performance of a Low-Power MPD Thruster with Applied Magnetic Nozzle

T. M. York,* C. Zakrzwski,† and G. Soulas†
Ohio State University, Columbus, Ohio 43210

This study evaluates the performance of a 50–150-kW thruster which was $\frac{1}{4}$-scale of a bench mark magnetoplasmadynamic (MPD) thruster; it was operated with and without applied magnetic nozzle fields. Capacitors (14 μF) and inductors (80 μH) in networks produced relatively constant currents for about 450 μs to generate the applied magnetic nozzle, and currents up to 2.3-kA constant for about 300 μs to drive the thruster. With the solid copper electrode, the applied magnetic field was excluded from the thrust chamber because of the short duration of the experiments. The $\frac{1}{4}$-scale device was mass starved below $\dot{m} = 0.135$ g/s; this was equivalent to 2 g/s for a full-scale MPD thruster with the same $\dot{m}/A$. With $\dot{m} > 0.25$ g/s, the device was found to operate smoothly and with little evident erosion. Current-voltage records were similar with and without applied magnetic nozzle fields, indicating little effect of the external nozzles on the power deposition. The current plume in the expansion region outside the thruster chamber was reduced in axial extent with the application of the magnetic nozzle in this transient experiment. Momentum flux in the exhaust flow was measured by local pressure probes. For the same arc power, impact pressures with magnetic nozzles applied were 3–4 times larger than the self-field cases. Also, impact pressure increased with thruster power. For the 1.15- and 2.30-kA cases, thrust from integrated impact pressure increased by a factor of 1.6 with magnetic nozzles applied. Local electron density and temperature were determined using Langmuir probes; these values along with impact pressure were used to determine flow velocity. For the 1.15- and 2.30-kA cases, values of exhaust velocity increased by factors of 1.1 and 1.6, respectively, when the magnetic nozzles were applied.

Nomenclature

A_{cs} = cross-sectional area
B = magnetic induction
e = charge of electron
f = force per volume
I = discharge current
j = current density
k = Boltzman constant
l = length
m = particle mass
$\dot{m}$ = propellant mass flow rate
n = number density
Q = collision cross section
R = electrical resistance
r = radial dimension
$R_{A,C}$ = radius of anode, cathode
RC = resistance-capacitance time constant
Re_m = magnetic Reynolds number
T = temperature
T_{em} = electromagnetic thrust component
T_{eth} = electrothermal thrust component
U_{em} = electromagnetic velocity component
V = voltage
z = axial dimension
z_{ac} = axial length of the arc discharge electrodes
λ = coulomb collision parameter
λ_D = Debye length
λ_{in} = ion-neutral mean free path
μ = magnetic permeability
σ = conductivity

Subscripts
EMF = electromotive
e = electron
eff = effective
enc = enclosed
F = electrode fall
f = fully ionized
Ω = Ohm
TOT = total
w = weakly ionized

Introduction

ALTHOUGH a practical magnetoplasmadynamic (MPD) thruster has yet to be used for primary space propulsion, the MPD thruster may be the best realistic candidate to perform a variety of missions.[1,2] Proposed missions would require[2] an MPD thruster operating in the 10–100-kW power range with a specific impulse of 1000–3000 s. At such power levels the efficiency of self-field MPD thrusters, which rely solely on magnetic fields generated by the current through the propellant, is unacceptably low.[2] The use of an applied magnetic field which can act as a nozzle for the plasma flow may also serve to reduce frozen flow losses, and therefore, increase the efficiency of the thruster.[3–11] Presently, the physical processes that occur in the flow from a thruster with an applied magnetic field acting as a nozzle are not well understood.

A comprehensive review of MPD thruster performance was recently reported[1]; also, an overview of work performed on applied-field thrusters had been given by Seikel et al.[2] For devices operating in the 10–100-kW range, even at modest applied fields (0.1–0.15 T), thrust efficiencies were shown to improve. Studies of the effects of applied fields on the performance of megawatt-level pulsed thrusters were also re-

---

Presented as Paper 90-2665 at the AIAA/DGLR/JSASS 21st International Electric Propulsion Conference, Orlando, FL, July 18–20, 1990; received Jan. 28, 1991; revision received March 6, 1993; accepted for publication March 24, 1993.

*Professor, Aeronautical and Astronautical Engineering Department. Member AIAA.

†Graduate Research Associate, Aeronautical and Astronautical Engineering Department.

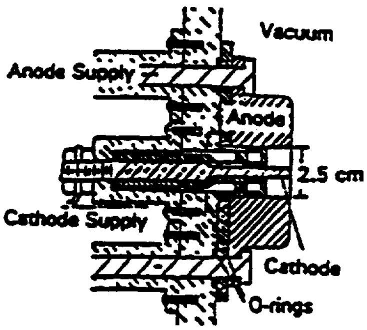

Fig. 1 Schematic of ½-scale thruster.

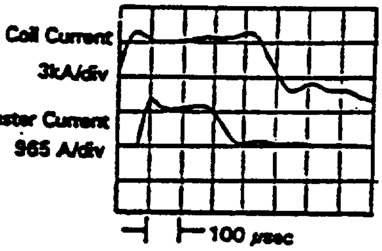

Fig. 2 Current waveforms for ½-scale thruster and applied magnetic field coil.

ported,[3] however, the acceleration processes in such devices were not understood. More extensive diagnostic studies were carried out on an applied-field pulsed megawatt MPD thruster experiment by Michels and York.[4,5] Results demonstrated that thrust and efficiency increased with applied fields. Derived values of thrust were observed to increase monotonically (*B*) with applied magnetic field strength.

Extensive diagnostic work was performed on a 25-kW applied-field lithium MPD thruster by Fradkin et al.[6] It was found that exit velocities approached 3×10^4 m/s, and thrust efficiencies approached 50%. A model proposed that the dominant acceleration contribution came from the conversion of rotational energy into directed energy by expansion in a magnetic nozzle.

In other work, Kimura and Yoshihiro[7] studied the reaction forces on a 300–1500 A MPD thruster and its surrounding magnetic nozzle coil; thrust stand measurements showed that thrust increased with magnetic field strength, which was varied up to 0.4 T. Tahara et al.[8] studied two versions of pulsed MPD thrusters which operated between 5–15 kA with various configurations of applied fields; field-related improvements included decreased discharge voltage, increased thrust, and decreased cathode erosion. Arakawa and Sasoh[9] studied a 10-kW power level thruster fitted with permanent magnets; electromagnetic forces related to the applied field contributed to a large percentage of the thrust. In an experimental study of significance to the present work, Kuriki and Okada[10] studied the effects of a magnetic nozzle arrangement on plasma generated by an 800-A arcjet. With T_e = 4000 K and $n_e = 5 \times 10^{13}$ cm^{-3}, the magnetic nozzle channeled the flow within the field lines and an electromagnetic force was involved in accelerating the weakly ionized plasma.

A more recent investigation of 100-kW class applied-field MPD thrusters was carried out by Mantenieks et al.[11] For all configurations tested, thrust increased with increased applied-field strength; for one configuration, the thrust increased by 64% when the magnetic field was increased to 0.3 T.

With the limited power available in space (100 kW), smaller size devices have the potential to be more efficient at low power levels.[12-14] Although various geometries (configurations)[12] have been evaluated, investigations of MPD thruster scaling have primarily considered pulsed thrusters operating in the megawatt range.[13,14] Gilland and Kelly[15] carried out a study of self-field MPD scaling using full- and ½-scale versions of both the bench mark and flared anode thrusters. The full-scale devices were found to be more efficient for almost all power levels at equivalent specific impulses. In the light of such conflicting evidence, it is important to attempt to clarify the performance of arc and MPD arc devices of various sizes and power levels.

Apparatus

½-Scale MPD Thruster

A schematic of the ½-scale MPD thruster is shown in Fig. 1. The thruster was constructed with a solid copper anode having an i.d. of 2.5 cm and an o.d. of 4.5 cm, and a solid 2% thoriated tungsten cathode having a diameter of 0.5 cm. The lengths of the anode and cathode were 1.25 cm, measured from the boron nitride backplate. This thruster was fashioned after the Air Force Aeronautics Laboratory (AFAL) ½-scale variable-geometry MPD thruster, so that direct comparisons between the two devices could be made. The propellant studied was nitrogen, which allowed comparison with earlier work.[4,5] The boron nitride backplate had 15 holes drilled to serve as gas feed ports.

Propellant was injected by means of a specially designed gas feed system. The components of this system included a reserve gas plenum, the plenum in the thruster, and a high-speed electrical valve between the plena. The electrical valve (Skinner model VS20B2100), with ¼-in.-diam passage, was overdriven to achieve fast opening. The pressure was seen to increase linearly for 5 ms, and then remain constant at the pressure of the reserve plenum. Mass flow rate determined from pressure probes in the chamber agreed with that determined from pressure drop in the reserve plenum.

The thruster pulse forming network (PFN) was designed to produce a 300-μs current pulse with amplitudes ranging from 0.7- to 2.3-kA constant for a quasisteady period of 200 μs. The magnetic nozzle system was designed to produce a 500-μs pulse for the solenoidal coil with currents between 1.3- and 2.7-kA constant for a quasisteady period of approximately 450 μs. The major components of each of the discharge systems included the PFN, switches for the PFN, a dc power supply capable of charging the PFN over a range of different voltages, and a timing system to control the firing sequence.

The PFN were separate inductance-capacitance (L-C) ladders operated independently. Typical current records are presented in Fig. 2; the thruster PFN was charged to 7 kV, and the magnetic field coil PFN to 13 kV. The thruster current was delayed 70 μs from the start of the magnetic field current; this delay allowed the magnetic field to establish itself before the steady-state portion of the thruster current occurred.

The main components of the vacuum system included 6-in.-diam "cross" and "T" shape Pyrex® ducts, a vacuum pump, gate valves, and vacuum gauges. These components were assembled to provide the optimum arrangement for thruster, magnetic field coil, and the performance of diagnostic studies. The thruster was mounted on one arm of the cross, with the coil encircling the vacuum vessel. The base pressure achieved in this system was less than 1 mTorr; the total volume enclosed above the gate valve was 0.0304 m^3.

Diagnostics Devices

Two Rogowski loops were used to monitor circuit currents; calibrations (with integrator time constant = 8.84 ms) were carried out with ringing L-C discharges. A 1000:1 voltage probe (P6105 High Voltage Probe, Tektronix, Portland, Oregon) was used.

Axial magnetic field probes and several probes that measured radial/azimuthal magnetic fields were fabricated from multiturn loops placed in a 6-mm o.d. Pyrex tube with a sealed end. The axial probe had 50 turns in 14-mm length; the radial/azimuthal probe had 140 turns in 3-mm length. An active integrator[14] was used. Calibration was carried out with a single-turn solenoid driven by an L-C discharge.

A pressure probe was used in this study to measure the impact pressure in the expansion region of the ¼-scale MPD thruster; it utilized a piezoelectric transducer enclosed in a 1-cm-diam quartz tube, sealed squarely at the end.[4] The system included a battery powered 10× amplifier and follower unit. A 1-cm-long, 1-cm-diam Pyrex isolator was attached to the sensing end of the quartz tube; it eliminated initial stress waves and acted as a thermal insulator. Probes were calibrated in a shock tube.

A double langmuir probe was used to determine electron temperature and number density in the exhaust. The probe electrodes were 0.127-mm-diam tungsten wire, 1-cm long and separated by a distance of 5 mm. The voltage bias across the probe elements was supplied by a variable charge 500-μF capacitor. The probe current was monitored with a Tektronix P6021 current probe.

Operating Conditions—Scaling Considerations

The variation of the size of thrusters is fundamental to the scaling process. Values for the sizes of thrusters of interest here are shown in Table 1.

The mass flow rate was scaled so that the mass flux ($\dot m/A_{an}$) of gas in the discharge chamber remained a constant; accordingly, the ¼-scale thruster mass flow rate was defined as $\frac{1}{16}$ the full-scale value (Table 1). Mass starvation effects were evident, and an acceptable mass flow rate for this device was determined by experiment to be 0.135 g/s.

Since the applied field did not penetrate the discharge chamber, the scaling of the ¼-size thruster will be treated as a self-field device. Some parameters considered when scaling thrusters are given in Table 1. While U_{em} has been used to scale thrusters, this study attempted to scale based on plasma interactions being locally equivalent to full scale: $\bar{j} \times \bar{B}$ and $\dot m/A_{an}$ were maintained. For the electromagnetic thrust mechanism the force density can be expressed as

$$\bar{f} = \bar{j} \times \bar{B} \propto [I^2/(r^2 \cdot z)] \propto j^2 z \qquad (1)$$

With the geometry being scaled by ¼, and the specification that $\bar{j} \times \bar{B}$ be maintained from the full- to ¼-scale, the ¼-scale thruster should then be operated at currents which are ⅛ of those in full-scale thrusters. For this study, the ¼-scale thruster was operated at two current levels, 1.15 and 2.3 kA, which correspond to full-scale currents of 9.2 and 18.4 kA, respectively.

The velocity associated with the electromagnetic-thrust component can be expressed as

$$U_{em} = \frac{T_{em}}{\dot m} = \left(\frac{I^2}{\dot m}\right)\frac{\mu_0}{4\pi}\ln\left(\frac{R_A}{R_C}\right) \qquad (2)$$

So

$$U_{em} \propto \frac{I^2}{\dot m} \propto \frac{j^2}{(\dot m/A_{an})} z^2 \propto \frac{jB}{(\dot m/A_{an})} z$$

If $\bar{j} \times \bar{B}$ and $\dot m/A_{an}$ were maintained, then I (scaled) would be decreased; $U_{em} \propto z$, and so would decrease with size, in this case by a factor of ¼.

For the electrothermal thrust component, velocity scaling depends on the plasma conductivity. The input power is determined by I^2R; this is proportional to the kinetic power of the exhaust, $\dot m u_e^2/2$. Therefore, taking $\bar{j} \times \bar{B}$ and $\dot m/A_{an}$ as fixed, if the resistance across the electrodes were a constant for different devices (i.e., if sheath drops were dominant) the electrothermal velocity component would scale with $z^{1/2}$. If the conductivity of the plasma were constant and plasma voltage drops were dominant, the electrothermal velocity would be a constant for different devices.

Typical geometry and current values for the bench mark[14] full-scale thruster and for the AFAL[15] ½-scale thruster are shown in Table 1 for comparison. Since I^2 is proportional to self-field thrust, $I^2/\dot m$ is proportional to the specific impulse for the self-field MPD thruster, assuming that the electromagnetic thrust component is dominant. Operation of the ¼-scale thruster at 2.3 kA produces $I^2/\dot m$ = 39 kA²·s/g, a value appropriate for comparison with a range of thrusters.

Applied Magnetic Nozzle Fields

The applied magnetic field geometry used to guide the plasma was generated by a solenoidal coil designed to produce magnetic field lines that diverged in a reasonable manner. The magnetic coil was constructed with five layers of ¼-in.-diam solid copper wire wrapped around an 8.75-in.-o.d. PVC pipe.

Table 1 Thruster scaling parameters

			Size[a]		
Scale	Cathode radius, cm	Anode radius, cm	Anode length, cm	Cathode depth, cm	R_A/R_C
¼ (OSU)	0.25	1.25	1.25	1.25	5.0
½ (AFAL)	0.50	2.50	Variable	Variable	5.0
Full (Princeton)	0.90	5.00	10.00	5.00	5.6
		Mass flow rate[b]; electromagnetic acceleration force density[c]			
	I, kA	R_A, cm	Z_{an}, cm	$j \times B_\theta$, kN/m³	
¼-Scale	1.25	1.25	1.25	25.46	
Full-scale	10.0	5.0	5.0	25.46	
		Electromagnetic velocity component[d]			
	$\dot m$, g/s	I, kA	$I^2/\dot m$, kA²·s/g	U_{em}, m/s	
Princeton-full scale	2.0	18.4	157	23,500	
	2.0	10.0	46	6,900	
OSU-¼ Scale	0.14	2.3	39	5,900	
	0.14	5.0	85	12,700	

[a] Principle: preserve length proportions. [b] Principle: preserve $\dot m/A_{an}$; $\dot m_{(1/4\text{-scale})} = (\frac{1}{16})\dot m_{(\text{full-scale})}$. [c] Principle: preserve force per unit volume. [d] Principle: preserve $U_{em} = T_{em}/\dot m$.

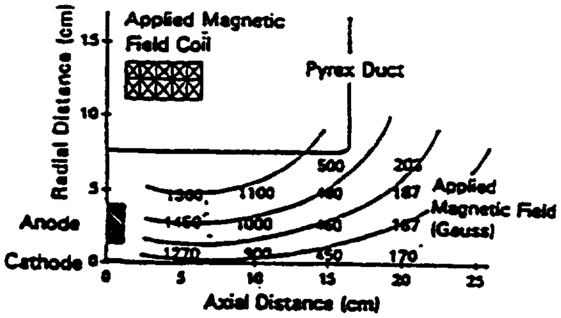

Fig. 3 Thruster, field coil, and vacuum vessel schematic with applied magnetic field lines (local values, in Gauss).

Current of 2.8 kA produced a maximum magnetic field strength of 1.27 kG along the axis of the coil when the ¼-scale thruster was in place.

The applied magnetic field strength distribution was mapped from measurements with radial and axial magnetic field probes. A sketch of the magnetic flux lines with respect to the position of the thruster is shown in Fig. 3; the throat, or minimum area, of the magnetic flux lines occurred at approximately 2.5 cm from the face of the thruster on the axis of the coil. The magnetic field distribution was influenced by the field exclusion from the solid copper anode during the time period of the experiment.

The magnitude of the magnetic field was appropriate for the confinement of the plasma with kinetic pressure ($nkT = 3 \times 10^3$ N/m^2 for $n_e = 10^{16}$ cm^3, $T_e = 2$ eV) exceeded by magnetic pressure ($B^2/8\pi = 4 \times 10^3$ N/m^2 for $B = 1$ kG).

One-Fourth Scale Thruster Experimental Data

Propellent Mass Flow Rate

The lower limit on $\dot{m}$ was determined using several diagnostics. Current-voltage characteristics for the thruster were first recorded for a mass flow rate of 0.034 g/s of nitrogen; this corresponded to 0.5 g/s full-scale. The voltage records indicated that the thruster was operating in an erratic fashion, with evident high-frequency oscillations. When the mass flow rate was increased to 0.068 g/s, the oscillations were significantly reduced, but occasionally there were still high-frequency oscillations at 1.15 kA. Local B_θ magnetic field probes in the exhaust plume showed large oscillations in the magnetic field during the steady-state portion of the thruster current history. The oscillations varied from shot-to-shot; they were typical of an unstable arc that may have been rotating.

It was concluded that the cathode was mass-starved because of an uneven distribution of gas in the discharge chamber; eight ports were located radially midway between the electrodes. To overcome this problem, seven gas ports (0.36-mm in diameter) were added around the base of the cathode, approximately 1.5 mm from the cathode radius. In the new injection configuration, a mass flow rate of 0.135 g/s was the lowest rate that produced smooth and predictable magnetic field records; these were taken as an indication of smooth discharge operation. All of the test results presented in this study used a mass flow rate of 0.135 g/s; this corresponds to a mass flow rate of 2.16 g/s for a full-scale thruster.

The background pressure for the ¼-scale MPD thruster was higher from beginning to end of the thrust period (1–7 mTorr) than those of bench mark[14] (0.1–4.0 mTorr), AFAL ¼ (0.1–3.5 mTorr) devices; however, evidence has suggested that background pressures of 10 mTorr or less have a minor effect on thrust and voltage measurements for steady-state self-field thrusters.

Current-Voltage Characteristics

Arc currents over the range of 0.86–2.3 kA were obtained by varying the thruster PFN voltage over the range of 5–13 kV. Anode-cathode voltage drops and discharge currents were measured for intervals of 0.5 kV on the thruster PFN.

The applied-field and self-field data are shown, with error bars, in Fig. 4. Each point represents data taken at a fixed time, 200 μs from the start of thruster current, for a large number (4–5) discharges of the thruster. Data were taken in intervals of 0.5 kV on the thruster PFN, going from low- to high-charge voltage and reversing the sequence; this was then repeated.

Local Magnetic Field Measurements

The current distribution in the electrical discharge of the ¼-scale MPD thruster was mapped from local azimuthal magnetic field measurements for thruster currents of 1.15 and 2.3 kA for both applied-field and self-field cases. Data were taken at radial positions varying from 0.6 to 2.5 cm, and at axial positions ranging from 0.3 to 25 cm from the backplate of the thruster.

The azimuthal magnetic field measurements were used to calculate the current enclosed within a given radius at a given axial position as

$$I_{\mathrm{enc}}(r, z) = [2\pi r B(r, z)/\mu_0] \tag{3}$$

A sketch of current profiles for self-field and applied-field cases is shown in Fig. 5; the dashed lines are extrapolations.

Impact Pressure Profiles

Radial profiles of impact pressure in the exhaust plume of the ¼-scale thruster were recorded for axial locations 5, 9, 14, and 20 cm from the face of the thruster. The pressure profiles were measured for 1.15- and 2.3-kA currents, and for both applied-field and self-field cases. The radial profiles for the 1.15-kA level are shown in Figs. 6 and 7. The pressure reported for each position is a value taken in the relatively constant current portion of individual pressure records after initial transients had terminated. The impact pressure data indicate that the exhaust plume was symmetrical about the

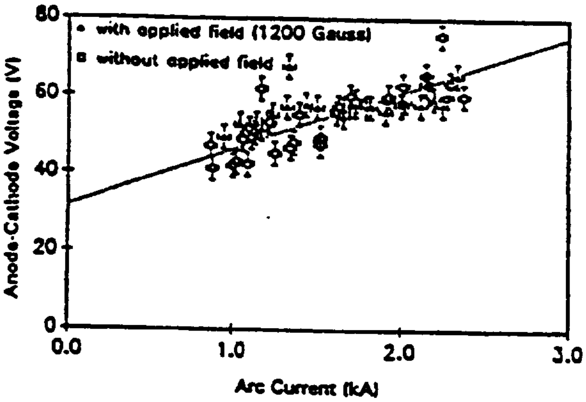

Fig. 4 Current-voltage characteristics of ¼-scale MPD arc thruster.

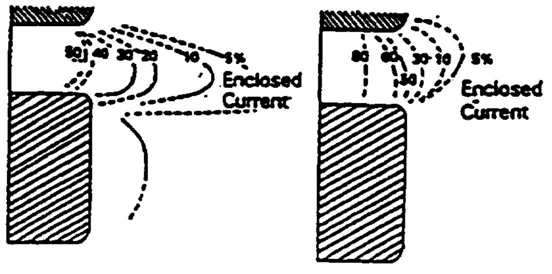

Fig. 5 Enclosed current contours without and with applied field with arc current, $I = 2.3$ kA and $\dot{m} = 0.135$ g/s.

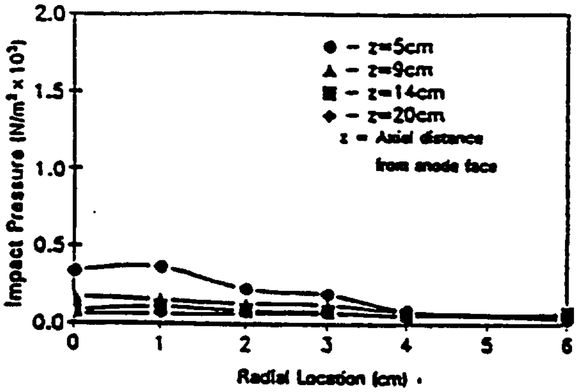

Fig. 6 Impact pressure radial profile with arc current, I = 1.15 kA, self-field.

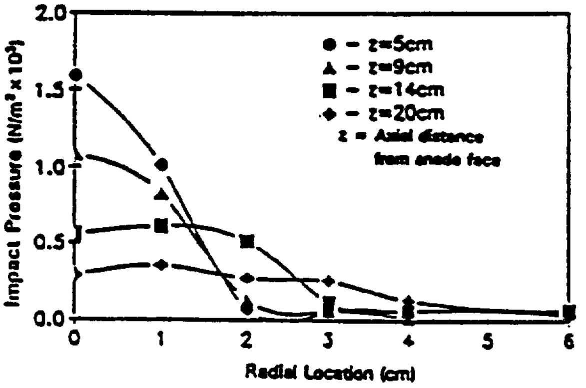

Fig. 7 Impact pressure radial profile with arc current, I = 1.15 kA, 1200 G applied field.

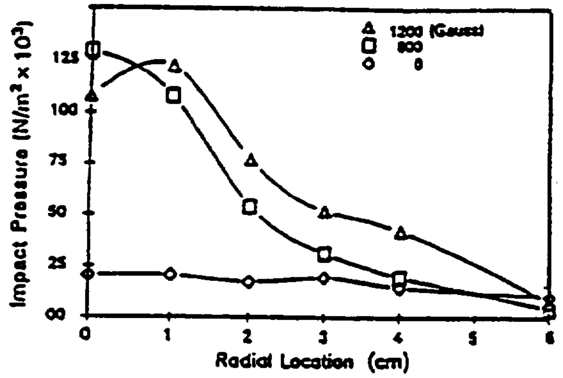

Fig. 8 Impact pressure radial profiles for self-field, 800-, and 1200-G applied fields (Z = 14 cm, I = 2.3 kA, $\dot{m}$ = 0.135 g/s).

axis and reproducible from shot-to-shot. Impact pressure data were also taken for a value of the applied magnetic field intermediate between 0 (self-field) and 1200 G. With a nominal value of 800 G at the center of the coil, impact pressure was measured at z = 14 cm with the thruster operating at 2.3 kA; pressure profiles for the 0, 800, and 1200 G cases are shown in Fig. 8.

Analysis and Interpretation of Data

Current-Voltage Measurements for the ½-Scale Thruster

The data points recorded with and without the applied nozzle followed similar trends (Fig. 5), with scatter typical of I-V data for these types of measurements. The I-V variation can be best described as linear over the range of currents studied; this indicates dominance of the electrothermal thrust component. The linear relationship for the applied-field case was found to differ only slightly from that for the self-field case, for lower (<2.0 kA) currents. At higher currents, the applied magnetic field resulted in a slight decrease in arc voltage, but this variation was within the error bars and so will not be considered quantitatively. The thruster power was determined from I-V, and the two operating conditions:

$$P_{TOT}(1.15\ \text{kA}) = 53\ \text{kW}$$

$$P_{TOT}(2.3\ \text{kA}) = 151\ \text{kW}$$

For a given current, the deposition of power can be understood from components of the total voltage across the electrodes:

$$V_{TOT} = V_{\Omega} + V_{EMF} + V_f \qquad (4)$$

$$V_{TOT} = \int j/\sigma\, dl + \int (V \times B)\, dl + V_f$$

The first term expresses the voltage drop due to the Ohmic resistance of the plasma. The second term is back-emf arising from the motion of the plasma normal to a magnetic field. The third term, V_f, is the electrode fall voltage; it includes electrode heating and plasma sheath losses. Losses due to dissociation and ionization are included in the Ohmic term and the fall voltage term. The fall voltage was determined by extrapolation of the voltage data to zero current (32.7 V). At the 1.15-kA level, the back-emf contributed 3 V, and at the 2.3-kA level it contributed 16.5 V. These estimates were made using a model for azimuthal magnetic field appropriate for MPD thruster blowing[19] and velocity values obtained from pressure measurements that will be described below.

Using the above evaluations, plasma temperatures can be estimated from the electrical conductivity of the plasma which was determined from the voltage measurements. Equation (4) can be rewritten

$$\sigma = (V_{TOT} - V_{EMF} - V_f)^{-1} \int J/(2\pi r z_0)\, dr \qquad (5)$$

Uniform current density is assumed along the electrode length, z_0, and σ is assumed to be constant; the electrical conductivities are then

$$\sigma(1.15\ \text{kA}) = 1900\ (\Omega\text{m})^{-1}$$

$$\sigma(2.3\ \text{kA}) = 2800\ (\Omega\text{m})^{-1}$$

An approximate relationship for conductivity was first given by Spitzer for fully ionized plasmas[20]

$$\sigma_f = T_e^{3/2}/(5.2 \times 10^{-5} \ln \lambda) \qquad (6)$$

where $\ln \lambda$ typically has a value of 10 for a wide range of plasma densities and temperatures, and T_e is given in eV. In a weakly ionized plasma, electron-neutral collisions dominate; in that case we have[21]

$$\sigma_{en} = 0.532[e^2/(m_e kT_e)^{0.5}][n_e/(n_n Q)] \qquad (7)$$

where n_e is the electron density, n_n is the neutral atom density, and Q is the electron-neutral atom collision cross section. Accordingly, for a plasma with an arbitrary degree of ionization the electrical conductivity can be approximated by[21]

$$\sigma = (1/\sigma_f + 1/\sigma_{en})^{-1} \qquad (8)$$

Using the above equations the electron temperatures are

$$T_e(1.15\ \text{kA}):\ 1.0\ \text{eV}$$

$$T_e(2.3\ \text{kA}):\ 1.3\ \text{eV}$$

Under the plasma conditions (n_e, T_e) in the experiment, the electron-ion equilibration time is about 3 μs, so $T_e = T_i$ is a reasonable assumption.

Current Distribution in the Exhaust Flow

For the self-field case (Fig. 5) as much as 40% of the current was blown past the end of the discharge chamber, typical for self-field MPD thrusters[14] with $Re_m \approx 10$. It has been shown to be desirable to have the current spread as far downstream as possible, because this enhances the electromagnetic thrust component.[22] However, the transient applied magnetic nozzle fields were found to restrict the discharge to a region closer to the chamber (Fig. 5). For the self-field case, 10% of the current was carried downstream a distance 2½ times the anode radius from the backplate. In contrast, for the applied-field case, 10% of the current was carried downstream a distance only 1½ times the anode radius from the backplate. For both cases, however, the same percentage of current moved past the arc chamber exit plane. With the langmuir probe indicated ×2 increase of temperature with applied nozzle, the Re_m would have increased ×3, which should enhance blowing effects. However, from the mapping of the magnetic flux lines and the tabulated values of magnetic field strengths, it is seen that the thruster exit plane lies in a region of converging magnetic field. It is probable that the magnetic field affected the confinement of the plasma carrying the current, holding it further upstream and channeling it along the axis through the magnetic nozzle in this transient discharge. The position $z = 2$ cm was the axial location nearest the thruster exit at which impact pressure was measured. For the self-field case $z = 2$ cm and $r = 1$ cm, the impact pressure was 3.9×10^3 N/m², while the calculated magnetic pressure at this point was 3.7×10^3 N/m².

Impact Pressure Measurements

From the impact pressure data, it is concluded that the applied magnetic nozzle fields significantly affected the plasma: the magnitude of the impact pressure increased within a 3-cm radius of the centerline for all axial positions. The magnitude of the discharge current also affected impact pressure, although 1.15- and 2.3-kA thruster currents exhibited similar radial profiles. The self-field pressure profiles for 1.15 kA (Fig. 6) have peak values of 100–400 Nm^{-2}, with e^{-1} radii of about 3 cm. Impact pressure decreased in magnitude downstream. The applied field pressure profiles are significantly different. For both 1.15- and 2.3-kA current levels a Gaussian-shaped profile was evident at the $z = 5$- and 9-cm locations, with the majority of the momentum flux being confined within a 2-cm radius. For the 1.15-kA level, peak pressures were 1500 Nm^{-2} and e^{-1} radius was about 1 cm, while for the 2.3-kA level the peak pressure was 3800 Nm^{-2} and e^{-1} radius was about 2 cm. At the $z = 14$-cm position the momentum flux for 1.15 kA was confined within the 3-cm radius, but for the 2.3-kA level, significant momentum flux occurred out to 5-cm radius. At the 20-cm location, both the 1.15- and 2.3-kA applied-field cases demonstrated broad, flat radial profiles.

The above data demonstrate that the applied magnetic nozzle fields generated impact pressures that were significantly higher than those for the self-field discharges at the same power level; the fields confined the plasma flow to smaller radii and allowed more gradual expansion. This is consistent with a degree of balance between the pressure from the applied magnetic field and the internal kinetic pressure of the plasma. Earlier reported experimental results[23] had shown that for a plasma in magnetic nozzle configurations, the plasma expansion was controlled by the magnetic pressure and was not controlled primarily by the shape of the magnetic field lines.

Langmuir Probe Measurements

The current-voltage characteristics of the cylindrical double langmuir probe were reduced to provide values of local electron temperature and electron number density. Analysis of the data included evaluation of the effects of low density (enhanced Debye collection), collisions, and magnetic field[24] on the particle collection. The size of the probe ($r = 6.35 \times 10^{-5}$ m) was on the order of the mean free paths ($\lambda_{ei} = 5 \times 10^{-5}$ m, $\lambda_{ie} = 5 \times 10^{-5}$ m) and Debye length ($\lambda_d = 10^{-6}$–10^{-7} m). Collision effects proved to be minimal, but corrections for the enhanced collection due to thick sheaths were necessary; the approximate method of Kiel[24] was used. Regarding applied magnetic field effects, ion and electron Larmor radii were large enough to allow the weak B-field approximation[24] to be made.

Radial variations of electron density and temperature generally reinforce the conclusion from impact pressure data, i.e., less uniform and more highly peaked distributions with the applied field nozzles. Specifically, for the self-field discharges the plasma was ejected with relatively uniform temperature; neither T_e or N_e was strongly focused on axis.

Axial variations of T_e and N_e (Figs. 9 and 10) show that, generally, both were higher for the applied-field cases than for the self-field cases. As with the impact pressure data, values of T_e and N_e with applied-field were much larger near the axis. As power input was the same without and with applied field nozzles, it can be concluded that compression effects were significant within the magnetic nozzle fields. These effects of magnetic nozzles are similar to those reported by Kuriki and Okada,[19] who examined flow from a lower current (800 A) arcjet in a much larger vacuum vessel and with a large gap between the arc plasma source and the nozzle fields.

Temperatures for the self-field cases determined from local langmuir probes are in reasonable agreement with the temperatures estimated from conductivity. With the magnetic nozzle fields applied, however, there was a temperature enhance-

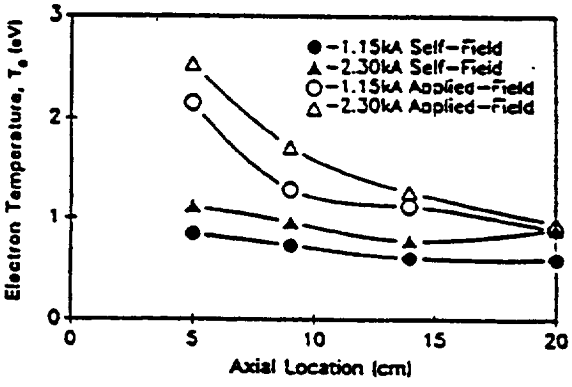

Fig. 9 Axial variation of Te from langmuir probe data.

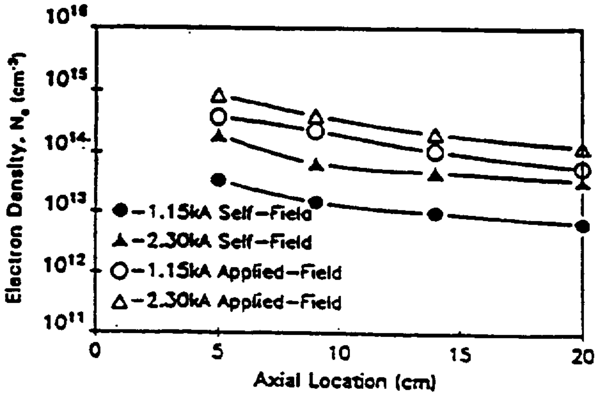

Fig. 10 Axial variation of Ne from langmuir probe data.

Table 2 One-fourth scale thruster performance parameters

	Electrothermal thrust, N	Electromagnetic thrust, N	Total thrust, N	Flow velocity, m/s
		1.15-kA Case		
Self-Field				
Theoretical	0.80	0.31	1.11	8,300
Experimental	—	—	1.17 (P^a)	6,950 (L, P^b)
Applied-Field				
Theoretical	0.80	0.31	1.11	8,300
Experimental	—	—	1.82 (P)	11,080 (L, P)
		2.30-kA Case		
Self-Field				
Theoretical	0.90	1.25	2.15	16,100
Experimental	—	—	3.02 (P)	10,030 (L, P)
Applied-Field				
Theoretical	0.90	1.25	2.15	16,100
Experimental	—	—	5.02 (P)	11,100 (L, P)

[a] P: Det. using impact pressure. [b] L, P: Det. using N_e, T_e from Langmuir, nmv^2 from pressure.

ment in the plasma which was not related to a voltage increase in the discharge chamber.

Thrust and Exhaust Velocity Evaluations

Using electrical discharge parameters, theoretical values of electrothermal and electromagnetic thrust for the device were evaluated. For the self-field discharge, electrothermal thrust was estimated using a limiting value which assumes complete expansion, $T_{eth} = \dot{m}(2C_pT_0)^{1/2}$; while the electromagnetic component was calculated using

$$T_{em} = (\mu_0 J^2/4\pi)[\ln(R_A/R_C) + \tfrac{3}{4}] \qquad (9)$$

Since the applied magnetic fields did not enter the discharge chamber and the power input with applied field nozzles did not change, these values will also be used for comparison with applied nozzle experiments.

Experimental values of thrust were evaluated by integrating impact pressure over a cross section of jet at an axial location where pressure signals reached their maximum. Values of velocity were evaluated from input pressure data, using N_e and T_e from langmuir probes. Using theoretical total thrust values, an effective velocity was evaluated from $U_{ef} = T/\dot{m}$. A compilation of plasma acceleration parameter is presented in Table 2. It can be concluded that for the self-field discharge, thrust increased with increased power. However, in both cases, the exhaust velocities derived from experiment were lower than the theoretical estimates by factors of 0.85 and 0.62. With the addition of applied magnetic nozzles, the thrust increased for both power levels by a factor of 1.6. The exhaust velocity derived from experiment increased by factors of 1.6 (1.15 kA) and 1.1 (2.3 kA) with the applied magnetic nozzles. These values of exhaust velocity derived from experiment were lower and higher than the theoretical estimates, so the details of plasma expansion in the two cases appear to be different.

Conclusions

The influence of applied magnetic nozzles on the performance of a low-power MPD thruster was examined in the unique condition where the magnetic field did not penetrate the discharge chamber or alter the power delivered to the thruster. The applied magnetic nozzles resulted in increased plasma density and temperature in the exhaust flow outside the discharge chamber. Thrust and exhaust velocities derived from experimental data were found to increase by factors of 1.6, due to the applied magnetic nozzles.

References

[1] Sovey, J. S., and Mantenieks, M. A., "Performance and Lifetime Assessment of MPD Arc Thruster Technology," AIAA Paper 88-3211, July 1988.

[2] Seikel, G. R., York, T. M., and Condit, W. C., "Applied-Field Magnetoplasmadynamic Thrusters for Orbit-Raising Missions," *Orbit-Raising and Maneuvering Propulsion: Research and Needs*, edited by L. H. Caveny, Vol. 89, Progress in Astronautics and Aeronautics, AIAA, New York, 1984, pp. 260–286.

[3] Connolly, D. J., Bishop, A. R., and Seikel, G. R., "Tests of Permanent Magnet and Superconducting Magnet MPD Thrusters," AIAA Paper 71-196, June 1971.

[4] Michels, C. J., and York, T. M., "Pressure Measurements in the Exhaust of a Pulsed Megawatt MPD Arc Thruster," AIAA Paper 71-196, Jan. 1971.

[5] Michels, C. J., and York, T. M., "Exhaust Flow and Propulsion Characteristics of a Pulsed MPD Arc Thruster," AIAA Paper 72-500, April 1972.

[6] Fradkin, D. B., Blackstock, A. W., Roehling, D. J., Stratton, T. F., Williams, M., and Liewer, K. W., "Experiments Using a 25-kW Hollow Cathode Lithium Vapor MPD Arcjet," *AIAA Journal*, Vol. 8, May 1970, pp. 886–894.

[7] Kimura, I., and Arakawa, Y., "Effect of Applied Magnetic Fields on Physical Processes in an MPD Arcjet," *AIAA Journal*, Vol. 15, May 1977, pp. 721–724.

[8] Tahara, H., Kagaya, Y., and Yoshikawa, T., "Quasi-Steady MPD Arcjets with Applied Magnetic Fields," AIAA Paper 85-2001, Oct. 1985.

[9] Arakawa, Y., and Sasoh, A., "Steady-State Permanent Magnet Magnetoplasmadynamic Thruster," *Journal of Propulsion and Power*, Vol. 3, No. 3, 1989, pp. 301–304.

[10] Kuriki, K., and Okada, O., "Experimental Study of Plasma Flow in a Magnetic Nozzle," *Physics of Fluids*, Vol. 13, Sept. 1970, pp. 2262–2268.

[11] Mantenieks, M. A., Sovey, J. S., Myers, R. M., Haag, T. W., and Raitano, P., "Performance of a 100 KW Class Applied Field MPD Thruster," AIAA Paper 89-2710, July 1989.

[12] King, D. Q., Smith, W. W., Jahn, R. G., and Clark, K. E., "Effect of Thrust Chamber Configuration on MPD Arcjet Performance," AIAA Paper 79-2051, Oct. 1979.

[13] Mead, F. M., and Jahn, R. G., "Scaling of MPD Thrusters," AIAA Paper 79-2075, Oct. 1979.

[14] Kaplan, D. L., "Performance Characteristics of Geometrically Scaled MPD Thrusters," M.S. Thesis, Princeton Univ., Princeton, NJ, Feb. 1982.

[15] Gilland, T. H., Kelly, A. J., and Jahn, R. G., "MPD Thruster Scaling," AIAA Paper 87-0997, May 1987.

[16] Minns, F. M., III, *Engineer's Mini-Notebook: Op-Amp Circuits*, Archer Pub., Ft. Worth, TX, 1985.

[17] York, T. M., "Stress Dynamics in High Speed Piezoelectric Pressure Probes," *Review of Scientific Instruments*, Vol. 41, April 1970, pp. 519–521.

[18] Kenney, T. M. P., "Measurements of Pressure Profiles in the Exhaust Plume of a Magnetoplasmadynamic Thruster," M.S. Thesis, Pennsylvania State Univ., University Park, PA, Dec. 1987.

[19] Jahn, R. G., *Physics of Electric Propulsion*, McGraw-Hill, New York, 1969.

[20] Chen, F. F., *Plasma Physics and Controlled Fusion*, Plenum Press, New York, 1984.

[21] Pai, S.-I., *Magnetogasdynamics and Plasma Dynamics*, Prentice-Hall, Englewood Cliffs, NJ, 1962.

[22] Yoshikawa, T., Kagaya, Y., and Tahara, H., "Thrust Measurement of a Quasi-Steady MPD Arcjet," AIAA Paper 85-2003, Oct. 1985.

[23] York, T. M., Mikellides, P., and Jacoby, B. A., "Plasma Flow Processes Within Magnetic Nozzle Configurations," *Journal of Propulsion and Power*, Vol. 8, No. 5, 1992, pp. 1023–1030.

[24] Chung, P. M., Talbot, L., and Touryan, K. J., *Electric Probes In Stationary and Flowing Plasma: Theory and Application*, Springer-Verlag, New York, 1975.

FINAL REPORT Grant No. NAS 3 - 843

APPENDIX II

NUMERICAL MODELING OF APPLIED-FIELD MPD THRUSTERS

P.G. Mikellides, P.J. Turchi and N.F. Roderick, "Analysis of Applied-Field Plasma Thrusters Using the MACH2 Code", 30th AIAA/SAE/ASME/ASEE Joint Propulsion Conference, Indianapolis, IN, (June 27 - 29, 1994). AIAA Preprint 94-3338

P.G. Mikellides, P.J. Turchi and N.F. Roderick, "Theoretical Model for Applied-Field MPD Thrusters", 31st AIAA/ASME/SAE/ASEE Joint Propulsion Conference, 10 - 12 July 1995, San Diego, CA. AIAA Preprint 95-2676

AIAA 94-3338

ANALYSIS OF APPLIED-FIELD PLASMA THRUSTERS USING THE MACH2 CODE

P.G. Mikellides and P.J. Turchi
Ohio State University
Columbus, OH

N.F. Roderick
University of New Mexico
Albuquerque, NM

30th AIAA/ASME/SAE/ASEE Joint Propulsion Conference

June 27-29, 1994 / Indianapolis, IN

ANALYSIS OF APPLIED-FIELD PLASMA THRUSTERS USING THE MACH2 CODE

Pavlos G. Mikellides* and Peter J. Turchi**
Ohio State University
Columbus, OH

Norman F. Roderick**
University of New Mexico
Albuquerque, NM

ABSTRACT

The time dependent, two-dimensional axisymmetric, magnetohydrodynamics code, MACH2 is utilized to model applied-field magnetoplasmadynamic (MPD) thrusters. It includes two-temperature effects, real equations of state, real viscosity, anomalous resistivity models, and Hall current effects. Predictions of the basic linear dependence of thrust and voltage on applied magnetic field strength and discharge current have fared well when compared to experimental data. MACH2 simulations have shown that thre main contribution to the voltage drop across the plasma is due to rotation in the axial magnetic field. The main acceleration mechanism is therefore conversion of energy deposired in the thrust chamber by means of the electromagnetic torque to directed energy. A linear dependence of thrust and voltage o applied-magnetic field strenth is calculated. Such dependence correlates with the observation that the rotational speed achieves a limiting value based on viscous drag within the thrust chamber.

I. INTRODUCTION

Research over the last thirty years has shown that pulsed, quasi-steady or steady-state applied-field magnetoplasmadynamic (MPD) thrusters can provide specific impulses in the range desirable for space applications.[1,2,3] However, as is the case with the self-field operated thrusters, they exhibit efficiencies that in general do not exceed 50 percent.[4] The application of an external in-plane magnetic field introduces a very complicated set of physical interactions that has made theoretical modeling almost impossible. Most studies[4] have been in general experimental and are thus limited by the operating conditions, particular geometries, and protocols of a limited number of thrusters. Performance limitations, acceleration mechanisms, and energy distribution are not completely understood.

One of the earlier theoretical approaches was that of Krulle,[5] who used a simple set of flow equations with an assumed applied-field distribution to study acceleration mechanisms at low current densities and mass flow rates. The model also assumed that the plasma was fully ionized and that the self induced field was negligible when compared to the applied field. He determined that a considerable part of the total thrust was due to pressure forces balancing the radial confinement by the $j_\theta B_z$ body force. It was also shown that substantial azimuthal Hall currents were present well downstream of the thruster's exit that increased in magnitude and extension with increasing applied field strength.

In their treatment of applied-field acceleration mechanisms, Tanaka and Kimura[6] used a two-dimensional set of electromagnetic equations with a quasi one-dimensional set of fluid equations. This model examined operation with Argon propellant at 0.1 g/s, discharge currents of 1000-2000 A, and applied magnetic field strengths of 0.1-0.2 T at the cathode tip. It showed that substantial Hall currents and plasma rotation were produced from the interaction of the applied magnetic field with the discharge current. This plasma rotation was then converted to axial momentum via expansion through a magnetic nozzle.

An experimental study of a 10-35 kW applied-field MPD thruster using Lithium was performed by Fradkin,[7] and produced simple analytic expressions for

---

* Graduate Research Associate, Member AIAA

** Professor, Senior Research Scientist, USAF Phillips Laboratory, Member AIAA the voltage, thrust, and efficiency that showed reasonable agreement with the empirical measurements. The data displayed mainly linear increases of voltage, thrust, and efficiency with applied field strength except for low currents (I<400 A) and input feeds ($\dot{m} < 30$ mg/s) for which the voltage increased parabolically with the magnetic field. A model was developed based on assumed profiles of plasam rotation and density. The voltage was calculated for homopolar motor operation and assumed that there exists a limiting rotational speed to explain the linear dependence of voltage on applied field strength.

The most recent and extensive experimental study was that of Myers[8,9] with a 100kW-level thruster. A wide range of geometries, for Argon and Hydrogen propellants was examined for applied field strengths of 0.03-0.12T at the cathode tip, discharge currents of 750-2000 A, and mass flow rates of 25-140 mg/s. It was shown that both voltage and thrust vary linearly with applied magnetic field independent of geometry and mass flow rate. A linear dependence of thrust and voltage on the discharge current was also observed.

Previous simulations[10] with the MACH2[11,12] code have shown the linear dependence of voltage and thrust on applied magnetic field, the theoretical predictions however, underestimated the experimental data, due to lack of proper viscosity and thermal conductivity models. This paper presents the most recent simulations of applied-field MPD thrusters using the MACH2 code with improved transport coefficient models, that more accurately include the varying degree of ionization.

II. THE MACH2 CODE

MACH2 is a time-dependent, two-dimensional, axisymmetric, single fluid, two-temperature, real viscosity, magnetohydrodynamics (MHD) code that has already modeled a variety of plasma experiments with great success.[11] A broad class of geometric configurations can be handled without any code modifications in either planar or cylindrical coordinates.[12]

MHD EQUATIONS

A set of a single quasi-neutral fluid equations is solved by MACH2 in a time-split manner. All three components of the vectors are computed but are not allowed to vary in the azimuthal direction when in cylindrical coordinates. They are presented below in tensor notation form:

Mass Continuity

$$\frac{\partial \rho}{\partial t} = -\left(u^i \nabla_i \rho + \rho \nabla_i u^i\right) \qquad (1)$$

represents conservation of mass, where ρ is the mass density and u the velocity of the fluid.

Momentum

$$\rho \frac{Du^i}{Dt} = \nabla_j \left[(-P+Q) g^{ij} + \sigma^{ji} + \frac{1}{\mu_o} \left(B^j B^i - \frac{1}{2} B^2 g^{ji} \right) \right] \qquad (2)$$

where D/Dt is the material derivative operator, P is the pressure, Q is the artificial viscosity, g is the metric tensor, B is the magnetic induction, and σ is the stress tensor that is expressed as follows:

$$\begin{aligned} &\text{Elastic:} \quad \frac{\partial \sigma_{ij}}{\partial t} = 2G\delta_{ij} - u^k \nabla_k \sigma_{ji} \\ &\text{Viscous:} \quad \sigma_{ij} = \mu \left(u_{i,j} + u_{j,i} - \frac{2}{3} \delta_{ij} u_{k,k} \right) \end{aligned} \qquad (3)$$

where G is the shear modulus, μ is the viscosity coefficient and δ is the Kronecker delta. The elastic model allows the user to handle material strength, while the viscous isotropic fluid model transforms the code into a Navier-Stokes equation solver. The viscosity coefficient for a gas mixture containing s number of different heavy species of approximately equal mass m is given by[13]

$$\mu = \tfrac{1}{2} \alpha m \bar{C} \sum_{i=1}^{s} n_i \lambda_i \qquad (4)$$

where α is a numerical factor[11] equal to 0.998, C is the mean thermal speed, n_i is the number density, and λ_i is the mean free path. The latter are obtained under the assumption that only neutral atoms and singly ions are present when the MACH2 computed degree of ionization is less than 1. If the degree of ionization is greater than 1 but less than 2 then only single and double ions are assumed to make up the plasma. This formulation continues to apply for any higher degree of ionization.

Electron Specific Internal Energy

$$\rho\frac{D\epsilon_e}{Dt} = -P_e g^{ji}\nabla_i u^j + \eta_{ij} J^2 g^{ij} + \nabla_i \kappa_e^{ij} \nabla_j T_{ej} - \dot{q}_{rad} - \rho \nu_{eI}(\epsilon_e - \epsilon_I) \qquad (5)$$

where ϵ is the specific internal energy, η is the electrical resistivity, J is the current density, κ is the thermal conductivity, T is the temperature, $\dot{q}_{rad}$ represents heat flux rate due to radiation, it can be modeled as radiation cooling in optically thin limit; equilibrium radiation diffusion in optically thick limit; or non-equilibrium radiation diffusion, and ν_{ei} is the thermal equilibration collision frequency.

The electrical resistivity tensor includes the effects of anomalous current conduction which are added to the classical Spitzer-Härm[15] expression.

$$\eta_\perp = 1.0328\times10^{-4}\frac{\zeta\ln\Lambda}{\mu_o T_e^{3/2}} + \frac{m_e}{\mu_o e^2 n_e}\sqrt{\frac{kT_e}{m_e}}\sigma_e n_o \qquad (6)$$
$$\eta_\parallel = \left[0.29325 - \frac{0.4335}{1+\zeta}\right]\eta_\perp$$

where ζ is the number of free electrons per ion ($\zeta \geq 1$). $\ln\Lambda$ is the Coulomb logarithm, m_e is the electron mass, e is the elementary charge, μ_o is the permeability of free space, σ_e is a user specified scattering cross-section, and n_o is the neutral number density. The anomalous resistivity model utilized for these MPD simulations, is based on the Lower-Hybrid Drift microinstability.[16]

$$\eta_a = \frac{0.7m_e}{e\mu_o\sqrt{\epsilon_o}}\sqrt{\frac{A}{\rho\zeta}}\left(1 - e^{-u_{de}/u_{ia}}\right)\left(1 + 0.3\frac{u_{de}}{u_{ia}}\sqrt{\frac{B^2}{B^2 + C\zeta\rho/A}}\right) \qquad (7)$$

where A is the atomic weight, u_{de} is the electron drift speed, u_{ia} is the ion acoustic speed, C is a constant equal to $6.1544\text{x}10^{7}$, and ζ is the unconstrained number of free electrons per ion

The electron thermal conductivity tensor is also based on the classical Spitzer-Härm[16] model.

$$\kappa_e = \frac{4.408\text{x}10^{12}\left(0.687 + \frac{0.3756}{0.2+\zeta}\right)\zeta\ln\Lambda\,\rho^2}{A^2 B^2\sqrt{T_e}} \qquad (8)$$

given in MACH2 units of J/m-sec-eV

Ion specific internal Energy

$$\rho\frac{D\epsilon_I}{Dt} = -(P_I + Q)g^{ji} + \sigma^{ji}_I\nabla_i u_j + \nabla_i \kappa_I^{ij}\nabla_j T_{Ij} + \rho\,\nu_{eI}(\epsilon_e - \epsilon_I) \qquad (9)$$

where the ion thermal conductivity expression is derived in a manner consistent with the viscosity coefficient model and is given by[13]

$$\kappa_I = \frac{fk}{(\gamma - 1)m}\mu \qquad (10)$$

where f is a numerical factor equal to 2.5 and γ is the ratio of specific heats.

Magnetic Induction

$$\frac{\partial\vec{B}}{\partial t} = \vec{\nabla}\times(\vec{u}\times\vec{B}) - \vec{\nabla}\times(\bar{\eta}\vec{\nabla}\times\vec{B}) - \vec{\nabla}\times\frac{1}{e\mu_o n_e}(\vec{\nabla}\times\vec{B}\times\vec{B}) \qquad (11)$$

is derived from Maxwell's and a generalized Ohm's law with ion slip and electron pressure gradients assumed negligible.

The equation set is closed with the addition of an equation of state and a caloric equation of state that prescribe the species' pressure and specific internal energy in terms of the species' temperatures and densities. They can be either analytical (ideal gas model) or tabular. The tabular model[17] in the code is the SESAME Equation-of-State Library[18] generated and maintained by the T-4 group of the Theoretical Division at Los Alamos National Laboratory. Its data base includes the standard thermodynamic quantities along with the fractional ionization state based on Local Thermodynamic Equilibrium (LTE), and transport coefficients.

BOUNDARY CONDITIONS

Magnetic field boundary conditions include expressions for idealized conductor, where the normal component of the magnetic field and the tangential component of the electric field must be continuous at the surface, and for idealized insulator, where the normal component of current is zero at the surface.[12] For steady state problems the poloidal magnetic field boundary conditions have to allow evolution in response to azimuthal currents generated and sustained by the plasma in addition to any other applied fields generated by external coils. This is accomplished by computing the poloidal field components at the boundaries of the computational region via the Biot-Savart law.[16]

Hydrodynamic boundary conditions can be either free slip or no slip, while thermal boundary conditions can also be of two types: no heat flux or conduction to a fixed surface temperature. Modeling of inlets requires values of the inlet temperature, density, and velocity while at an outlet the conditions inside the boundary determine the state outside the boundary. This is accomplished by setting the normal component of the derivative equal to zero at the boundary.

The available boundary condition set is completed by the reflection of the conditions just inside of the boundary onto those outside of it at the axis of cylindrical symmetry.

NUMERICAL SCHEME

The physical model described in the previous sections is solved numerically by a time-split, time-marching algorithm.[12] Time-splitting consists of the sequential application of separate portions of a system of equations, rather than the simultaneous solution of the entire set. The thermal and resistive diffusion, and the Lagrangian hydrodynamics are carried out with implicit time differencing, while convective transport and the Hall effect are solved with explicit differencing. MACH2 controls the time step such that the stability of the explicit differencing is maintained.

The finite volume approach is utilized for the spatial differencing formulas. The advantage of this scheme is that conservation laws involving the vector integral theorems are well respected by the differencing since that differencing is derived from those theorems.

MACH2 is capable of simulating a large range of geometric configurations since the computational region is divided into appropriate block-like regions that are in turn transformed into logical rectangular blocks where the computations take place. Communication between these blocks and application of the boundary conditions is achieved via the ghost cell technique. Each side of a block's boundary is extended by one more row of cells, the ghost cells. Then the full difference equations may be applied to points on the region boundary just as to the interior points, since the region containing data is larger than the physical region. The principal advantage of this technique is that the boundary condition expressions need not be special difference equations, and thus are simpler to derive and code

III. MPD SIMULATIONS

The NASA LeRC 4" diameter thruster[8] was selected for the MACH2 simulations due to the large amount of available experimental data. The particular geometry chosen which is shown in Figure 1, was operated with Argon at a mass flow rate of 0.1 g/s injected through holes located near the midradius of the anode and cathode and through an annulus at the cathode base. The discharge current was varied between 1000 and 1500 A and the applied magnetic field strength between 0.034 and 0.12T as measured at the cathode tip before propellant injection. The external magnet coil consisted of 28 turns of 1.9 cm diameter tubing. The calibrated values yielded a slope of 8.48×10^{-5} as a function of the magnet current.

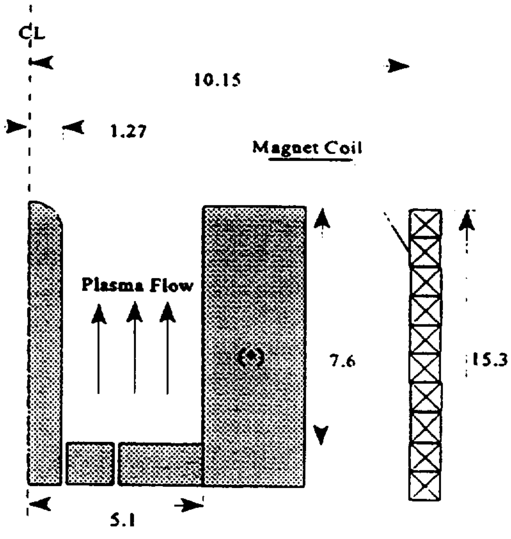

Figure 1 The geometry of the NASA LeRC 4" diameter cylindrical thruster. Dimensions are in cm.

The MACH2 simulations assumed a uniform mass injection over the backplate at sonic speed, for three different applied magnetic field strengths of 0.034, 0.052 and 0.102 T as initially computed at the cathode tip. The fluid formulation was two-temperature, viscous, with real equation of state. Hydrodynamic boundary conditions assumed no slip at the walls while thermal boundary conditions assumed a fixed wall temperature of 0.2 eV and 0.1 eV at the cathode and anode respectively. The computational domain was extended to 30 cm downstream of the backplate for the 0.034 . 0.102 T cases and to 20 cm for the 0.052 T case. Thrust was calculated at the ends of the computational region via

$$T = \int_0^R (p + \rho u_z^2)dA + \int_{z_A}^{z_F} \rho u_r u_z dA \qquad (12)$$

where R =6.7 cm is the distance from the centerline to the end of the computational region. z_F is the distance from the anode face to the end of the computational region. and z_A is the anode length. Plasma voltage was also calculated at the insulating backplate by

$$V = \int_{R_C}^{R_A} \vec{E}\cdot d\vec{r} \qquad (13)$$

where R_C is the cathode radius and R_A is the anode radius. Steady state was achieved at approximately 0.5 msec of computational time and was confirmed by changes in the terminal variables as well as internal flowfield variables of less than 0.5% with respect to time.

Thrust predictions by MACH2 are presented in Figure 2 and compared to the experimental data[19] as a function of applied magnetic field strength at the cathode tip for a discharge current of 1000 A.

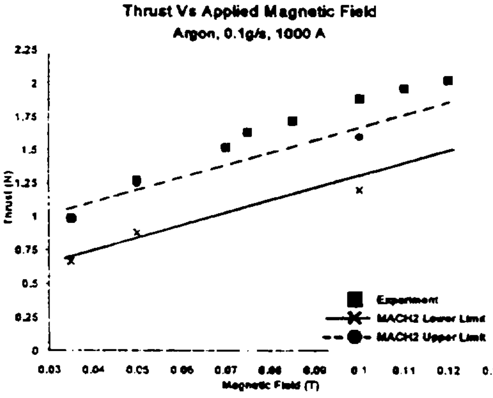

Figure 2 Thrust Vs Applied Magnetic Field strength at the cathode tip for the NASA LeRC MPD thruster

Thrust is shown to vary almost linearly with magnetic field strength in accordance with the experiment. The lower limit predictions are calculated at the downstream boundaries of the computational region and underestimate the experimental values. This underestimation is due to practical limits of the computational region. Total conversion of azimuthal kinetic energy and static enthalpy into directed energy has not yet occured by the time the flow exits the computational boundaries. Figures 3 and 4 show

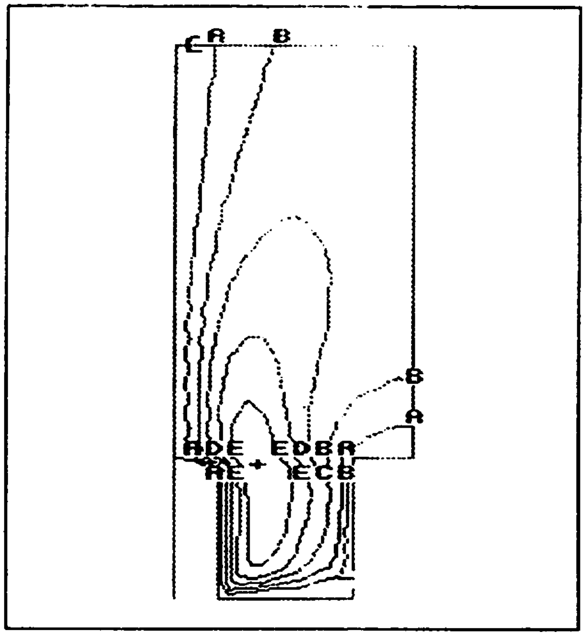

Figure 4 Azimuthal speed distribution for the 0.102T case. A=1.8, B=3.7, C=5.7, D=7.6, E=9.5, +=11 (km/s)

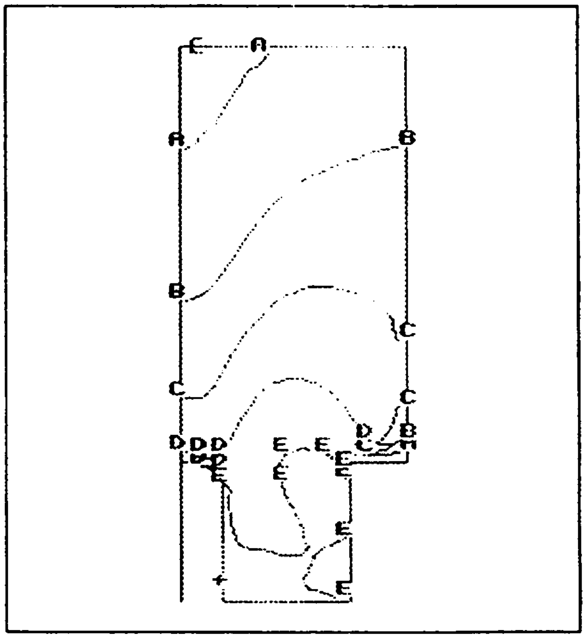

Figure 3 Pressure distribution for the 0.102T case. A=0.34, B=1.4, C=5.7, D=23, E=95, +=390 (Pa).

significant values of rotational speed. (an average of 4 km/s). and pressure at the boundaries of the computational region. An extrapolation of the thrust calculation to zero rotational speed and pressure was performed to produce the upper line thrust variation in Figure 2. This was carried out based on conservation of total enthalpy assuming that all remaining rotational energy and sensible enthalpy will be converted to kinetic energy of axial motion. (Thus, profile effects and internal energy conversion were not included.) This extrapolation correlates well with the experimental data, but should still underestimate thrust values since additional power deposited in the plasma from electrode fall regions is not included. At the present. MACH2 does not model electrode processes.

The possibility of converting rotational evergy ans sensible enthalpy to kinetic energy of axial versus tadial motion depends on the detaols of the pressure and magnetic dield distributions in the exhaust plume. In Figure 5. for example. pressure gradient forces point inward for the entire portion of the computational downstream of the B contour. It is likely therefore. that mucg of the rotational and pressure-based energy of this portion of the flowcan be converted to axially directed kinetic energy. Those portions o_r the flow that exit upstream of the B contour may also contribure rotational and presslkure-based energy to the directed exhaust, but further computation is required to acgiebe accurate assesments.

From an engineering point of view. however. it certainly appears reasonable to extend the applied-fiels coil structure downstream of the anode face so that expansion of the exhaust flow can occur with a gentler effective divergence angle. (The trade -off herem apart from possible coil weight penalties. os not due to solid-nozle viscous drag. but the drag on the plasma due to resistive diffusion and coupling to additional magnetic flux.

In the NASA LeRC experiments[8] the electrode heat transfer was obtained by monitoring the cooling water temperature change (±0.5 C) and flow rate (±2%). This was interpreted as the power deposited to the anode which in turn resulted in an experimental value for the anode fall voltage (cathode fall voltage was assumed negligible[9]) by

$$V_A = \frac{P_A - P_r}{I} - \frac{5kT_e}{2e} - \phi \qquad (14)$$

where P_A was the anode power, P_r was an assumed value for the plasma and cathode radiation power, electron temperature was assumed at 2 eV. and ϕ was the copper work function (4.6 V). The anode fall voltage values were then subtracted from the total measured discharge voltage to provide the voltage drop across the plasma. These values are compared to MACH2 predictions in Figure 5 as a function of the applied magnetic field strength.

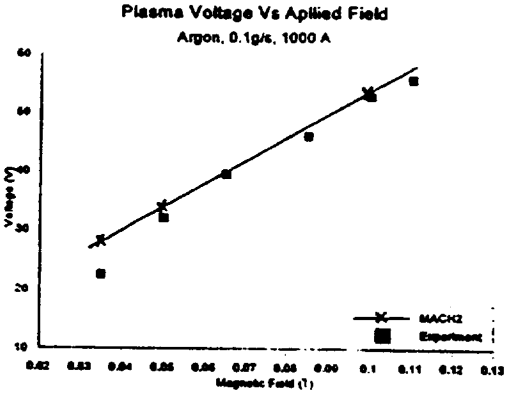

Figure 5 Plasma Voltage Vs Applied Magnetic Field strength at the cathode tip for the NASA LeRC MPD thruster.

Theoretical predictions agree well with experiment and show the linear dependence of voltage with applied magnetic field strength This linear increase is contrary to intuitive predictions suggesting that the voltage increases parabolically with magnetic field if the main contributions are rotation of the plasma in the axial magnetic field, and the Hall electric field. Insight into the behavior of the plasma voltage is offered by examining the relative magnitudes of the components that make up the total radial electric field An integration of the generalized Ohm's law

$$V = \int (\eta j_r - u_\theta B_z + j_\theta B_z / e n_e) dr \qquad (15)$$

gives the various contributions to the total voltage. If the rotational velocity is directly proportional to $j_r B_z$ and if $j_\theta B_z$ balances the centrifugal force due to the ion rotation then it is clear that the voltage drop across the plasma should be proportional to B^2. These contributions are shown in Table 1 for two different axial locations at the midradius of the discharge chamber

z (cm)	ηj_r	$j_\theta B_z/en_e$	$-u_\theta B_z$
3.165	-84	-89	-1382
6.33	-75	-147	-1181

Table 1. Electric field components (V/m) at the midradius of the discharge chamber for the 0.102T case.

It is apparent that the main contribution to the total radial electric field in the middle of the chamber is a result of plasma rotation regardless of axial position. This in turn suggests that the voltage drop across the plasma is mostly due to the back electromotive force. Figure 6 shows the variation of the maximum rotational speed as a function of applied field strength as predicted by MACH2

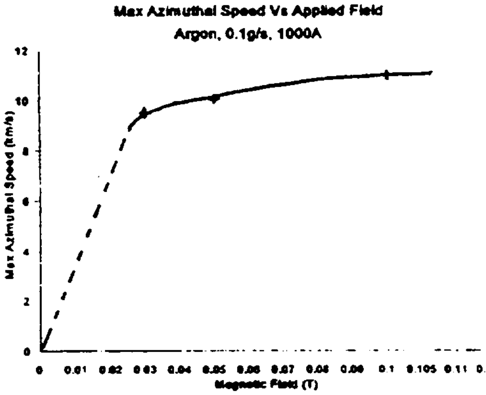

Figure 6 Maximum azimuthal Speed Vs Applied Magnetic Field strength at the cathode tip for the NASA LeRC MPD Thruster.

It is clearly shown that for this regime of operation the maximum rotational speed does not linearly increase with magnetic field, as would be expected from the increased electromagnetic torque on the plasma mass flow, but rather asymptotes to a constant value. This behavior would explain the linear dependence of voltage on magnetic field. An examination of the flowfield inside the discharge chamber shows that this limitation on azimuthal speed is due to viscous effects. As the magnetic field increases, centrifugal forces on the plasma increase the mass density near the outer wall of the discharge chamber, thereby increasing the importance of viscous effects. That is, more of the mass flow is forced into regions of higher azimuthal-velocity shear. Furthermore depletion of density between the electrodes also increases the importance of viscous diffusion. The azimuthal speed profile remains about the same, with increasing magnetic field, but the maximum speed is limited.

IV. CONCLUSIONS

Several simulations of the NASA LeRC 4" diameter cylindrical steady state applied-field MPD thruster have been performed using the time dependent, 2-dimensional axisymmetric MHD computer code, MACH2. Comparisons with experimental data of thrust and plasma voltage showed fairly good agreement. Conversion of azimuthal kinetic energy and sensible enthalpy to directed energy takes place in the plume region and can contribute significantly (20%) to the total final thrust values. The efficiency of this conversion diminishes as we move radially outward due to insufficient electromagnetic confining force magnitudes. This suggests that some improvement of performance can be achieved by extension of the applied-field coil structure downstream of the anode face.

It is shown that the main contribution to the voltage drop across the plasma is due to the back emf. The linear dependence of plasma voltage on applied magnetic field strength, shown by both the experiment and the theoretical predictions, is explained by a limiting maximum azimuthal speed due to increased viscous effects as the plasma is centrifugally-forced against the outer electrode of the thrust chamber.

Future goals include further analysis of the internal flowfield and more detailed investigation of the aformentioned findings. Such analysis may lead to simple analytical expressions for thrust and voltage. In addition simulations will be performed to examine the effects of varying discharge current, and propellant type.

V. ACKNOWLEDGEMENTS

This effort was supported by the NASA Lewis Research Center and the Ohio State Supercomputer Center. The authors especially thank Dr. Roger Myers for providingf the experimental data and his constant encouragement.

REFERENCES

1. Seikel, G.R., York, T.M., and Condit, W.C., "Applied-Field Magnetoplasmadynamic Thrusters for Orbit-Raising Missions," in Orbit-Raising and Maneuvering Propulsion: Research Notes and Needs, Caveny, L.H., (ed), Progress in Astronautics and Aeronautics, vol 89, 1984, pp 260-286.

2. Sovey, J., and Mantenieks, M., "Performance and Lifetime Assesment of MPD Arc Thruster

Technology." AIAA 88-3211. July 1988.

3. Gilland, J.H., Myers, R.M., and Patterson, M.J., "Multimegawatt Electric Propulsion System Design Considerations." AIAA 90-2552, July 1990.

4. Myers, R.M., Mantenieks, M., and LaPointe, M.R., "MPD Thruster Technology." AIAA 91-3568, September 1991.

5. Krulle, G., "Theoretical Treatment of Current, Mass Flow, and Related Distributions in MPD Plumes." AIAA 72-501.

6. Tanaka, M., and Kimura, I., "Current Distribution and Plasama Acceleration in MPD Arcjets with Applied Magnetic Fields." Journal of Propulsion and Power, 4(5), Sept.-Oct. 1988, pp 428-436.

7. Fradkin, D.B., "Analysis of Acceleration Mechanisms and Performance of an Applied Field MPD Arcjet." Ph.D. Dissertation No. 1088-T, Department of Mechanical and Aerospace Engineering, Princeton University, Princeton, NJ, March 1973.

8. Myers, R.M., "Applied-Field MPD Thruster Technology." AIAA 91-3568, Sept. 1991.

9. Myers, R.M., "Scaling of 100kW Class Applied-Field MPD Thrusters." AIAA 92-3462, July 1992.

10. Mikellides, P.G., Turchi, P.J., and Roderick, N.F., "Theoretical Modeling of Magnetoplasmadynamic Arcjets." IEPC 93-189, Sept. 1993.
11 Peterkin, R.E., Jr., Buff, J., Frese, M.H., and Giancola, A.J., "MACH2: A Reference Manual -- Fourth Edition." MRC/ABQ-R-1207, Mission Research Corporation, 1989

12 Frese, M.H., "MACH2: A Two-Dimensional Magnetohydrodynamic Simulation Code for Complex Geometric Configurations." AMRC-R-874, Mission Research Corporation, 1987

13. Chapman, S., and Cowling, T.G., The Mathematical Theory of Non-Uniform Gases, 3rd Edition, Cambridge University Press, 1970.

14. Enskog, D., Phys. Zeit., 12, 56 and 533 (1911); Annln Phys., 38, 731 (1912); *Inaugural Dissertation*, Uppsala, 1917

15. Spitzer, L., Physics of Fully Ionized Gases, 2nd Edition, Interscience, New York, 1962

16. Chodura, R., "A Hybrid Fluid-Particle Model of Ion Heating in High Mach Number Shock Waves." Journal of Nuclear Fusion, Vol. 15, pp 55, 1975.

17. Cranfill, C.W., "EOSPAC: A Subroutine Package for Accessing the Los Alamos Sesame EOS Data Library," LA-9728-M, Los Alamos National Laboratory, August 1983

18. Holian K.S., ed. "T-4 Handbook of Material Properties Data Base, Vol Ic: EOS," LA-10160-MS, Los Alamos National Laboratory, November 1984.

19. Myers, R.M., Personal Communication.

AIAA 95-2676
THEORETICAL MODEL FOR APPLIED-FIELD MPD THRUSTERS

P.G. Mikellides and P.J. Turchi
The Ohio State University
Columbus, OH

N.F. Roderick
The University of New Mexico
Albuquerque, NM

31st AIAA/ASME/SAE/ASEE
Joint Propulsion Conference and Exhibit
July 10-12, 1995/San Diego, CA

Theoretical Model for Applied-Field MPD Thrusters

Pavlos G. Mikellides[1] and Peter J. Turchi[2]
The Ohio State University
Columbus, OH
and
Norman F. Roderick[2]
The University of New Mexico
Albuquerque, NM

Abstract

Numerical modeling of the NASA LeRC 100 kW, steady-state, applied-field MPD thruster is performed using the magnetohydrodynamics code, MACH2, for a range of applied magnetic field strengths and discharge currents. Overall performance trends, obtained experimentally, are captured by the simulations. Magnitudes of plasma voltage versus applied field strength also agree well. Interrogation of the calculated flowfield offers a new visualization of applied-field MPD thruster operation, comprising the following elements: a) the back electromotive force is the dominant contributor to the plasma voltage for the geometry examined. b) viscous forces oppose applied azimuthal electromagnetic forces and limit the maximum rotational speed to a constant independent of applied field or current value. c) viscous heating and conversion of thermal energy to axial directed kinetic energy is the main acceleration mechanism. d) the low density, low conductivity plasma for the regime examined does not interact with the applied field in the manner of a magnetic nozzle.

Nomenclature

ρ	mass density, kg/m^3
u	flow velocity, m/s
Q	numerical viscosity term, J/m^3
μ_o	permeability of free space, H/m
g	metric tensor
δ	Kronecker delta
ϵ	specific internal energy, J/kg
κ	thermal conductivity, J/m-s-eV
e	elementary charge, C

t	time, sec
P	pressure, J/m^3
σ	stress tensor, J/m^3
B	magnetic induction, T
G	shear modulus, kg/m-s^3
μ	viscosity coefficient, kg/m-s
η	electrical resistivity / μ_o, m^2/s
$T_{e,I}$	electron, ion temperature, eV
n	number density, / m^3

---

[1] Research Associate, Member AIAA

[2] Professor, Senior Research Scientist, USAF Phillips Laboratory, Senior Member AIAA

I	current, A	j	current density, A/m^2
V	plasma voltage, V	ζ	number of free electrons/ion
w	azimuthal speed, m/s	A	atomic weight, amu

Subscripts

e, I, o	electron, ion, neutral
r, θ, z	physical dimensions; radial, azimuthal, axial

Introduction

Applied-field magnetoplasmadynamic (MPD) thrusters offer specific impulse values that are unattainable by conventional chemical or nuclear propulsion. The simple design and robustness of MPD thrusters are attractive features compared to other electric propulsion devices. The lower current requirement and generally higher exhibited efficiency of applied-field devices also provide an advantage over self-field thrusters for lower power missions. To date however, applied-field MPD thrusters have not consistently demonstrated adequate efficiencies (>40 %). This may be due to insufficient comprehension of acceleration and power loss mechanisms, the latter shown to be dominated by anode power deposition.[1] Research over the last thirty years has mainly been empirical and thus is only able to address the geometries and operating conditions of a limited number of thrusters. Theoretical attempts have not produced models that capture the trends and magnitudes of the experimental data, without resort to arbitrary assumptions about velocity limits or conversion of rotational energy.

The concept of the applied-field MPD acceleration is based on conversion of rotational energy via expansion in a magnetic nozzle. This rotational energy is provided by the electromagnetic force due to the interaction of the applied in-plane magnetic field and the discharge current as shown in Figure 1. Induced azimuthal Hall currents interact with the applied magnetic field to produce a radially confining electromagnetic force, $j_\theta B_z$. This confinement in the exhaust region presents the opportunity of azimuthal kinetic energy conversion into axially directed thrust energy. All previous efforts have concentrated in either modeling such a process or providing scaling laws based on the assumption that this type of conversion is the main thrust contributor.

One of the earlier theoretical approaches was that of Krulle[2] who used a simple set of flow equations with and assumed applied-field distribution to study acceleration mechanisms at low current densities and mass flow rates. The model assumed that the plasma is fully ionized and the self induced fields were negligible when compared to the applied field. He determined that a considerable part of the total thrust was due to pressure forces balancing the radial confinement by the $j_\theta B_z$ body force. Substantial azimuthal Hall currents were also calculated well downstream of the thruster's exit. The magnitude of these currents and their persistence downstream of the exhaust plane increased with increasing applied field strength.

In their treatment of applied-field acceleration mechanisms, Tanaka and Kimura[3] used a two-dimensional set of electromagnetic equations with a quasi one-dimensional set of fluid equations. This model examined operation with argon propellant at 0.1 g/s, discharge currents of 1000-2000 A, and applied field strengths of 0.1-0.2 T at the cathode tip. It showed that substantial Hall currents and plasma rotation were produced from the interaction of the applied field with the discharge current. This plasma rotation was the converted to axial momentum via expansion through a magnetic nozzle.

In an experimental study with a 10-35 kW steady state applied-field MPD thruster using lithium, Fradkin[4] found a linear variation of thrust with the product of discharge current and applied magnetic field strength, IB. He also observed two operating modes for the arc voltage; a "high voltage mode," ($I<400$ A, $\dot{m}<30$ mg/s), during which the voltage varied parabolically with applied field strength, and a "low voltage mode," in which the same relation was linear. These were explained via a rotating plasma model that assumed the plasma rotates as a homopolar motor. The rotational energy was assumed to be converted completely to axial kinetic energy. This produced simple analytic expressions that scaled thrust as IB and voltage as IB^2 and B for the "high" and "low" voltage modes respectively. The latter linear behavior with B was based on the assumption of limiting the rotational speed to Alfvén critical velocity.

The most recent and extensive experimental study of applied-field MPD thrusters was that of Myers[5] with a 100 kW-level steady state thruster. A wide range of geometries, for argon and hydrogen propellants was examined for applied field strengths of 0.03-0.2 T at the cathode tip, discharge currents of 750-2000 A, and mass flow rates of 25-140 mg/s. It was observed that both thrust and voltage seemed to increase linearly with increasing applied magnetic field strength and discharge current. This was independent of geometry, mass flow rate, and propellant type. Thrust and discharge voltage increased parabolically with increasing anode radius, but decreased with increasing cathode radius. Thrust magnitudes improved with increasing electrode length. The voltage was independent of cathode length, but increased with decreasing anode length. A significant portion of the power was deposited in the anode, for all operating conditions. Thrust efficiencies did not exceed 30%.

Sasoh and Arakawa[6] developed a thrust equation for an applied-field MPD thruster based on energy conservation considerations. They assumed that the work done by the electromagnetic forces is all converted into axial directed kinetic energy. The acceleration mechanisms considered were Hall, rotational, and self-magnetic accelerations. This formula showed that for moderate applied magnetic field strengths (0.07-0.19 T) the Hall and swirl accelerations are the main thrust contributors for the low discharge currents ($I<400$ A) and mass flow rates ($\dot{m} < 30$ mg/s). Comparisons with experiments were limited and constrained by gross assumptions to be considered reliable. For higher discharge currents and mass flow rates the thrust formula underestimates the experimental thrust, suggesting an increasingly important electrothermal component.

The highly interactive physical processes present in the applied-field MPD thruster require a complete theory rather than examination of isolated phenomena or gross assumptions. Solution of the set of equations that include all the possible relevant physics is necessary. This is one of the objectives of the present paper in which numerical techniques are employed to simulate thruster behavior. Once accomplished, interrogation of the simulated flowfield can define the dominant acceleration process and provide additional insights. A companion paper utilizes these insights to derive simple analytic expressions for the thrust and voltage that capture trends and magnitudes exhibited in the experiments.

The MACH2 Code

MACH2 is a time dependent, two-dimensional axisymmetric, single fluid, multi-temperature, non-ideal radiation, magnetohydrodynamics (MHD) code that has been used to model a variety of laboratory plasma experiments.[7] In all cases, the use of the code has allowed better understanding of the physical phenomena involved, and had great success in developing ways to improve experimental performance.

Axisymmetry implies that the code includes spatial variation in two dimensions. All three components of velocity and magnetic field, are computed however, as functions of the two spatial coordinates. The code provides computation in either planar of cylindrical geometry and can manage almost any geometric configuration without any code modification. This broad geometric class of domains is handled by division of the physical domain into appropriate block-like regions which in turn are transformed into logical rectangular blocks that make up the computational domain.[8] Initial conditions require the input of mass density, temperature(s), and applied magnetic field for each physical block. A variety of distributions is available for each of the variables without code modification.

MHD Equations

The single fluid MHD equations used in MACH2 include the continuity equation, the momentum equation in three vector form, a set of energy equations, and the magnetic field transport equation. (Summation is indicated by repeated indices.)

Continuity:

$$\frac{\partial \rho}{\partial t} = -\left[u^i \nabla_i \rho + \rho \nabla_i u^i \right] \tag{1}$$

Momentum:

$$\rho \frac{Du^i}{Dt} = \nabla_j \left[(-P+Q) g^{ij} + \sigma^{ji} + \frac{1}{\mu_o} \left(B^j B^i - \frac{1}{2} B^2 g^{ji} \right) \right] \tag{2}$$

where the stress tensor can have the following two representations, depending on the problem at hand:

Stress Tensor:

$$\text{Elastic: } \frac{\partial \sigma_{ij}}{\partial t} = 2G\delta_{ij} - u^{k}\nabla_{k}\sigma_{ji}$$
$$\text{Viscous: } \sigma_{ij} = \mu\left(u_{i,j} + u_{j,i} - \frac{2}{3}\delta_{ij}u_{k,k} \right) \tag{3}$$

The elastic model allows the user to handle material strength, while the viscous isotropic fluid model transforms the code into a Navier-Stokes equation solver.

Electron Specific Internal Energy:

$$\rho\frac{D\epsilon_{e}}{Dt} = -P_{e}g^{ji}\nabla_{i}u^{j} + \eta_{ij}J^{2}g^{ij} + \nabla_{(}\kappa_{e}^{ij}\nabla_{j}T_{e)} - q_{rad} - \rho v_{el}(\epsilon_{e} - \epsilon_{I}) \tag{4}$$

where v_{el} is the thermal equilibration frequency. The radiation models available include radiation cooling in optically thin limit, and equilibrium radiation diffusion along with a non-equilibrium radiation diffusion theory.

Ion Specific Internal Energy:

$$\rho\frac{D\epsilon_{I}}{Dt} = {}_{[}-(P_{I} + Q)g^{ji} + \sigma^{ji}{}_{]}\nabla_{i}u_{j} + \nabla_{i(}\kappa_{I}^{ij}\nabla_{j}T_{I)} + \rho v_{el}(\epsilon_{e} - \epsilon_{I}) \tag{5}$$

Magnetic Induction:

$$\frac{\partial \vec{B}}{\partial t} = \bar{\nabla}\times(\alpha\times\vec{B}) - \bar{\nabla}\times(\eta\bar{\nabla}\times\vec{B}) - \bar{\nabla}\times\frac{1}{e\mu_{o}n_{e}}(\bar{\nabla}\times\vec{B}\times\vec{B}) \tag{6}$$

The set of equations is closed with the addition of an equation of state and a caloric equation of state that prescribe the species' pressure and specific internal energy in terms of the species' number densities and temperatures. They can be either analytical or tabular, the analytical equations include the ideal gas model and a model appropriate for solids. The tabular model[9] in the code is the SESAME Equation-of-State Library[10] generated and maintained by the T-4 group of the Theoretical Division at Los Alamos National Laboratory. Its data base includes the standard thermodynamic quantities, along with the fractional ionization state based on thermodynamic equilibrium (LTE) and transport coefficients. The tabular look-up aspect of the code is easily adapted to input tabular equation of state models supplied by the user.

Transport Coefficients

The viscosity coefficient model is appropriate for a two-temperature, partially ionized gas that contains s number of different heavy species of approximately equal mass, m, it is given by[11]

$$\mu = \tfrac{1}{2}\alpha m\bar{C}\sum_{i=1}^{6} n_i\lambda_i \tag{7}$$

where $\bar{C}$ is the mean thermal speed, n_i is the number density, λ_i is the mean free path, and α is a numerical factor equal to 0.998. The model assumes that for a degree of ionization between zero and one only atoms and single ions constitute the gas, for a degree of ionization between one and two only single and double ions exist in the plasma, and so on, up to an unlimited degree of ionization.[12] The ion thermal conductivity model is derived in consistency with the aforementioned model, under the assumption of a constant Prandtl number of 2/3:

$$\kappa_i = \frac{fk}{(\gamma-1)m}\mu \tag{8}$$

where f is a factor equal to 2.5 (it never exceeds 2.511 for atoms repelling each other with a force that varies inversely with some power of the distance, and it never exceeds 2.522 for rigid elastic spheres[11]), k is the Boltzmann constant, and γ is the ratio of specific heats. The classical Spitzer-Härm model[13] is implemented for the electron thermal conductivity

$$\kappa_e = \frac{3.103\text{x}10^4\left(4.1-\dfrac{15.5}{4+\zeta}\right)T_e^{5/2}}{\zeta^2\ln\Lambda} \quad \text{(J/m-sec-eV))} \tag{9}$$

where A is the atomic weight, $\ln\Lambda$ is the Coulomb logarithm, and ζ is the number of free electrons per ion ($\zeta \geq 1$ when used in these models).

The electrical resistivity models simulate both classical particle-particle interactions and anomalous particle-turbulent fields interactions. The classical component is based on the Spitzer-Härm[13] model for fully ionized gas but include contributions from electron-atom collisions:

$$\eta_\perp = 1.0328\times10^{-4}\frac{\zeta\ln\Lambda}{T_e^{3/2}} + \frac{m_e}{e^2 n_e}\sqrt{\frac{kT_e}{m_e}}\sigma_e n_o \tag{10}$$

where n_o is the neutral number density, and σ_e is a user-specified scattering cross section. The first term on the right hand side represents electron-ion collision while the second represents the electron-atom collision contributions. The anomalous resistivity model[14,15] utilized for the present calculations is based on the assumption that the Lower-Hybrid Drift microinstability is the dominant contributor to any particle-wave interactions and adds to the above classical value,

$$\eta_a = \frac{0.7 m_e}{e\sqrt{\varepsilon_o}} \sqrt{\frac{A}{\rho\zeta}}\, (1 - e^{-u_{de}/u_{ia}}) \left(1 + 0.3 \frac{u_{de}}{u_{ia}} \sqrt{\frac{B^2}{B^2 + C\zeta\rho/A}} \right) \qquad \textbf{(11)}$$

where u_{de} is the electron drift speed, u_{ia} is the ion acoustic speed, and C=6.1544 x 10^7 m^3-T^2.

Boundary Conditions

Application of the boundary conditions n MACH2 is carried out if unique fashion. The premise is that the conditions at a physical boundary are the limit of those in the fluid, thus they are related by, at most, simple instantaneous geometric expression. This is accomplished by the ghost-cell technique, discussed in more detailed later, which eliminates the need for special boundary differencing expressions.

Magnetic field boundary conditions include appropriate expressions for idealized conductor and insulator surfaces, and the axis of cylindrical symmetry. For steady state problems the poloidal magnetic field boundary conditions have to allow evolution in response to azimuthal currents generated and sustained by the plasma in addition to any other applied fields generated by external coils. This is accomplished via the Biot-Savart law under the assumption that individual cells generated by the computational grid act as circular, current-carrying filaments that contribute to the total poloidal field at the boundaries.[12] Any external field coil windings add their contributions in the same manner. Hydrodynamic boundary conditions can be either free slip or no slip while thermal conduction boundary conditions can also be of two types; no heat flux (adiabatic) or conduction to a fixed wall temperature. Modeling of inlets requires input of the inlet temperature(s), density, and velocity, while at an outlet the conditions inside the boundary determine the state outside by not allowing any gradients perpendicular to the boundary. The axis of cylindrical symmetry reflects that the conditions just outside the problem boundary are the mirror image of those just inside of it.

Numerical Scheme

The physical described if the previous sections is solved numerically by a time-split, time-marching algorithm. Time splitting consists of the sequential application of separate portions of a system of equations, rather than the simultaneous application of the entire set. The thermal and equilibrium radiation diffusion, resistive diffusion, and the Lagrangian hydrodynamics are done with implicit time differencing while radiation cooling, coordinate system motion, convective transport, and the Hall effect are carried out with explicit differencing. MACH2 controls the time step such that the stability of the explicit differencing is maintained.

The finite volume approach is utilized for the spatial differencing formulas. The advantage of this scheme is that conservation laws involving the vector integral theorems are well respected by the differencing since that differencing is derived from those theorems. The adaptive ideal coordinate system is generated by solving a variational problem of the block complex using a weight function selected from a standard family of user specified parameters. Its mesh smoothness, desired concentration, and orthogonality can be easily manipulated via input parameters, thus allowing the user to dictate the mode of calculation for a given problem. The grid's subsequent motion utilizes an Arbitrary-Lagrangian-Eulerian (ALE) approach. This allows it to move in either Lagrangian, Eulerian, or arbitrary fashion with respect to the fluid. This method provides a means of avoiding negative aspects that can arise from purely Lagrangian (coordinate distortion) or purely Eulerian (numerical diffusion) calculations, while providing higher resolution in regions of physical interest and solution confirmation.

Application of the boundary conditions, and communication between neighboring blocks that make up the computational domain are carried out by the ghost-cell technique. Each side of a block's boundary is extended by one more row of cells, the ghost cells. Then the full difference equations may be applied to points on the region boundary just as to the interior points, since the region containing data is larger than the physical region.

Theoretical Calculations

MACH2 was used to simulate a steady-state, applied-field MPD thruster at the NASA Lewis Research Center because of the wide range of experimental data[5,16] available. The configuration, shown in Figure 2, consists of a 1.27 cm radius cathode and a 5.1 cm radius anode both of which are 7.6 cm long. The magnet coil that provides the applied field is 15.3 cm long with a 10.15 cm radius and is placed with one end flush with the exit plane. The experimental operating conditions simulated were argon propellant at 0.1 g/s under the assumption of uniform mass injection at the backplate. The applied magnetic field strength was varied from 0.034 to 0.102 T, as measured at the cathode tip, and the discharge current from 750 to 1250 A. The fluid formulation was two-temperature, viscous, with real equations of state. No slip was assumed at the walls, and the cathode and anode were fixed at temperatures of 0.2 and 0.1 eV respectively. The partially ionized gas viscosity and thermal conductivity models along with the anomalous electrical resistivity model previously outlined, were incorporated. The computational grid was Eulerian and extended 30 cm downstream of the backplate, in order to capture any plume processes.

Overall Modeling

The five steady-state cases computed provide thrust and plasma voltage variations with respect to applied magnetic field strength and discharge current. Steady-state was numerically confirmed when three criteria were satisfied: terminal variables such as thrust and voltage display variations with time of less than 1%, specific variables such as temperature, density and velocity at different axial and radial locations vary with time by less than 3%, and overlay of two-dimensional distributions of the latter do not show any variations with time. The very low density environment typical of these thrusters resulted in quite a computationally adverse series of simulations. Numerical time steps were limited to the order of a few nanoseconds, but steady-state typically was not attained until half a millisecond of operation. This in turn implies that numerical energy losses and round off errors may be increased, as compared to unsteady problems, due to the increased number of cycling through the full set of equations.

Thrust is computed at the outlet boundaries of the computational region, the results of which are compared with experiment in Figures 3 and 4. The seemingly linear increase of thrust with applied field and discharge current is apparently captured by the theory, suggesting that the main acceleration mechanisms that provide such behavior are included in MACH2. The aforementioned numerical considerations may be used to explain the underestimated magnitudes. This is supported by the underestimated slopes, since for the higher magnetic field and discharge current cases computations advanced at lower timesteps and thus required a larger number of iterations to reach steady state.

Plasma voltage predictions are compared with experimental data in Figures 5 and 6. The linear voltage dependence on the applied field strength is accurately predicted, establishing that the manner by which energy is deposited in the plasma is contained in the MACH2 physics. The behavior of voltage with increasing discharge current, although linear in accordance with experiment, is somewhat overestimated for the 1250 A case. Eventhough the discrepancy at this current setting is only 9%, it implies a finite positive slope that is not suggested by the experiment. It is thus recognized that an additional simulation run for the higher current setting of 1750 A may have been appropriate to confirm that discrepancies remain within experimental error.

Detailed Modeling

With a considerable amount of confidence in the predictive capabilities of the theory, we now proceed to interrogate the basic flowfield properties with the following objectives; identify the main plasma energy deposition source(s), explain the dependence of voltage on controlled external parameters, and identify the main acceleration mechanism(s). These will be accomplished by examining the distributions of the principal variables in both the discharge chamber and plume for the 0.102 T, 1000 A simulated case.

Figures 7, 8, 9 and 10 depict the two-dimensional distributions of the enclosed current contours, magnetic flux, azimuthal speed, and in-plane velocity vectors. We note a small distension of current downstream of the exit plane, allowing an accurate calculation of the total applied azimuthal electromagnetic force by integration of the body force over the chamber's volume. This results in a total force of 3.486 N, which shows the insignificance of current distribution when compared to a simple calculation of $IB(r_a-r_c)$ of 3.91 N. The rotational force implies expected azimuthal speeds (at 0.1 g/s) in the excess of 30 km/s. This expected magnitudes however, are contradicted by the calculated ones (figure 9) which never exceed 11 km/s. This implies the existence of an opposing force which the azimuthal momentum equation suggests can only be viscous drag. In addition other acceleration mechanisms (besides conversion of azimuthal kinetic energy to axial energy) are needed to account for the generally higher axial speeds depicted in the vector display (figure 10). Self-field acceleration is excluded as an explanation for this additional acceleration since its value is only 0.08 N. The aforementioned statement is supported by the electron and ion temperature distributions, Figures 11 and 12 respectively, which show that the plasma consists of a hot ion gas and a moderate temperature electron gas. The elevated ion temperatures suggest a direct mechanism for heating the ions (as opposed to Joule heating and subsequent thermal equilibration with the electrons) namely viscous heating. The magnitudes of the ion temperatures further imply that these viscous effects are quite significant. The importance of viscous effects in limiting the attainable rotational speeds and providing the heavy particle heating, can be easily seen by a simple calculation of the Reynolds and Hartmann numbers. The former is of the order of 10, suggesting that viscous forces are quite significant when compared to inertial forces, and the latter is also of the order of 10, exhibiting the importance of viscous forces when compared to electromagnetic forces.

We note from Figure 13 that the back emf contribution is the dominant one despite the speed limitation. This was consistent for all the cases simulated. The Hall effect and resistive drop account for 14 V of the total voltage, as opposed to 40 V due to a spinning plasma. A further insight in the behavior of the rotational speed as a function of the applied electromagnetic force is drawn by inspection of Figure 14. We note, that as the azimuthal force is increased, the maximum speed reaches a limiting value rather than increase linearly with the force for constant mass flow rate. This not only shows the dramatic effects of viscosity, but also explains the linear increase of voltage with applied field and constancy with discharge current when combined with the fact that the back emf dominates.

$$\begin{aligned} &\text{Unlimited rotation:} \; w \sim IB \rightarrow V \sim wBf(r) \sim IB^2 f(r) \\ &\text{Limited rotation:} \; w \sim c \rightarrow V \sim wBf(r) \sim cBf(r) \end{aligned} \qquad (12)$$

where f(r) is some function accounting for the profile effects, and c is a constant.

This limitation should have profound effects on propellant acceleration as well, especially if conversion of azimuthal kinetic energy to thrust energy is substantial. This conversion can only be accomplished if plasma expansion from the chamber occurs in a manner of a properly designed nozzle. An insight to the degree of such confinement by the electromagnetic force, $j_\theta B_z$, is given by calculation of the electron Hall parameter, Ω, and the actual electrical resistivity of the plasma. Distributions of the Hall parameter and the ratio of anomalous to classical resistivity as calculated by MACH2 are depicted in Figures 15 and 16 respectively. They show the dramatic effects of the latter on the former as the Hall parameter for the main plasma expanding core is only 2. The consequences can be readily seen when one compares this value to the magnitudes of $16 < \Omega < 100$ that can be obtained by excluding anomalous resistivity effects. Although the latter may imply the capability of inducing strong azimuthal currents that will create the magnetic nozzle, the former show that this capability is quite diminished, especially when combined with the fact that current distension downstream of the exit is insignificant (figure 7). In addition, the magnetic Reynolds number (including anomalous effects) never exceeds the moderate value of 0.3, which implies inadequate magnitudes of azimuthal current densities for radial confinement of the plasma. The lack of this confinement is confirmed by a detailed accounting of the azimuthal and radial kinetic energy in the plume region. This is carried out in Figure 17 and shows that the sum of azimuthal and radial kinetic energies is constant as a function of axial distance downstream of the thruster's exit. Thus, the azimuthal kinetic energy is mainly converted to radial kinetic energy consistent with an unconfined expansion. Based on the same energy accounting, in conjunction with the ion temperature distribution in the plume region (figure 10) the main acceleration mechanism is the conversion of thermal energy, provided by viscous heating, to axially directed kinetic energy.

The significance of viscous effects in these low density thrusters warrants further investigation. Variation of the mass flow averaged viscosity coefficient at the exit of the thruster as the applied azimuthal electromagnetic is increased is depicted in Figure 18, and provides a non-intuitive, yet extremely important result. The ratio of IB/μ is constant, and defines the limiting characteristic rotational speed, subject only to profile effects. The value of this ratio is 1.667×10^6 m/s for this particular geometry and operating conditions. This can be explained by the following argument: As IB increases the heavy particles are heated directly by viscous forces. Electron temperatures, however, remain moderately constant implying an approximately constant degree of ionization. Under such conditions the viscosity coefficient is an increasing function of ion temperature. It is calculated by the MACH2 model that this function is the same as the one by which ion temperature increases as IB is elevated. It is readily apparent that such an insight would never have been captured if the viscosity coefficient model developed for these simulations did not include two-temperature effects.

Conclusions

Simulations of a steady-state, applied-field MPD thruster[5] at NASA Lewis Research Center using the time dependent, two-dimensional, axisymmetric, magnetohydrodynamics code, MACH2, provided thrust and plasma voltage values that were compared with the experimental ones. Predicted thrust for a range of applied magnetic field strengths and discharge currents underestimated the experimental data, but captured the ostensible linear increase of thrust with both applied field and current. Plasma voltage predictions captured both the magnitude and linear increase with increasing magnetic field strength but overestimated the dependence on current.

For the operating geometry and conditions examined, calculations indicate that the radially confining electromagnetic forces are inadequate for magnetic nozzle behavior. The low density, moderate Hall parameter, ($\Omega \sim 2$), plasma was highly resistive, ($\eta_a/\eta_{cl} \sim 10$), especially in the exhausting plume region, and thus did not sufficiently interact, ($Rm_{max} \sim$

0.3) with the in-plane magnetic field. The electromagnetic azimuthal force applied to the plasma is opposed by viscous forces that limit the maximum attainable rotational speed to magnitudes much smaller than values expected only from inertia. The main acceleration mechanism was found to be conversion of thermal energy, developed largely by viscous heating, as the plasma exhausted from the discharge chamber. The limitation of the maximum rotational speed in conjunction with the dominance of the back electromotive force of the plasma voltage explains the linear dependence of the latter of applied magnetic field strength and the constancy of plasma voltage under varying discharge current. These new insights can be utilized to develop simple analytic expressions that predict thrust and voltage.

Acknowledgements

The authors acknowledge the support of the NASA Lewis Research Center, under grant NAG843 and the Ohio Supercomputer Center. We especially thank Dr. Roger M. Myers for his personal interest and assistance with the NASA LeRC thruster data.

References

1. Myers, R.M., "Anode Power Deposition in Applied-Field MPD Thrusters," AIAA 92-3463, 28th Joint Propulsion Conference, July 1992.

2. Krulle, G., "Theoretical Treatment of Current, Mass Flow, and Related Distributions in MPD Plumes," AIAA 72-501.

3. Tanaka, M., and Kimura, I., "Current Distribution and Plasma Acceleration in MPD Arcjets with Applied Magnetic Fields," Journal of Propulsion and Power, 4(5), Sept-Oct. 1988, pp 428-436.

4. Fradkin, D.B., "Analysis of acceleration Mechanisms and Performance of an Applied Field MPD Arcjet," Ph.D. Dissertation No. 1088-T, Department of Mechanical and Aerospace Engineering, Princeton University, Princeton, NJ, March 1973.

5. Myers, R.M., "Geometric Effects in Applied-Field MPD Thrusters," AIAA 90-2669, July 1990.

6. Sasoh, A., and Arakawa, Y., "Thrust Formula for an Applied-Field MPD Thruster Derived from Energy Conservation Equation,"

7. Peterkin, R.E., et. al., "MACH2: A Reference Manual, 4th and 5th Editions, November 1986 and July 1992, Weapons Laboratory, Kirtland Air Force Base, NM 87117-6008, References therein.

8. Frese, M.H., "MACH2: A Two-Dimensional Magnetohydrodynamics Simulation Code for Complex Experimental Configurations," NumerEx, 1400 Central Avenue SE, Suite 3200, Albuquerque, NM 87106-4811.

9. Cranfill, C.W., "EOSPAC: A Subroutine Package for Accessing the Los Alamos Sesame EOS Data Library," LA-9728-M, Los Alamos National Laboratory, August 1983.

10. Holian, K.S., ed, :T-4 Handbook of Material Properties Data Base, Vol Ic: EOS," LA-10160-MS, Los Alamos National Laboratory, November 1984.

11. Chapman, S., and Cowling, T.G., The Mathematical Theory of Non-Uniform Gases, 3rd Ed., Cambridge University Press, 1970.

12. Mikellides, P.G., "A Theoretical Investigation of Magnetoplasmadynamic Thrusters," Ph.D. Dissertation, Department of Aeronautical and Astronautical Engineering, The Ohio State University, 1994.

13. Spitzer, L., Physics of Fully Ionized Gases, 2nd Edition, Interscience, New York, 1962.

14. Chodura, R., "A Hybrid Fluid-Particle Model of Ion-Heating in High Mach Number Shock Waves," Nuclear Fusion Journal, Vol. 15, pp 55, 1975.

15. Payne, S.S., et. al., "Two-Dimensional MHD Simulations of Magnetic Field Penetration in the Plasma Opening Switch," IEEE Trans. on Plasma Science, Vol ps/15, No. 6, pp 725, Dec 1987.

16. Myers, R.M., Personal Communication.

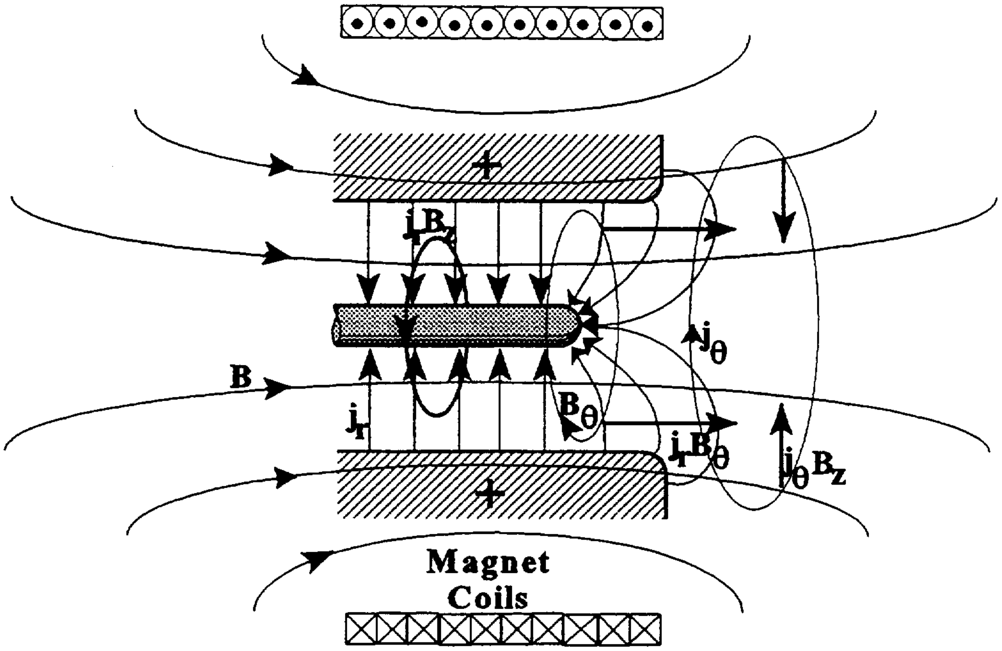

Figure 1. Applied-field MPD thruster schematic with applied and induced fields and currents and dominating electromagnetic forces shown.

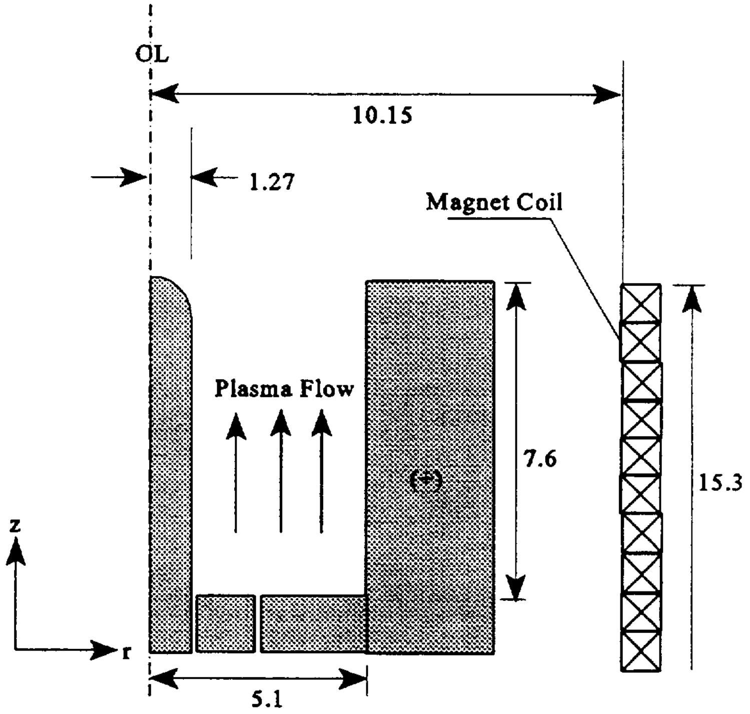

Figure 2. The geometry of the particular NASA LeRC 4" diameter applied-field MPD thruster used for the theoretical computations. All dimensions are in centimeters. The upright configuration is for consistency with MACH2 displays.

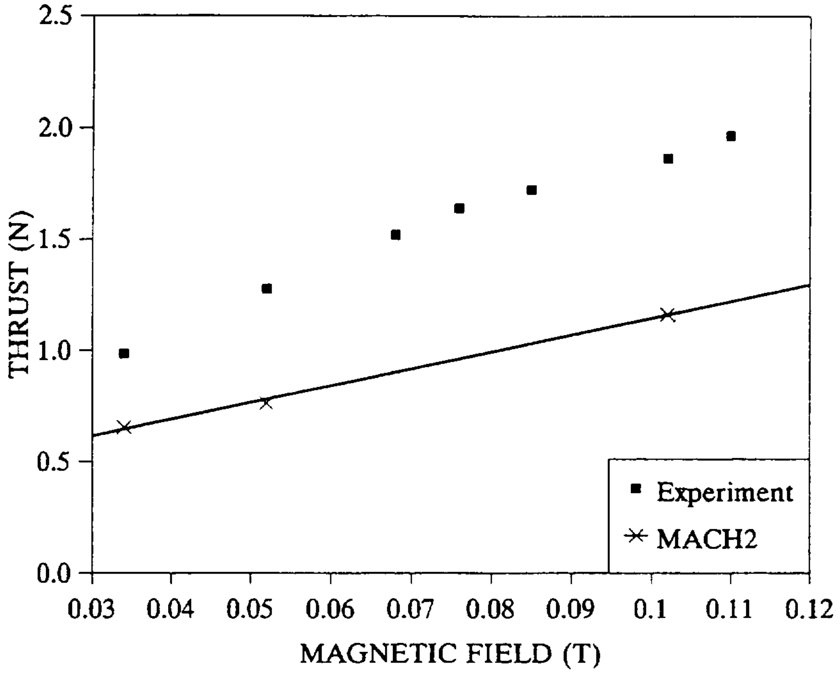

Figure 3. Thrust Vs Applied Magnetic Field Strength (at the cathode tip). Argon at 0.1 g/s and discharge current of 1000 A.

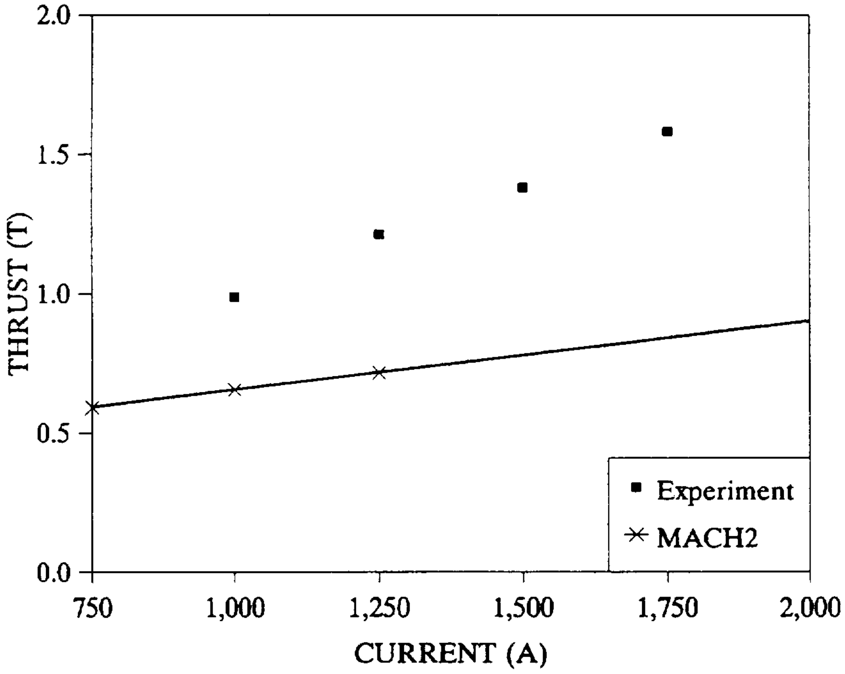

Figure 4. Thrust Vs Discharge Current. Argon at 0.1 g/s and applied field strength strength of 0.034 T (at the cathode tip).

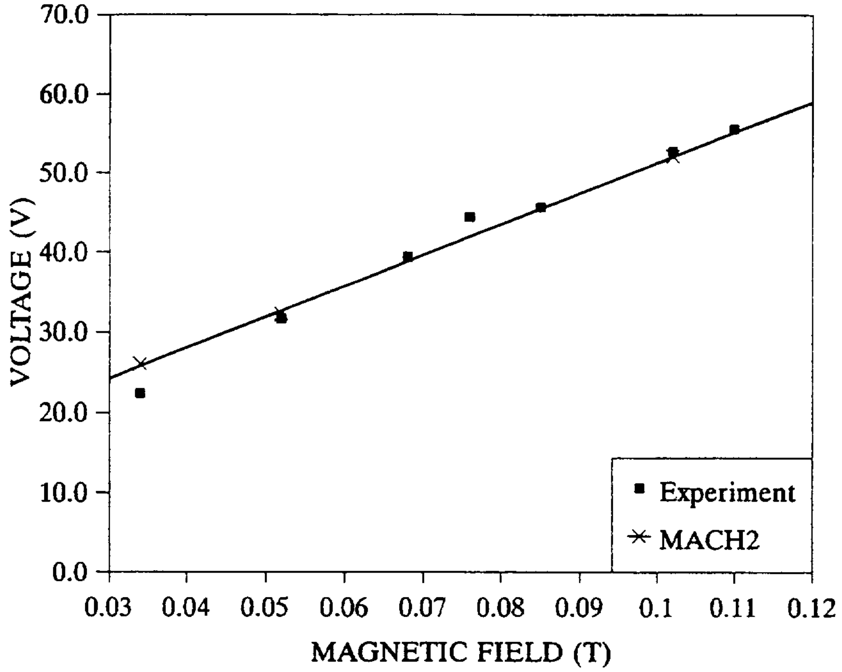

Figure 5. Plasma voltage Vs Applied Magnetic Field Strength (at the cathode tip). Argon at 0.1 g/s, and discharge current of 1000 A.

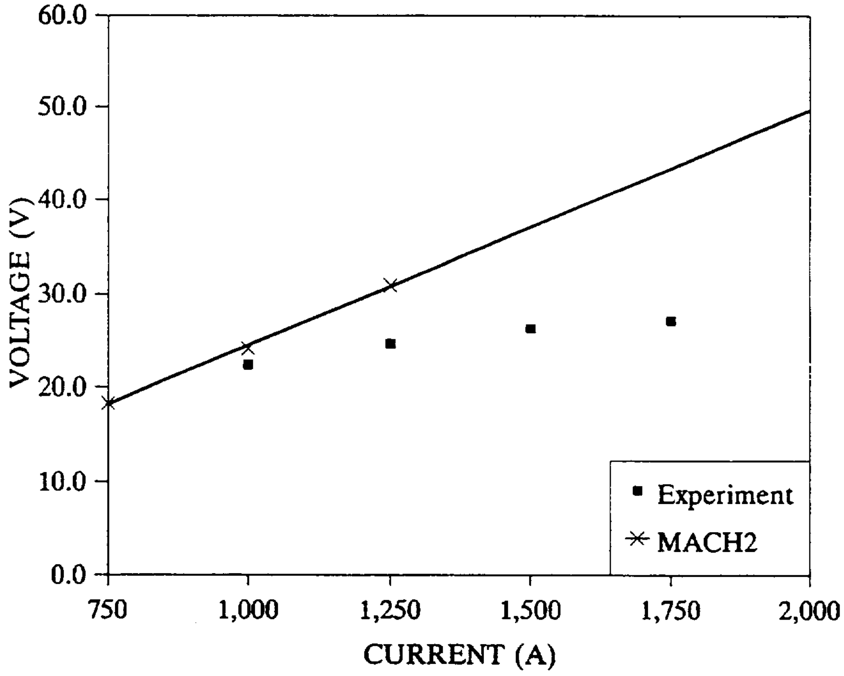

Figure 6. Plasma Voltage Vs Discharge Current. Argon at 0.1 g/s and applied magnetic field of 0.034 T (at the cathode tip).

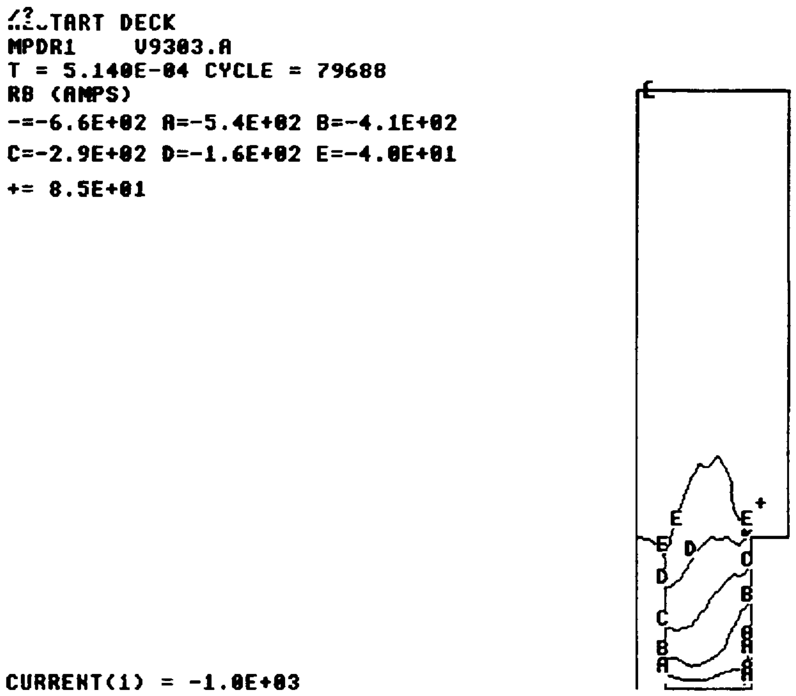

```
/?.TART DECK
MPDR1     V9303.A
T = 5.140E-04 CYCLE = 79688
RB (AMPS)
-=-6.6E+02 A=-5.4E+02 B=-4.1E+02
C=-2.9E+02 D=-1.6E+02 E=-4.0E+01
+= 8.5E+01

CURRENT(1) = -1.0E+03
```

Figure 7. Enclosed Current (rB_θ) distribution for the 0.102 T, 1000 A case.

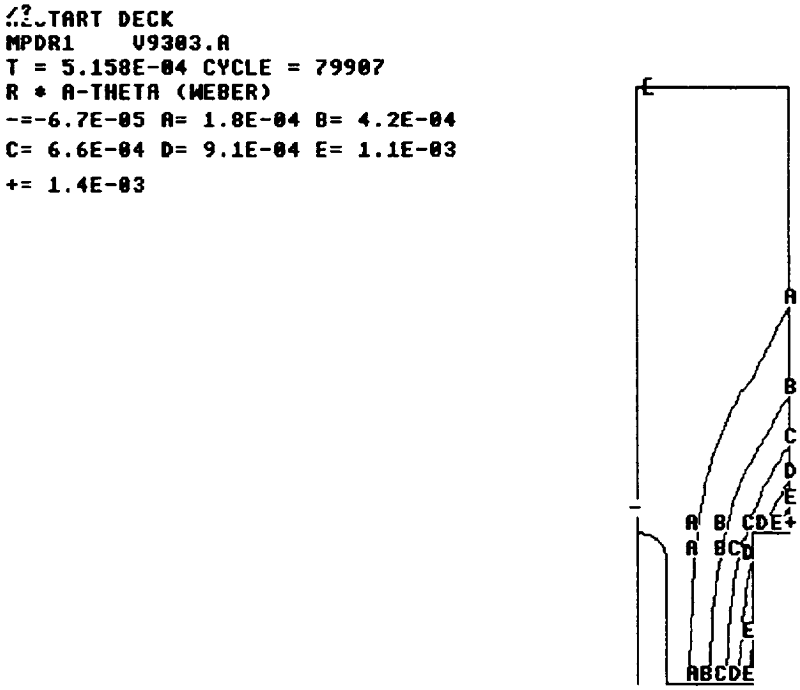

```
/?.TART DECK
MPDR1     V9303.A
T = 5.158E-04 CYCLE = 79907
R * A-THETA (WEBER)
-=-6.7E-05 A= 1.8E-04 B= 4.2E-04
C= 6.6E-04 D= 9.1E-04 E= 1.1E-03
+= 1.4E-03
```

Figure 8. Magnetic Flux lines for the 0.102 T, 1000 A case.

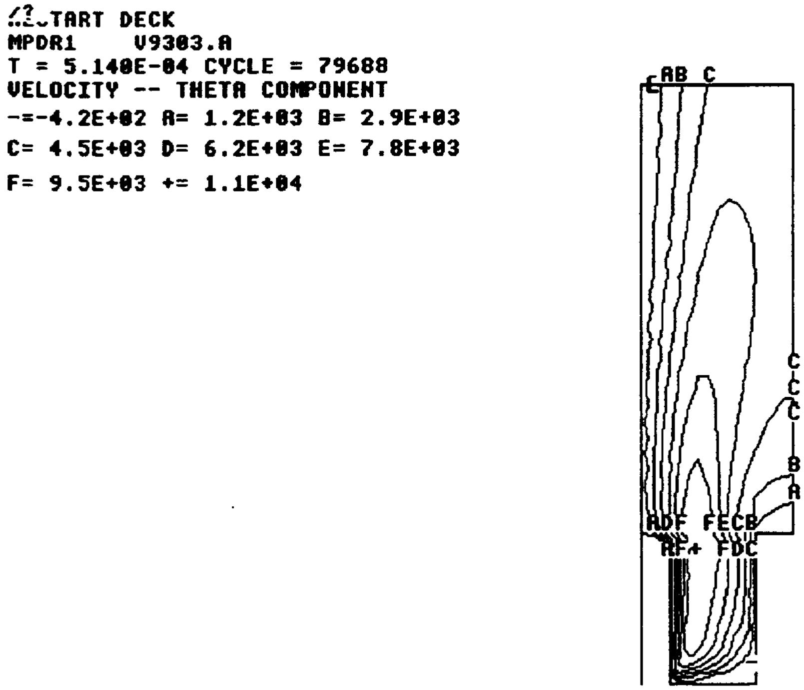

Figure 9. Azimuthal Velocity distribution (m/s) for the 0.102 T, 1000 A case.

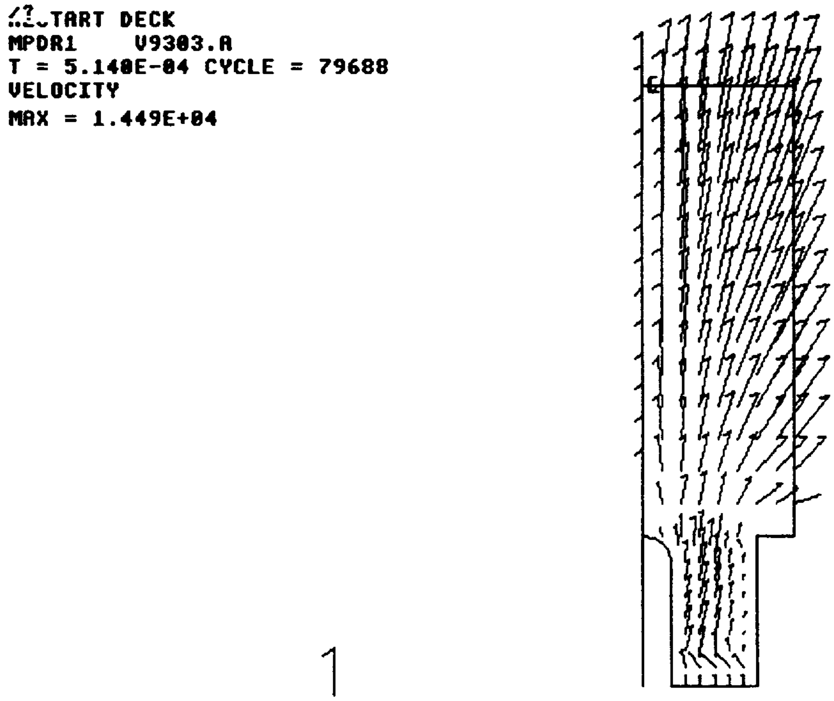

Figure 10. In-Plane Velocity Vectors (m/s) for the 0.102 T, 1000 A case.

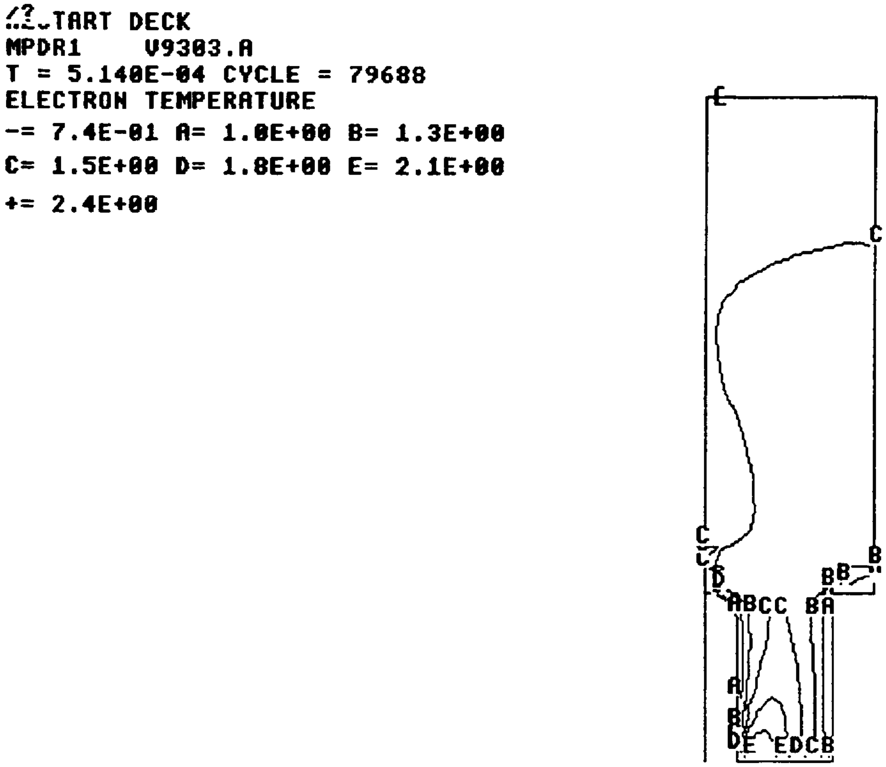

```
?.TART DECK
MPDR1     V9303.A
T = 5.140E-04 CYCLE = 79688
ELECTRON TEMPERATURE
-= 7.4E-01 A= 1.0E+00 B= 1.3E+00
C= 1.5E+00 D= 1.8E+00 E= 2.1E+00
+= 2.4E+00
```

Figure 11. Electron Temperature (eV) Distribution for the 0.102T, 1000A case.

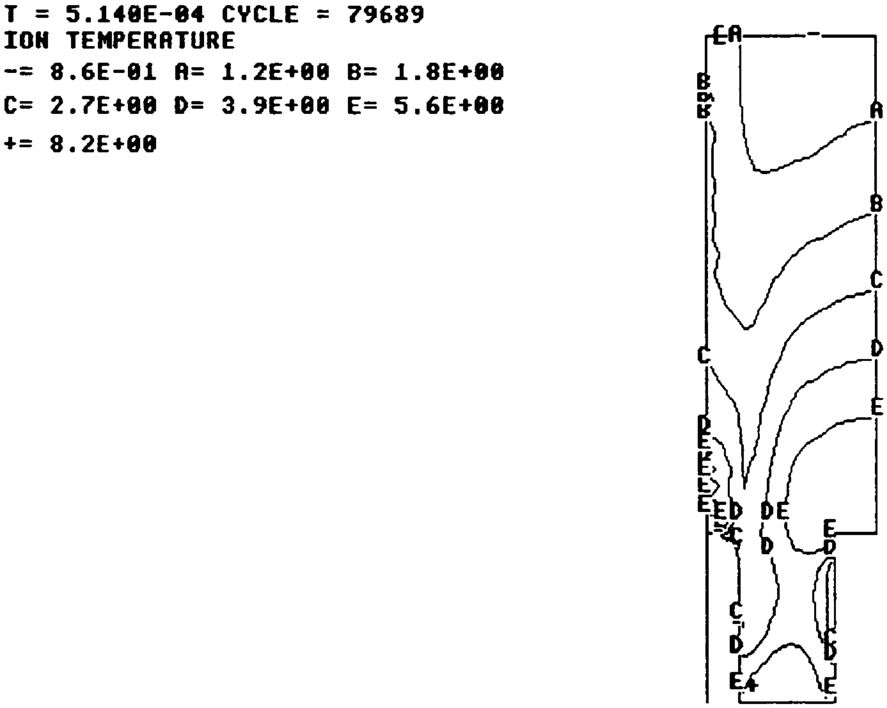

```
T = 5.140E-04 CYCLE = 79689
ION TEMPERATURE
-= 8.6E-01 A= 1.2E+00 B= 1.8E+00
C= 2.7E+00 D= 3.9E+00 E= 5.6E+00
+= 8.2E+00
```

Figure 12. Ion Temperature (eV) Distribution for the 0.102T, 1000A case.

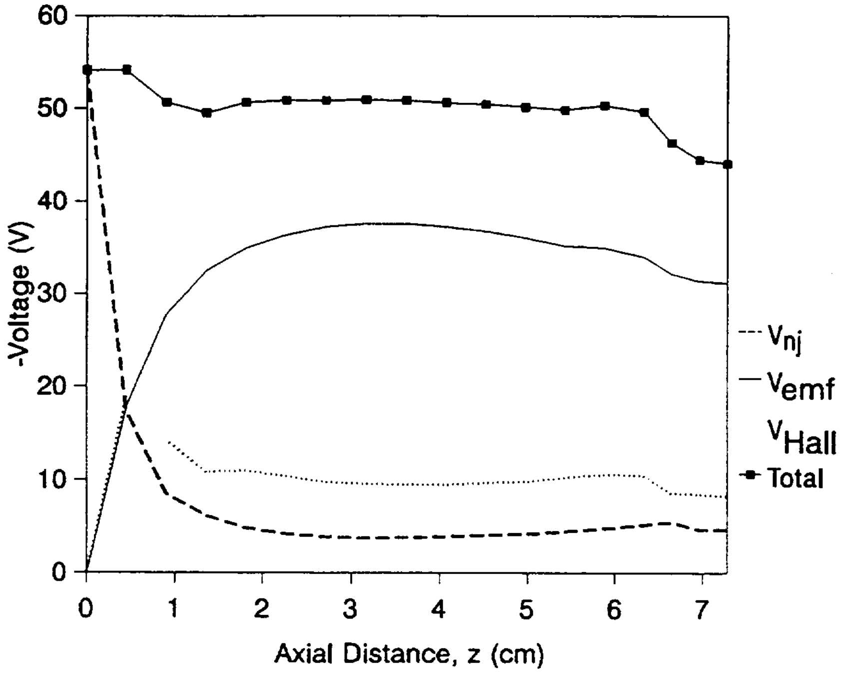

Figure 13. Plasma Voltage contributions for the 0.102T, 1000A case.

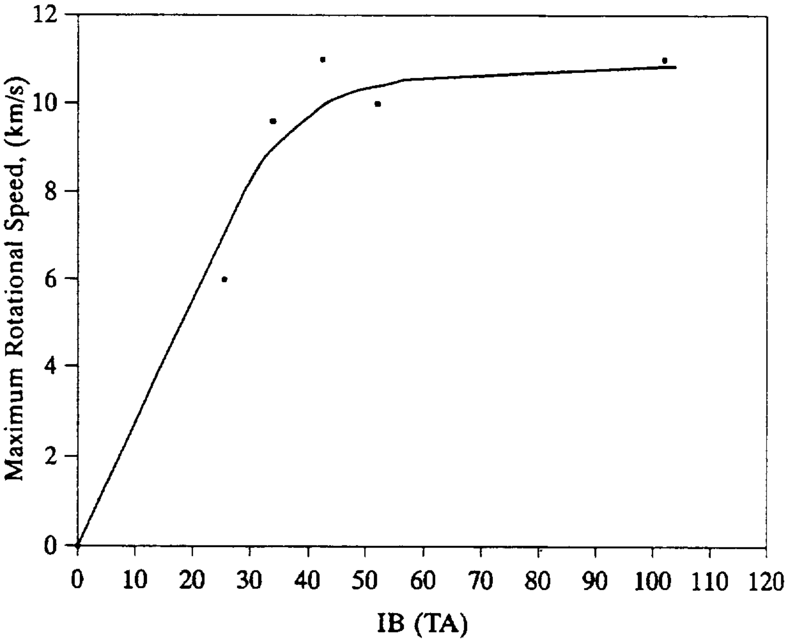

Figure 14. Maximum Rotational Speed vs the product of Discharge Current and Applied Magnetic Field Strength.

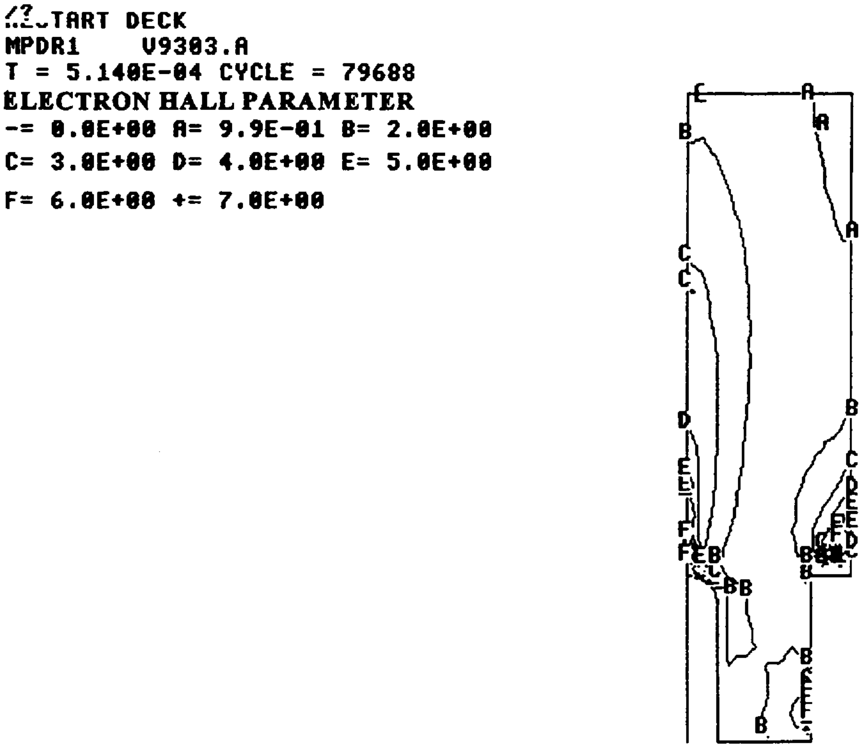

```
/?_TART DECK
MPDR1     V9303.A
T = 5.140E-04 CYCLE = 79688
ELECTRON HALL PARAMETER
-= 0.0E+00 A= 9.9E-01 B= 2.0E+00
C= 3.0E+00 D= 4.0E+00 E= 5.0E+00
F= 6.0E+00 += 7.0E+00
```

Figure 15. Electron Hall Parameter Distribution for the 0.102T, 1000A case.

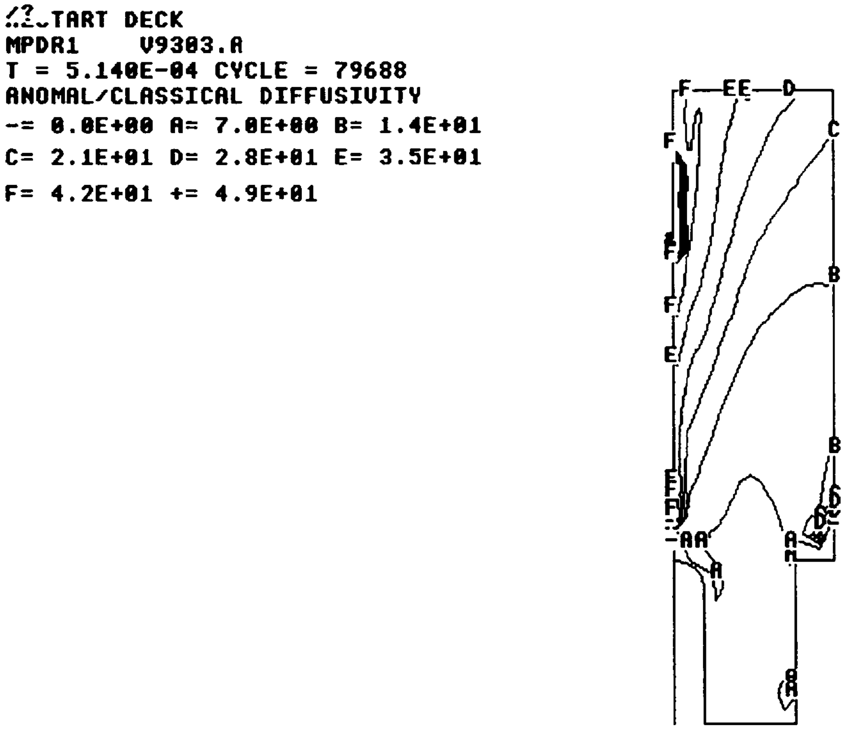

```
/?_TART DECK
MPDR1     V9303.A
T = 5.140E-04 CYCLE = 79688
ANOMAL/CLASSICAL DIFFUSIVITY
-= 0.0E+00 A= 7.0E+00 B= 1.4E+01
C= 2.1E+01 D= 2.8E+01 E= 3.5E+01
F= 4.2E+01 += 4.9E+01
```

Figure 16. Anomalous/ Classical Electrical Resistivity Ratio for the 0.102T, 1000A case.

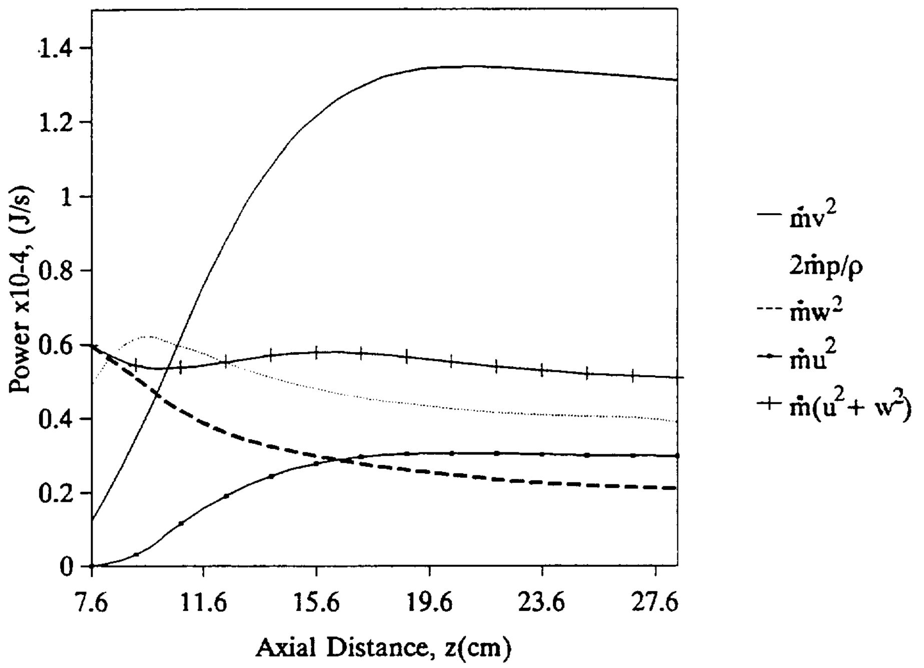

Figure 17. Power distribution as a function of axial distance for the 0.102T, 1000A case.

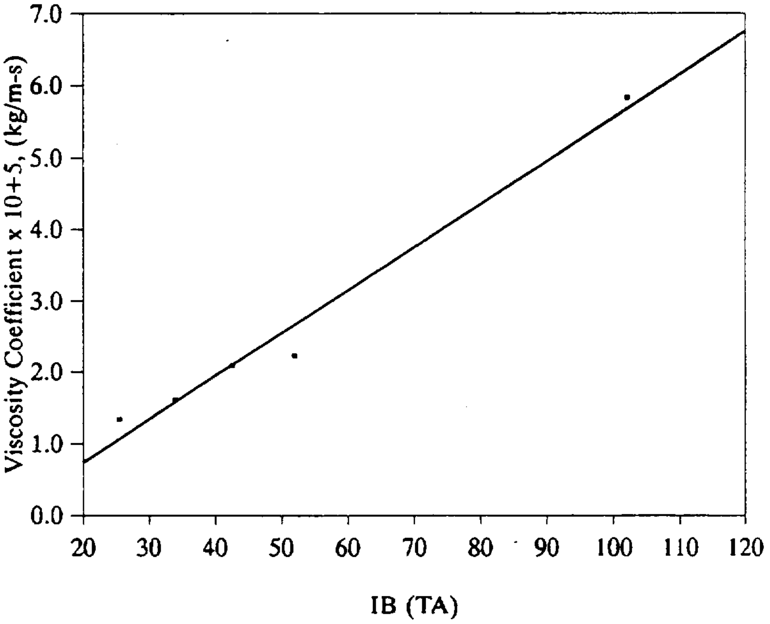

Figure 18. Viscosity Coefficient as a function of the product of Discharge Current and Applied Magnetic Field Strength.

FINAL REPORT Grant No. NAS 3 - 843

APPENDIX III

THEORETICAL AND EXPERIMENTAL STUDIES OF HOLLOW CATHODES

A. Salhi and P.J. Turchi, "Theoretical Modeling of Orificed Hollow Cathode Discharges", submitted to Journal of Propulsion and Power, September 1994

A. Salhi, P.J. Turchi and R.M. Myers, "Experimental Investigation of a Hollow Cathode Discharge", ibid

A. Salhi and P.J. Turchi, "Scaling Relations for Design and Operation of Orificed-Hollow Cathodes", 30th AIAA/SAE/ASME/ASEE Joint Propulsion Conference, Indianapolis, IN, (June 27 - 29, 1994). AIAA Preprint 94-3133

P.J. Turchi and A. Salhi,"Low Power Plasma Thruster Based on a Hollow Cathode Discharge", ibid. AIAA Preprint 94-3126

THEORETICAL MODELING OF ORIFICED, HOLLOW CATHODE DISCHARGES*

A. Salhi† and P. J. Turchi‡

The Ohio State University

Columbus, Ohio

Abstract

New physical aspects have been introduced in previous hollow cathode modeling. In contrast to the assumption of thermal equilibrium between the cathode wall and the heavy particles in the internal plasma column, the gas temperature is determined by a balance of electron heating (of plasma ions) and heavy particle heat conduction. This results in significantly higher heavy particle temperature near the center line compared to the cathode wall. Theoretical predictions of hollow cathode discharge are compared to recent experimental data. In addition, some analyses are presented to explain the consistency of the measured plasma conditions.

---

*Presented at the International Electric Propulsion Conference, Seattle, Washington, September 1993. Paper No. 93-024.

†Research Associate, Department of Aeronautical & Astronautical Engineering, Member AIAA.

‡Professor, Department of Aeronautical & Astronautical Engineering, Senior Research Scientist, USAF Phillips Laboratory, Member AIAA.

Nomenclature

a	speed of sound, m/s
A	area, m^2
A_R	Ridchardson's constant, $1.2 \times 10^6 A/m^2.^\circ K^2$
e	electron charge, 1.602×10^{-19} $Coul$
E	electric field, V/m
f	view factor
h	Planck's constant, $6.626 \times 10^{-34} J/^\circ K$
I	current, A
J	current density, A/m^2
k	Boltzman's constant, $1.381 \times 10^{-23} J/^\circ K$
L_e	emission surface length, m
m	particle mass, Kg
$\mathcal{M}$	Atomic mass, $a.u.$
$\dot{m}$	mass flow rate, Kg/s
n	particle number density,m^{-3}
p	internal cathode pressure, N/m^2
p	pressure, N/m^2
Q	cross section, m^2
q_r	radiative heat flux, W
r	radial coordinate

R	radius, m
t	characteristic time, s
T	temperature temperature. °K
u	flow velocity. m/s
V	potential. V
x	axial coordinate
Z	partion function or number of charges
α	degree of ionization
ϵ_o	permittivity of free space
ε	normalized electric field
η	plasma resistivity, $Ohm - m$
η_c	normalized fall voltage
η_o	normalized ion energy at the sheath edge
ϕ	work function. eV
κ	thermal conductivity, $W/K - m$
λ	mean free path, m
λ_D	Debye length. m
$ln\Lambda$	Coulomb logarithm
ν_i	ion to electron number density ratio at the sheath edge
ρ^c	charge density, $coul/m^3$
σ	electric conductivity, $(\Omega - m)^{-1}$
θ	electron to heavy particle temperature ratio

Subscripts

a	neutrals
b	normalized
c	cathode
D	discharge
e	electrons
F	fall
h	heavy particles
i	ions
eff	effective
eq	time for energy equipartition
or	orifice
s	surface or sheath edge
th	thermionic emission

I. Introduction

The integration of hollow cathode technology in plasma thrusters has intensified the need for adequate design of this device in high current regimes. Because of the difficult, sometimes unfeasible, experimental diagnostics at these high current levels, it is crucial to acquire theoretical understanding of hollow cathode operation. The latter is implemented to establish engineering guidelines that allow analysis of hollow cathode discharge, in order to define the optimal conditions and determine possible limitations under desired operation. Theoretical solutions are also preferred because they can save cost in, otherwise, expensive experimental studies.

The hollow cathode has been the focus of numerous theoretical efforts aimed at the understanding of the physical processes describing both internal plasma column and the overall cathode operation[1-4]. Because of the challenging nature of the problem, only some physical aspects were dealt with. A more general model was developed[5] in an attempt to establish a theoretical tool that could be applied to study and design hollow cathodes under various operating conditions. The particular intent has been to cast the model in terms of controllable parameters such as, current, mass flow rate, propellant and geometry, without reliance on experimental data or formulas. In light of recent experimental work[6], this theoretical model has been subject to validation and further improvements. This paper presents the new analyses introduced and demonstrates the capability of the theoretical model.

II. Basic Model

The cathode geometry considered for the study of hollow cathode arc discharge is a cylindrical cavity with a a relatively small orifice[5]. In such configuration, the energy losses associated with radiation, positive ions and excited atoms are substantially reduced. Therefore, the cathode fall is expected to be reduced while large currents can still be carried by the discharge. This geometry also allows for reasonable boundary conditions vital to the solution of this problem. The theoretical approach includes two-dimensional variation in plasma potential with uniform particle temperatures and densities. The gas temperature (i.e., heavy particle temperature) is assumed to be equal to the wall temperature.[1,4] One particular aspect of this formulation is the specification of an adiabatic wall. This condition reflects a special interest in high power density operation in which the principal cooling mechanism of the surface is thermionic electron emission and radiation. The basic model takes into account the Ohmic heating due to a resistive plasma. To a first approximation the conductivity of the plasma is considered to be that of a fully ionized gas. This assumption is reasonably justified due to the fact that hollow cathode can sustain highly ionized discharges.[7,8] Finally, in line with the nearly closed geometry of the problem, plasma composition is determined by a two-temperature Saha equation.[9,10] The set of algebraic equations governing power balance within the hollow cathode and the double sheath at the emitting surface are solved to obtain the dependence of various characteristics on terminal parameters such as, discharge current, mass flow rate, gas properties. material work function and geometry.

Thermionic emission current density

The thermionic current density is given by Richardson-Schottky equation:

$$J_{th} = A_R T_c^2 exp\left(-\frac{\phi_{eff}}{kT_c}\right) \tag{1}$$

where the effective work function given by:

$$\phi_{eff} = \phi - \sqrt{\frac{e|E_c|}{4\pi\epsilon_o}} \tag{2}$$

for field-enhanced emission (Schottky effect) in terms of the electric field E_c at the cathode surface. The electric field at the cathode can be estimated from the double sheath analysis governed by Poisson's equation:

$$\nabla^2 V = -\frac{\rho^c}{\epsilon_o} \tag{3}$$

A solution of this equation was presented by Prewett and Allen[11] where the electric field was given by:

$$\varepsilon_c = \{4\nu_i\eta_o[(1+\eta_c/\eta_o)^{1/2} - 1] - 2J_b(2\eta_c)^2$$

$$+ 2exp(-\eta_c) - 2\}^{1/2} \tag{4}$$

where the nondimensional parameters are defined as follows:

$$\varepsilon_c = \frac{E_c e \lambda_D}{kT_e} \tag{5}$$

$$\lambda_D = \left(\frac{\epsilon_o k T_e}{n_e \epsilon^2} \right)^{\frac{1}{2}} \tag{6}$$

$$\eta_c = \frac{eV_F}{kT_\epsilon} \tag{7}$$

$$J_b = \frac{J_{th}}{en_e \left(\frac{kT_e}{m_e} \right)^{\frac{1}{2}} (2\eta_c)^{\frac{1}{2}}} \tag{8}$$

$$\nu_i = 1 + 2\eta_c J_b \tag{9}$$

$$\eta_o = \frac{1 + 2\eta c J_b}{2(1 - J_b)} \tag{10}$$

Ion current density

The ion flux density to the cathode surface is assumed to be the random thermal flux:

$$J_i = en_i \left(\frac{kT_i}{2\pi m_i} \right)^{1/2} \tag{11}$$

Plasma electron current density

Plasma electrons are assumed to have a Maxwellian distribution, and only electrons with energies higher than the fall voltage are able to reach the cathode surface. Therefore, the plasma electron flux to the cathode can be expressed by:

$$J_e = e n_e \left(\frac{kT_e}{2\pi m_e}\right)^{1/2} exp\left(-\frac{eV_F}{kT_e}\right) \tag{12}$$

The fall voltage V_F is considered across a non-neutral, collisionless region between the cathode surface and the plasma.

Discharge current

Based on the contribution of all particle fluxes at the cathode surface, the discharge current can be expressed by:

$$I_D = I_{th} + I_i - I_e \tag{13}$$

For orificed hollow cathodes, as a boundary condition, the discharge current is also given by:

$$I_D = e n_e \left(\frac{kT_e}{2\pi m_e}\right)^{1/2} A_{or} - \alpha I_{eq} \tag{14}$$

where the equivalent flow rate is defined by:

$$I_{eq} = \frac{Ze\dot{m}}{m_i} \tag{15}$$

for a degree of ionization:

$$\alpha = \frac{n_i}{n_i + n_a} \tag{16}$$

Cathode internal pressure

Assuming that all particles behave like a perfect, dilute gas, the plasma pressure in the hollow cathode can be evaluated from the equation of state:

$$p = n_e k T_e + n_i k T_i + n_a k T_a \quad . \tag{17}$$

Assuming that the heavy particles have the same temperature and combining equations (16) and (17) we may write:

$$p = (n_i + n_a) k T_i \left(1 + \alpha \frac{T_e}{T_i}\right) \tag{18}$$

Mass flow rate

Under the consideration of a small orifice area compared to the cross section area of the hollow cathode, a simple force balance at the orifice could be expressed as:

$$p A_{eff} = p_{or} A_{eff} + \dot{m} u_{or} \tag{19}$$

The effective orifice area in equation (19) reflects the assumption of a parabolic velocity profile due to viscous effects. In this case the effective area is equal to one half the cross section area. Furthermore, considering isothermal sonic conditions at the orifice and defining a hybrid speed of sound for the electron and heavy particles as:

$$a = \sqrt{\frac{kT_i}{m_i}\left(1 + \alpha\frac{T_e}{T_i}\right)} \tag{20}$$

equation (19) reduces to:

$$\dot{m} = \frac{p}{4\sqrt{\frac{kT_i}{m_i}\left(1 + \alpha\frac{T_e}{T_i}\right)}} A_{cr} \tag{21}$$

Two-temperature Saha equation

For the evaluation of the neutral number density, a two-temperature Saha equation has been derived based on chemical equilibrium[9,10]:

$$n_e\left(\frac{n_i}{n_a}\right)^{1/\theta} = \frac{2Z_i}{Z_a}\left(\frac{2\pi m_e kT_e}{h^2}\right)^{3/2}$$

$$\times\, exp\left(-\frac{\epsilon_i}{kT_e}\right) \tag{22}$$

$$\theta = \frac{T_e}{T_i} \tag{23}$$

This modified form of the Saha equation was used successfully by Kannapan and Bose [12], but is the subject of continued study.

Power balance

The cathode surface receives energy from ions accelerated through the fall. plasma electrons having energies exceeding the fall barrier and all other processes taking energy out of the plasma (e.g. excited atom flux and photons). In the limit of high power density, the cathode cools itself primarily by electron emission, so the power balance at the cathode surface is written as:

$$\int J_{th} \left(\phi_{eff} + \frac{5kT_c}{2e} \right) dA_e =$$

$$\int J_i \left(\epsilon_i + V_c - \phi_{eff} \right) dA_e +$$

$$\int J_e \left(\phi_{eff} + \frac{5kT_e}{2e} \right) dA_e + f q_r \tag{24}$$

where the view factor f is expressed as:

$$f = \frac{Ae}{As} \tag{25}$$

Here integrals over the surface are needed to allow variation of current density along the surface. Electron emission provides energy to the plasma in the form of electrons accelerated by the cathode fall. This energy is utilized to ionize and excite the gas, and heat the plasma electrons. Energy is also added to the plasma by ohmic heating with plasma electrical resistivity η. Energy is lost by particles flowing out of the hollow cathode in the form of enthalpy. This power balance is given by:

$$\int J_{th} \left(V_c + \frac{5kT_c}{2e} \right) dA_e + \int \eta J^2 dV =$$

$$\int J_i \left(\epsilon_i + \frac{5kT_i}{2e} \right) dA_s + \int J_e \left(\frac{5kT_e}{2e} \right) dA_s +$$

$$(I_D + \alpha I_{eq})\left(\frac{5kT_e}{2e}\right) + I_{eq}\left(\frac{5kT_e}{2e}\right) + q_r \qquad (26)$$

where the ionization/excitation energy per ion is lost to both the cathode surface and the orifice exit area so the ion flux J_i is integrated over the total surface area A_s.

Plasma conductivity

In this analysis the plasma conductivity is approximated to that of a fully ionized gas since hollow cathodes are expected to have reasonable degree of ionization (α greater than 10^{-3}). Hence[13],

$$\sigma = \frac{1.53 \times 10^{-2}}{\log \Lambda} T_e^{3/2} \qquad (27)$$

where:

$$\Lambda = 1.24 \times 10^{-7} \left(\frac{T_e^3}{n_e}\right)^{1/2} \qquad (28)$$

Plasma potential distribution

In this study an axisymmetric two-dimensional system is considered. The plasma potential distribution in the hollow cathode is solved from Laplace equation governing a neutral plasma:

$$\nabla^2 V = 0 \qquad (29)$$

with the following boundary conditions specified at the sheath edge (r = R), cathode inlet (x = 0) and orifice (x = L_e):

$$\frac{\partial V}{\partial r} = \eta J_s \quad at \quad r = R_c$$

$$\frac{\partial V}{\partial x} = \begin{cases} \eta J_{or} & \text{at } 0 \leq r \leq R_{or} \text{ and } x = L_e \\ 0 & \text{at } R_{or} \leq r \leq R_c \text{ and } x = L_e \end{cases} \tag{30}$$

$$\frac{\partial V}{\partial x} = 0 \quad at \quad 0 \leq r \leq R_c \quad and \quad x = 0$$

where:

$$\int J_s dA_s = I_D \tag{31}$$

$$\int J_{or} dA_{or} = I_D \tag{32}$$

Laplace equation is solved numerically using finite difference technique. This solution is part of the overall solution which is obtained through an iterative process.

III. Radial variation of the gas temperature

Recent experimental measurements[6] of the gas temperature along the cathode center line indicate that the heavy particle temperature is higher than that of the wall. Consideration of the thermal conductivity for the conditions indicated by the basic model suggests that the electron temperature is rather uniform in the main body of the cathode plasma (i.e.. away from the high density at the orifice). The heavy particle thermal conductivity, however, is dominated by atom-atom collisions and allows a significant temperature gradient between the cathode wall and center line. The heavy particle temperature distribution can be estimated by balancing electron collisional heating[13] of ions with heavy particle heat conduction in the radial direction: It is assumed here that the ions immediately come to a thermal equilibrium with the neutral atoms. Hence,

$$\frac{1}{r}\frac{d}{dr}\left(r\kappa\frac{dT_h}{dr}\right) = -n_e\frac{T_e - T_h}{t_{eq}} \tag{33}$$

where t_{eq}, the time for energy equipartition, is given by:

$$t_{eq} = 5.87 \times 10^6 \frac{\mathcal{M}_e\mathcal{M}_i}{n_e Z_e^2 Z_i^2 ln\Lambda}\left(\frac{T_e}{\mathcal{M}_e} + \frac{T_i}{\mathcal{M}_i}\right)^{3/2} \tag{34}$$

An approximate formula for the thermal conductivity κ of the heavy particles, for partially ionized gas, could be derived based on the mean-free-path concept as[14]:

$$\kappa = \frac{15}{8}kn_h\lambda_h\left(\frac{8kT_h}{\pi m_h}\right)^{1/2} \tag{35}$$

where λ_h represents the heavy particles mean free path defined by:

$$\lambda_h = \frac{1}{\sqrt{2} n_h Q_{hh}} \tag{36}$$

Here. Q_{hh} is the average heavy particle cross section including neutral-neutral, neutral-ions and ions-ions collisions. It is important to point out that for weakly ionized gas, conduction is dominated by neutral-neutral collisions.

The heavy particle temperature is determined by solving equation 33 numerically in conjunction with the following boundary conditions:

$$T_h = T_c \quad at \quad r \;=\; R \tag{37}$$

$$\frac{dT_h}{dr} = 0 \quad at \quad r \;=\; 0 \tag{38}$$

The electron and ion particle densities are determined from the total particle density with the condition of uniform (total) pressure and the assumption of uniform degree of ionization based on the electron temperature. In view of the simplicity of the formulation. no attempt has been made to iterate this first order correction for the heavy particle temperature and density with the zero order model for the basic plasma conditions.

IV. Results

In order to determine the validity of the theoretical model, it is necessary to make a comparison between the theoretical predictions and the experimental measurements of the plasma conditions and wall temperature under identical operating conditions[6]. Therefore, the plasma properties and cathode surface temperature were plotted against the operating conditions (discharge current, mass flow rate, propellant and cathode geometry).

Cathode temperature

The external surface temperature is compared to the calculated insert temperature. Since the insert work function has been reported by Forman[15] to vary in the range 1.8 - 2.0 eV, these two limits were used to predict the wall temperature. In figures 1 and 2 , in addition to the measured tip temperature, the calculated temperature is plotted against the discharge current for two different values of the material work function. These figures indicate that the present model prediction of the cathode temperature coincides with the cathode tip temperature (maximum temperature). The agreement obtained in all cases, supports the assumption that thermionic (vs photo-) emission is the most important surface electron emission mechanism.

Cathode internal pressure

The cathode internal pressure is one of the important parameters that describes the contributions of the operating conditions in establishing the final state of the internal plasma column. Figures 3 and 4 show that for a given flow rate, propellant and cathode geometry the internal pressure increases with the discharge current. This behavior could be explained by the increase in the heavy particle temperature with discharge current. which then requires higher pressure for mass flow through a choked orifice. The agreement obtained between the computed and measured pressure provides confidence in the theoretical prediction of the gas temperature (figure 5).

Plasma conditions

In the experimental investigation the plasma potential was estimated based on the measured floating potential and electron temperature[16]. The results are compared to the calculated plasma potential for similar operating conditions in figures 6 and 7. Agreement is obtained for discharge currents higher that 3 A. It is important to point out that low currents as well as low mass flow rates tend to induce an instable discharge that manifests itself in higher discharge voltages.

The internal plasma column was observed in the experiment to extend over two-insert diameters. Within this length the plasma density varied from 10^{12} to 10^{15} cm^{-3}. Agreements of the theoretical predictions are realized in the upper limit (figures 8). This is related to the fact that the theory does not allow for density variation within the internal plasma column. On the other hand, the prediction of the maximum plasma density inside the hollow cathode is important to define the state of the plasma before leaving the cathode.

The calculated electron temperature is compared to the one experimentally predicted using electrostatic probe and spectroscopic diagnostics (figures 9). Satisfactory agreements are realized with the spectroscopic measurements. On the other hand, the substantial variation of the electron temperature (0.6-2.0 eV for argon and 0.6-1.6 eV for xenon), determined from the electrostatic probe measurements along the cathode center line, prevents a direct comparison. Measurements based on line ratios can be subject to misinterpretation of electron vs "configuration" temperatures.[17] It has been suggested that there is insufficient residence time of atoms in the cathode to allow even restricted LTE to be established.[18] This will result in higher electron temperature values than the present model predictions, which will bring the theory to a closer agreement with the experiment.

VI. Conclusions

The main objective of the basic theory[5] has been achieved through the generally good agreements obtained with experiment. The theoretical model includes enough physics, founded on first-principles, to enable adequate prediction of the cathode discharge under desired operation. Optimization of hollow cathode design, particularly as a subsystem of an overall thruster or plasma contactor, could be achieved by using the model to seek the best combination of operating conditions. Among the many results obtained, both theory and experiment show that the discharge current, for a given cathode configuration, is the key operator that controls the cathode operation and wall temperature. On the other hand the mass flow rate has a rather minor role. Furthermore, the wall cooling mechanism is realized by thermionic emission. Since the model indicates that the length of the emission region is scaled by the insert diameter. it is necessary to increase the diameter of the cathode with the square root of the discharge current in order to achieve sufficient emission for a given material work function. As usual the material work function is a critical parameter that dictates the cathode temperature and consequently its lifetime.

References

1. J. L. Delcroix, H. Minoo, and A. R. Trindade. Establishment of a general rule for a hollow cathode arc discharge. *Journal de Physique*, 29(6):605-610, July 1968.

2. A. Lorente-Arcas. A model of the discharge in the hollow cathode. *Plasma Physics*, 14(6):651-659, 1972.

3. C. M. Ferreira and J. L. Delcroix. Theory of the hollow cathode arc. *Journal of Applied Physics*, 49(4), April 1978.

4. D.E. Siegfried and P. J. Wilbur. A model for mercury orificed, hollow cathodes: Theory and experiment, *AIAA Journal* 22(10), October 1984.

5. A. Salhi and P. J. Turchi. A first-principles model for orificed, hollow cathode operation. *AIAA Paper No. 92-3742*, July 1992.

6. A. Salhi, R. M. Myers and P. J. Turchi. Experimental investigation of a hollow cathode discharge. *IEPC Paper No. 93-025*, September 1993.

7. L. M. Lidsky, S. D. Rothleder, D. J. Rose, and S. Yoshikawa. Highly ionized

hollow cathode discharge. *Journal of Applied Physics*, 33(8):2490- 2497, August 1962.

8. G.V. Babbkin, V. G. Mikhalev, E. P. Morozov, and A. V. Potatov. Experimental investigation of the plasma in multichannel cathode. *Journal of Applied Mechanics and Technical Physics*, 17:767-770. November-December 1976.

9. A.V. Potapov. Chemical equilibrium of multitemperature systems. *High Temperature*, 1:48-51, January-February, 1966.

10. S. Veis. The Saha equation and lowering of the ionization energy for a two-temperature plasma. *Czechoslovak Conference on Electronics and Vacuum Physics*, Edited by Libor Pathy (Charles University, Prague), pp. 105-110, 1968.

11. Prewett P. D. and Allen J. E. "Double Sheath Associated with a Hot Cathode". Proceeding of Royal Society of London, Ser A (341):435-446, April 1976.

12. Kannapan D. and Bose T. K. "Transport Properties of a Two-Temperature Argon Plasma". The Physics of Fluids, 20(10):1668-1672, October 1977.

13. L. Spitzer, Jr. Physics of fully ionized gases. *Interscience Publishers, Inc*, New York, 1956.

14. M. Mitchner and C. Kruger. Partially ionized gases. *John Wiley & Sons, Inc.*, New York, pp. 88-93, 1973.

15. R. Forman. Surface studies of thermionic cathodes and the mechanism of operation of an impregnated tungsten cathode. *NASA TN D-8295*, September, 1976.

16. F. F. Chen. Electric Probes. in R. H. Huddlestone and S. L. Leonard. Plasma diagnostic techniques. *Academic Press Inc., New York.* Chapter 4, pp. 178, 1965.

17. B. van der Sijde. Configuration temperature in a hollow argon arc and transition probabilities of the Argon II spectrum. *J. Quant. Spectrosc. Radiat. Transfer*, 12:703. 1971.

18. I. Katz. Private communication.

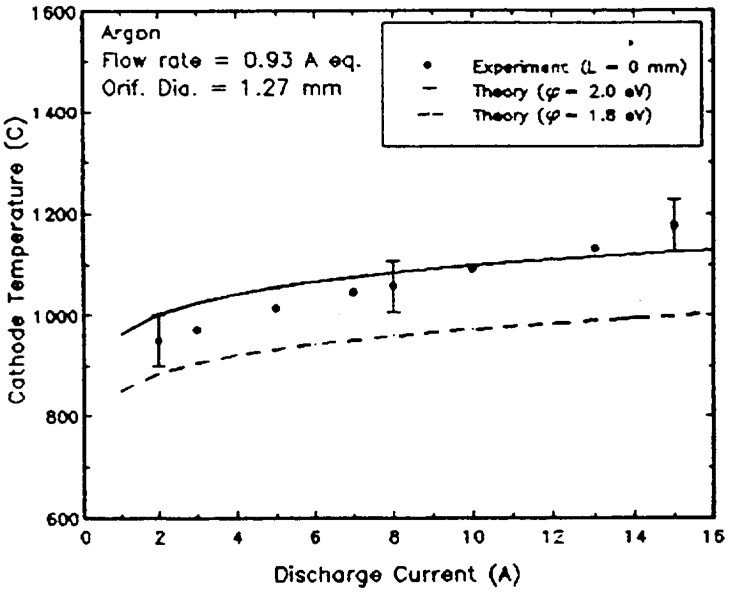

Figure 1: Effect of discharge current on cathode surface temperature (comparison between theory and experiment, argon, $\dot{m} = 0.93\,A\,eq.$, $d_o = 1.27\,mm$).

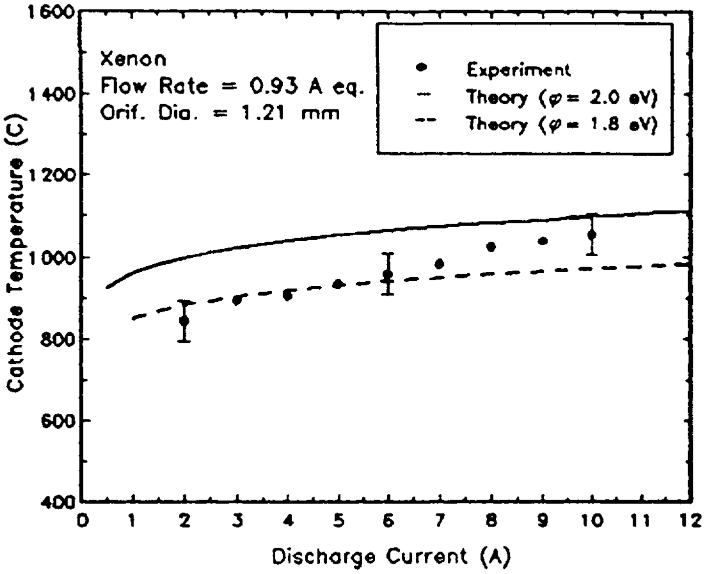

Figure 2: Effect of discharge current on cathode surface temperature (comparison between theory and experiment, xenon, $\dot{m}$ = 0.93 $A\ eq.$, d_o = 1.21 mm).

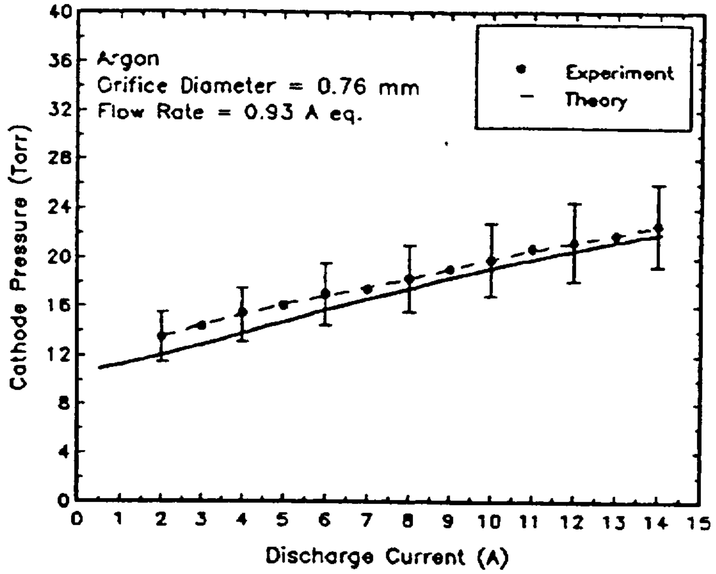

Figure 4: Effect of discharge current on cathode internal pressure (comparison between theory and experiment, xenon, $\dot{m}$ = 0.93 $A\ eq.$, d_o = 1.21 mm).

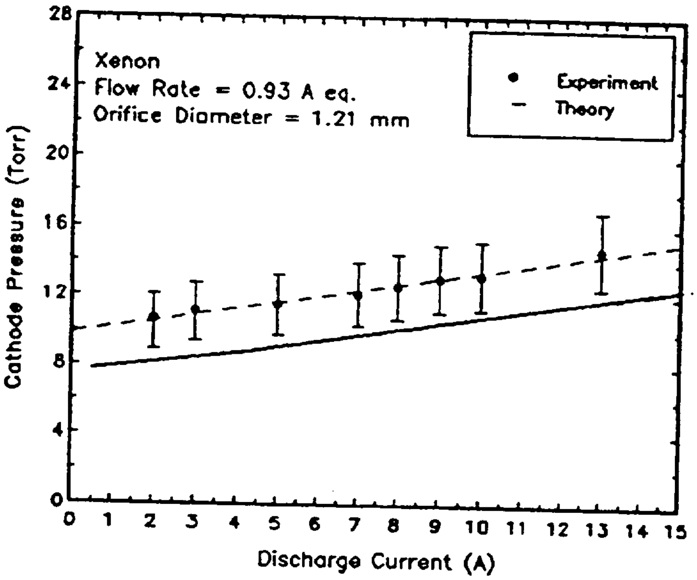

Figure 3: Effect of discharge current on cathode internal pressure (comparison between theory and experiment, argon, $\dot{m}$ = 0.93 $A\ eq.$, d_o = 0.76 mm).

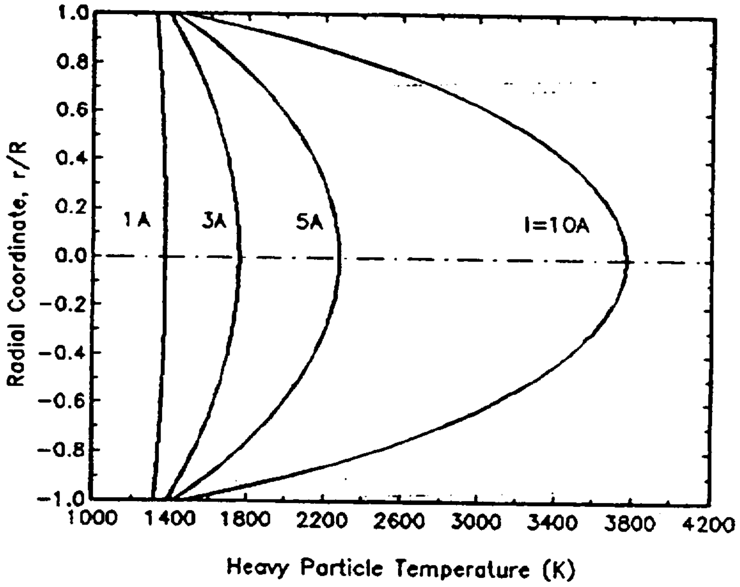

Figure 5: Theoretical prediction of the radial distribution of the heavy particles temperature (argon, $\dot{m}$ = 0.5 $A\ eq.$, d_o = 0.76 mm, R = 1.9 mm.

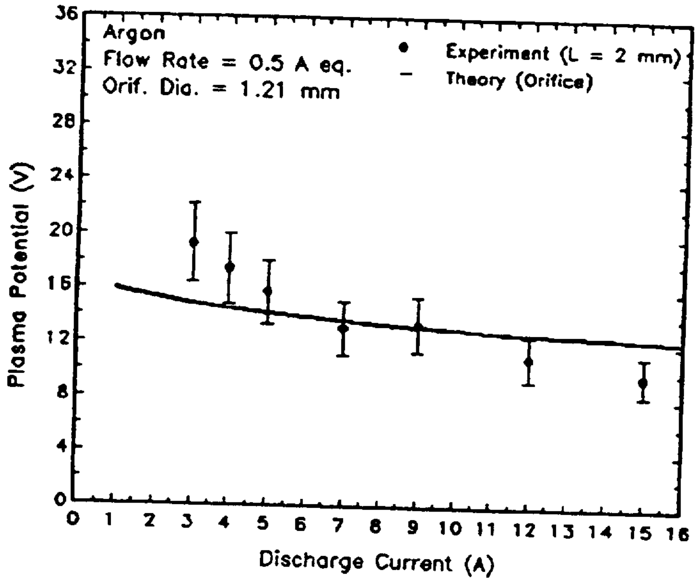

Figure 6: Effect of discharge current on plasma potential (comparison between theory and experiment, argon, $\dot{m} = 0.5\,A\,eq.$, $d_o = 1.21\,mm$).

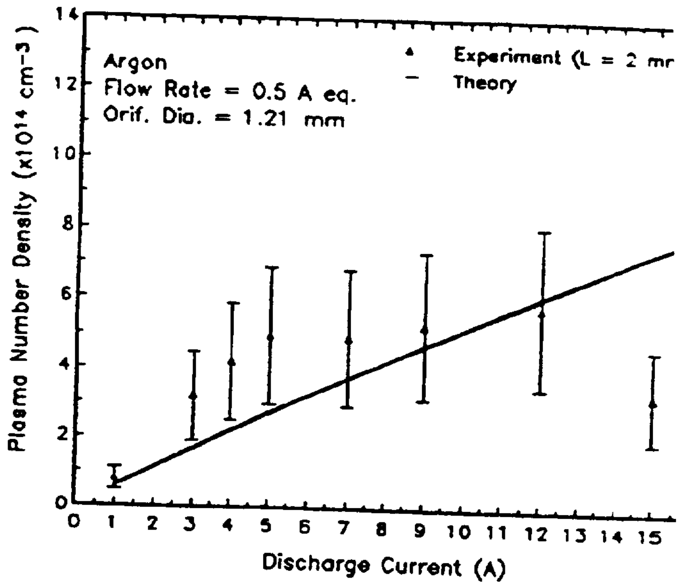

Figure 8: Effect of discharge current on electron number density (comparison between theory and experiment. argon, $\dot{m} = 0.5\,A\,eq.$, $d_o = 1.21\,mm$).

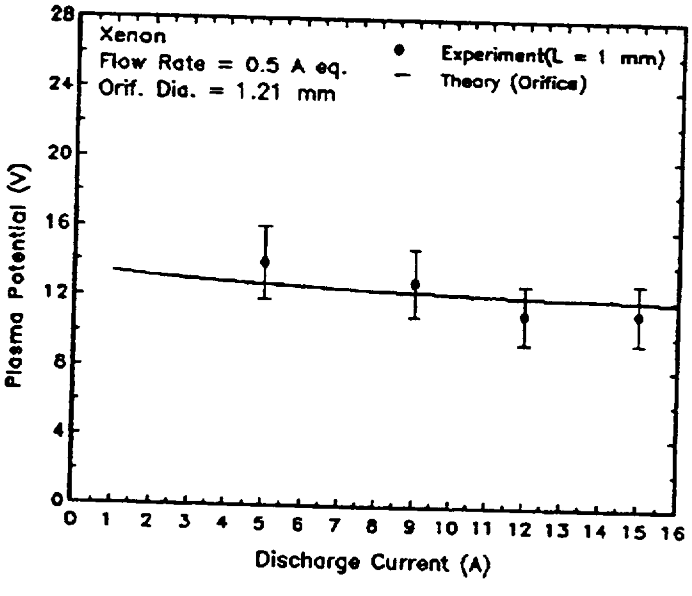

Figure 7: Effect of discharge current on plasma potential (comparison between theory and experiment, xenon, $\dot{m} = 0.5\,A\,eq.$, $d_o = 1.21\,mm$).

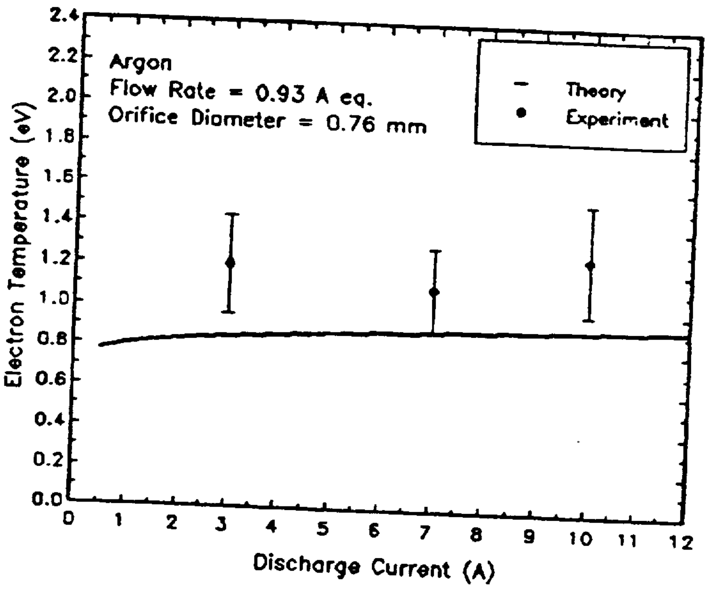

Figure 9: Effect of discharge current on electron temperature (comparison between theory and spectroscopy, argon, $\dot{m} = 0.93\,A\,eq.$, $d_o = 0.76\,mm$).

EXPERIMENTAL INVESTIGATION OF A HOLLOW CATHODE DISCHARGE[•]

A. Salhi[*], R. M. Myers[†] and P. J. Turchi[‡]
The Ohio State University
Columbus, Ohio 43210

Abstract

An experimental investigation of an orificed, hollow cathode was undertaken to obtain more detailed information than that previously available, in order to compare with recent theoretical modeling. Three diagnostic techniques were applied: single Langmuir probes, spectroscopy and pyrometry. The measurements were aimed primarily at the determination of plasma properties, such as electron temperature, electron number density and plasma potential within the hollow cathode. In this experimental study, both argon and xenon were used in an attempt to establish the effect of propellant on the hollow cathode characteristics. Furthermore, orifice diameters of 0.76 mm, 1.21 mm, and 1.27 mm were

---

[•] Presented at the International Electric Propulsion Conference, Seattle, Washington, September 1993. Paper No. 93-025.

[*] Research Associate, Department of Aeronautical & Astronautical Engineering, Member AIAA.

[†] Propulsion Engineer, Sverdrup Technology, Inc., NASA-Lewis Research Center Group, Member AIAA.

[‡] Professor, Department of Aeronautical & Astronautical Engineering, Senior Research Scientist, USAF Phillips Laboratory, Member AIAA.

used to determine the effect of geometry on cathode discharge. Langmuir probe diagnosis was performed along the cathode center line. These measurements allowed determination of the axial distributions of plasma conditions. In addition to plasma properties, it was essential to measure the cathode external and internal surface temperatures to identify the different emission mechanisms and emission current density profile. It was found that the hollow cathode discharge was governed primarily by the discharge current. Both the surface electron emission region and the length of the internal plasma column scaled with the cathode inner diameter. Furthermore, the gas temperature was deduced to be higher than the wall temperature.

Nomenclature

e	electron charge, 1.602×10^{-19} $Coul$
k	Boltzman's constant, 1.381×10^{-23} J/K
m_e	electron mass, 9.1×10^{-31} kg
m_i	ion mass, kg
T_e	electron temperature, K
V_f	floating potential, V
V_p	plasma potential, V

I Introduction

The combination of low temperature and adequate lifetime exhibited by low work function hollow cathodes has led to their use in numerous plasma applications. The hollow cathode has been widely used in ion thruster technology since 1962[1]. After the development and use of the hollow cathode in the SERT II as a neutralizer by Rawlin and Pawlik[2] and as the main cathode of the SERT II thruster by Kerslake et al.[3], all ion thrusters have adopted hollow cathodes. In addition to ion engines, hollow cathode technology has been applied successfully to a steady-state 100 KW class MPD thruster[4]. Moreover, these devices were used as high current density ion sources to heat plasmas in controlled thermonuclear reaction experiments[5]. In this case, hollow cathodes offered, through adequate selection of the operating conditions, independent optimization and control of the discharge parameters. Hollow cathodes were also utilized as a spectroscopic source to study gas spectra and to determine transition probabilities.[6,7] Recently, the hollow cathode has found other applications such as plasma contactors[8] where this device provides a spacecraft with the ability to emit or collect charged particles from a surrounding plasma environment.

Because of their wide range of application, it becomes essential to understand fully the physical processes governing hollow cathode discharges. This knowledge would allow the successful design of the hollow cathode and optimization of its operation. In spite of numerous experimental investigations[9-13] and theoretical work[14–19] conducted in this area, the hollow cathode still imposes several challenges (e.g., the proper selection of the operating conditions to meet mission requirements). It is the intent of this paper to address these questions through the identification of the primary mechanisms of hollow cathode arc discharges.

II Experimental Apparatus

An experimental program was carried out at the NASA-Lewis Research Center's Electric Propulsion Laboratory (EPL). All tests were run in Bell Jar 6 (BJ6), a 0.53 m diameter, 0.36 m long stainless steel vacuum chamber (figure 1). BJ6 was evacuated using a turbomolecular pump, in conjunction with a roughing pump, which was capable of pumping 260 liters/sec of air at a range of 1 to 10^{-6} Pa ($7.5\text{x}10^{-3}$ to $7.5\text{x}10^{-9}$ Torr). The gas feed system consisted of two independent gas injection ports, one feeding gas into the hollow cathode with the other feeding gas into BJ6. In this fashion the pressure in the chamber could be varied independently of the cathode flow rate. The gas system consisted of a number of precision leak valves that allowed fluctuations in flow rate to be eliminated. A Hastings linear mass flowmeter was used to establish the desired flow rates. The gas feed system was also equipped with a capacitance manometer, rated for 100 Torr maximum pressure, that allowed measurement of the pressure upstream of the hollow cathode. Ultra high purity grade (99.999 %) gases such as argon, xenon were used as propellant in this facility. They were delivered from high pressure (250 psig) bottles.

A power supply capable of delivering 600 volts was used with a current regulator. This setup allowed operation at currents ranging from 1 to 30 A and voltages between 10 and 60 V depending on the anode size, flow rate and distance between the electrodes. The facility was also equipped with 1 kV ignitor required for arc ignition.

The hollow cathode assembly (figure 2) consisted of an insert, cathode body. an orifice plate, a heater and a radiator shield. The insert was 3.81 mm inner diameter, 5.33 mm outer diameter and 25.4 mm long tube. It was made of low work function material (1.8-2.0 eV): tungsten impregnated with barium compounds ($4BaO\text{-}CaO\text{-}Al_2O_3$). The low work function allowed the operation of the cathode at low temperatures (1000 C). The insert was housed in a molybdenum-rhenium cathode body: 5.59 mm inner diameter. 6.35 mm outer diameter and 63.5 mm long tube. A 2% thoriated tungsten orifice plate was electron-beam welded at one end of the cathode body. It had 5.84 mm outer diameter, 1.24 mm thickness and came in different orifice sizes. The orifice sizes used in this research were 0.76, 1.21 and 1.27 mm diameters. The orifice outlet was designed with a 45-degree chamfer. An 8-turn coiled heater is used to heat the cathode during activation and ignition procedures. The heater consisted of a coaxial tantalum wire and tube insulated by magnesium oxide tubing. The heater was shielded by a 0.013 mm thick, 30.5 mm wide and 457 mm long tantalum foil wrapped around it. To complete the electric circuit a 152 x 102 mm tantalum plate was used as anode.

Two different plasma diagnostic techniques were used in the experimental investigation of the hollow cathode discharge: single Langmuir probes and visible light emission spectroscopy. The probes used were single Langmuir probes in which a thin tungsten wire 0.127-0.254 mm in diameter and 1-2 mm long was supported by a 99.8% alumina tube (maximum operating temperature 1950 C). The probe current-voltage characteristics were displayed and recorded on a digital oscilloscope (Nicolet 310).

The experimental spectroscopic setup consisted of a 500M Czerny-Turner and an optical spectrometric multichannel analyzer (OSMA) used for fast spectral data acquisition. The OSMA, a computer - controlled multichannel image detector. had the capability of detecting. measuring and manipulating spectra at high acquisition rates. The OSMA consisted of a computer console, a detector controller (ST-120) and an IRY detector head. The detector head consisted of an optoelectronic image device with the necessary electronics for its optimized manipulation. It was a self-scanning photodiode arrays with 1024 pixels arranged linearly on a 25.4 mm long single line. The detector was characterized by its wide spectral range, high dynamic range. geometric accuracy, thermal and temporal stability and the lack of readout lag problems. The detector received power, thermostated and timed signals from an ST-120 detector controller. The

ST-120 coordinated data collection with the experiment, digitized and averaged data, set exposure time. stored and transmitted data to the computer and provided a real-time display of the free running detector readout. The spectrometer received light through a single mode optical fiber. This fiber had a core diameter of 200 μm, a cladding diameter of 250 μm. a jacket diameter of 1000 μm, a numerical aperture of 0.2 and an aperture half angle of 11.5 degrees. To improve fiber to spectrometer coupling an achromatic lens was positioned between the fiber and the entrance slit. In this fashion. the fiber beam was adjusted to the focal ratio of the spectrometer. The alignment of the optical fiber with the spectrometer entrance slit was achieved by a 0.5 mW compact He-Ne laser.

The internal surface temperature of the hollow cathode was determined using pyrometry by coupling a quartz rod to a two-color photodiode. The two-color photodiode is a silicon/germanium "sandwich" detector. The high performance silicon detector mounted over the germanium detector responds to radiation from 400 nm to 1000 nm while the germanium responds to longer wave length 1000 nm to 1800 nm that pass through the silicon photodiode. This kind of detector is suitable for two-color temperature measurements from 500 C to 2000 C. A clear fused quartz rod was used to transmit radiation from cathode surface to the detector. The quartz rod was designed to withstand maximum working temperature of 950 C and 1200 C in a continuous and short-term operations respectively. It had a constant index of refraction for a wide wavelength band and exhibited a fairly constant transmission efficiency more than 90% in the range of wavelengths between 200 nm and 2000 nm. The 1 mm diameter quartz rod used, was supported by a 99.8% alumina tube. To reduce the sight of light of the plasma radiation, the quartz rod was cleaved at 45 degrees, coated by a tantalum film few microns thick and covered by a layer of ceramic adhesive. A small window was left uncoated so that the incoming radiation through the window could be reflected by the 45-degree surface and transmitted through the fiber to the detector. The pyrometric probe had to be manually moved rapidly in order to minimize the exposure time so that the optical properties of the material would not degrade. In this case. the high sampling rate required was achieved by automating the reading of both probe position and radiation intensity signals. This task was accomplished by the use of a multiple-channel A/D card. The use of a computer allowed fast data reading, processing and storing.

The cathode external surface temperature was measured using type R thermocouples (maximum working temperature 1600 C). In an attempt to determine the axial temperature distribution on the cathode surface five thermocouples were embedded between the heater turns through small holes (1 mm in diameter) in the radiation shield. Ceramic (99.8% alumina) tubes were used as insulation for its high working temperature. The presence of the heater coil and the radiation shield surrounding the cathode tube minimizes the thermal losses from the cathode surface. Thus, the uncertainty in temperature measurements due to thermocouple-surface contact, was reduced considerably.

III Discussion of the results

Plasma properties

In the case of the single Langmuir probe, a sawtooth voltage pulse at frequencies of 1,000 to 10,000 Hz was applied to the probe which allowed the entire probe characteristic to be obtained in tenths of a millisecond. In all measurements more than five probe traces were recorded, analyzed and averaged. Due to the high probability of contamination, special care was taken in cleaning the probe before each measurement by drawing saturation current to heat the probe tip until probe emission is observed. In addition, the probe was kept under a negative bias (-50 V) for one to five minutes between pulses.

Electron temperature

Electron temperature was measured using both diagnostic techniques for both argon and xenon. Under operating discharge currents ranging from 1 to 20 A, electron temperatures from 0.6 to 2.2 eV for argon and 0.6 to 1.4 eV for xenon were measured along the cathode center line using single Langmuir probes. In all measurements, the probe traces exhibited behavior consistent with Maxwellian distributions of the plasma electron speeds. Figure 3 indicates that the electron temperature slightly decreases linearly as the discharge current is increased. This behavior is found at all distances from the cathode orifice. On the other hand, the gas flow rate has very little effect on the electron temperature (figure 4). Figure 5 shows a substantial variation in electron temperature along the cathode center line. Figure 6 illustrates the increase of electron temperature with the orifice diameter. The effect of propellant is illustrated in figure 7. The lower electron temperature obtained in the case of xenon is consistent with the lower ionization potential of xenon compared to argon.

In attempt to shed some light on the state of the plasma within the hollow cathode, spectroscopy was employed under a wide range of operating conditions. The particular question was whether or not the plasma was in local thermodynamic equilibrium (LTE) and the consequent physical sense of the temperature determined using relative intensity measurements. Using argon II spectral lines in the range 400-500 nm with excitation energies from 19 to 23 eV, and xenon II in the spectral range 400-700 nm with excitation energies from 14 to 18.5 eV, Boltzmann plots were constructed (figure 8 and 9). In most cases, deviations from a straight line were less than 15%. Using relative-intensity measurements, temperatures from 0.91 to 1.3 eV for argon and 0.98 to 1.09 eV for xenon were calculated for discharge currents varying from 1 to 20 A. The results obtained showed a weak dependence of the "electron temperature" on the operating conditions, and agreement with the average electron temperature obtained using Langmuir probe.

Electron number density

The electron number density was determined using cylindrical Langmuir probes. Due to the small size of the cathode insert. a few millimeters in diameter, all measurements were performed along the cathode center line, with the probe inserted from the back of the cathode. The probe diagnosis was conducted using argon and xenon under a wide range of discharge currents, mass flow rates and orifice sizes. In the regions where the plasma density reached 10^{14} cm^{-3} or higher, it became difficult to obtain the electron saturation current without severely perturbing the discharge. These perturbations were usually reflected in a rapid increase of the cathode surface temperature and fluctuations in discharge current and voltage. In this case, the probe bias was offset to avoid reaching the electron saturation current and consequently, the calculation of the plasma density was performed using the ion saturation current by applying Lafromboise's theoretical results[20]. It is important to point out that the difference between electron number densities obtained based on Lafromboise's results and the thermal electron saturation current (for densities less than 10^{14} cm^{-3}) varied from 1% to a maximum value of 20%.

In general, plasma densities of $10^{11} - 10^{15}$ cm^{-3} were calculated under the range of operating conditions applied in these experiments. The electron number density reached a maximum value in the vicinity of the orifice and decreased as we moved away from the orifice to values of the order of 10^{12} cm^{-3} at approximately two insert diameters. Farther away. the plasma density dropped drastically to values difficult to measure by the probe setup. The data (figure 10) indicated the existence of three different zones within the cathode. It is believed that the active zone where the ionization takes place started at about one insert diameter from the orifice, the second zone, a diffusion sheath[11], extended also to about one insert diameter and the last zone described the neutral gas. The xenon plasma region within the cathode was larger than that of argon (figure 11). This difference is consistent with the fact that xenon has a lower ionization potential than argon. It was found that larger orifice diameter induced higher electron density (figure 12). This effect appears to be related to the higher electron temperature measured in the case of the larger orifice size. On the other hand, this difference may be very small in reality due to the errors associated with measurements and probe theory. While the electron density was strongly dependent on the discharge current (figure 13), it appeared weakly affected by the flow rate (figure 14). It is important to point out that the maximum values of the electron densities measured are similar to the one calculated using the law of mass action for typical operating parameters of the cathode.

Plasma potential

Under the conditions presented here, the hollow cathode operated at total discharge voltages from 10 V to 40 V. The maximum plasma potentials measured within the hollow cathode did not exceed 35 V. In general, lower discharge voltages were obtained with the cathode operating with xenon. Also, an increase of orifice size caused lower discharge voltages.

In the vicinity of the orifice where a full probe trace was not obtained for the reason mentioned in the previous section, the plasma potential was estimated from the following equation[21]:

$$V_p = V_f - \frac{kT_e}{2e} ln \left(\frac{\pi}{2} \frac{m_e}{m_i} \right) \tag{1}$$

In all cases, the plasma potential for both argon and xenon decreased with the discharge current (figures 15 and 16). This behavior was related in part to to the increase in the electron number density and the decrease in the internal plasma column length. The plasma potential decreased rapidly as we moved away from the cathode orifice (figure 17). The plasma potential for argon was higher, in most case, than that of xenon but the difference in voltage decreased with the increase in discharge current (figure 18). In addition, this comparison showed clearly that the length of xenon internal plasma column was much longer than that of argon. Even though the cathode with 1.21 mm orifice diameter operated at lower discharge voltages, the estimated plasma potential was higher than that of the cathode with 0.76 mm orifice size (figure 19). This high potential was attributed mainly to the length of the conduction path of the internal plasma column.

Cathode internal pressure

The cathode internal pressure was measured upstream of the cathode using a highly accurate (0.1% accuracy) capacitance manometer rated for 100 Torr. Cathode internal pressures from 5 to 30 Torr were measured depending on flow rate, discharge current and orifice size. In an attempt to determine the dependence of the cathode internal pressure on the operating conditions, the pressure was plotted against the discharge current and flow rate in figures 20 and 21, respectively. The results showed that the pressure increased linearly with the discharge current for a fixed gas flow rate. Furthermore, it was interesting to notice that the ratio of the slopes of those straight lines was equal to the ratio of the gas flow rates. That is. the pressure is proportional to the mass flow rate which is consistent with the theoretical formulation of the mass flow rate of a choked flow. The effect of the propellant on the pressure is illustrated in figure 22. By comparing xenon and argon, the pressure ratio was found to be equal to the square root of the ratio of the atomic weights, which is also an indication of the validity of choked flow at the orifice. Finally, to establish the effect of the orifice size, the pressure was plotted against the discharge current for two different orifice sizes (figure 23). It was found that the pressure variation with discharge current was substantially magnified as the orifice diameter was decreased.

Wall temperature

In an attempt to understand fully the hollow cathode operation, it is important to investigate the cathode wall temperature and its dependence on the operating conditions. Also. the knowledge of the surface temperature is vital to identify the important mechanisms of electron emission from the cathode surface. These different aspects of the cathode surface emission are related to the lifetime of the cathode which represent a central question for the suitability of hollow cathodes for space applications.

In this study, there has been a special interest in determining the temperature of both external and internal surfaces of the hollow cathode. In order to obtain the temperature profile on the external surface of the cathode, type R thermocouples were attached to the surface at several positions through the radiator shield and the heater of the hollow cathode. This setup allowed construction of figure 24 which describes the temperature distribution under various operating conditions. It was evident that the wall temperature reached a maximum in the vicinity of the orifice plate and then decreased rapidly as we moved further upstream. In general, there was a difference of 300 to 400 C in temperature along the cathode surface. The cathode temperature depended strongly on the discharge current (figure 25) while it appeared insensitive to the gas flow rate (figure 26). However, at very low mass flow rate, the cathode temperature increased substantially. This effect is related directly to the increase of the discharge voltage and subsequently the occurrence of fluctuation patterns of the discharge luminosity and voltage. The effects of propellant and orifice size on the cathode temperature were apparently not significant (figures 27 and 28).

The insert temperature was determined using the pyrometry technique described in Section II. The knowledge of the insert temperature is extremely important in establishing the surface plasma-wall interaction, surface cooling capability by electron emission, surface work function and the upstream limit of the active zone. The insert temperature profile was compared to the external surface temperature (figure 29). It was found that both profiles were similar and the temperature difference was small (less than 5%) . This observation is consistent with the fact that the cathode wall was very thin and that the cathode was shielded on the outside. In this fashion, the radial heat loss through the wall was extremely low. Therefore, the outer temperature, which was easy to measure, could be used to predict the insert temperature and its axial distribution.

The analysis of the thermionic current density allowed identification of the part of the surface that contributed mostly in the emission and comparison with previous predictions of scale size of the internal plasma column. It was found that the current density fell drastically beyond one insert diameter from the orifice. The scale size of the emission surface was comparable to the scale size of the plasma internal column described earlier. Furthermore, the work function of the impregnated tungsten insert is known to be in the range of 1.8-2.0 eV[22].

The deduced effective work function based on thermionic emission (Richardson equation) and the measured cathode wall temperature fell in this range.

IV Conclusions

The experimental work conducted on orificed, hollow cathode arc discharges has shown that the cathode operation, for a given geometry, is defined primarily by the discharge current. Beyond some minimum values, the mass flow rate has little effect on the cathode operation. On the other hand the propellant has direct impact on the discharge and ignition voltages. For cylindrical cathodes, the inner diameter is an important parameter that represents the scaling length for the surface emission and the internal plasma column. Because, the hollow cathode operates under thermionic emission, larger diameters would allow lower emission current densities and therefore, lower wall temperatures. The latter would substantially increase the cathode lifetime.

Acknowledgments

This work was supported by NASA-Lewis Research Center. The authors would like to thank David C. Byers, James S. Sovey, Maris A. Mantenieks, Vincent K. Rawlin, Michael J. Patterson, Timothy R. Verhey, and George C. Soulas, NASA-Lewis Research Center, for their assistance, support and invaluable suggestions. The technical assistance of Fred Jent and his team is sincerely appreciated.

References

1. R. C. Speiser and L. K. Branson. *American Rocket Society*, Paper No. 2664-62, 1962.

2. V. K. Rawlin and E. V. Pawlik. *AIAA Paper No. 67-670*, 1967.

3. W. R. Kerslake, D. C. Byers and J. F. Staggs. *AIAA Paper No. 67-700*. 1967.

4. M. A. Mantenieks. Preliminary test results of a hollow cathode MPD thruster. *IEPC Paper 91-076*, October 1991.

5. J. S. Sovey and M. J. Mirtich. A hollow cathode hydrogen ion source. NASA TM-73783, 1977.

6. K. Danzmann and M. Kock. Improved Ar(II) transition probabilities. *J. Quant. Spectrosc. Radiat. Transfer*, 29(6):517-520, 1983.

7. B. van der Sijde. Configuration temperature in a hollow argon arc and transition probabilities of the ArgonII spectrum. *J. Quant. Spectrosc. Radiat. Transfer*, 12:703, 1971.

8. J. D. Williams. An experimental investigation of hollow cathode-based plasma contactors. *NASA CR-187120*, May 1991.

9. G.V. Babbkin, V. G. Mikhalev, E. P. Morozov, and A. V. Potatov. Experimental investigation of the plasma in multichannel cathode. *Journal of Ap plied Mechanics and Technical Physics*, 17:767-770, November-December 1976.

10. D. B. Fradkin and A. W. Blackstock et al. Experiments using 25-KW hollow cathode lithium vapor MPD arcjet. *AIAA Journal*, 8(5):886-894, 1970.

11. L. M. Lidsky, S. D. Rothleder, D. J. Rose, and S. Yoshikawa. Highly

ionized hollow cathode discharge. *Journal of Applied Physics*, 33(8):2490- 2497, August 1962.

12. D.E. Siegfried. Xenon and Argon hollow cathode research. *NASA CR-168340*, page 76, January 1984.

13. D.E. Siegfried and P. J. Wilbur. A model for mercury orificed, hollow cathodes: Theory and experiment. *AIAA Journal*. 22(10), October 1984.

14. J. L. Delcroix, H. Minoo, and A. R. Trindade. Establishment of a general rule for a hollow cathode arc discharge. *Journal de Physique*, 29(6):605-610, July 1968.

15. J. L. Delcroix, H. Minoo and A. R. Trindade. Gas-fed multichannel hollow cathode arcs. *Rev. Sci Instrum.*, 40(12):1555-1562. 1969.

16. A. Lorente-Arcas. A model of the discharge in the hollow cathode. *Plasma Physics*, 14(6):651-659, 1972.

17. A. Salhi and P. J. Turchi. A first-principles model for orificed, hollow cathode operation. *AIAA Paper No. 92-3742*. July 1992.

18. A. Salhi and P. J. Turchi. Theoretical modeling of orificed, hollow cathode discharges. *IEPC Paper No. 93-024*, September 1993.

19. D.E. Siegfried and P. J. Wilbur. Phenomenological model describing orificed, hollow cathode operation. *AIAA Journal*, 21(1):5, January 1983.

20. P. M. Chung, L. Talbot and K. T. Touryan. Electric probes in stationary and flowing plasmas. *AIAA Journal*, 12(2):133-144, February 1974.

21. F. F. Chen. Electric Probes, in R. H. Huddlestone and S. L. Leonard. Plasma diagnostic techniques. *Academic Press Inc.*, *New York*, Chapter 4, pp.

178,1965.

22. R. Forman. Surface studies of thermionic cathodes and the mechanism of operation of an impregnated tungsten cathode. *NASA TN D-8295*, September 1976.

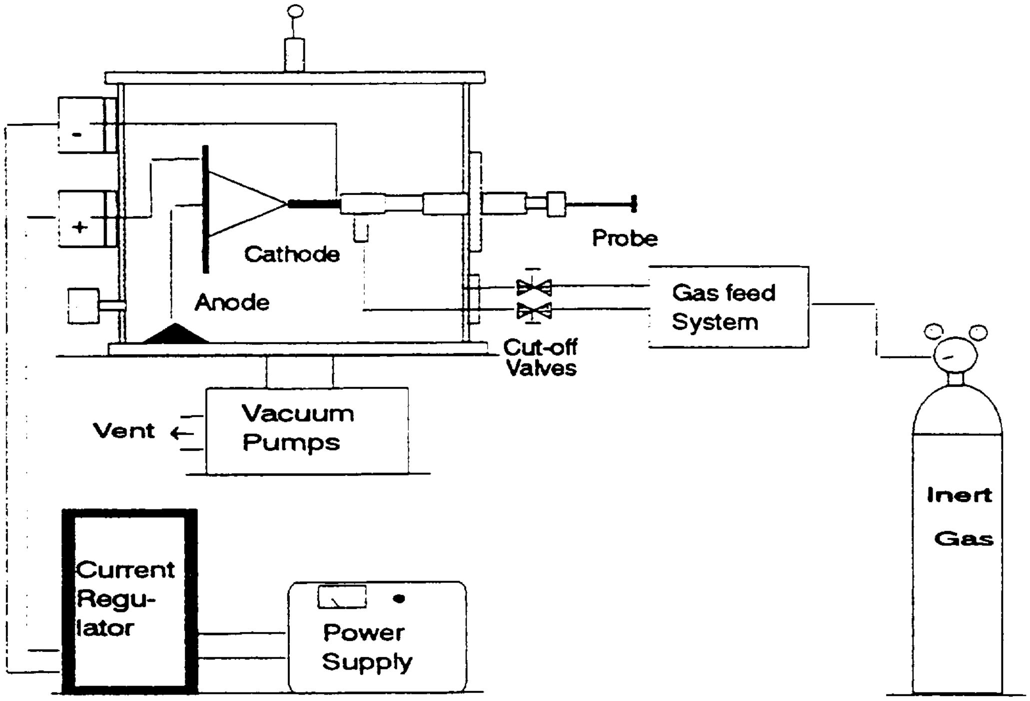

Figure 1: Schematic of hollow cathode test facility

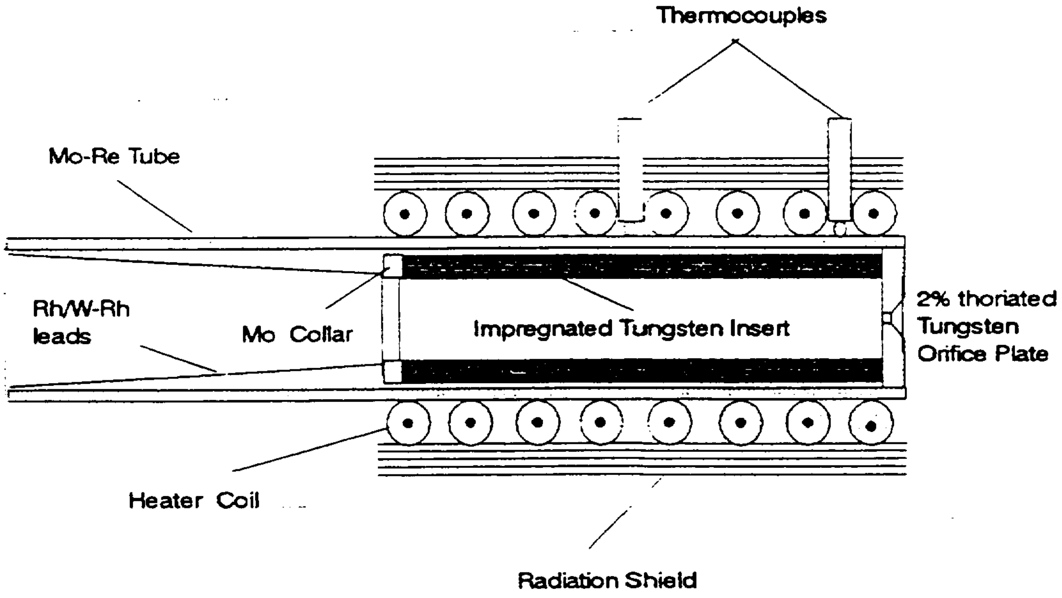

Figure 2: Schematic of the hollow cathode assembly

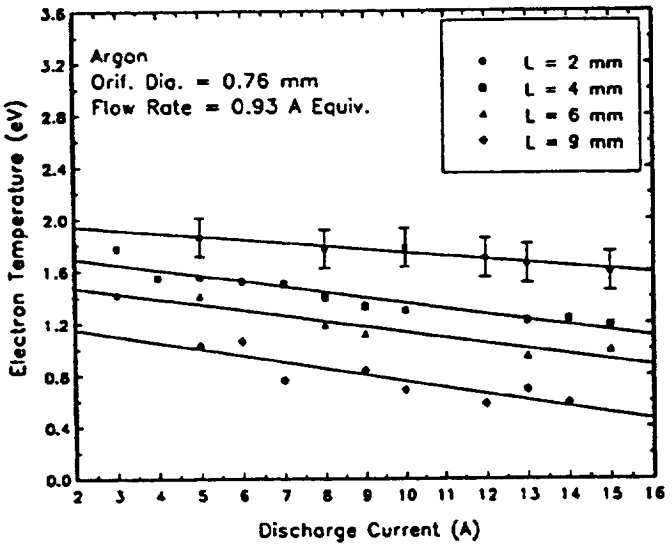

Figure 3: The effect of discharge current on electron temperature along the cathode center line at different distances from the orifice .

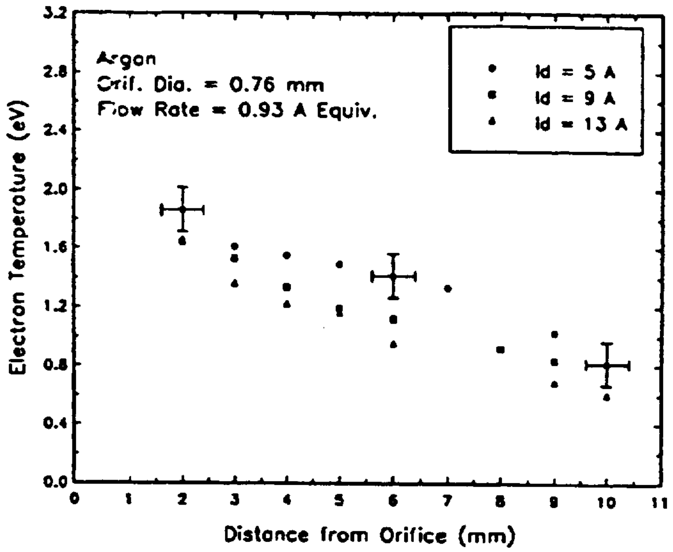

Figure 5: Axial distribution of electron temperature along the cathode center line at different discharge currents.

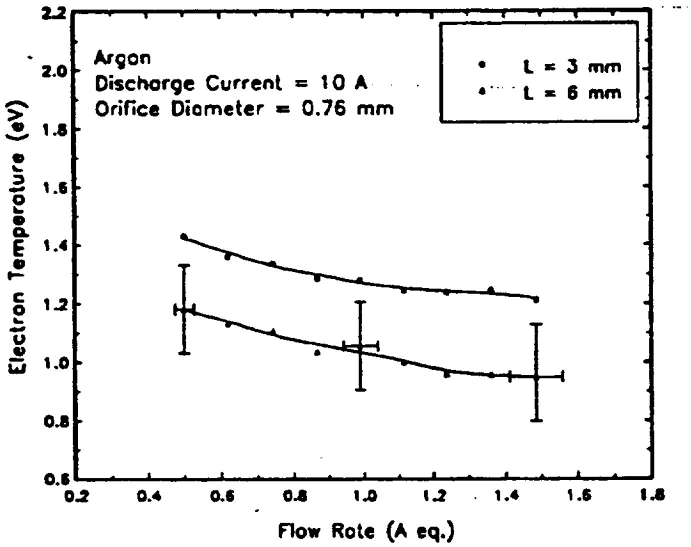

Figure 4: The effect of flow rate on electron temperature along the cathode center line at different distances from the orifice.

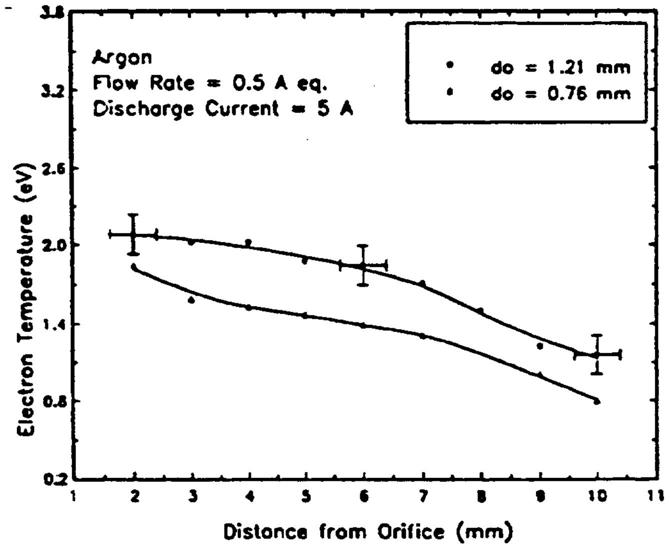

Figure 6: Axial distribution of electron temperature along the cathode center line for different orifice sizes.

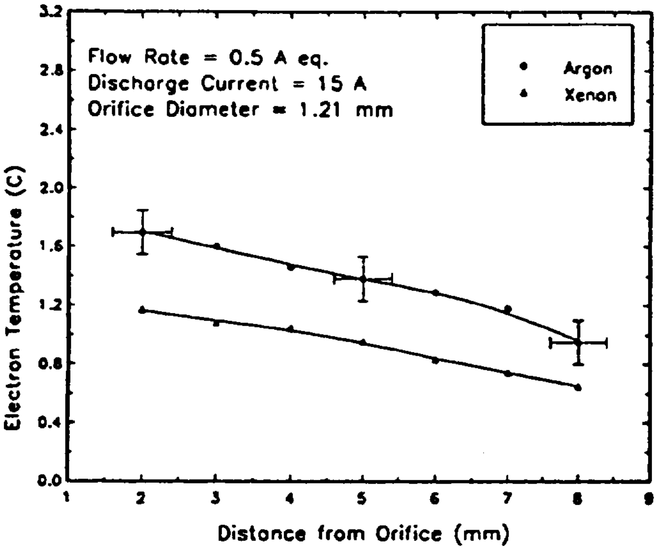

Figure 7: Axial distribution of electron temperature along the cathode center line in argon and xenon discharges.

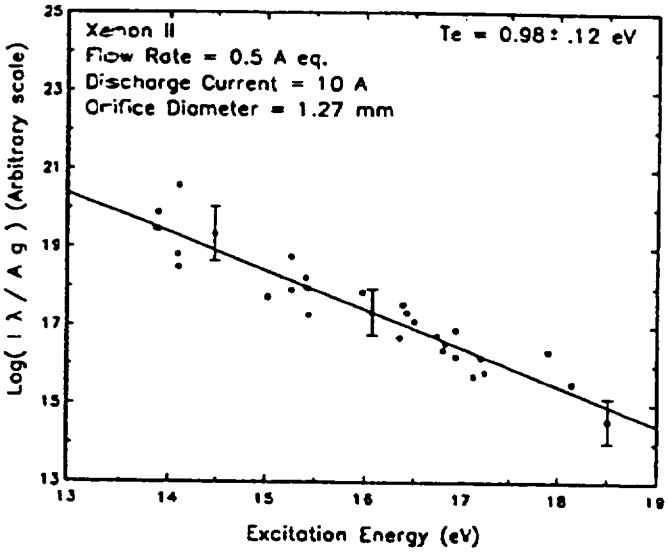

Figure 9: Calculation of the electron temperature using relative line intensity ratio.

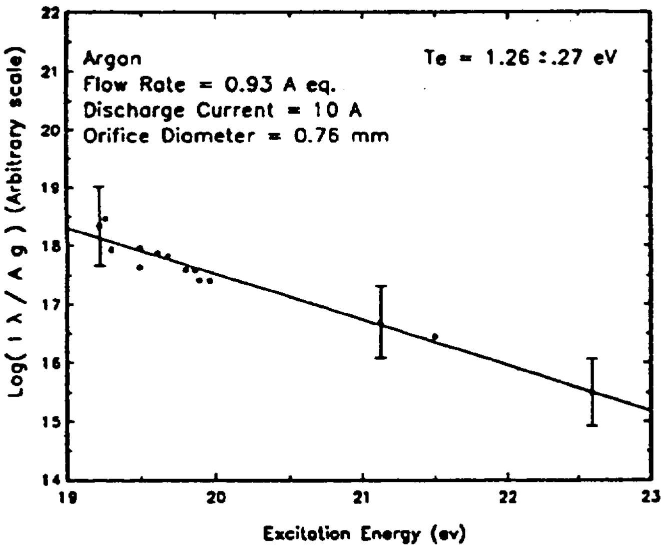

Figure 8: Calculation of the electron temperature using relative line intensity ratio.

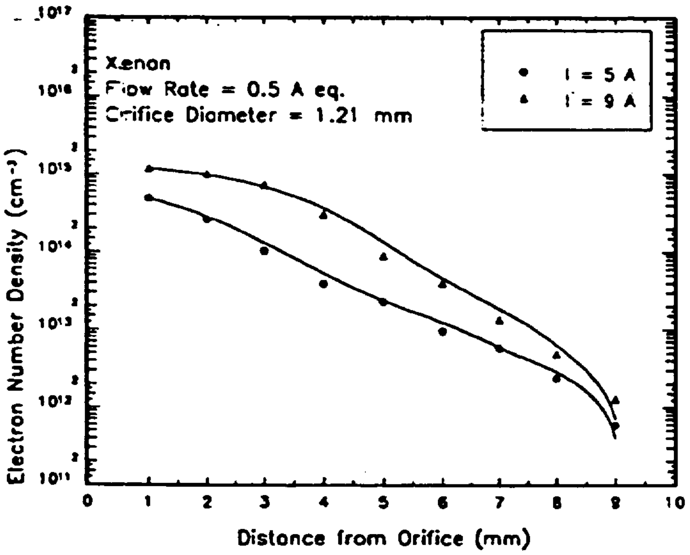

Figure 10: Axial distribution of electron number density along the cathode center line at different discharge currents.

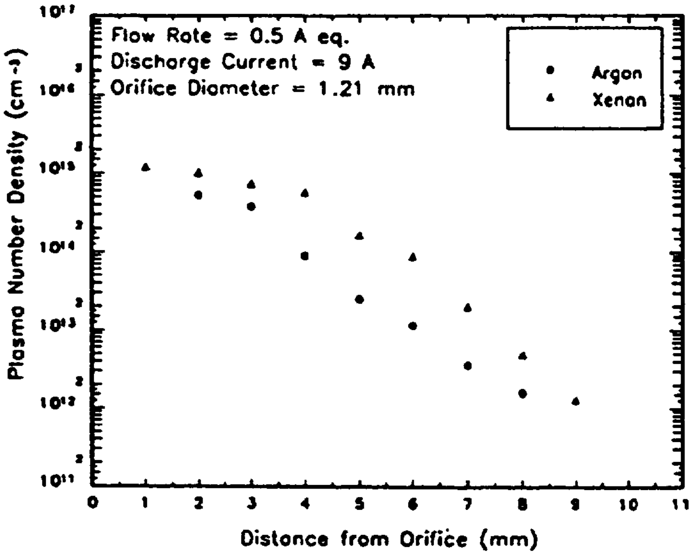

Figure 11: Axial distribution of electron number density along the cathode center line in argon and xenon discharges.

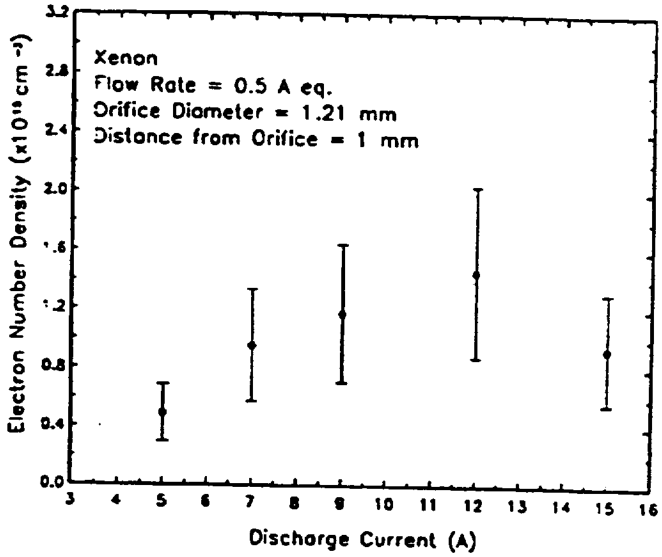

Figure 13: Effect of discharge current on electron number density along the cathode center line.

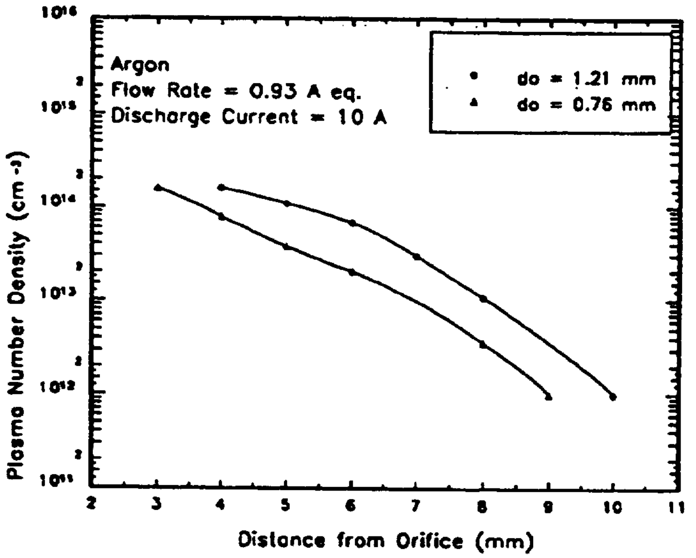

Figure 12: Axial distribution of electron number density along the cathode center line for different orifice sizes.

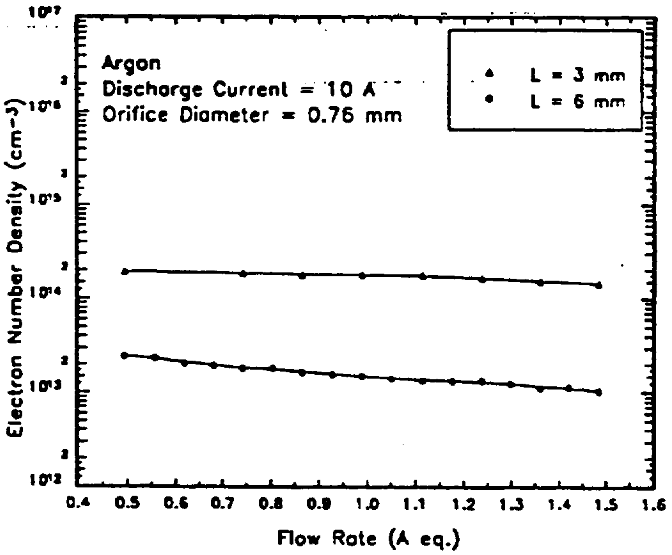

Figure 14: Effect of flow rate on electron number density along the cathode center line at different distances from orifice.

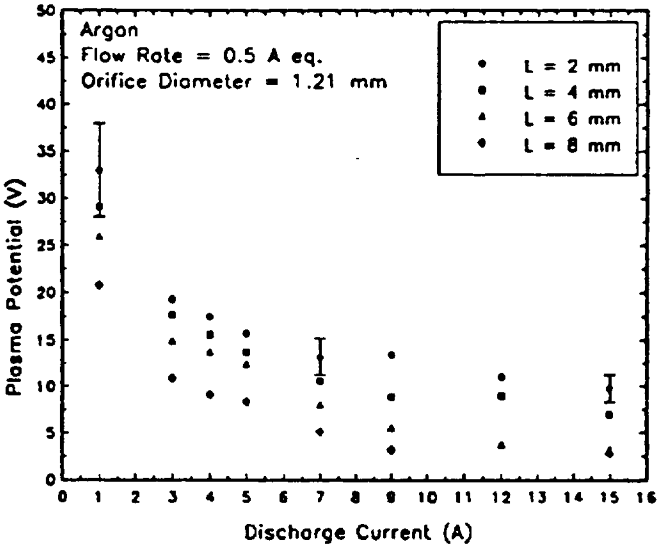

Figure 15: Effect of discharge current on plasma potential along the cathode center line at different distances from orifice.

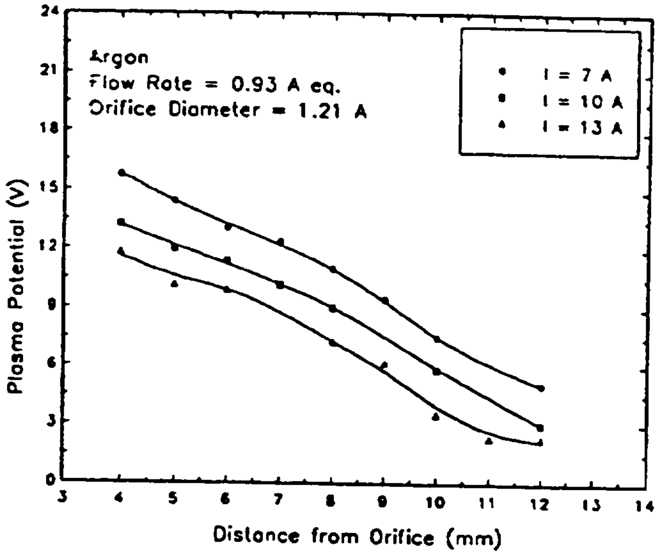

Figure 17: Axial distribution of plasma potential along the cathode center line at different discharge currents.

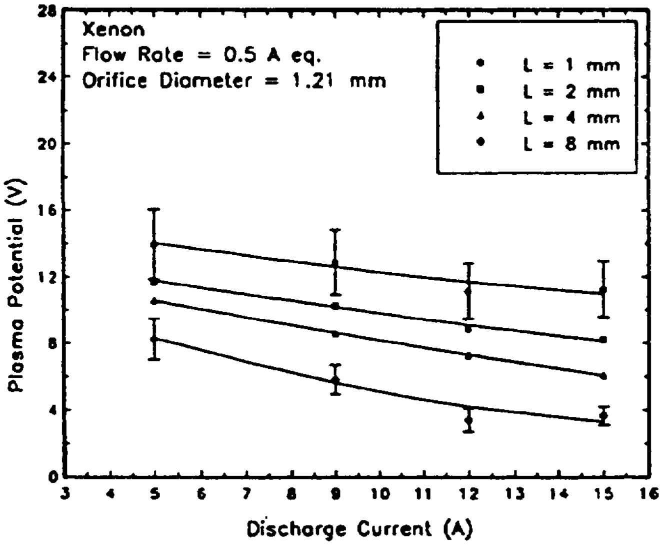

Figure 16: Effect of discharge current on plasma potential along the cathode center line at different distances from orifice.

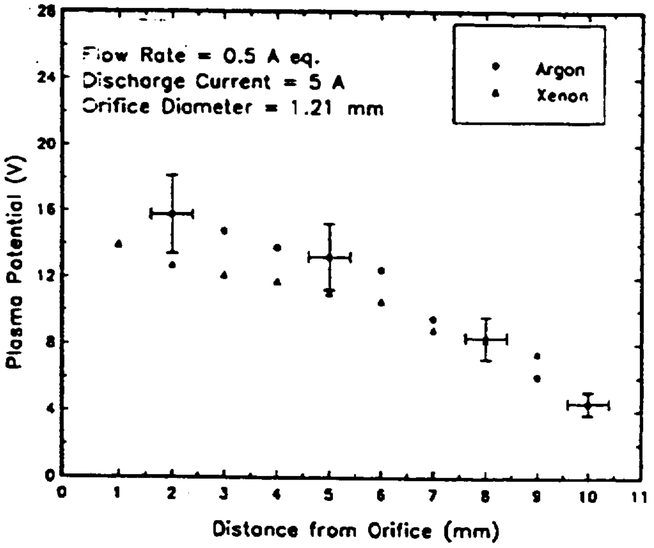

Figure 18: Axial distribution of plasma potential along the cathode center line in argon and xenon discharges.

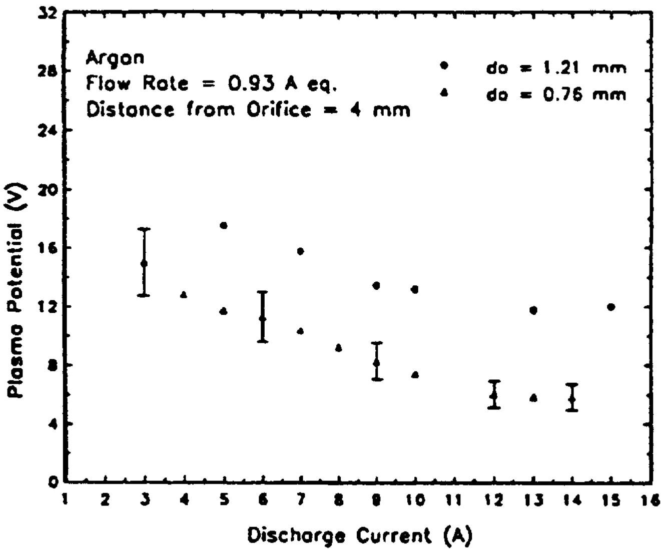

Figure 19: Effect of discharge current on plasma potential along the cathode center line for different orifice sizes.

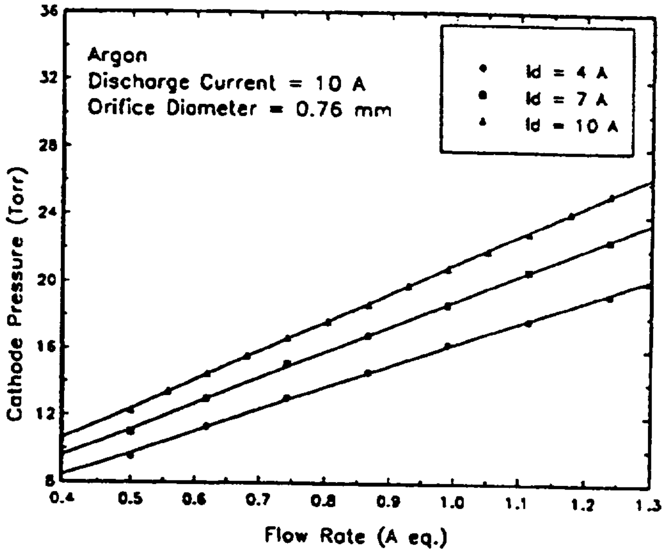

Figure 21: Effect of flow rate on cathode internal pressure along the cathode center line at different discharge currents.

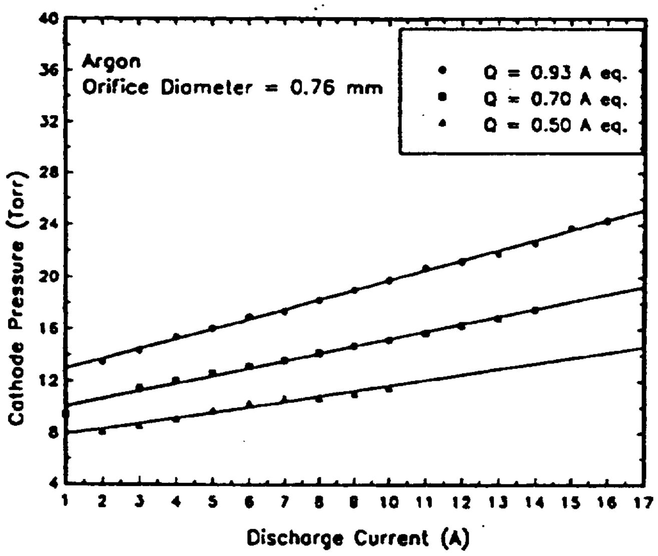

Figure 20: Effect of discharge current on cathode internal pressure along the cathode center line at different flow rates.

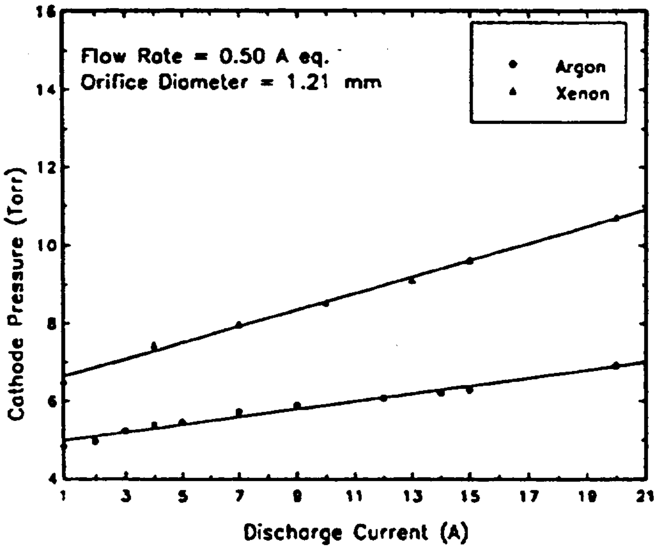

Figure 22: Effect of discharge current on cathode internal pressure along the cathode center line in argon and xenon discharges.

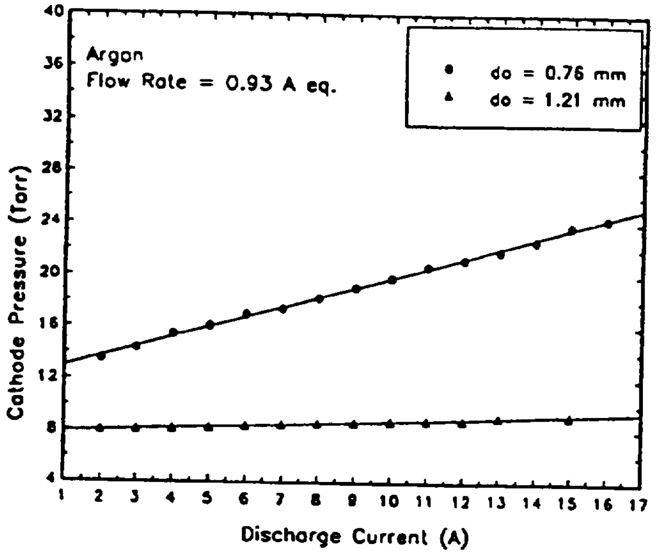

Figure 23: Effect of discharge current on cathode internal pressure along the cathode center line for different orifice sizes.

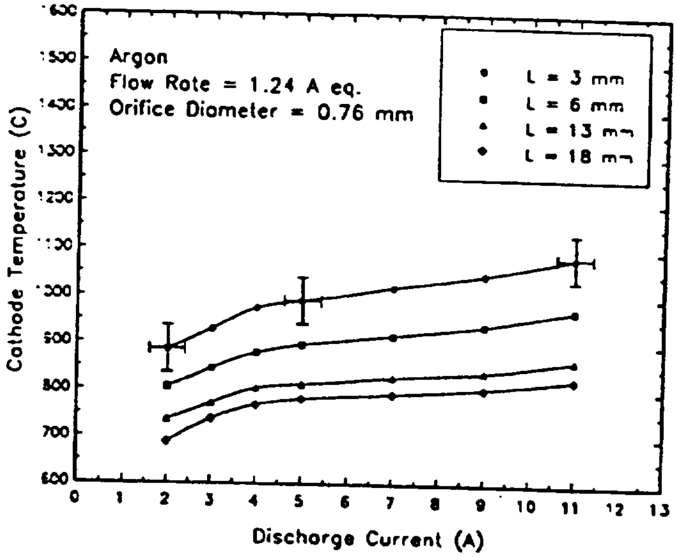

Figure 25: Effect of discharge current on cathode external surface temperature at different distances from the orifice.

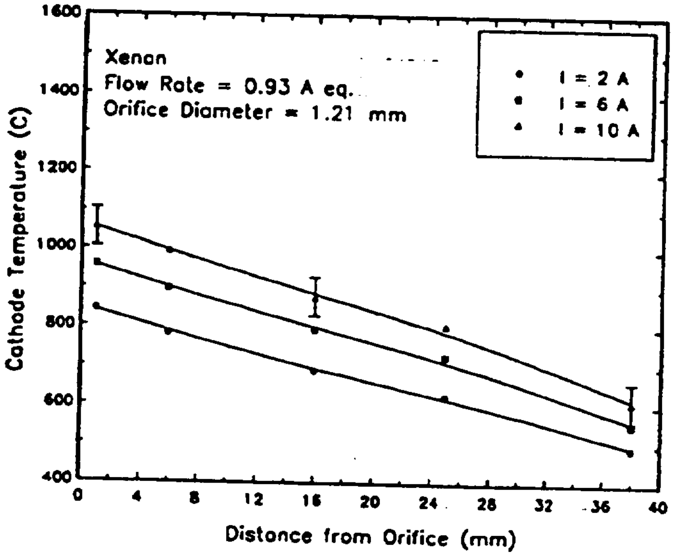

Figure 24: Axial distribution of cathode external surface temperature at different discharge currents.

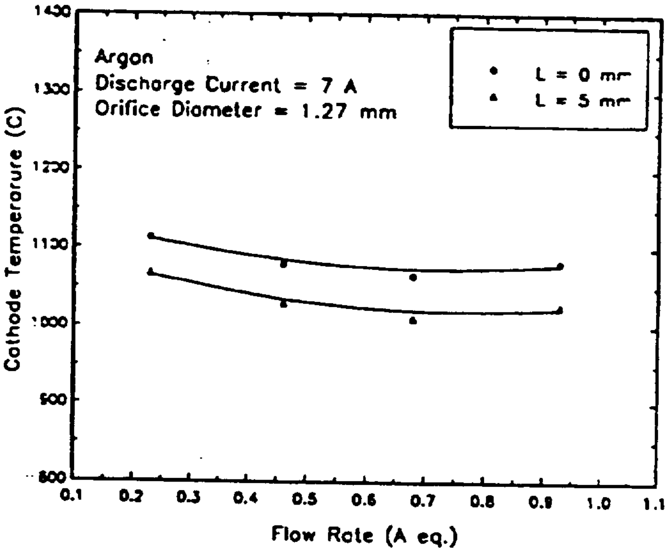

Figure 26: Effect of flow rate on cathode external surface temperature at different distances from the orifice.

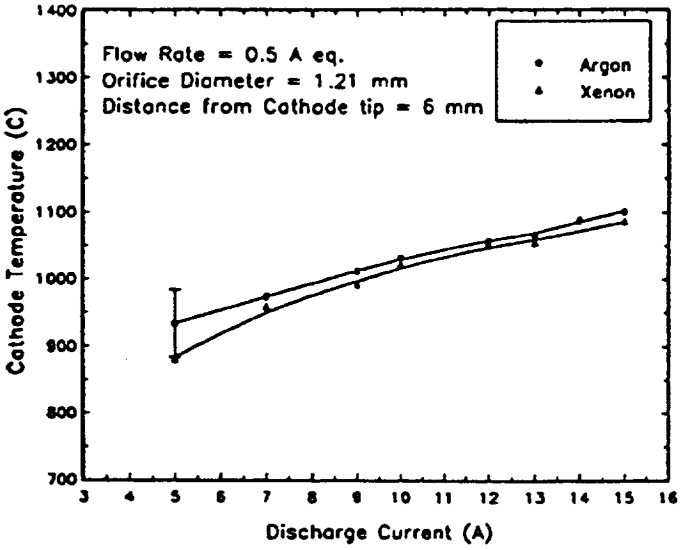

Figure 27: Effect of discharge current on cathode external surface temperature in argon and xenon discharges.

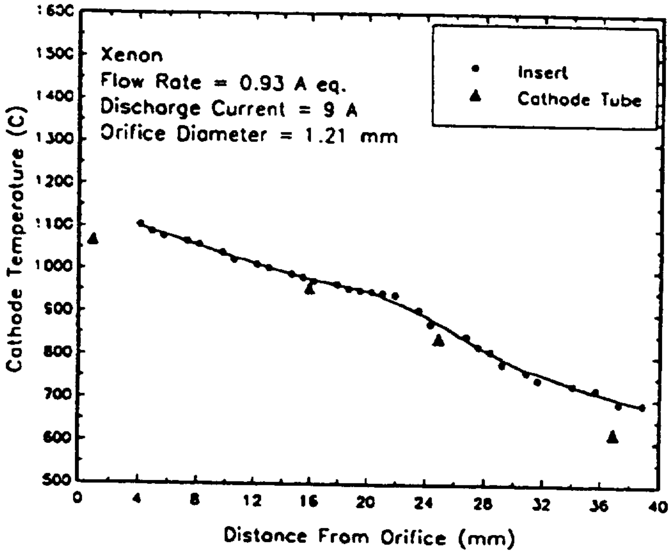

Figure 29: Comparison of axial distributions of internal and external cathode surface temperatures.

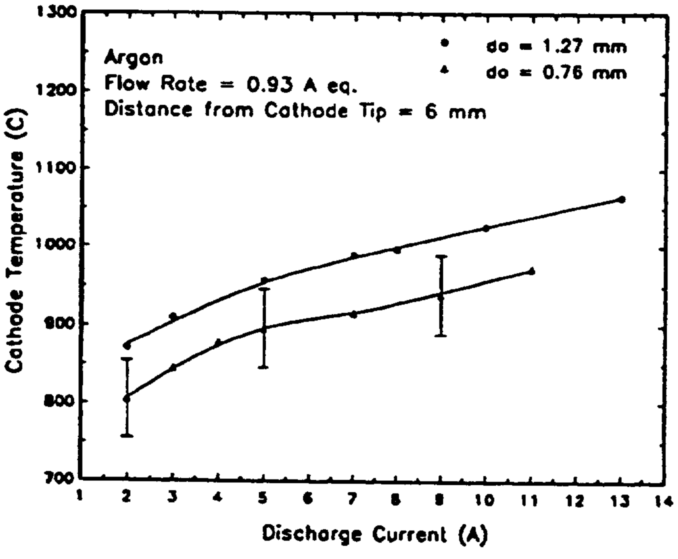

Figure 28: Effect of discharge current on cathode external surface temperature for different orifice sizes.

AIAA-94-3133

Scaling Relations for Design and Operation of Orificed-Hollow Cathodes

A. Salhi
AIME Technologies, Inc.
Columbus, OH

P. J. Turchi
The Ohio State University
Columbus, OH

30th AIAA/ASME/SAE/ASEE Joint Propulsion Conference
June 27-29, 1994 / Indianapolis, IN

SCALING RELATIONS FOR DESIGN AND OPERATION OF ORIFICED-HOLLOW CATHODES

A. Salhi*
AIME Technologies, Inc.
Columbus, Ohio

P. J. Turchi†
The Ohio State University
Columbus, Ohio

Abstract

An analysis of hollow cathode scaling is conducted by applying a theoretical model based on first-principles. It is found that self-consistent, steady-state solution of the governing equations for energy and particle fluxes is not possible above a critical current/diameter, dependent on the orifice-to-insert diameter ratio. This result is consistent with empirical evidence for experimental hollow cathode operation. Other results of the model indicate the physical basis for hollow cathode design.

Nomenclature

A	area, m^2
AR	orifice-to-insert cross section ratio
D	cathode inner diameter, m
e	electron charge, $1.602 \times 10^{-19} Coul$
I	current, A
k	Boltzmann's constant, $1.381 \times 10^{-23} J/K$
T_e	electron temperature, K
V	volume, m^3
η	plasma resistivity, $\Omega - m$

I. Introduction

Despite the extensive research conducted on hollow cathode arc discharges, many aspects of this device have remained unsolved. Some of these aspects are: the state of the plasma inside the cathode, the surface emission area, the interaction between plasma and solid boundary, the effect of cathode configuration, the effect of the propellant, the erosion rate, and the optimum operating conditions. Answers to these questions and better understanding of the physical processes governing hollow cathode arc discharges would allow the design of reliable, long lasting and efficient devices suitable for space applications.

A theoretical model[1] has been developed to conduct design analyses and predict proper terminal conditions for orificed, hollow cathodes. The cathode geometry considered for study of a hollow cathode arc discharge is a cylindrical cavity with a relatively small orifice (figure 1). In such a configuration, the energy losses associated with radiation, positive ions and excited atoms are substantially reduced. Therefore, the cathode fall is expected to be reduced while large currents can still be carried by the discharge. This geometry also allows for reasonable boundary conditions vital to the solution of this problem. The theoretical approach includes two-dimensional variation in plasma potential with uniform electron temperature. The heavy particle temperature distribution is estimated by balancing electron collisional heating[2]

---

[*] Research Engineer, Aerospace Technology Division, Member AIAA.

[†] Professor, Department of Aeronautical & Astronautical Engineering, Senior Research Scientist, USAF Phillips Laboratory, Member AIAA.

of ions with heavy particle heat conduction in the radial direction. One particular aspect of this formulation is the specification of an adiabatic wall. This condition reflects a special interest in high power density operation in which the principal cooling mechanism of the surface is thermionic electron emission and radiation. The model takes into account the Ohmic heating due to a resistive plasma. To a first approximation the conductivity of the plasma is considered to be that of a fully ionized gas. This assumption is reasonably justified due to the fact that hollow cathode can sustain highly ionized discharges.[3,4] Finally, in line with the nearly closed geometry of the problem, plasma composition is determined by a two-temperature Saha equation.[5,6] The set of algebraic equations governing power balance within the hollow cathode and the double sheath at the emitting surface are solved to obtain the dependence of various characteristics on terminal parameters such as, discharge current, mass flow rate, gas properties, material work function and geometry.

II. Hollow Cathode Scaling

The cathode lifetime depends strongly on the wall temperature. For impregnated porous tungsten inserts, a maximum lifetime of 100,000 hours was estimated at a temperature of 1000°C while, at a temperature of 1100°C, only 30,000 hours were expected[7,8]. Existing hollow cathodes (for ion engines) operate at maximum wall temperatures less than 1200°C for discharge currents ranging from 1 to 20 Ampere. Thus, there is a need to establish hollow cathode scaling that will permit higher current operation at temperature below this design limit. The present theoretical model[1] can be used to determine the best cathode configuration that meets mission requirements (power level and lifetime). Some theoretical results depicting the limiting discharge current for typical operating conditions are summarized in figures 2 through 7. In these calculations, the current is limited either by the computed cathode temperature or the inability to achieve a steady-state, self-consistent solution to the governing equations of the model. For example, in figure 6, it is seen that the cathode temperature would exceed the specified maximum value for an insert diameter of 4 mm and current in excess of 40 A. Larger cathodes, however, are limited in current by lack of self-consistent operating parameters.

It is important to note that the maximum discharge current is proportional to the cathode diameter rather than the expected dependence on the square of the diameter (figure 2). This trend is consistent with the empirical results of Kaufman[9]. Physically, this behavior can be explained by analyzing the balance between the energy loss through the cathode orifice and the energy production in the internal plasma column. The energy loss is primarily proportional to the discharge current I while the energy production within the hollow cathode is attributed in part to the energy of the emitted electrons accelerated through the fall and to the resistive heating (which is proportional to I^2). The energy balance determines the magnitude of the fall voltage. As the current increases, the fall voltage needed for the energetic operation of the plasma can decrease to relatively low values allowing for the following approximation:

$$\eta \left(\frac{I}{A}\right)^2 V \simeq I \left(\frac{5kT_e}{2e}\right) \qquad (1)$$

where A and V are the insert cross section and volume of the internal plasma column respectively. As a consequence of the Laplace equation for the resistive voltage in the plasma, the length of the plasma column scales to one-insert diameter[10] , equation 1 may thus be written as:

$$\frac{I}{D} \simeq \frac{5\pi kT_e}{8e\eta} \qquad (2)$$

Because the electron temperature is a slow-varying function of the current[10], the limiting discharge current is proportional to the diameter:

$$I \alpha D \qquad (3)$$

In figure 5, the limiting current is associated with reduction of the cathode fall to a few eV. Another interesting behavior of the theoretical solution regarding the relationship between the maximum discharge current and the propellant flow rate is described in figure 6. In this case, the current varies linearly with the flow rate up to a maximum value and then levels off. The previous analysis of the effects of the geometrical parameters on the maximum discharge current was conducted for a relatively high flow rate (1 A equivalent). This situation corresponds to the horizontal part of the curve in figure 7. Calculations for other equivalent current values along this part of the curve differ negligibly from the results presented. In the linear region (low flow rate), the degree of ionization is unity. As long as the mass flow rate is higher than the minimum value associated with the condition of a fully ionized gas, the orifice size is the sole parameter that limits the discharge current. (Attempts were made to include the second degree of ionization, but, no solution was obtained for currents higher than the limiting values corresponding to a singly ionized gas.)

III. Conclusions

The results obtained show that one of the primary operating parameters that govern hollow cathode discharges is the geometry, in particular, the insert and orifice diameters. Smaller orifice size induce lower limiting discharge currents. This behavior results from the tendency of the cathode to operate too efficiently (very low fall voltage). In this case, the fall voltage reaches a minimum at which the back-streaming of plasma electrons to the cathode surface is relatively high. The lowering of the fall voltage is a manifestation of the increase in energy production in plasma column by resistive heating. Under the assumption that thermionic emission is the primary emission mechanism, the analysis indicates that there exists a maximum discharge current beyond which a given hollow cathode configuration cannot operate properly. High current levels should be possible by increasing the size of the cathode in accord with a current-to-insert diameter ratio of 12 A/mm (for AR = 0.20). Relations between current level, cathode size and other design parameters can be established theoretically for a variety of desired operating conditions.

Acknowledgements

This work is an extension of previous research conducted under a grant from the Electric Propulsion Laboratory at NASA-Lewis Research Center, Cleveland, Ohio.

References

1. A. Salhi and P. J. Turchi. Theoretical modeling of orificed, hollow cathode discharges. *AIAA Paper No. 93-024*, September 1993.
2. L. Spitzer, Jr. Physics of fully ionized gases. *Interscience Publishers, Inc.* New York, 1956.
3. L. M. Lidsky, S. D. Rothleder, D. J. Rose, and S. Yoshikawa. Highly ionized hollow cathode discharge. *Journal of Applied Physics*, 33(8): 2490-2497, August 1962.
4. G.V. Babbkin, V. G. Mikhalev, E. P. Morozov, and A. V. Potatov. Experimental investigation of the plasma in multichannel cathode. *Journal of Applied Mechanics and Technical Physics*, 17: 767-770, November-December 1976.
5. A.V. Potapov. Chemical equilibrium of multitemperature systems. *High Temperature*, 1:48-51, January-February, 1966.
6. S. Veis. The Saha equation and lowering of the ionization energy for a two-temperature

plasma. *Czechoslovak Conference on Electronics and Vacuum Physics*, Edited by Libor Pathy (Charles University, Prague), pp. 105-110, 1968.

7. M. J. Mirtich and W. R. Kerslake. Long lifetime hollow cathodes for 30-cm mercury ion thrusters. *NASA TM X-73523*, November 1976.

8. R. L. Poeschel and J. R. Beattie. Primary electric propulsion technology study. *NASA CR-159688*, November 1979

9. H. R. Kaufman. Technology of electron-bombardment ion thrusters. *Advances in Electronics and Electron Physics* V..36. pp. 352. 1974.

10. A. Salhi. Theoretical and experimental studies of orificed, hollow cathode operation. Ph.D. Dissertation. The Ohio State University, Department of Aeronautical and Astonautical Engineering. December 1993.

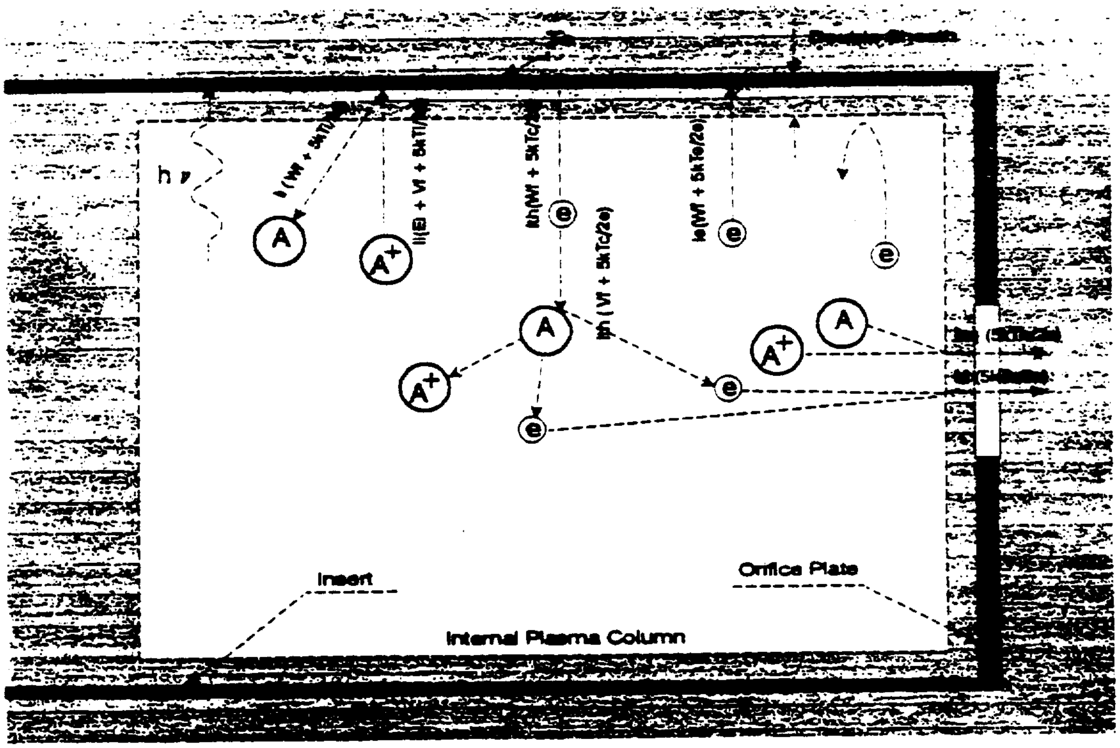

Figure 1: Description of hollow cathode physical processes

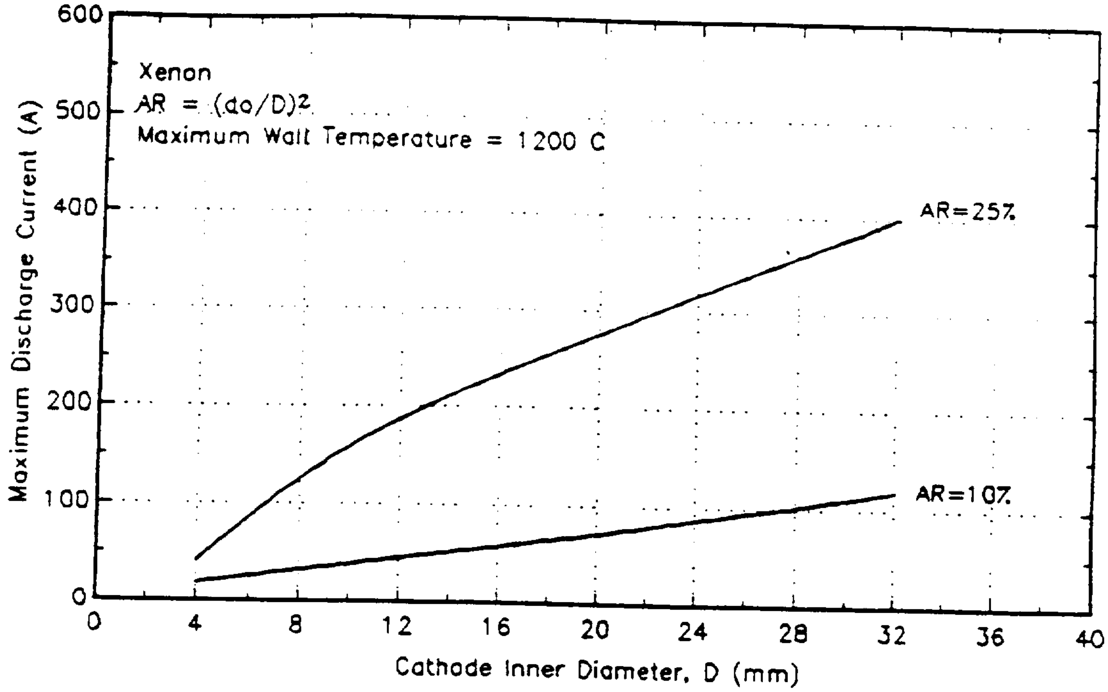

Figure 2: Theoretical prediction of the effect of cathode inner diameter on the maximum discharge current.

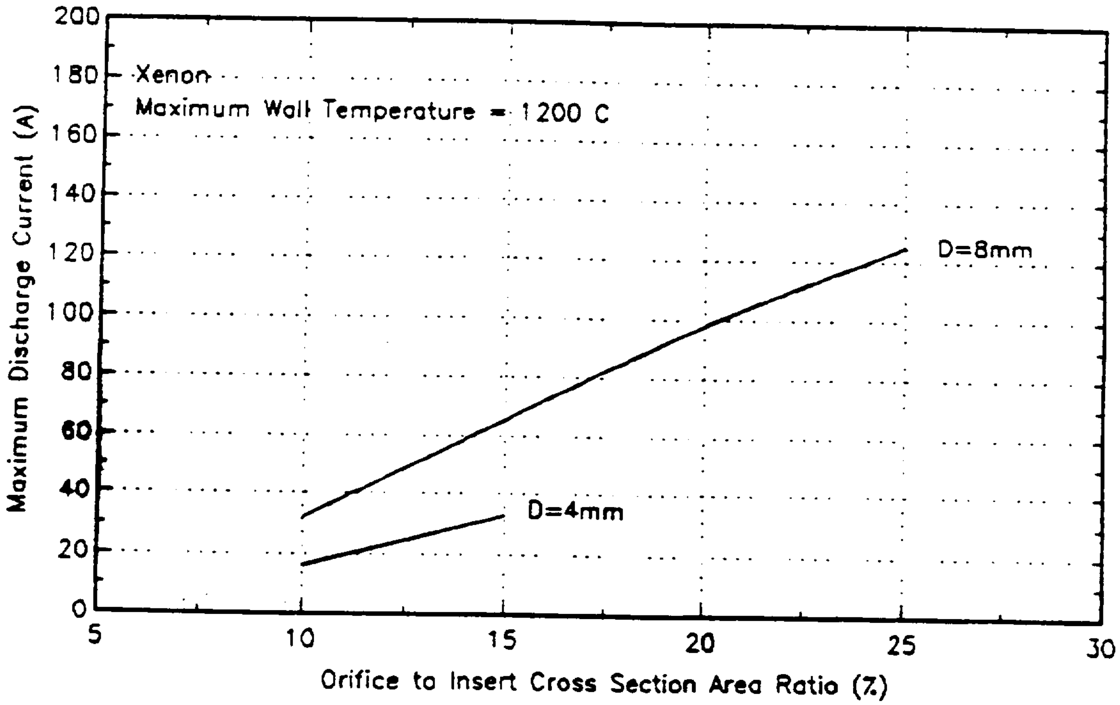

Figure 3: Theoretical prediction of the effect of orifice to insert cross section area ratio on the maximum discharge current.

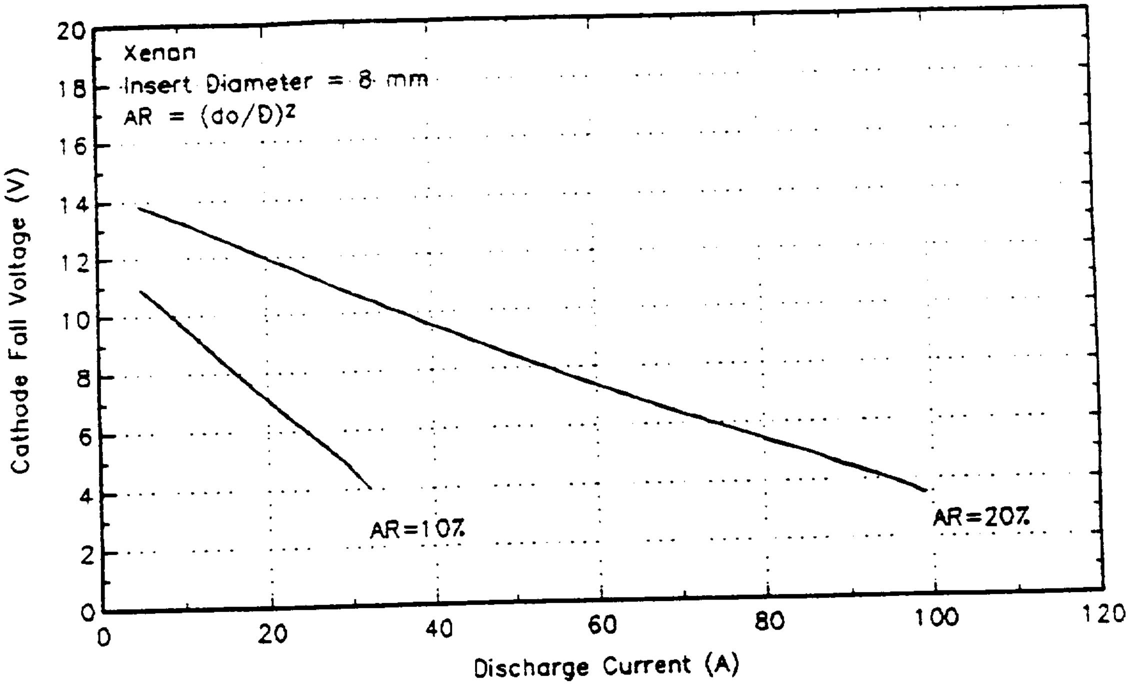

Figure 4: Theoretical prediction of the effect of discharge current on the fall voltage for different orifice sizes.

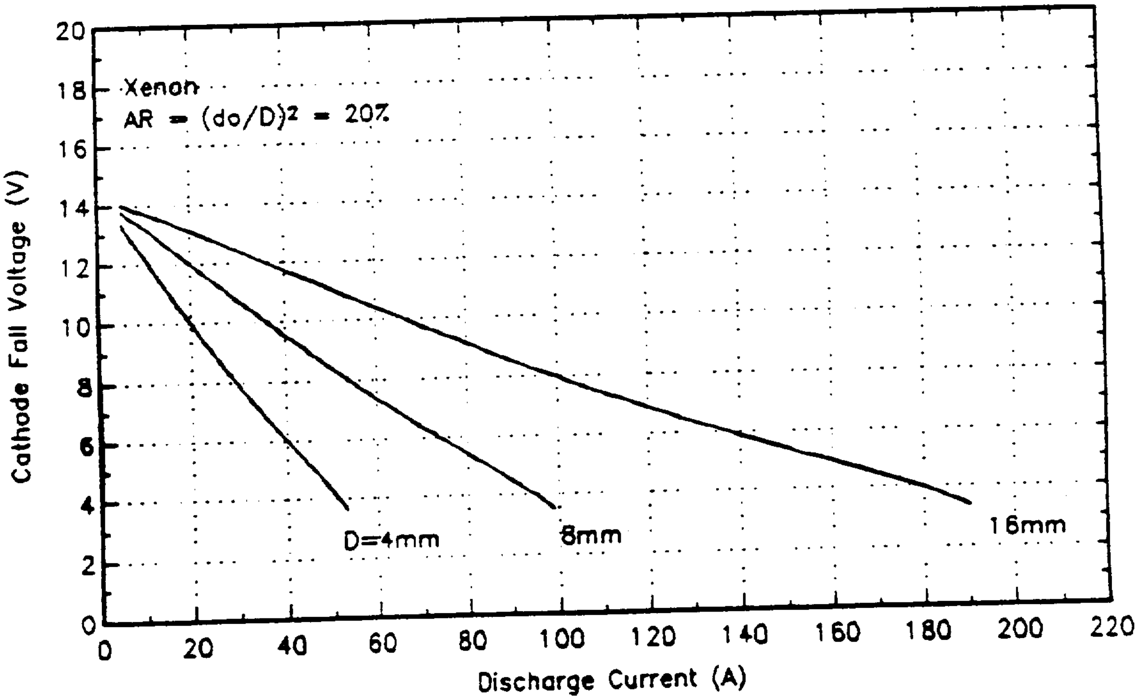

Figure 5: Theoretical prediction of the effect of discharge current on the fall volta for different insert diameters.

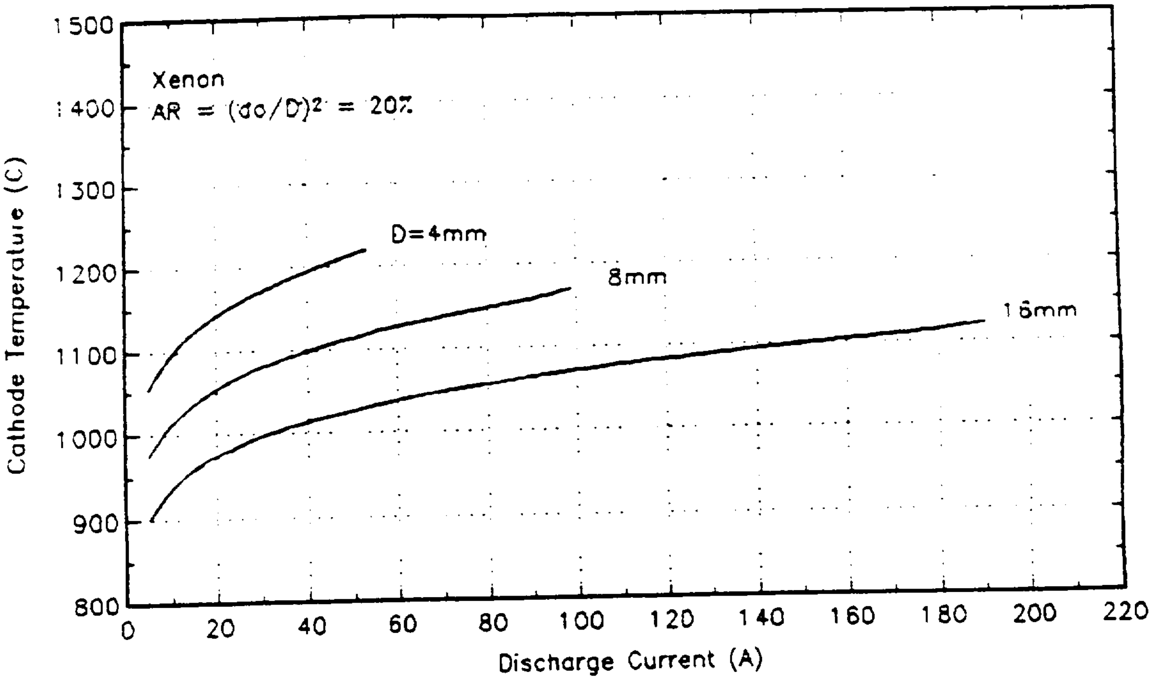

Figure 6: Theoretical prediction of the effect of discharge current on cathode temperature.

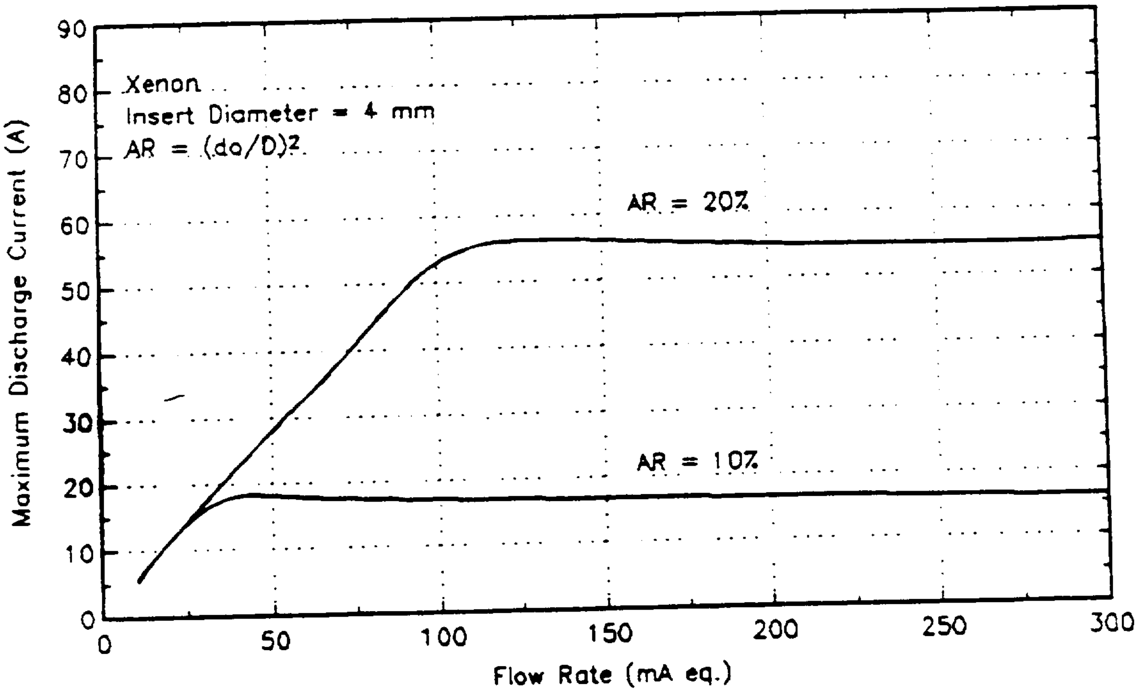

Figure 7: Theoretical prediction of the effect of flow rate on the maximum discharge current.

AIAA-94-3126

LOW POWER PLASMA THRUSTER BASED ON HOLLOW CATHODE DISCHARGE

P.J. Turchi
The Ohio State University
Columbus, Ohio

A. Salhi
AIME Technologies, Inc.
Columbus, Ohio

30th AIAA/ASME/SAE/ASEE Joint Propulsion Conference
June 27-29, 1994 / Indianapolis, IN

LOW POWER PLASMA THRUSTER BASED ON HOLLOW CATHODE DISCHARGE

P.J. Turchi

The Ohio State University, Columbus, Ohio

A. Salhi

AIME Technologies, Inc., Columbus, Ohio

ABSTRACT

Recent success with a first-principles model for orificed-hollow cathode operation provides some insight into the possibilty of creating diffuse discharges with application to low-power plasma thruster designs. Predictions of the model include the cathode operating voltage, limiting current-to-diameter ratios, electron, heavy particle and cathode surface temperatures, and the relationships of these quantities to the geometry of the cathode, and to the terminal parameters of total current and mass flow rate. At high currents and mass flow rates, resistive heating within the hollow cathode plasma provides sufficient power to allow cathode fall voltages of only a few volts, with little dependence on the mass flow (equivalent current flow) rates. Peak heavy particle temperatures also increase to values substantially above the cathode material temperature, (4000 vs 1200 C). Such temperatures may permit exhaust speeds of interest for low-power plasma thruster applied in station-keeping missions.

INTRODUCTION

Hollow cathodes have received considerable study as useful sources for charged-particles and radiation. Applications have been found within electron bombardment ion sources for ion engines, and in plasma contactors to control spacecraft charging. Recently [1], a first-principles model has been formulated and solved that provides a method for predicting the behavior of orificed hollow cathodes based on the cathode size, proportions (orifice-to-insert diameter ratio), gas specie and cathode material properties, (ionization potential and work function, respectively), and the terminal parameters of total current and mass flow rate. (No adjustable or empirical factors are involved). A result of this model is the associated ability to predict a diffuse plasma discharge that might have useful applications for space propulsion, especially in the low power, lower specific impulse regimes appropriate for station-keeping. The present paper provides some initial exploration of the possible design of a plasma thruster based on hollow cathode operation.

BACKGROUND

The basic approach followed for the development of a first-principles model of a hollow-cathode involved simple power balance equations for steady-state operation at the cathode surface and within the overall volume. These relations are depicted schematically in Figure 1. Various equations were introduced to connect the separate physical parameters required by these overall balances, but dependence on empirical information, beyond design-specified quantities, (e.g., total current, known work function, insert diam), was avoided.

The initial model provided quite reasonable agreement with experimental data, even though no provision was included for variation of plasma properties within the cathode volume. Experiments [2], performed at the NASA Lewis Research Center, confirmed the basic predictions of the model, but also indicated some features that might be addressed with a slight extension of the formulation. In particular, the basic model predicted that the operating pressure would be

---

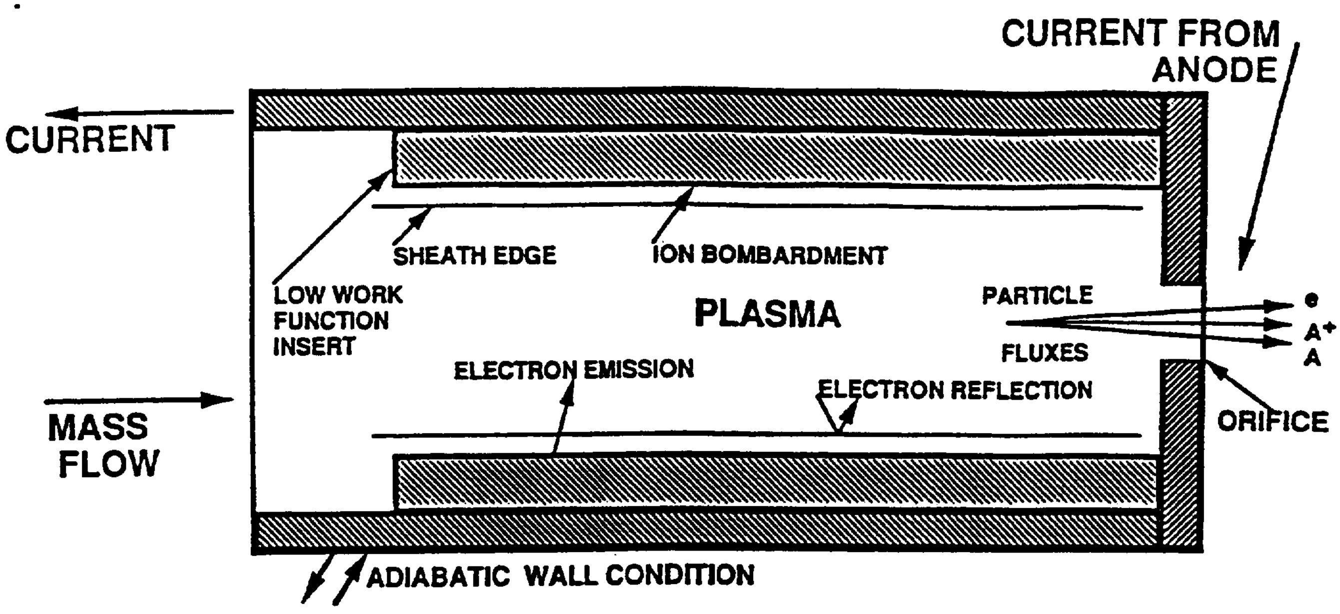

Figure 1: Hollow Cathode Model

independent of discharge current (at fixed mass flow rate), while the experiment indicated that the pressure actually increased slightly with higher currents, (Figure 2). The model was altered to allow for an increase of heavy particle temperature from values near the wall, (i.e., cathode surface temperature) to higher values, near the exit orifice, (which would require higher operating pressures in order to pass the specified mass flow rate). A radial distribution of heavy particle temperature was derived from a balance of volumetric heating of the ions by elastic collisions with plasma electrons, immediate sharing of energy between ions and neutral atoms, and heavy-particle heat conduction to the colder (cathode) boundary.

The electrons are heated (and cooled) by a variety of processes, including resistive dissipation in the plasma volume and electron fluxes through the cathode fall. The electron temperature, which determines the heat transfer to the ions, is determined by the overall power balances of the model. No direct connection is specified between the current flow and the heating of the ions. The improved model, nevertheless, correctly predicts the slight, linear increase of operating pressure with discharge current.

PROPELLANT HEATING

A consequence of the improved model is that the heavy particle temperature can be substantially higher than the cathode surface temperature. Profiles of heavy particle temperature variation with radius are shown in Figure 3 for several values of discharge current, and a single mass flow rate. These particular plots are for argon at an equivalent current of 0.5 A, orifice and insert diameters of 0.76 mm and 1.9 mm, respectively, and work functions of 2 eV (solid lines) and 4.5 eV (dashed lines). The variations of cathode surface temperature and peak (centerline) gas temperature vs discharge current are displayed for hydrogen propellant and two values of cathode work function, 2 eV (Figure 4) and 4.5 eV (Figure 5). In both cases, the mass flow rate is equivalent to a current of 1 A.

Higher gas temperatures are obtained with higher currents, but the cathode surface temperatures are also higher. Furthermore, there are limits to the operating current level that depend on the work function. These current limits [3], which correlate well with empirically-determined rules [4] for proper operation of orificed hollow cathodes, are associated with reductions in the cathode fall voltage, as indicated in Figure 6; (the solid lines and dashed lines provide cathode fall and total voltages for work functions of 4.5 eV and 2 eV, respectively.) Such reductions appear to occur because there is sufficient resistive heating in the volume at higher currents to balance the energy flux from the hollow cathode without requiring large fall voltages. As the fall voltages decrease, however, (and the plasma density near the cathode surface increases with the operating pressure), the flux of electrons to the cathode from the plasma increases. This would require greater thermionic electron emission to account for the net current, but the fall voltage would then have to be still lower to avoid additional heating of the plasma by this increased electron flux from the cathode. The net result is that are limiting values of current-to-diameter ratio above which steady-state solution of the model cannot be achieved. Figures 7 and 8 display examples of the dependence of limiting current on cathode insert diameter, (shown as the limiting values of cathode fall), and on the mass flow rate, expressed as equivalent-current.

From such calculations, with equivalent currents out to 50 A, it appears that, after a linear rise at low mass flow rates, the limiting current does not depend on the equivalent current; the electron temperature also is relatively insensitive to the mass flow rate. Furthermore, the cathode fall values reach the same minimum values independent of the actual value of limiting current. These minimum values appear to be a factor of a few higher than the electron temperature, but this factor depends on the cathode work function.

Basic scaling, obtained by non-dimensionalizing the equation of heavy particle heat conduction balancing ion heating by electrons, indicates that the peak heavy particle temperature should increase with the square-root of equivalent-current. (Higher peak gas temperature requires increased operating pressure, so particle densities for collisional heating are higher in most of the cathode volume.) As the heavy particle temperature increases toward the electron temperature, however, collisional heat transfer diminishes. It appears from the model that gas temperatures do not exceed about a third to a half of the electron temperature, even at high equivalent-currents. It should be reasonable, therefore, to attain gas temperatures in excess of 3000 K

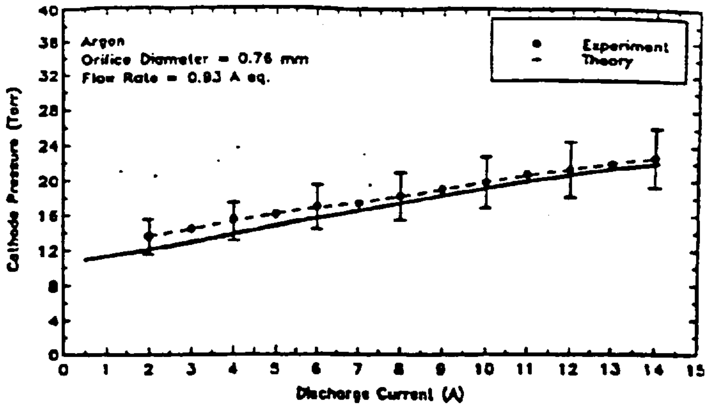

Figure 2: Cathode pressure [torr] vs current [A].

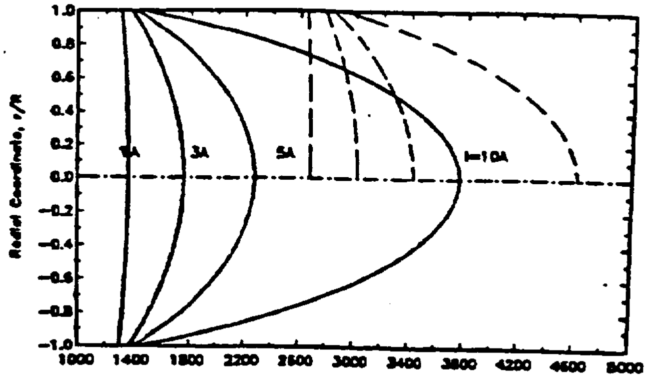

Figure 3:Profiles of argon temperature for different current levels and work functions.

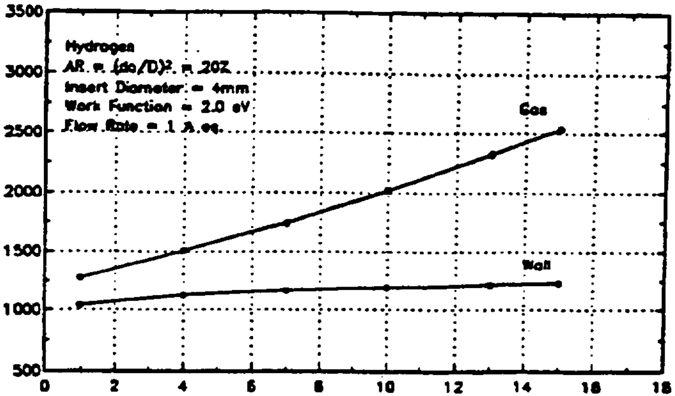

Figure 4: Temperatures vs current for hydrogen, with cathode work function of 2 eV.

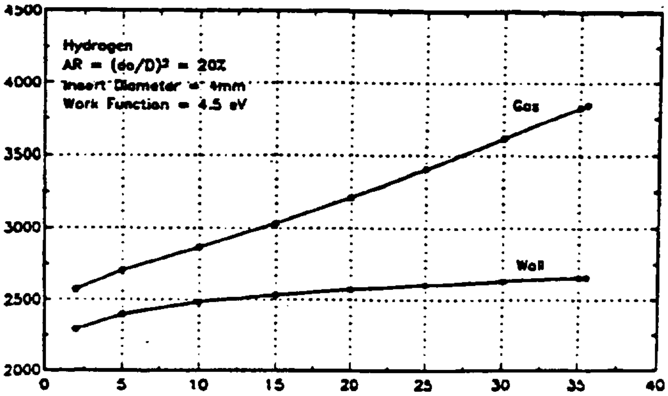

Figure 5: Temperatures vs current for hydrogen, with cathode work function of 4.5 eV

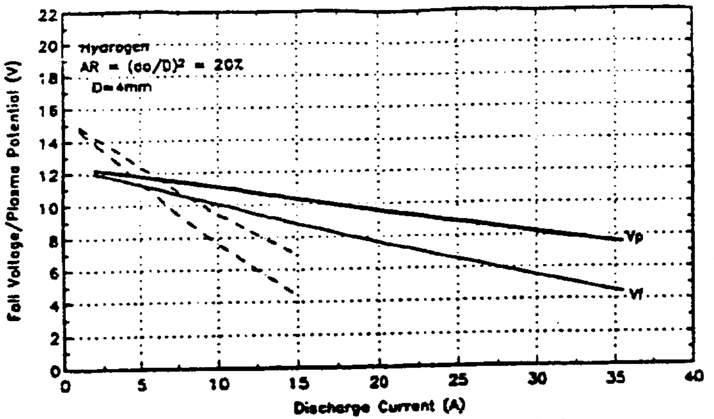

Figure 6 : Voltages [V] vs current [A], for hydrogen, with work functions of 2 and 4.5 eV.

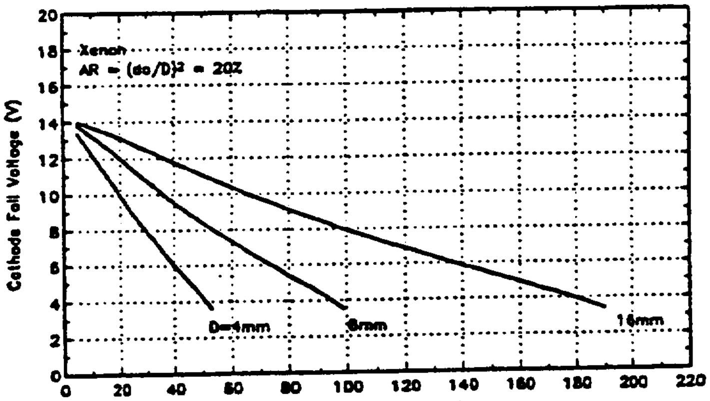

Figure 7: Cathode fall voltage [V] vs current [A], xenon, with different diameters.

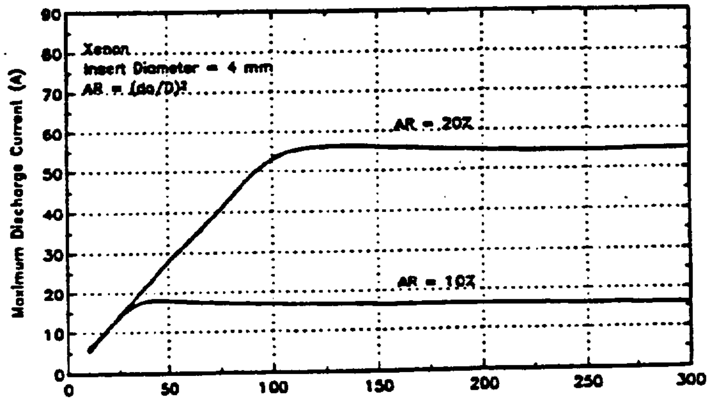

Figure 8: Limiting-current [A] vs equivalent current (mass flow rate) [mA]. Xenon, with 4 mm insert diam and work function of 2 eV.

---

without requiring cathode surface temperatures above 1500 K.

OPERATING CHARACTERISTICS

From the many separate results of the hollow cathode model, several operating characteristics may be summarized near the condition of maximum current-to-diameter ratio. These characteristics include the reduction of the cathode fall voltage to a minimum value that is independent of the actual current, as long as the orifice diameter is adjusted to the value for maximum current-to-diameter ratio, (see Figure 7). Under this condition, resistive heating in the plasma volume balances the energy flux out the orifice, (which is mainly the flow of electron enthalpy, since the degree of ionization is typically less than a few per cent). The limiting current may thus be written approximately in terms of simpler algebra than the full nonlinear system of equations actually solved in the model:

$$J^2 R = J\,(5/2)\,kT_e/e \qquad (1)$$

where J is the discharge current, which is nearly equal to the electron flux from the orifice, and kT_e/e is the electron temperature in volts; the resistance, R, may be related to the electrical resistivity, η, in terms the effective path length, L, and cross-sectional area, A, for the current flow:

$$R = \eta L \,/\, A \qquad (2)$$

The actual two-dimensional, current distribution is determined in the model by solving Poisson's equation. For given proportions (e.g., orifice-to-insert diameter ratio), the length-to-area quotient may be written as a constant of proportionality K divided by the orifice diameter, d. Thus, a simple formula for current-to-diameter ratio may be obtained:

$$J \,/\, d = (5 \,/\, 2K)\, kT_e \,/\, e\eta \qquad (3)$$

A consequence of this relationship, which describes the condition of the limiting current for a given diameter, is that the resistive voltage drop across the plasma is constant:

$$JR = (5 \,/\, 2)\, kT_e \,/\, e \qquad (4)$$

(This behavior is evident again to reasonable approximation in the results at limiting-current values in Figure 6, for which the work function of the cathode is changed at fixed diameter). Since the cathode fall also has a nearly constant value at the different values of limiting-current, the total voltage across the cathode can decrease to the same value independent of the current (and therefore total power level) as long as the diameter is scaled appropriately.

For conditions calculated by the present model, the heavy particle flux leaving the cathode is not highly ionized, and, therefore, does not represent a strong factor relative to the power balance in Equation (1). For molecular gases, such as hydrogen or nitrogen, the model must still be extended to include the effects of energy loss due to significant levels of dissociation. It is expected that the same basic behavior will be observed in regard to attainment of limiting current values when resistive heating is able by itself to balance power loss through the orifice: the cathode fall will again decrease to a minimum value below which there is insufficient reflection of the plasma electron flux toward the cathode surface to permit solution of the model. It is anticipated that, while the cathode fall voltage will be similar to previous limiting values, the resistive voltage across the plasma will increase. This should be expected because higher limiting-currents will be necessary to balance the increased power loss due to efflux of dissociated gas.

In the same spirit as the previous power balance at the limiting-current, the resistive heating now must account for the additional flux of energy due to the mass flow of (partially) dissociated gas. In terms of the equivalent-current (of atoms), J_{eq}, the power loss due to the heavy particle efflux is:

$$P_h = J_{eq}\,(\,\alpha_d E_d + (5/2)\,kT_h\,(1 + \alpha_d)/2)\,/\,e \tag{5}$$

where α_d is the degree of dissociation at the orifice, E_d is the dissociation energy (per atom), and T_h is the heavy particle temperature at the orifice. Note that, for this reduced version of the full hollow cathode model, it is still assumed that the heavy particle flux is not substantially ionized. The discharge current and current due to electron efflux are thus still approximately equal, so the limiting-current is increased over its previous value by a factor that involves P_h, (and the solution of a quadratic equation):

$$J/J_o = \{1 + [\,1 + 4P_h/(J_o\,(5\,kT_e/2\,e))]^{1/2}\}\,/2 \tag{6}$$

where J_o is the limiting-current (for a given orifice diameter) based only on the electron enthalpy flux. Since the model has previously indicated reasonable insensitivity of the electron temperature to equivalent-current level, the resistance of the cathode discharge should remain approximately constant, and the resistive voltage drop will scale with the increased value of the limiting-current due to dissociated mass flow. In this way, the power cost of dissociation is included in the overall operation of the cathode.

The efficiency of converting electrical power to the enthalpy of the propellant flow can then be written in terms of the ratio of equivalent-current to limiting-current (without dissociation) and various ratios of particle energies:

$$\varepsilon_h = P_h\,/\,VJ \tag{7}$$

$$\text{with } V = (V_o - V_f)\,J\,/\,J_o + V_f\,,$$

where V_o is the total voltage without dissociation, and V_f is the cathode fall. This efficiency may then expressed as:

$$\varepsilon_h = \frac{\{(J_{eq}/J_o)\,(\alpha_d E_d + (5/2)\,kT_h\,(1 + \alpha_d)/2)/eV_f}{\{(V_o/V_f - 1)(J\,/\,J_o) + 1\,\}\,(J\,/\,J_o)} \tag{8}$$

where $J\,/\,J_o$ is given by Equation (6) in terms of $J_{eq}\,/\,J_o$, and E_d and T_h vs T_e . It is evident that there is an optimum value of $J_{eq}\,/\,J_o$ in order to maximize the efficiency of converting electrical energy into gas energy. The efficiency also is highest with the lowest value of cathode fall voltage, which corresponds to operation at the limiting-current for any choice of parameters. Since V_o/V_f at the limiting-current tends to be a constant, as does the ratio of T_h to T_e, and V_f to T_e, the efficiency can always be optimized to about the same value, independent of the actual current and power level.

Furthermore, since the current scales as the diameter, and the electron and heavy particle temperatures will be approximately constant (for operation always at the limiting-current), the particle densities will scale inversely with the linear size of the device. This implies that the Knudsen number of the flow is the same for all sizes. The Mach numbers are also constant, so the viscous Reynolds number will be maintained, even in reducing the size and power of the discharge. (This scaling presumably continues until other physical phenomena introduce additional characteristic dimensions, such as optical mean free paths.)

SAMPLE THRUSTER DESIGN

History indicates that electric propulsion finds employment on spacecraft to the extent that available electric power sources are utilized. Kilowatt-level, steady-state arcjets are already operating on commercial satellites, and pulsed plasma thrusters have been working successfully in space for decades. Steady-state operation of plasma thrusters at sub-kilowatt levels, to service small satellites will require reduced costs for electrode falls and propellant ionization. The particular potential attraction of a hollow cathode plasma discharge for space thruster applications is the possibility that relative low power systems could be developed with adequate efficiency and specific impulse.

A first attempt at a thruster design based on a hollow cathode plasma can employ the conditions indicated by the previous modeling. Suppose an electron temperature of about 1 eV, so the heavy particle temperature may be estimated as 2500 K, with a cathode surface temperature in the range of 1200 C. If the propellant is hydrogen, then the following values may be inserted into Equations (6) and (8): $E_d = 2.24$ eV (per atom), $V_f = 4.2$ V, and $V_o = 7$ V. Suppose, for example, the current $J_o = 15$ A, and let the equivalent-current also equal 15 A (atom flow). For a fully dissociated flow, the limiting-current is increased by $J / J_o = 1.67$. The total voltage is then 8.9 V, and the input power is 222 W.

For the same assumptions, the efficiency (Equation (8)) is 18.7 %. The extent to which the gas energy can be converted into useful directed kinetic energy is a subject for more extensive calculation. The limiting values of specific impulse can range from the extreme optimism of full conversion ($I_{sp} = 2300$ s) to the more modest value derived from merely converting the sensible enthalpy to directed energy ($I_{sp} = 1017$ s); for the latter value, the thrust efficiency is less than four per cent. This result is consistent with crude extrapolation from higher pressure (1 - 100 atm) calculations [5] for hydrogen arcjets in the same temperature regime that suggest thrust efficiencies of less than twenty per cent would be encountered at the relatively low pressures (0.01 to 0.1 atm) in the hollow cathode.

CONCLUDING REMARKS

The primary limitation on efficiency appears to results from the separate scalings of heavy particle temperature and cathode fall voltage with electron temperature. The cathode fall needs to be a multiple of the electron temperature, while heavy particle heating by collisions with electrons limits the heavy particle temperature to a fraction of the electron temperature. Improvements in thrust efficiency may be possible with low mass, monatomic propellants. Dissociation increases the limiting-current, which improves the conversion of electrical energy to gas energy. This improvement merely increases the total power level without benefit to thruster performance, if the dissociation energy cannot be re-claimed in the exhaust. Improvements in thrust efficiency must be explored in the context of system integration, based on the availability and reliability of the propellant system, and the impact of lower efficiency vs higher specific impulse at low total power levels.

Finally, it should be noted that the hollow cathode discussed here must be part of a full discharge circuit. Such a circuit would have features typical of arcjet thrusters (e.g., arc column connecting to anode, with surrounding flow to protect walls). Thus, it is not unreasonable to expect that the present modeling can be employed to design hollow cathode operation for use in low power arcjet systems.

REFERENCES

1. A. Salhi and P.J. Turchi, "A First-Principles Model For Orificed Hollow Cathode Operation", AIAA Pre-print 92-3742, (July, 1992).

2. A. Salhi, R.M. Myers, P.J. Turchi, "Experimental Investigation of a Hollow Cathode Discharge", IEPC-93-025, International Electric Propulsion Conference, Seattle, WA, (Sept, 1993).

3. A. Salhi and P.J. Turchi, "Scaling Relations for Design and Operation of Orificed-Hollow Cathodes", AIAA Pre-print 94-3133, (June, 1994).

4. J.S. Sovey and M.J. Mirtich, "A Hollow Cathode Hydrogen Ion Source", NASA TM-73783, (October, 1977).

5. D.L. DeVincenzi, et al, "Elite System Analysis", AIAA Pre-print 90-2530, (July, 1990).

APPENDIX IV

THEORETICAL, NUMERICAL AND EXPERIMENTAL STUDIES OF PULSED PLASMA THRUSTERS

P.J. Turchi and P.G. Mikellides, “Modeling of Ablation-Fed Pulsed Plasma Thrusters”, 31st AIAA/ASME/SAE/ASEE Joint Propulsion Conference and Exhibit, San Diego, CA, July 10-12, 1995.
AIAA 95-2915

P.G. Mikellides and P.J. Turchi, “Modeling of Late-Time Ablation in Teflon Pulsed Plasma Thrusters”, 32nd AIAA/ASME/SAE/ASEE Joint Propulsion Conference and Exhibit, Lake Buena Vista, FL,
July 1-3, 1996. AIAA 96-2733

R.J. Leiweke, P.J. Turchi, H. Kamhawi, and R.M. Meyers, “Experiments with Multi-Material Propellants in Ablation-Fed Pulsed Plasma Thrusters”, 31st AIAA/ASME/SAE/ASEE Joint Propulsion Conference and Exhibit, San Diego, CA, July 10-12, 1995.
AIAA 95-2916

P.J. Turchi, R.J. Leiweke, and H. Kamhawi, “Design of an Inductively-Driven Pulsed Plasma Thruster”, 32nd AIAA/ASME/SAE/ASEE Joint Propulsion Conference and Exhibit, Lake Buena Vista, FL,
July 1-3, 1996. AIAA 96-2731

H. Kamhawi, P.J. Turchi, R.J. Leiweke, and R.M. Meyers, “Design and Operation of a Laboratory Bench-Mark PPT”, 32nd AIAA/ASME/SAE/ASEE Joint Propulsion Conference and Exhibit, Lake Buena Vista, FL, July 1-3, 1996. AIAA 96-2732

AIAA 95-2915

MODELING OF ABLATION-FED PULSED PLASMA THRUSTERS

P.J. Turchi and P.G. Mikellides
The Ohio State University
Columbus, OH

31st AIAA/ASME/SAE/ASEE
Joint Propulsion Conference and Exhibit
July 10-12, 1995/San Diego, CA

MODELING OF ABLATION-FED PULSED PLASMA THRUSTERS

P.J. Turchi and P.G. Mikellides

The Ohio State University
Columbus, OH

ABSTRACT

Design of the proper power system for an improved ablation-fed pulsed plasma microthruster (PPT) requires the ability to specify amplitudes, risetimes, waveforms and pulsetimes in relation to propellant properties and thrust chamber dimensions. Numerical modeling techniques, such as the MACH2 code, along with analytical modeling, are needed to provide guidance. Stationary operation in the limit of high magnetic Reynolds number may be characterized by a discharge thickness adjacent to the surface that scales inversely with the exhaust speed, resulting in a resistance that is approximately constant for fixed surface proportions and material. Heat transfer to the surface occurs in a thinner layer within this discharge, and provides a mass flow rate proportional to the electrical power. The mass ablated per shot then scales as the stored electrical energy, in agreement with experiments over a wide range of operations. Start-up and shut-down transients, (e.g., flux vs thermal skin-depths), can significantly alter this simple behavior. A new ablation-physics routine has been added to the MACH2 code to examine the time-dependent operation of the PPT discharge. Comparisons of numerical results with data from the LES 6 PPT are encouraging, even with present, idealized models for Teflon plasma properties.

INTRODUCTION

Recently, interest has returned to performing space missions in the near earth environment with systems that are capable of more efficient operation at lower overall cost. This interest is driven largely by reduced budgets in the post-Cold War era, but is also informed by experiences and policy changes over the last decade in regard to launch vehicle costs. In particular, it has been recognized that substantial savings can be achieved by using advanced sensors and electronics to reduce the mass of satellites, thereby allowing launch of satellite systems with less expensive boosters. Previously, in the heyday of Space Shuttle enthusiasm, launch costs were fixed by the decision to use the Shuttle for all transportation to orbit. There was little incentive to press for reductions in the spacecraft payload mass or the mass needed for on-board propulsion during the life of the mission.

With a return to expendable boosters for many unmanned space missions, and the success of systems such as Pegasus in launching small satellites, there is interest in spacecraft packages with total masses of less than a hundred kilograms, including payload, on-board thrusters and propellant. The challenge of reducing the payload mass is being met quite successfully, and may devolve to questions of the optimum number of elements in constellations of individual satellites. Flying such constellations, particularly in the near earth environment, requires consideration of on-board propulsion techniques. Special interest continues to be properly invested in the possibility of achieving high values of specific impulse in order to reduce the relative mass required for propellant. Over the years, this has been a principal factor for pursuing electric propulsion. The new element at this time is the development of such propulsion technology within the constraints of small satellite design. Deficiencies of understanding, however, prevent ready scaling to small-satellite use of proven propulsion techniques, such as the pulsed plasma microthruster (PPT)[1]. In particular, improved modeling of the composition and transport properties of two-temperature, molecular plasmas is needed in order to predict ablated-mass, specific impulse and efficiency for the next generation of plasma thrusters.

In 1982, as part of a study for AFOSR, a strategy[2] was presented for the development of electric propulsion techniques based on the successful, operational use of the pulsed plasma microthruster (PPT). The essential recognition of this strategy was that acceptance of electric propulsion depended on successful flight-use, but such use was not possible without previous acceptance of electric propulsion technology. To break out of this futile cycle, it was suggested that thrusters could be developed in which the PPT would provide the complex, high-risk portion of the system, while performance enhancement would be accomplished by basically passive elements. In this way, the improved thruster might more readily achieve acceptance by claiming flight experience for complicated parts, such as the ignition system. An important feature of the overall strategy was the ability to adapt the specific thruster design to available mission opportunities by varying the pulse repetition rate and the energy of the passive portion of the thruster system, while sharing flight experience over the entire family of thrusters.

In the context of small-satellite projects, the focus of development will be on smaller and lower-power electric propulsion systems. There are two parts to such development. Existing thrusters can be scaled down, while attempting to preserve or improve intrinsic performance values, such as efficiency and specific impulse. The associated power circuitry must also be improved in order to match the thruster needs to power levels and masses available in small satellite systems. This latter area encounters limitations on the minimum masses of components that have adequate energy- or power-per-unit-mass values for the currents and lifetimes required by the propulsion system design. These limitations force changes in the power delivery to the thruster, (e.g., different current waveforms). The process of scaling down operation of thrusters to small-satellite levels thus involves an interplay of the physical regime of thruster operation with the input power characteristics.

BASIC MODELING

Details of transport within the discharge channel can dramatically affect the mode of operation of the thruster and the relationship of the discharge dynamics to the electrical circuitry. This relationship determines the ultimate efficiency and available specific impulse levels of the PPT. Figure 1 depicts two basic modes of operation of an ablation-fed, plasma thruster. In the so-called "plasma-slug" mode, a discrete mass of plasma is accelerated by the magnetic-pressure difference across an electrical discharge that travels downstream with the plasma. Plasma ablated from the solid, propellant surface is also accelerated by the magnetic-pressure difference across the discharge in the quasi-steady mode, but the discharge remains adjacent to the surface, rather than propagating downstream. A third kind of operation is also depicted in Figure 1, and results from a transition between the plasma-slug mode and the quasi-steady mode. This occurs when the voltage across the moving plasma-slug and the continued evolution of conducting material from the propellant become sufficient to drive current near the surface. (The new conducting material acts as short across the linear electric-motor represented by the magnetically driven plasma-slug. In plasma accelerators, this situation is often referred to as a 'restrike' at the insulator surface.) The single pairs of electrodes shown in the sketches in Fig. 1 could be combined (in either mode) to create two-stage plasma accelerators[2] in order to achieve improved performance.

For the quasi-steady mode, it is possible to estimate the impedance of the ablation-fed discharge in the limit of high magnetic Reynolds number, $R_m = \sigma \mu u L \gg 1$. This corresponds to a streamwise-extent of the thruster electrodes much greater than the characteristic streamwise-thickness, Δ, of the discharge for which $R_m = 1$. Thus,

$$\Delta = 1 / \sigma \mu u_1 \qquad (1)$$

where σ is the electrical conductivity, μ is the permeability of freespace, and u_1 is the characteristic speed of the plasma flow. The resistance of the plasma discharge adjacent to the ablating surface is then (see Appendix I):

$$R = Eh / J_1$$

$$= \mu u_1 h / w \qquad (2)$$

where h is the length of the discharge (along the current path) and w is the width of the discharge. The total current in the layer is J_1, and the electric field across the flow is $E = u_1 B_1$, where $B_1 = \mu J_1 / w$. (Equation (2) results from Faraday's law for a steady-state, plasma accelerator flow.)

It may be shown[3] for steady-state, self-field, plasma accelerators that the characteristic speed is proportional to the square of the discharge current divided by a mass-flow rate that can include ablated material in addition to the propellant supplied to the thrust chamber. In the limit of an ablation-fed thruster, such as the PPT in quasi-steady mode, the mass-flow rate is proportional to the square of the discharge current, so the plasma speed becomes a constant that depends on the propellant material. This speed is proportional to Alfven critical speed, based on the total energy, Q_a required to ablate, dissociate and ionize a propellant molecule (see Appendix I):

$$u_1 \simeq (2 Q_a / m)^{1/2} \qquad (3)$$

where m is the mass of the propellant molecule (accelerated to speed u_1).

There are two important system implications from Eqns. (2) and (3). First, the specific impulse of PPTs operating in the ablation-fed, quasi-steady mode should be approximately constant, with a value that depends on the details of the propellant material and its chemistry within the plasma discharge, (e.g., values of Q_a and m). The second implication follows from the constant value of u_1, namely, the impedance of the ablation-fed, plasma discharge should be approximately constant in the quasi-steady mode.

Constant electrical impedance means that perfect coupling to the driving circuit can be readily achieved. For example, a uniformly-distributed, LC-ladder, pulseforming network (PFN), has a line impedance

$$Z = (L / C)^{1/2} \qquad (4)$$

where L and C are the inductance and capacitance per section of the transmission line. If this impedance is much greater than other circuit resistances and the PFN and plasma discharge are designed for Z = R, complete transfer to the plasma discharge of energy stored initially in the PFN can be expected. Driving the discharge with a simple inductive store would also completely transfer stored electromagnetic energy, (as long as circuit resistances are negligible vs R).

The energy delivered to the discharge will be divided between the cost of creating the plasma and the kinetic energy of the exhaust. With an exhaust speed based on Alfven critical speed, frozen-flow loss (if complete) would limit the thrust efficiency to about 50%. Proper matching of the ablation-fed discharge to the electrical circuit could thus improve the performance of PPTs by factors of 5 -10 over present thrust efficiencies (that are only several per cent), provided that the discharge operates in the quasi-steady mode.

In the plasma-slug mode, the changing impedance of the dynamic discharge prevents perfect matching to simple circuitry. Experience with various changing-inductance loads, however, indicates that conversion of stored electromagnetic energy into kinetic energy can be accomplished with efficiencies in excess of 25%. Optimum performance is achieved by matching the acceleration times of the plasma-slug to the current rise-time (in capacitively-driven circuits[4]) or by insuring that the inductance change due to discharge motion is comparable to the value of the storage inductor (in circuits using magnetic energy storage).

The principal technical deficiency in attempting to develop the PPT for small-satellite applications is the long-standing inability to predict the mass of plasma accelerated as a function of circuit values and arrangement, propellant type, and thrust channel dimensions. This inability includes prediction of the operating mode (quasi-steady vs plasma-slug) and the effects of current amplitude and rise-time on subsequent performance. The interaction of the plasma discharge with the solid surface certainly depends on the properties of the propellant material, but cannot be predicted until detailed specification of the complex, partially-ionized, molecular plasma is available. The behavior of such a plasma must then be combined with the basic electromagnetic and gas dynamic relationships of the discharge flow-field in order to comprehend and control PPT operation.

MACH2 MODELING OF THE PPT

With the MACH2 code, in its form at The Ohio State University, it is now possible to address a broad range of plasma thrusters, including self-field and applied-field devices, both steady-state and pulsed. In a recently completed, extensive effort on applied-field MPD thrusters[6], MACH2 results guided analytical modeling, which has provided scaling relationships for thruster behavior as a function of input current, applied field, propellant type and thruster geometry. These relationships successfully match a broad range of existing experimental data and indicate that possible, optimum performance values were missed by empirical studies. It should now be reasonable to apply MACH2 to model PPT behavior in detail, provided that sufficient research attention is given to fundamental processes of mass, momentum, energy and magnetic-flux transport in the complex, molecular plasmas formed from practical propellant materials. In particular, as a minimum for accurate calculations, transport coefficients are needed for heat conduction, viscosity, radiation and magnetic-diffusion for partially-ionized, partially-dissociated mixtures of atoms and molecules of different species, with separate electron and heavy-particle temperatures.

MACH2 incorporates essentially all the relevant physics available in the context of local thermodynamic equilibrium (LTE) and continuum flow. For example, the effects of plasma microinstabilities on transport are accessible through phenomenological models based on kinetic calculations. The effects of separate heavy-particle and electron temperatures on transport in a partially-ionized gas are also included. Indeed, experience in modeling the applied-field MPD thruster[6] demonstrated that both these non-standard elements of physics were critical for successful simulation. The anomalous resistivity limited the electron Hall parameter to modest values, and the two-temperature plasma formulation allowed the viscosity of the partially-ionized flow to increase, rather than decrease, with flow temperature.

Recently, a new surface ablation model has been added to MACH2 at Ohio State. It accounts for the energy deposition in the solid propellant due to heat conduction, radiation and convection from the plasma. The deposited energy is stored near the exposed surface in a volume whose depth increases as the square root of elapsed-time, in accord with the diffusive, thermal skin-depth in the solid. The temperature of the heated skin-depth defines the surface temperature from which the pressure and density of the equilibrium vapor[7] are computed. These values are used to provide hydrodynamic boundary conditions for the differential equations of MACH2 in order to compute the mass ablated from the surface (or condensing on the surface from the plasma).

Calculations have been performed for PPTs using the presently available equation-of-state for Teflon in the SESAME tables. This equation-of-state, however, is for a single-temperature plasma, and the associated opacity values are also based on equal heavy-particle and electron temperatures. Furthermore, the thermal conductivity of the plasma only utilizes electron transport, (albeit with cross-field and anomalous effects included). In the immediate vicinity of the surface, however, energy transport by chemically-active, heavy-particles should be important. These initial calculations nevertheless provide results that correlate with experimental data, and thereby encourage further effort.

Calculations were set up (see Fig. 2) to resemble the LES 6 PPT[1], with electrode separation h = 3 cm, electrode width w = 1 cm, and electrode length in the streamwise direction Δz = 0.6 cm. This last dimension forces at least portions of the discharge to remain near the propellant surface, which enhances the opportunity for ablation. (Otherwise, there is the strong tendency for the discharge, through the initial mass from the sparkplug, to accelerate downstream before significant ablation occurs. This was observed experimentally with two-stage PPTs until the electrode length was reduced to within about 1 cm from the propellant surface.) In the four sets of figures depicting the behavior of the discharge flow, a non-conducting, rectangular channel continues (at constant h and w) upward for 6 cm from the propellant surface (bottom of each figure). The top boundary of the flow is open, with the so-called 'continutive' condition of MACH2 for which all spatial variations normal to the boundary are set to zero.

An LRC-circuit, using values for LES 6, drives the discharge with a sinusoidal current waveform that peaks in 0.4 μsec. In figures 3 - 18, contours of constant density, temperature and downstream current are shown, along with velocity vectors, for 0.2, 0.4, 0.6 and 1.0 μsec. To simulate the plasma from the sparkplug, an initial plasma distribution was assumed with T = 1 eV and a mass density distribution (uniform for the first 0.6 cm, then decreasing linearly by 60%) that corresponded to a total initial mass of 0.1 μg, (about 2% of total mass ablated experimentally). Figure 19 displays the current and voltage vs time. Although the peak current, voltage and times all agree rather well with experimental results, there are many parameter variations still to be explored to explain variances, such as the double-peaked behavior of the experimental current waveform (Fig. 20).

The expelled mass and impulse, determined at the open end of the calculational region, are shown in Fig.21. Note that the expelled mass increases faster than the impulse at later times, suggesting the decrease in PPT performance due to late-time mass evolution from the heated propellant surface. Figure 22 indicates the variation of ablated mass (computed at the propellant surface at 2.8 μsec) with initial energy stored in the capacitor (at different initial voltages). It should be noted that, in these calculations, energy transport from the initial plasma can cause surface ablation, even when the circuit energy ($CV_0^2/2$) is zero. The linear increase of ablated mass with energy is heartening in relation to similar trends obtained experimentally, but more work is needed.

Such work should include more accurate representations of energy transport in two-temperature plasmas (which is expected relieve the locally high values of temperature in the present calculations). In addition, the diffusive skin-depth representation used in computing the surface temperature needs to be improved. Furthermore, the inclusion of viscous effects in the flow channel should help define the allowable inductance change for the energy input in the plasma-slug mode. Although the MACH2 version at Ohio State operates as a full Navier-Stokes solver, no model of viscosity for Teflon is available for the present calculations, so the viscous-effects option was turned off. This model will need to be two-temperature to capture the effects of high temperature heavy-particles in a low electron-temperature plasma. Radiative transfer of energy to the propellant surface must also be explored more fully to assess the possible need for improving the opacity data presently available from the single-temperature SESAME tables.

FUTURE IMPROVEMENTS

There are still technical deficiencies in MACH2 that could be important in modeling some plasma thruster regimes. In particular, non-continuum processes are not explicitly accessible with a hydrodynamics code, non-LTE effects beyond separate electron and heavy-particle temperatures (e.g., non-local chemistry) are not treated, and non-neutral regions, such as electrode falls, are not considered. The principal area that requires immediate attention, however, is the development of data and data manipulation techniques to extend the equations-of-state and transport properties needed by MACH2 to the molecular gases typically used for space propulsion. MACH2 presently accesses the SESAME tables, developed at Los Alamos National Laboratory, which includes many useful data, but some properties or materials critical for electric thrusters are simply not available.

The structure of MACH2 permits improvement in some of the areas of concern. For example, it is possible to manipulate the velocity and temperature boundary conditions to allow for non-continuum effects in the form of velocity slip and temperature jumps. The boundaries can also be modified to allow for energy interchange associated with particle-kinetics and electrode falls. Recent modifications of MACH2 allow for motions of multiple materials (e.g., metal from conductors vs plasma) and ablation of solid surfaces as a result of heat transfer from the plasma (e.g., ablation-fed plasma thrusters). Also very recently, a five-component equation-of-state model for partially-ionized, molecular nitrogen has been introduced, along with self-consistent viscosity and thermal conductivity coefficients.

Calculations of the PPT with MACH2 are restricted to two-dimensions. To date, these have only been employed in the plane containing the current and electromagnetic force vectors. It will be useful to perform calculations also in the plane orthogonal to the current vector in order to examine the effects of nonuniform distribution of current-density along the width of the propellant surface. At some point in the future, the experience and insights gained with these simulations can be used to guide calculations with MACH3, a three-dimensional MHD code[8] recently initiated at USAF Phillips Laboratory (PL/WSP), Kirtland AFB, NM. This new capability is still under development, but already includes many features needed for relatively low-density, electric thruster plasmas, such as anomalous resistivity and Hall effect. It is expected that the ablation modeling and the results of research on transport in molecular plasmas will eventually be used in MACH3.

ACKNOWLEDGEMENTS

Work supported by the NASA Lewis Research Center, Cleveland, OH, under grant NAG3-843, and the Ohio Supercomputer Center.

REFERENCES

1. A. Solbes and R.J. Vondra, "Performance Study of a Solid Fuel-Pulsed Electric Microthruster", J. Spacecraft and Rockets 10,406 (1973).

2. P.J. Turchi, "An Electric Propulsion Development Strategy Based on the Pulsed Plasma Microthruster", AIAA Preprint 82-1901.

3. P.J. Turchi, "Critical Speed and Voltage-Current Characteristics in Self-

Field Plasma Thrusters", J. Propulsion and Power 2, 398 (1986).

4. P.J. Turchi and W.L. Baker, "Generation of High Energy Plasmas by Electromagnetic Implosion", J. Applied Physics 44, 4936 (1973).

5. M.H. Frese, "MACH2: A Two-Dimensional Magnetohydrodynamic Simulation Code for Complex Geometric Configurations", AMRC-R-874, Mission Research Corp. (1987).

6. P.G. Mikellides, P.J. Turchi, N.F. Roderick, "Theoretical Model of an Applied-Field MPD Thruster", AIAA Preprint 95-2646.

7. T. Wentink, Jr., "High Temperature Behavior of Teflon", AFBMD-TN-59-15, AVCO-Everett Research Laboratory, Everett, MA (July, 1959).

8. R.E. Peterkin, Jr., personal communication.

APPENDIX I

Derivation of Exhaust Speed for Ablation-fed, Quasi-steady, PPT

In the limit of steady operation at high magnetic Reynolds number, it is reasonable to divide the discharge flow-field in the PPT into three regions: 1) a layer of high current density adjacent to the ablating propellant-surface; 2) a one-dimensional channel in which the flow is sonic and conducts little, if any, current; and 3) a two- or three-dimensional expansion of highly magnetized plasma to the field-free vacuum. The multi-dimensional expansion of last region avoids the artificial heating (and choking) of the flow that results from demanding the magnetic field decrease to zero at the end of the one-dimensional channel.

The thickness of the first region is scaled by the distance for which the competing processes of convection and diffusion of magnetic flux are both important:

$$\Delta = 1 / \sigma \mu u_1 \qquad \text{(A.1)}$$

where σ is the electrical conductivity, μ is the permeability of freespace, and u_1 is properly the speed of the plasma after it passes through this region. The thickness of the region characterizes the current density in terms of the magnetic field difference:

$$j = (B_0 - B_1) / \mu\Delta \qquad \text{(A.2)}$$

where B_0 and B_1 are the magnetic field values at the entrance and exit of the first region.

In steady-state, the resistive electric field at the entrance equals the back-electromotive field in the current-free channel that starts at the exit of the region:

$$E = E_0 = E_1 \qquad \text{(A.3)}$$

$$\eta j = u_1 B_1 \qquad \text{(A.4)}$$

so, $(B_0 - B_1) = B_1$, and $B_1 = B_0 / 2$. The total current in the first region is then

$$J_1 = B_0 \, w / 2\mu \qquad \text{(A.5)}$$

where w is the width of the discharge (perpendicular to both the current and flow directions).

The power deposited in the first region is needed to create the plasma conditions and velocity in the second region:

$$EhJ_1 = u_1 B_o^2 wh / 4\mu$$

$$= \rho_1 u_1 wh \{ u_1^2 / 2 + Q_a / m + \gamma RT_1 / (\gamma - 1) \} \quad (A.6)$$

where ρ_1 and T_1 are the mass density and temperature, respectively, in the one-dimensional channel flow, Q_a is the energy needed to evaporate, dissociate, and ionize the propellant atom or molecule of mass m, and γ is the effective specific heat ratio for the flow. The gas constant, R, includes the electrons; for full, single-ionization, (and equal ion and electron temperatures), $R = 2k/m$.

The second flow region has constant cross-sectional area and exhausts to supersonic expansion in the third region. It is appropriate therefore to apply a sonic condition to the one-dimensional channel flow:

$$u_1^2 = B_1^2 / \rho_1 \mu + \gamma RT_1 \quad (A.7)$$

$$= B_o^2 / 4\rho_1 \mu + \gamma RT_1$$

In combination with Eqn. A.6, the flow speed in the channel is found:

$$u_1 = (2 Q_a / m)^{1/2} \{1 + \gamma^2 \theta / (\gamma - 1)\}^{1/2} \quad (A.8)$$

where $\theta = RT_1/(Q_a/m)$ is typically much less than unity.

For supersonic expansion in the limit of high magnetic Reynolds number, the frozen-flux approximation implies that the magnetic field can be decreased to zero without resistive heating. The complete and total enthalpy of the flow (including the contributions of magnetic energy and chemical energy) is therefore conserved during the expansion. It is reasonable, however, to consider the flow at the low densities of the PPT to be chemically-frozen, so the kinetic energy per unit mass of the final exhaust is:

$$u_f^2 / 2 = u_1^2 / 2 + B_1^2 / \rho_1 \mu + 5 RT_1 / 2 \quad (A.9)$$

With substitutions and rearrangement, the exhaust speed is then:

$$u_f = (2 Q_a / m)^{1/2} \{3 + \theta [(4\gamma^2 + 5\gamma + 1)/2(\gamma - 1)]\}^{1/2} \quad (A.10)$$

For Teflon, the propellant plasma is a rather complicated mixture, so the exact value of the quantity in braces may vary with operating conditions. As a numerical example, suppose $Q_a = 61.5$ eV, m = 50 AMU, $T_1 = 2$ eV and $\gamma = 1.4$, then Alfven critical speed is:

$$v_A = (2 Q_a / m)^{1/2}$$

$$= 15.4 \text{ km/sec} \quad (A.11)$$

and the exhaust speed is higher by a factor of about two, (depending on the coupling of ions and electrons in the expanding flow). If the flow is properly expanded, the specific-impulse value would be over 3000 sec. This value is higher than typically obtained with ablation-fed thrusters, which may reflect differences in operating mode, (i.e., not quasi-steady and high magnetic Reynolds number). Also, substantial profile-loss may occur in present devices, which would reduce the directed exhaust velocity to values that are less than the ideal (albeit, chemically-frozen) result computed here.

PPT CAN HAVE TWO LIMITING MODES OF OPERATION AND MAY CHANGE MODES DURING THE CURRENT PULSE

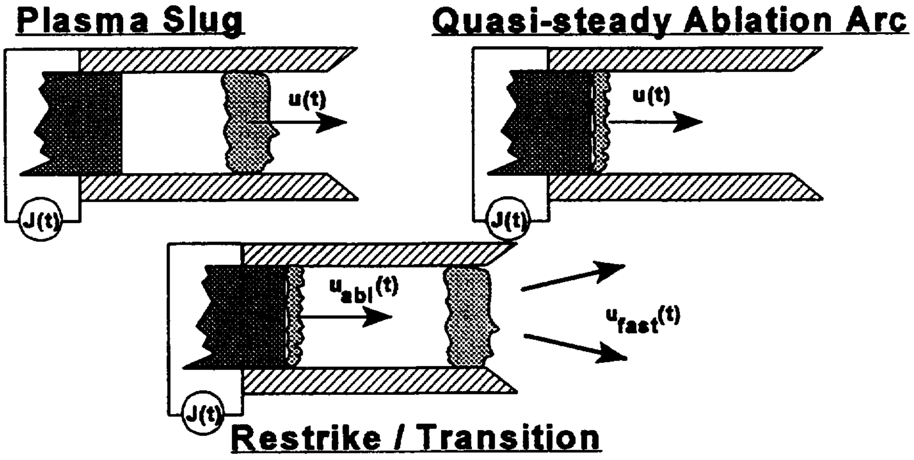

Efficiency and specific impulse will depend on operating mode and circuit interaction

Figure 1. Basic modes of operation of an ablation-fed plasma thruster.

MACH2 TEFLON PULSED PLASMA THRUSTER SIMULATION

PHYSICS

SINGLE TEMPERATURE
REAL EQUATIONS OF STATE

INITIAL CONDITIONS

TEMPERATURE, 1eV
DENSITY: (INITIAL MASS :0.1 μg)
ρ = CONSTANT; 0 ≤ y ≤ 0.6
ρ = LINEARLY DECREASING; 0.6 ≤ y ≤ 6

CIRCUIT

VOLTAGE = 1360 V
CAPACITANCE = 2 μF
INDUCTANCE = 34 nH
RESISTANCE = 30 mΩ

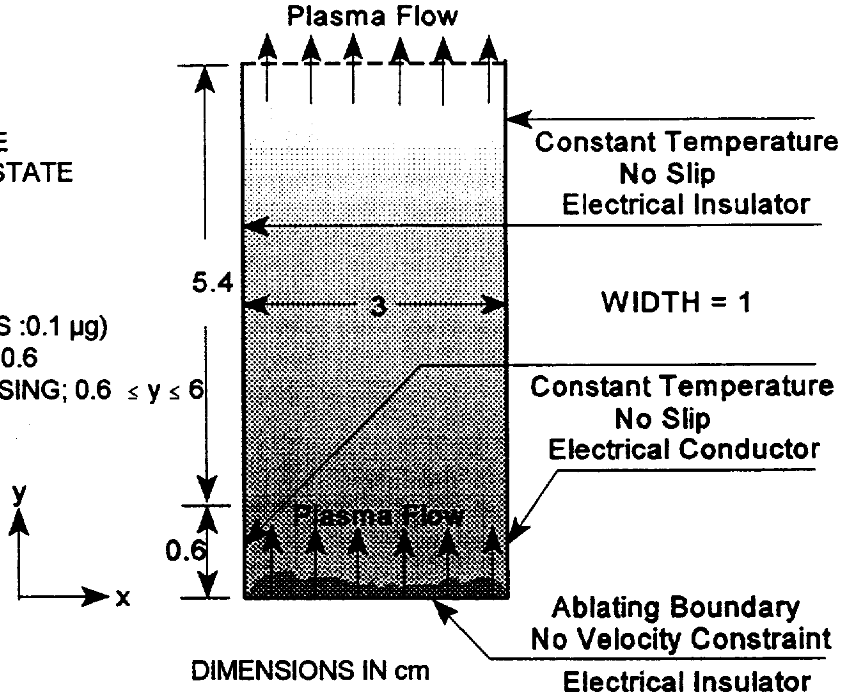

Figure 2. MACH2 parameters and geometry for the PPT simulation.

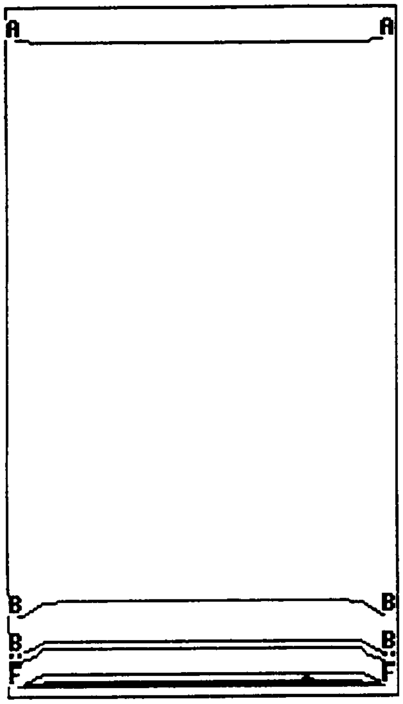

Figure 3. Mass Density distribution at 0.2 µsec. Max(+)=2.4, F=1.1, E=0.39, D=0.14, C=0.05, B=0.018, A=0.0065, Min(-) = 0.0023 (g/m^3).

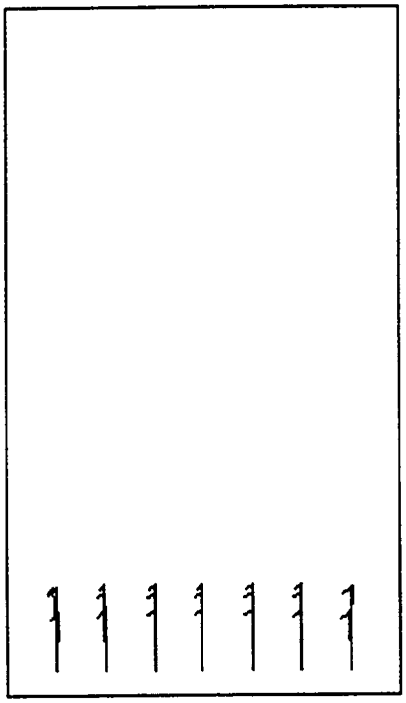

Figure 4. In-plane velocity vector distribution at 0.2 µsec. Maximum magnitude = 64.09 km/s.

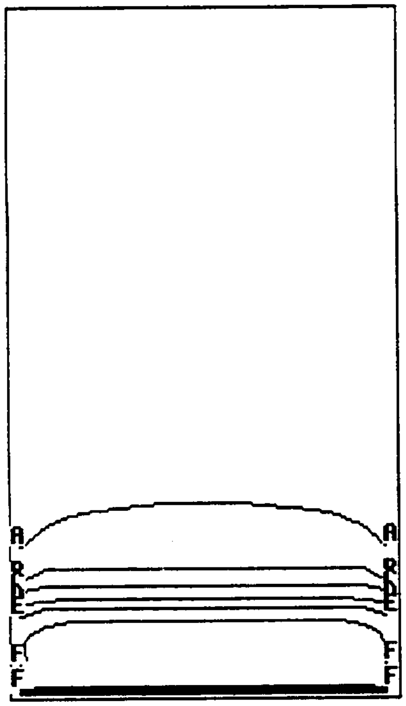

Figure 5. Temperature distribution at 0.2 µsec. Max(+)=14, F=9.2, E=6.0, D=3.9, C=2.6, B=1.7, A=1.1, Min(-)=0.73 (eV).

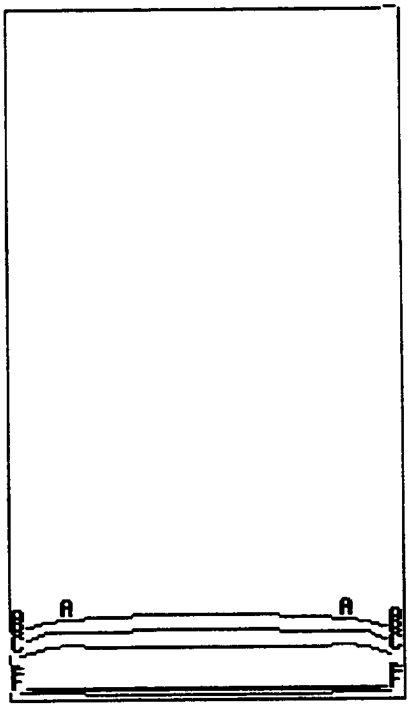

Figure 6. Current distribution at 0.2 µsec. Max(+)=4.3, F=3.3, E=2.6, D=2.0, C=1.5, B=1.2, A=0.93, Min(-)=0.72 (kA).

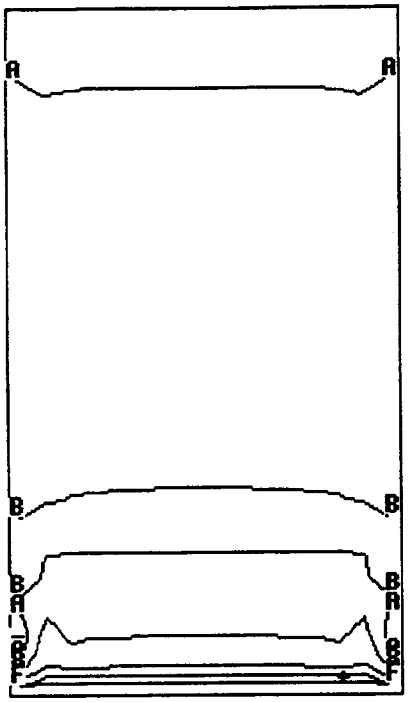

Figure 7. Mass Density distribution at 0.4 μsec. Max(+)=7.8, F=2.4, E=0.76, D=0.24, C=0.074, B=0.023, A=0.0072, Min(-) = 0.0022 (g/m^3).

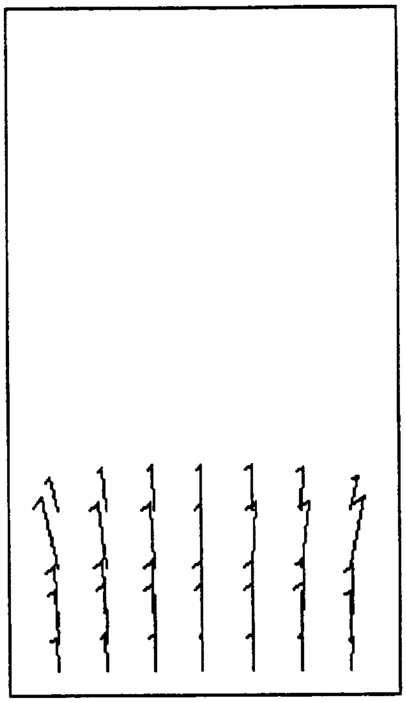

Figure 8. In-plane velocity vector distribution at 0.4 μsec. Maximum magnitude = 71.22 km/s.

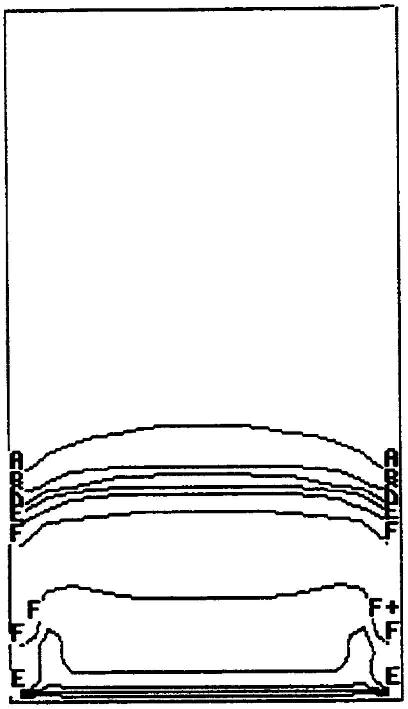

Figure 9. Temperature distribution at 0.4 μsec. Max(+)=14, F=9.2, E=6.0, D=3.9, C=2.6, B=1.7, A=1.1, Min(-)=0.73 (eV).

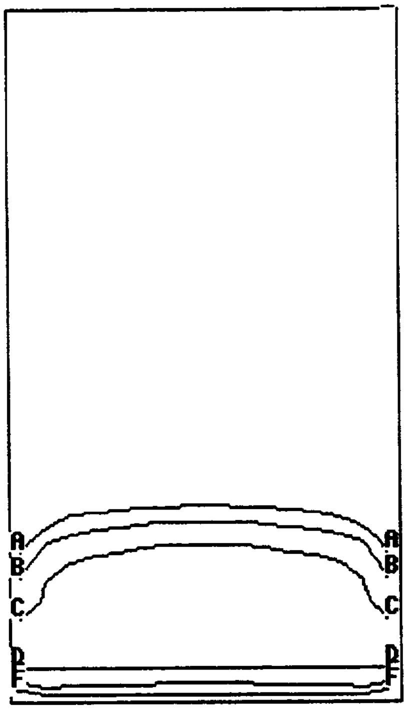

Figure 10. Current distribution at 0.4 μsec. Max(+)=4.9, F=3.8, E=3.0, D=2.3, C=1.8, B=1.4, A=1.1, Min(-)=0.85 (kA).

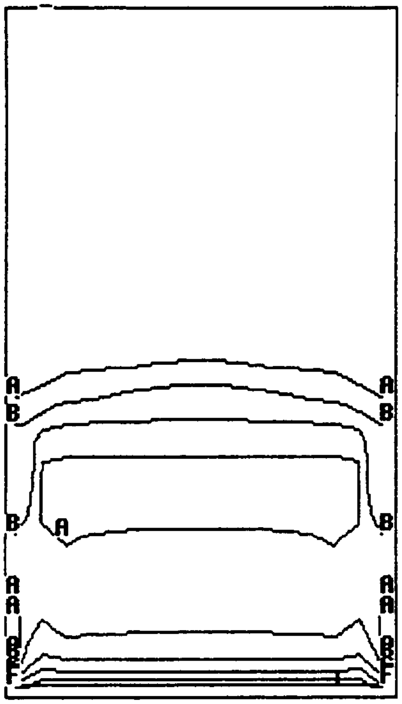

Figure 11. Mass Density distribution at 0.6 µsec. Max(+)=11, F=3.8, E=1.3, D=0.45, C=0.15, B=0.053, A=0.02, Min(-) = 0.0063 (g/m^3).

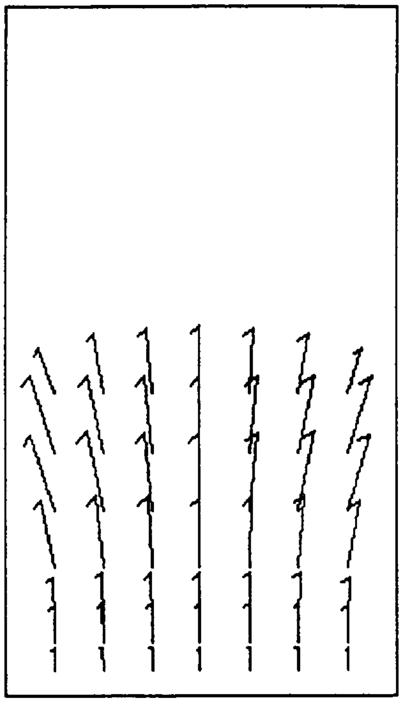

Figure 12. In-plane velocity vector distribution at 0.6 µsec. Maximum magnitude = 59.96 km/s.

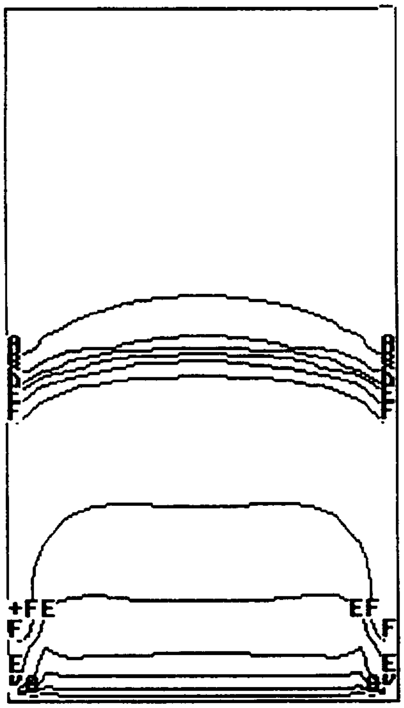

Figure 13. Temperature distribution at 0.6 µsec. Max(+)=12, F=8, E=5.3, D=3.6, C=2.4, B=1.6, A=1.1, Min(-)=0.71 (eV).

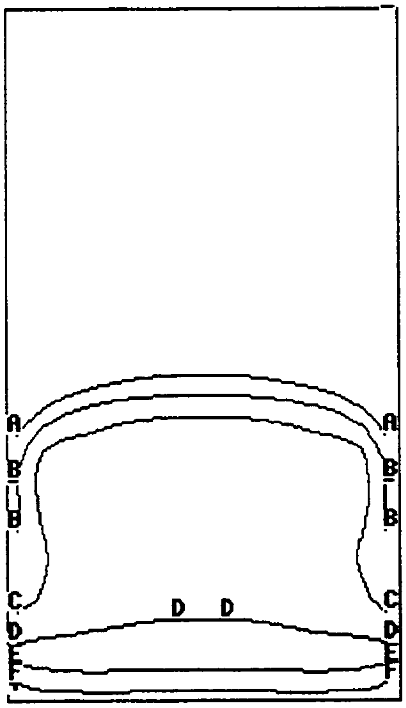

Figure 14. Current distribution at 0.6 µsec. Max(+)=3.6, F=2.8, E=2.2, D=1.7, C=1.3, B=1, A=0.77, Min(-)=0.6 (kA).

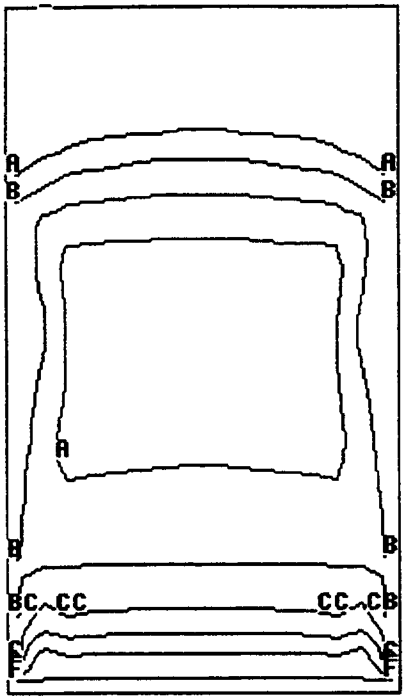

Figure 15. Mass Density distribution at 1 µsec. Max(+)=10, F=3.5, E=1.3, D=0.43, C=0.15, B=0.052, A=0.18, Min(-) = 0.0064 (g/m^3).

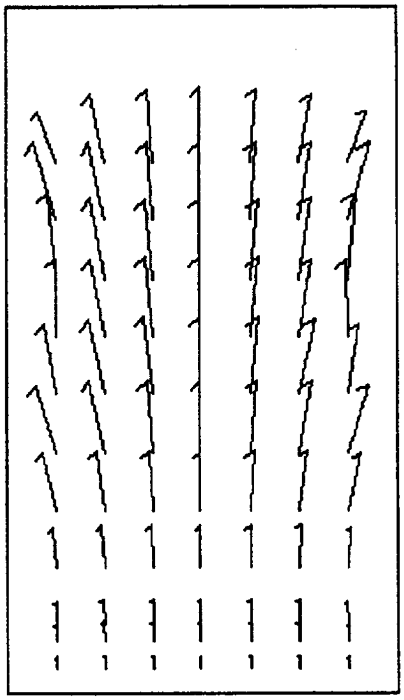

Figure 16. In-plane velocity vector distribution at 1 µsec. Maximum magnitude = 46.36 km/s.

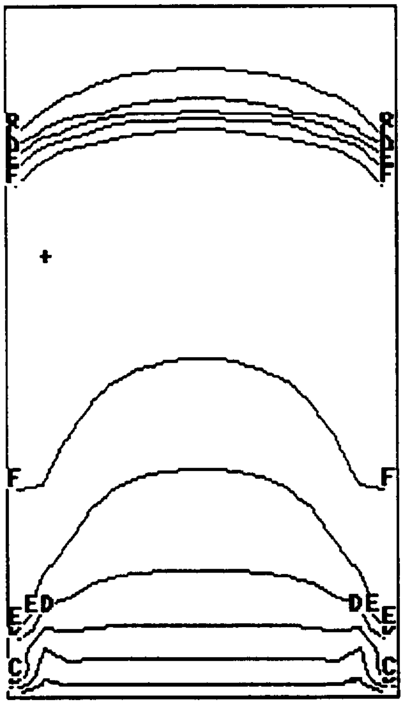

Figure 17. Temperature distribution at 1 µsec. Max(+)=9.1, F=5.8, E=3.8, D=2.4, C=1.5, B=1, A=0.64, Min(-)=0.41 (eV).

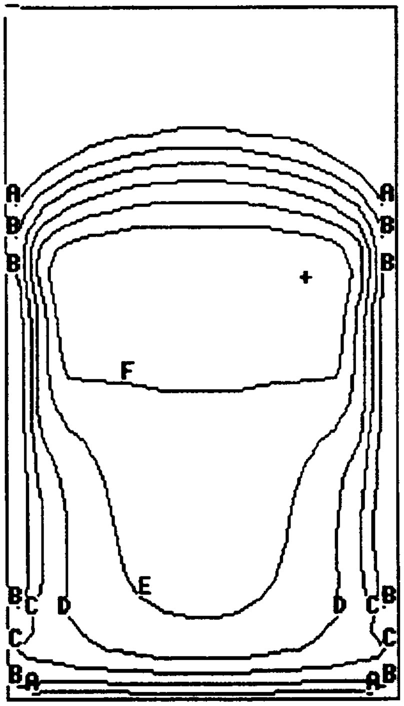

Figure 18. Current distribution at 1 µsec. Max(+)=1.1, F=0.85, E=0.66, D=0.51, C=0.4, B=0.31, A=0.24, Min(-)=0.19 (kA).

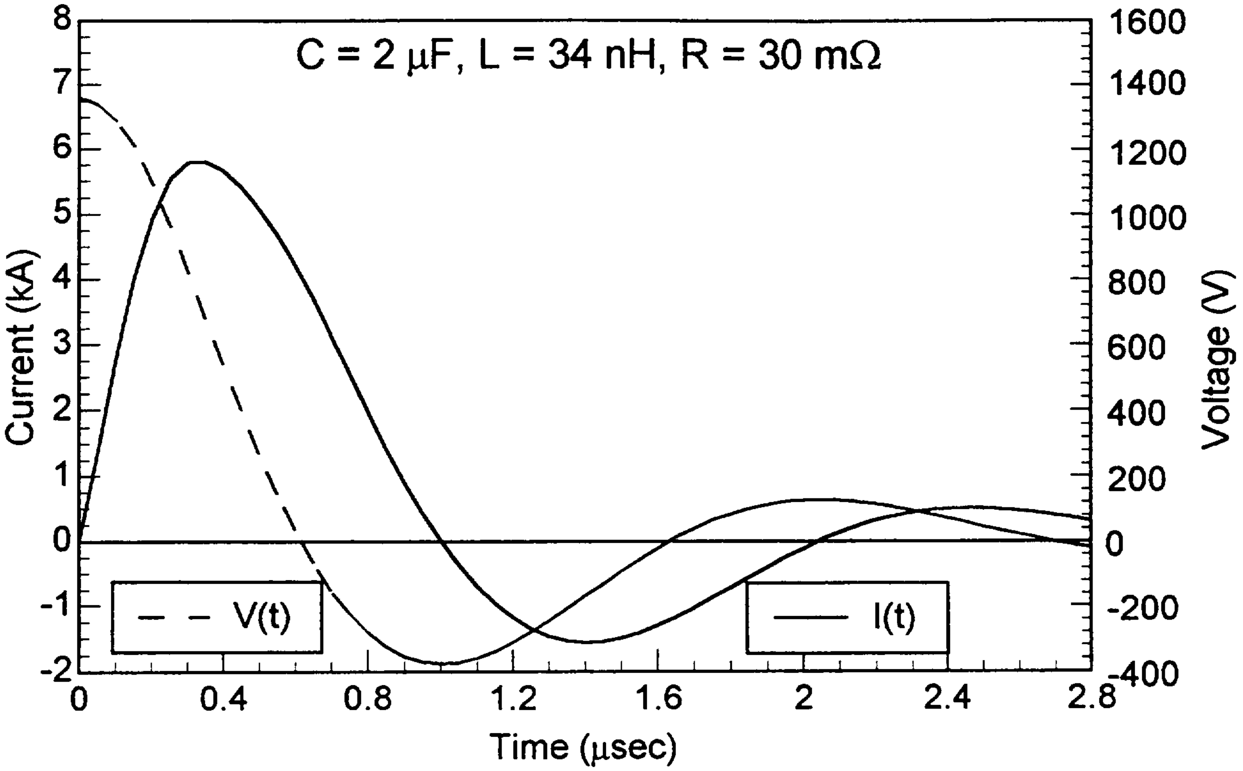

Figure 19. MACH2 calculated current, I(t), and capacitor voltage, V(t), waveforms.

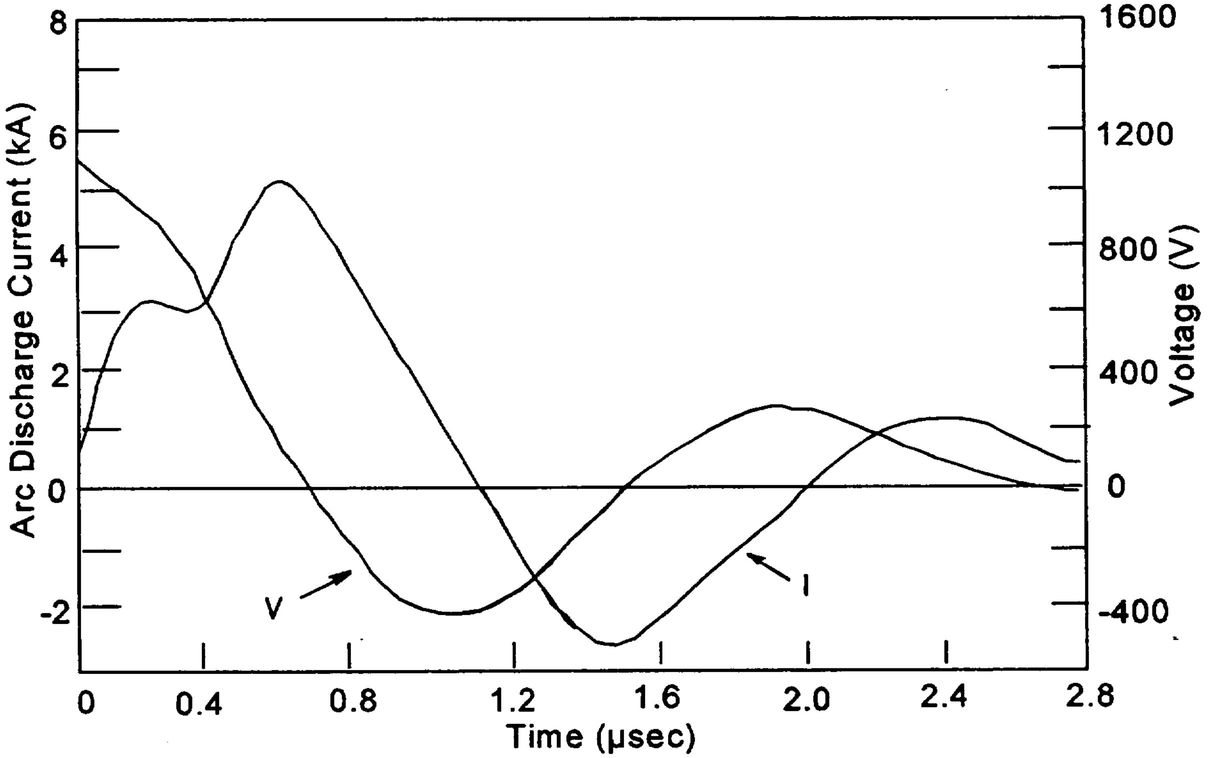

Figure 20. Experimental voltage waveform, V, and deduced current waveform, I.

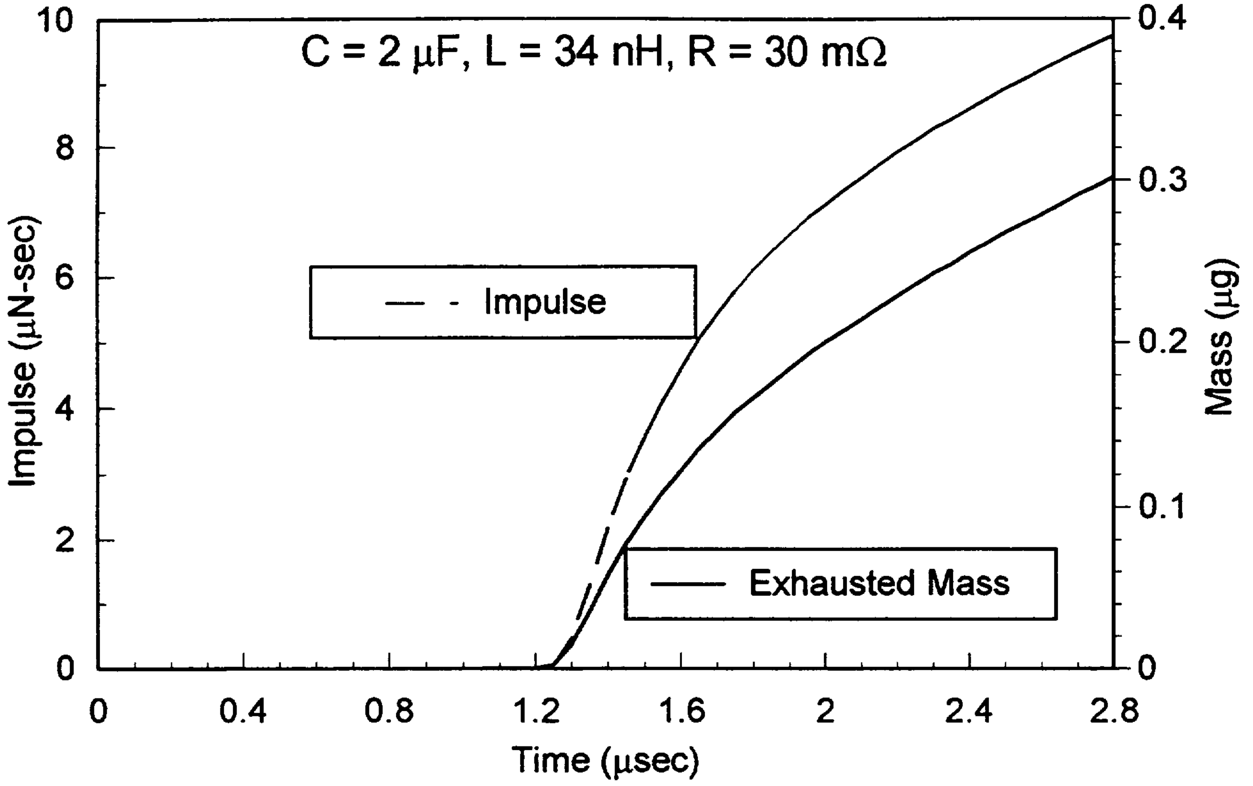

Figure 21. MACH2 calculated impulse and exhausted mass at the chamber's exit.

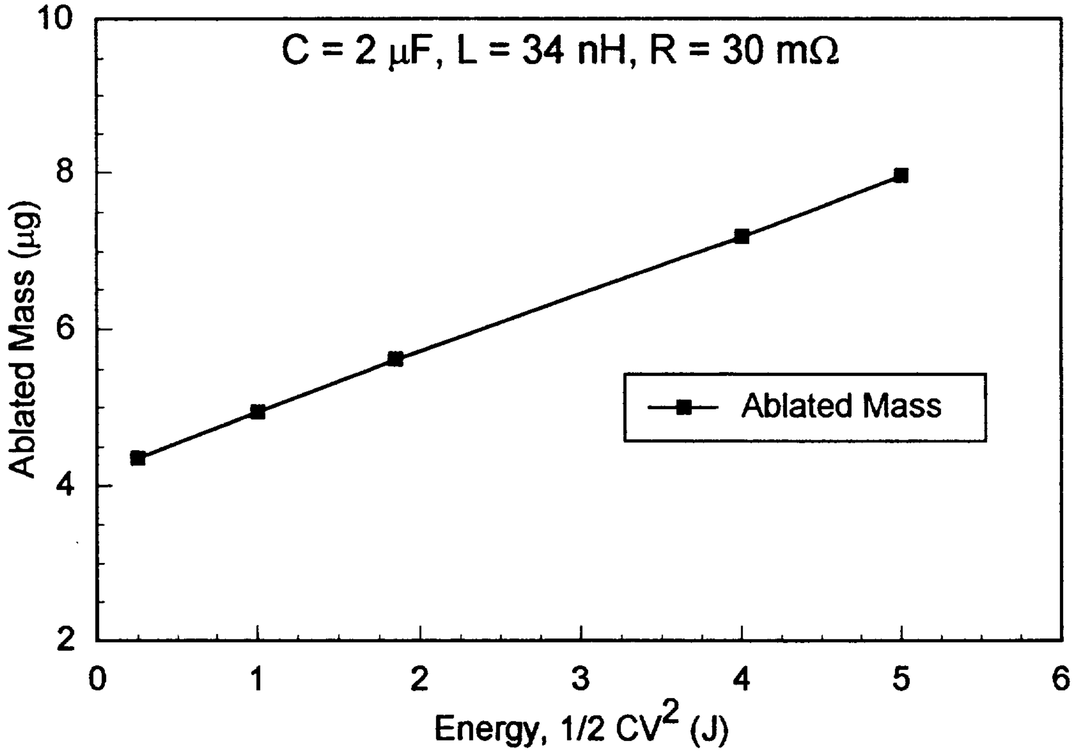

Figure 22. MACH2 calculated ablated mass (at the backplate and at 2.8 μsec) Vs capacitor energy. Closed points correspond to the actual simulation values.

AIAA 96-2733

MODELING OF LATE-TIME ABLATION IN TEFLON PULSED PLASMA THRUSTERS

P.G. Mikellides and P.J. Turchi
The Ohio State University
Columbus, OH

32nd AIAA/ASME/SAE/ASEE
Joint Propulsion Conference and Exhibit
July 1-3, 1996/Lake Buena Vista, FL

MODELING OF LATE-TIME ABLATION IN TEFLON PULSED PLASMA THRUSTERS

P.G. Mikellides and P.J. Turchi
The Ohio State University
Columbus, OH

ABSTRACT

The MACH2 code has been modified to include non-monotonic heat flux to ablating surfaces in order to study late-time mass evolution in the pulsed plasma microthruster (PPT). Comparisons of predicted mass ablated and impulse bit with experimental data offer several insights into the operation of the PPT. Only a small fraction of the total ablated mass is produced during the current pulse and has the opportunity to be ionized and magnetically accelerated to high exhaust speeds. The rest gradually evaporates during much later times as a neutral gas that expands at relatively low speeds. Reduction of this low speed mass evolution would significantly improve the specific impulse and efficiency of the thruster.

INTRODUCTION

The ablation-fed pulsed plasma microthruster (PPT) has been studied empirically for over thirty years. These efforts, in conjunction with attention to engineering development, have led to successful application of PPTs on satellite station-keeping missions. Renewed interest for small satellite needs has prompted further investigation of PPT behavior in order to achieve improved performance and better insight for scaling operation to lower powers and higher exhaust speeds.

The conventional pulsed plasma thruster utilizes an arc discharge across a Teflon surface within a generally simple geometric configuration. Its system simplicity, robustness, and ability to provide small impulse bits and high specific impulse make it an attractive device for the aforementioned missions. During an intense period of experimental investigation and development in the 1960's and 70's however, the PPT had failed to operate consistently at adequate efficiencies. Although some isolated laboratory devices have displayed efficiencies of up to 50%[1,2], the PPT generally operates in the range of 2% to 12%.

One of the primary reasons for the failure to improve efficiency is the lack of complete understanding of the PPT behavior. The lack of appropriate theoretical tools has limited studies to purely empirical insights that are in turn limited by the specific geometries and operating conditions. The luxury of detailed interrogation of pertinent parameters has not here to fore been available.

This paper presents the most recent results of modeling the PPT using full numerical simulations. An appropriate Teflon ablation model has been developed and incorporated into the 2-dimensional, time-dependent MHD code, MACH2.[3] This model now includes non-monotonic (time-varying) heat flux to the solid surface. The simulations presented are compared with experimental data and offer a source of additional insights that have not been available from the previous empirical studies.

THEORETICAL MODELING

The MACH2 code, developed by the Mission Research Corporation, along with a new solid ablation model, developed at The Ohio State University, is utilized to model the physical processes within ablation-fed Teflon pulsed plasma thruster (PPT).

MACH2 solves the time-dependent magnetohydrodynamic (MHD) equations in two dimensions. It is a single fluid, multi-temperature, time-split model that includes several radiation models, real equations of state, (SESAME tables developed and supported by the T-1 Division at Los Alamos National Laboratory), Hall effect, real viscosity effects, several models for anomalous transport, and a multi-ported circuit solver. It provides the capability of plane parallel or cylindrically symmetric simulations within complex geometries, along with an Arbitrary-Lagrangian-Eulerian adaptive mesh. The numerical methods utilized by MACH2 are also state of the art, with a combination of implicit and explicit differencing, and multigrid diffusion schemes for optimization of computational times. It has been applied to a diverse range of plasma problems with great success.

The fundamental notion utilized for the development of the ablation model is that vapor is created at the equilibrium vapor pressure based on the temperature of the solid surface. This temperature is calculated by accounting for the net heat flux to the surface due to energy transfer from the local plasma (conduction, condensation) versus evaporation of the surface. The net heat flux serves as a boundary condition for a 2-dimensional diffusion equation within a semi-infinite solid. This diffusion solver utilizes a second-order accurate numerical scheme in both space and time with the option of an adaptive grid for better gradient resolution at the ablating surface. The solid surface temperature and thus the vapor temperature, is used to calculate the vapor pressure based on an appropriate Teflon vapor pressure curve.[4] This in turn implies a vapor density under the ideal gas assumption. The vapor temperature and density are sufficient boundary conditions for the 2-dimensional evolution of the plasma calculated by MACH2.

MACH2 computes the velocity at the ablating boundary, as a consequence of the pressure gradient, which in turn defines a mass flow rate that can be integrated over time to provide a value of the ablated mass. Integration of the total pressure at the downstream exhausting boundary provides thrust values which are also time-integrated to yield the impulse bit.

LES-6 SIMULATIONS

During the late 1960's, a research program was initiated at the Lincoln Laboratory for the further development of thrusters for the LES series of satellites. The effort consisted of a number of experiments that provided a substantial amount of empirical data. One particular configuration, the LES-6[5] thruster is chosen for these simulations.

The rectangular, parallel rail geometry of the LES-6 thruster consisted of two 6 mm long, 1 cm wide electrodes, that are 3 cm apart. The MACH2 modeling included these electrodes and the extended 5.4 cm long insulating section, as shown in Figure 1. The LRC circuit used a 2 μF capacitor, with the initial voltage varying from 1100 to 2000 V. The external resistance (including that of the capacitor) and inductance were 30 mΩ and 34 nH, respectively.

The plasma was modeled as a single temperature inviscid fluid with real equations of state for Teflon and classical (Spitzer-Härm) transport coefficients. The electrodes and the extended electrical insulator surfaces were modeled as adiabatic walls with a freeslip hydrodynamic boundary condition. The downstream boundary employs a boundary condition that forces the gradients of the main variables to zero and thus allowing the flow to exhaust in a non-reflective manner. Plasma initial conditions assume the existence of a small fraction of mass produced during the ignition of the spark plug. The Teflon solid has an initial temperature profile that assumes some thermal penetration due to the initial spark discharge. The temperature of this thin thermal layer was in accordance with pressure equilibrium between the plasma and the surface vapor. The rest of the solid had a uniform initial profile at room temperature (300K). The side boundaries utilized adiabatic conditions while the back end was held at room temperature.

The characteristic diffusion length, $d = (\alpha t)^{1/2}$, where α is the thermal diffusivity of the solid and t is the time, for times on the order of msec is approximately 0.025 mm. Thus, to assure proper capture of the temperature profile the depth of the solid was defined at three times the diffusion length.

Three different cases were modeled representing three different initial capacitor energy values, 1.21J (1100V), 1.85J (1360V), and 4J (2000V). Experimental current and voltage waveforms were available for the 1360V case, so comparisons are made with the theoretical waveforms in Figures 2 and 3. They show that theory does reasonably well in capturing the experimentally-deduced waveforms. The following series of figures, 4-15, depict the evolution of the main variables in a two-dimensional format at different times during the current pulse. They illustrate the introduction of mass from the ablating surface. This mass is then accelerated downstream via electromagnetic forces. They also illustrate the MACH2 capability to interrogate the history and profiles of variables such as current and mass densities, and temperature, with relative ease, something that is quite difficult and limited via experimental procedures.

Figures 16 and 17 depict, for the 1360 V case, the evolution of the ablated mass, calculated at the ablating boundary, and the impulse bit, calculated at the downstream boundary. Although these simulations were carried out well beyond the end of the current pulse (1-2 msec), only relatively early periods are depicted in this figures to favor illustration of certain features. The ablated mass history reveals that most of the mass is ablated during the first current rise (<0.4 μsec) with much less contributions from the subsequent peaks. It also illustrates a period of condensation that takes place after the end of the current pulse (~3 μsec) quickly asymptoting to a value of about 1 μg. A simple monotonic increase describes the history of the impulse bit which reaches a value of about 30 μN-sec.

The most profound insight however, is apparent in the following two graphs (Figures 18 and 19) where the theoretical calculations of ablated mass and impulse bit are compared with experiment as a function of total initial capacitor energy. Although the impulse bit results are in excellent agreement with experiment, capturing the apparent linear increase of impulse bit with energy, the predicted ablated mass during the current pulse grossly underestimates the total ablated mass. This implies that the majority of the ablated mass occurs during the time between thruster firings which is typically 1/2 sec. Such late-time mass does not have the opportunity to be electromagnetically accelerated downstream and thus does not substantially contribute to the impulse bit. Obviously, the above conclusion has substantial implications as far as the performance of the thruster is concerned and thus requires confirmation. A further investigation of the late behavior of the thruster is warranted.

Initially, the simulation for the 1360 V case was continued well beyond 1 msec. The Teflon solid returns to its base temperature (for the particular case 300K) implying that the total heat remaining in the solid is conducted away to the colder end on times that are short compared to pulse interval times (1/2 sec). The ablating surface reaches a steady state at a very low, but constant mass flow rate. These observations raise further inquiry into the effects of the temperature to which the solid Teflon slab subsides and the consequent constant ablation rate. Additional simulations were performed varying the initial, base temperature of the Teflon. In all three cases, the solid returned to this base temperature and reached a steady-state ablation rate. They are presented in Table I (for the 1360 V case) :

Table I

Base Teflon Temperature (K)	Mass flow rate (μg/s)
500	0.546
520	19.13
662	1.66×10^5

It is apparent that for a half-second pulse interval, a base temperature of 520 K results in approximately 9.5 μg of additional ablated mass which would account for the remaining mass that was experimentally measured.

Specific impulse could substantially improve if this late ablation which does not contribute effectively to the total impulse bit can be diminished or totally prevented. The efficiency will also dramatically improve. These effects can be more clearly seen if we express the above quantities by distinguishing between pulsed and late time ablated mass contributions.

$$I_{sp} = I / m_{tot} g = [\, I / mg \,] \times [\, 1 / (1+M) \,] \quad (1)$$

$$\eta = I^2 / 2 m_{tot} E = [\, I^2 / 2mE \,] \times [\, 1/(1+M) \,] \quad (2)$$

where M is the ratio of ablated mass during between shots to that ablated during the discharge pulse. For the particular case of 1360 V (E = 1.85J) this ratio is 9 which implies an order of magnitude improvement in both average specific impulse and efficiency (from 3% to 30%).

The MACH2 simulations have shown that the heat deposited during the current pulse is not substantial. For the particular case of 1360 V, this value was approximately 0.02J. The average heating from the plasma does not contribute at a rate that determines the elevated Teflon base temperature to explain late ablation.

It may thus be deduced that surrounding sources of heating, such as warm electrodes, are the cause of this higher temperature. This indeed is very plausible because elevated electrode temperatures, which increased with time, have been experimentally observed.[6] Relatively simple avenues for diminishing late ablation, such as minimizing heat transfer from surrounding sources, may thus be available.

CONCLUSIONS

Theoretical modeling of the LES-6 pulsed plasma thruster has been performed by utilizing the MHD computer code, MACH2, with an appropriate 2-dimensional solid diffusion model that provides the mass ablated rate at the plasma exposed Teflon surface. The simulations were carried well beyond pulse time. Comparisons of ablated mass and impulse bit generated during the pulse time with experimental data have shown that MACH2 largely underestimates the former, but is in excellent agreement with the latter. Late-time simulations have offered an explanation for this contradiction. The Teflon solid may overheat to a uniform constant base temperature for which surface ablation occurs at a constant rate. The value of the mass flow rate strongly depends on the base temperature, and can readily account for the major portion of the total experimentally-observed mass loss per shot. This late-time mass is exhausted at very low speeds, and does not contribute significantly to the total impulse bit.

It has also been suggested here that the elevated base Teflon temperatures are not a consequence of the heat pulse from the plasma. Instead, surrounding heating sources, such as warm electrodes, could be causing the Teflon to operate at elevated (albeit moderate) temperatures. Designs that reduce heat transfer from the surroundings to the Teflon (while still allowing propellant-slab advancement into the thrust chamber) could expect substantially improved performance.

REFERENCES

1. Guman, W. and Palumbo, D.J., "Effects of Propellant and Electrode Geometry on Pulsed Ablative Plasma Thruster Performance," AIAA 75-409, 11th Electric Propulsion Conference, New Orleans, LA,1975.

2. Myers, R.M., "Electromagnetic Propulsion for Spacecraft," AIAA 93-1086, Aerospace Design Conference, Irvine, CA, 1993.

3. Peterkin, R.E. Jr., Giancola, A.J., Frese, M.H. and Buff, J., "MACH2: A Reference Manual-Fourth Edition," Mission Research Corporation, 1989.

4. Wentink, T., Jr., "High Temperature Behavior of Teflon," AVCO-EVERETT Research Laboratory, Contarct No. AF 04(647)-278, July 1959.

5. Vondra, R.J., Thomassen, K. and Solbes, A., "Analysis of Solid Teflon Pulsed Plasma Thruster", *Journal of Spacecraft and Rockets,* Vol. 7, No 12, Dec. 1970, pp. 1402-1406.

6. Leiweke, R.J., "Multi-Material Fuel for Ablation-fed Pulsed Plasma Thrusters," Report, The Ohio State University and NASA Lewis Research Center, Electric Propulsion Laboratory, June 1995.

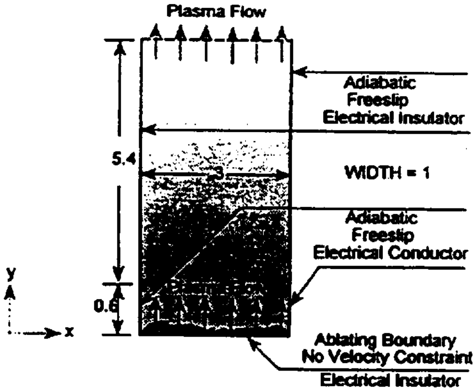

Figure 1. The MACH2 modeling of the LES-6 geometry. Dimensions in cm.

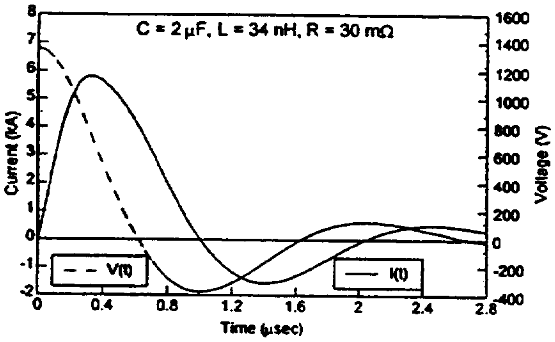

Figure 2. Theoretical Current and Voltage waveforms for the 1360V case.

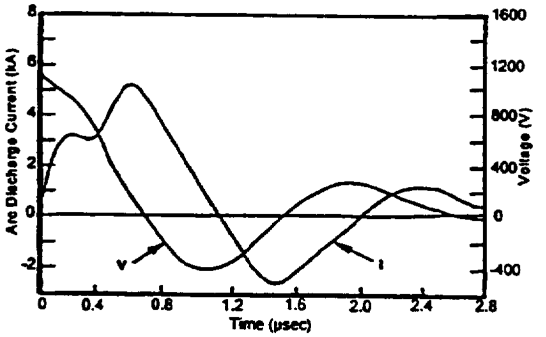

Figure 3. Experimental Current and Voltage waveforms for the 1360V case.

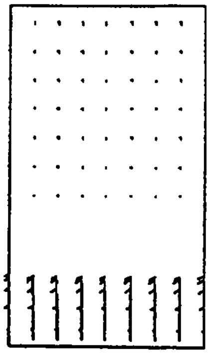

Figure 4. Vector Velocity distribution at 0.2 μsec. Maximum = 42.7 km/s.

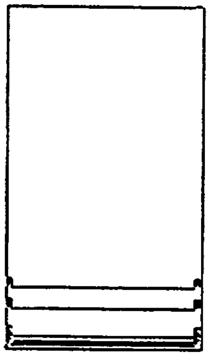

Figure 5. Mass Density distribution at 0.2 μsec. B=2.4e-5, E=4.4e-5, Max(+)=3.1e-3 kg/m^3.

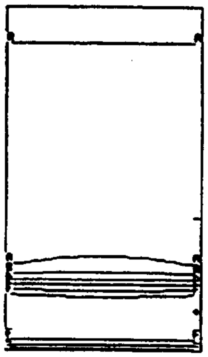

Figure 6. Temperature distribution at 0.2 μsec. B=1.5, E=3.9, Max(+)=7.5 eV.

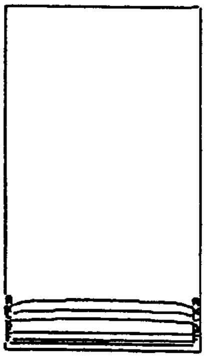

Figure 7. Enclosed Current contour distribution for 0.2 μsec. B=1.2, E=3, Max(+)=4.2 kA.

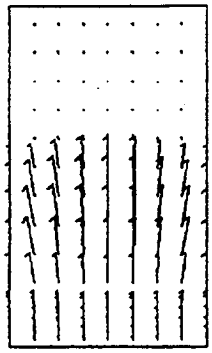

Figure 8. Vector Velocity distribution at 0.6 μsec. Maximum = 56.19 km/s.

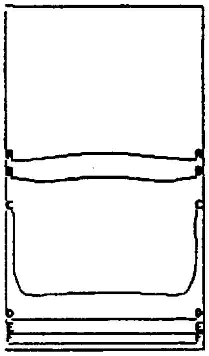

Figure 9. Mass Density distribution at 0.6 μsec. B=2.6e-5, E=5.5e-4, Max(+)=4.2e-3 kg/m^3.

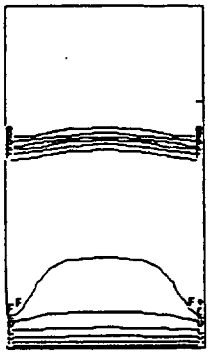

Figure 10. Temperature distribution at 0.6 μsec. B=1.8, E=4.2, Max(+)=7.5 eV.

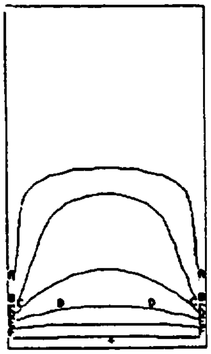

Figure 11. Enclosed Current contour distribution at 0.6 μsec. B=1.2, E=2.9, Max(+)=4 kA.

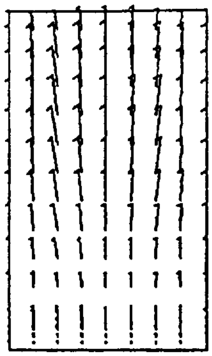

Figure 12. Vector Velocity distribution at 1 μsec. Maximum = 54.11 km/s.

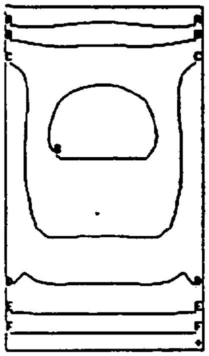

Figure 13. Mass Density distribution at 1 μsec. B=2.2e-5, E=2.8e-4, Max(+)=1.5e-3 kg/m^3.

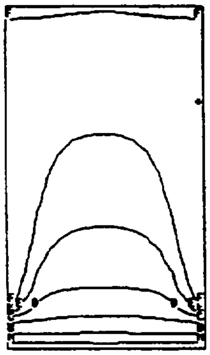

Figure 14. Temperature distribution at 1 μsec. B=1.5, E=3.9, Max(+)=7.5 eV.

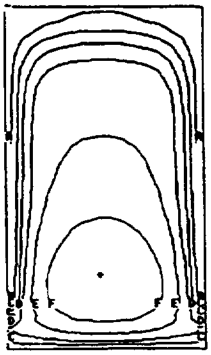

Figure 15. Enclosed Current contour distribution at 1 μsec. B=0.31, E=0.75, Max(+)=1 kA.

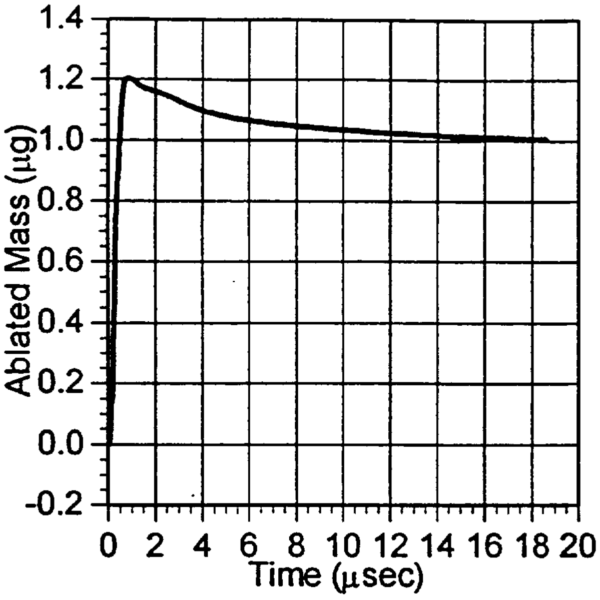

Figure 16. MACH2 predicted ablated mass due to the current pulse (~3 μsec) for the 1360V case.

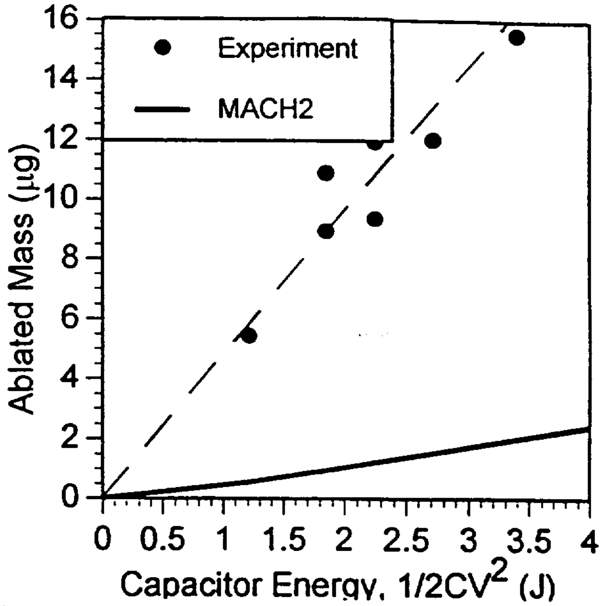

Figure 18. Experimental total ablated mass comparisons with MACH2 predicted ablated mass due to the current pulse Vs total initial capacitor energy.

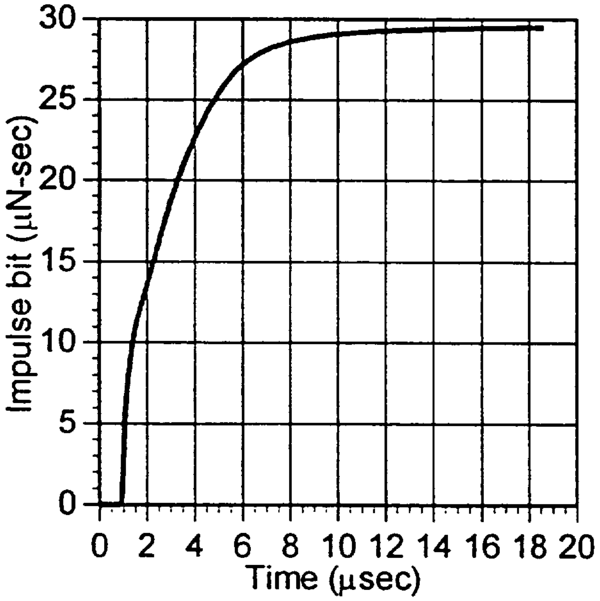

Figure 17. MACH2 predicted Impulse bit as computed at the thruster's exit for the 1360V case.

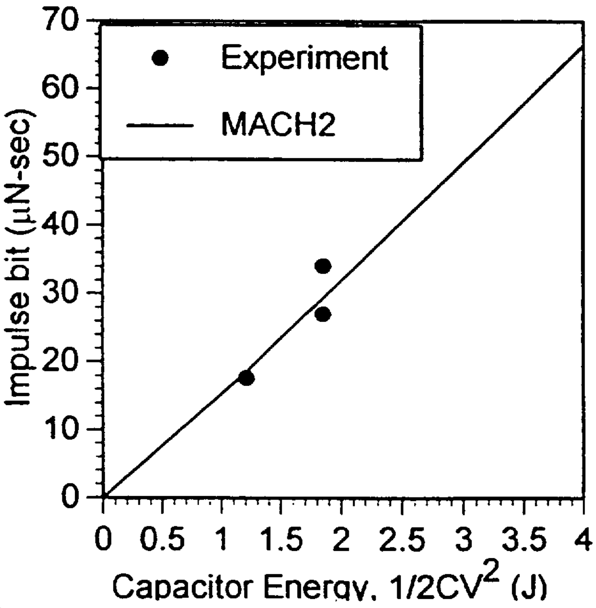

Figure 19. Comparisons of MACH2 predicted Impulse bit with experiment as a function of total initial capacitor energy.

AIAA 95-2916

EXPERIMENTS WITH MULTI-MATERIAL PROPELLANTS IN ABLATION-FED PULSED PLASMA THRUSTERS

R.J. Leiweke, P.J. Turchi, H. Kamhawi
The Ohio State University
Columbus, OH

R.M. Myers
NASA Lewis Research Center/NYMA
Cleveland, OH

31st AIAA/ASME/SAE/ASEE
Joint Propulsion Conference and Exhibit
July 10-12, 1995/San Diego, CA

EXPERIMENTS WITH MULTI-MATERIAL PROPELLANTS IN ABLATION-FED PULSED PLASMA THRUSTERS

R.J. Leiweke, P.J. Turchi, H. Kamhawi, The Ohio State University, Columbus OH, and R.M. Myers, NASA Lewis Research Center/NYMA, Cleveland, OH

ABSTRACT

The pulsed plasma microthruster (PPT), which has been successfully employed for spacecraft control for over two decades, has traditionally used ablation of a solid, oblong block of Teflon as its propellant source. Recent interest in achieving higher performance from such thrusters has led to re-examination of options for propellant materials, arrangements and operating conditions. In particular, the relatively high atomic mass of fluorine in the Teflon propellant has directed attention to other plastics that would have lower effective molecular weights, due to higher hydrogen and lower fluorine , oxygen, and nitrogen content. To explore the potential benefits of hydrogenic plastics, without incurring the loss of voltage hold-off strength on the exposed surface due to carbon build-up, a new arrangement is employed in which alternating layers of the candidate plastic and Teflon are substituted for the uniform Teflon propellant block. For simplicity of initial testing, a portion of the Teflon propellant block from the LES8/9 version PPT was modified to carry the multi-material, laminated propellant block. Tests involving tens of thousands of discharges were made with polyethylene and Teflon layers, sixteenth- and eighth-inch thick, in various combinations, typically comprising seven layers between the sides of the Teflon supporting block. While the exposed polyethylene surfaces blackened, partially melted and became conducting, voltage hold-off was maintained. Thrust measurements indicate comparable specific impulse, but lower thrust efficiency for polyethylene-Teflon propellant compared to pure Teflon.

INTRODUCTION

Thrust efficiencies of most pulsed plasma microthrusters (PPT) have been low, ranging from 1.5% to 12%, although a few laboratory devices have shown values up to 52%.[1,2,3,4] PPT's have gained interest for satellite station keeping and drag makeup because of their inherent simplicity. One way that the efficiency might be improved is through the use of alternative propellants. Almost all PPT's to date have used solid Teflon (polytetrafluoroethylene, or PTFE) as the propellant because it does not exhibit carbon buildup on itself or the surrounding structure.[5] Such carbon buildup can result in electrical short-circuits, preventing proper operation.

To increase specific impulse, Teflon is not the ideal polymer because of its high molecular weight. By exploring various mixtures, one may take advantage of the improved specific-impulse properties of an alternative polymer while still retaining the voltage hold-off of Teflon in repetitive operation. High density polyethylene (HDPE) is one possible polymer to be used in conjunction with Teflon because of its high atomic fraction of hydrogen. HDPE used on a PPT can double the specific impulse[6], but exhibits carbonization of the fuel, electrodes, and exhaust channel.

The present report describes preliminary results from experiments in which alternating layers of Teflon and high density polyethylene (HDPE) were used to provide a lower average-molecular weight propellant in an existing PPT. The layers are arranged parallel to the equipotential surfaces, so the voltage holdoff of the assembly may be adequate even with some carbonization of the polyethylene surfaces.

EXPERIMENTAL FACILITIES

Multi-material experiments were performed at the NASA Lewis Research Center Electric Propulsion Laboratory, Cleveland, Ohio. The vacuum facility consists of a stainless steel bell-jar (Bell Jar #4) with an inside diameter of 51 cm and height of about 71 cm. An instrument rack containing the power supply and vacuum controls was located about 1.8 m from the bell-jar.

The flight-certified LES 8/9 PPT, constructed in the early 1970's at M.I.T. Lincoln Laboratories, was used as a testbed for new propellant arrangements. This PPT has a thrust efficiency of about 9%, a specific impulse of 1000s, and impulse bit of 300 μN-s (67 μlb-s).[4] The LES 8/9 has a single 17 μF oil-filled capacitor that is charged to 1,538 Volts, corresponding to a discharge of about 20J/shot.[4] The particular unit used in this study was LES 8/9 PPT#4. The LES 8/9 PPT requires a nominal 28 VDC input.[4] Previous experiments to determine the operational status have shown a requirement of a 100W power supply, since the current drawn was estimated to be about 3 A. A Sorensen power supply, model SRL 40-6, was used for all experiments. The PPT was mounted and placed in the bell-jar such that the exhaust channel was oriented upwards. Also, the PPT was positioned such that the face of the multi-material propellant was observable through the bell-jar quartz window. Bell-jar pressure was measured with an ion gauge.

MULTI-MATERIAL FUEL

The LES 8/9[4] fuel feed configuration consists of two 2.7 cm x 2.2 cm x 68.0 cm long bars of Teflon pushed toward the retaining shoulder by a negator spring, as sketched in Figure 1. For the purpose of attitude control, its two exhaust channels are inclined 30° to either side of the thruster axis, again shown in Figure 1. The fuel bars slide parallel to the axis, but the faces are cut at a 60° angle. The exposed length of surface parallel to the current path is therefore 2.56 cm (2.22 cm ÷ cos30°).

In order to test combinations of polymers with Teflon, a four inch length of the original Teflon fuel bar was cut off and made into a fuel "fork", as shown in Figure 2. The fuel fork holds alternating layers of HDPE and Teflon sheets, cut to fit within the gap so that the "laminate" edges and the fork ends become the fuel face. Figure 3 gives an example of the laminates before testing. The laminates were arranged such that no two pieces of like material were touching. This requires an odd number of sheets. The fork itself provides final layers of Teflon in order to maintain the vacuum-plastic-metal, triple-point condition at the thruster electrodes. The combined slant distance of the two fork ends is 1.47 cm (2 x 0.635 cm ÷ cos30°). The polyethylene used in all experiments is Resinol Type F (HDPE) purchased from Allied Resinous Products.

Two multi-material propellant configurations involving Teflon and high density polyethylene (HDPE) were prepared for testing: Case 1 and Case 2. For both cases, two test runs were performed. Case 1a and 1b used three 1/8" thick laminates (one Teflon, two HDPE) and Case 2a and 2b used seven 1/16" thick laminates (three Teflon, four HDPE). Three 1/8" and seven 1/16" laminates require that the fuel fork have an opening of 3/8" (9.525 mm) and 7/16" (11.112 mm), respectively. Thus, for the Case 2 laminates, 1/32" (0.79 mm) was filed off the inside of each fuel fork arm to provide proper clearance. However, Case 1b was performed after the Case 2 tests, thus requiring the use of a 1/16" Teflon laminate to fill the gap in the modified fuel fork. This laminate was positioned between one Teflon fuel fork arm and the laminate nearest the anode. The total areas of Teflon and HDPE for both cases 2a and 2b are equal.

During fuel preparation the lengths were cut so that the laminate edges protruded about 2 mm out from the fuel fork face. A coarse-grit belt sander was then used to make the fuel face flush at a 60° angle (see Figure 3). The laminates were then hand sanded with 180 grit sandpaper. After sanding, all of the laminates and the fuel fork were washed with a non-abrasive hand-soap and water, towel dried, and allowed to air dry for about 30 minutes. After this, the pieces were reassembled back into the fuel fork. The fuel fork was then loaded back into the LES 8/9 feed mechanism.

EXPERIMENTAL TESTS

Case 1a: N=3, (19,267) shots

After about 1,488 shots, both of the HDPE laminate fuel faces had become slightly discolored, indicating that some charring was beginning to occur. The middle Teflon laminate was free of discoloration. When the multi-material fuel had experienced 4,013 discharges, there was increased carbon coverage on the HDPE laminate faces, but almost none on the middle Teflon laminate. Some charring was also occurring on the corners of the Teflon fuel fork. When intermittency problems began to occur, the PPT was fired continuously at a 1 Hz repetition rate for 8,040 pulses on the multi-material fuel and 6,360 pulses on the pure Teflon fuel. Experiments were then conducted in 2 Hz auto-mode with both fuels for 6,600 more shots. The total number of discharges with the pure Teflon fuel and the multi-material fuel were 7,885 and 19,267, respectively.

After the 19,267 discharges, the Teflon laminate in the center was devoid of charring (see Figure 4). Significant amount of charring occurred on the two polyethylene laminates surrounding the Teflon. The top HDPE laminate, which is nearest to the cathode containing two spark plugs, exhibited a pair of regions free of charring. Measurements of the LES 8/9 geometry indicates that the spark plug separation distance is 1.73 cm. It is interesting to note that the centers of the two char-free regions are separated by this distance. The bottom HDPE laminate has a small oval area devoid of charring. The entire face of the fuel fork and laminates is slightly cupped, indicating the discharge is ablating more material near the middle than at the outer edges. This cupping is also observed with the pure Teflon fuel.

Case 1b: N=3, (13,288) shots

This test used three 1/8" laminates and one 1/16" Teflon laminate to fill the 7/16" modified fuel fork gap. This case was run in 2 Hz auto-mode for 13,288 shots (approximately 1.8 hours). Carbon-free regions were observed near the mid-width of both HPDE laminates (see Figure 5). The carbon-free region on cathode was larger than that of the laminate near the anode. The 1/16" Teflon spacer laminate near the anode shows very little carbon buildup. Teflon laminate charring is confined to the left edge for both Case 1a and Case 1b.

The mass loss of each laminate was determined by weighing individual pieces. These mass loss values are then divided by the exposed surface area and the number of shots to obtain the mass loss flux [μg/shot-cm^2]. Further division by the material density [μg/cm^3], then provides the average recession of the surface.

Using the mass loss data from Table 1, calculations of average recession distances (based upon the laminate thickness) are shown in the fifth column of Table 1. Mass loss fluxes (based on the slant area) are shown in the fifth column of Table 2.

Case 2a: N=7,(67,560) shots

Case 2a laminates were prepared in the same manner as described for Case 1. This fuel was subjected to 7,560 shots in auto-mode, allowed to cool down to initial temperature, and then run for 16,800 more shots. The next day, an additional 43,200 shots were fired successively in auto-mode for a total of 67,560 shots.

Figure 6 is a photograph of the Case 2a post-test results. The top laminate is nearest to the cathode. Notice the evidence of two arc channels that appear to intersect five laminates down from the top. The separation distance of the two channels is about 1.6 cm. Visual inspection of the cupping of the fuel fork suggested that this single channel continues to the anode. The two spark-plugs in the cathode fire in alternation, so the damage pattern is the result of single paths, rather than a bifurcated discharge.

Figure 7 shows a sketch of the Case 2a laminates. Measurements using a machinist's rule indicate that the Teflon has receded about 1 mm below the HDPE laminates. Also, the Teflon fuel fork has a cupped shape at the lower left edge. This edge is located at the fuel retaining shoulder at the anode. Visual inspection of the HDPE laminates shows considerable deformation at the exposed fuel face.

Case 2b: N=7, (13,221) shots

For Case 2b, a second set of seven laminates were prepared for measurement of mass loss and plasma voltage drop across the electrodes. Before testing, the mass of each laminate was measured once individually, and then once all together using a Mettler AE163 balance. Since the fuel fork mass was too large for the Mettler AE163 balance, it was measured with a Mettler B4C-1000 mechanical balance sensitive to one milligram.

The PPT was run without interruption at 2 Hz auto-mode for 13,221 shots. The post-test laminates were measured individually three times using three different balances. Two measurements were performed on a Mettler AE100 balance and one on a AE163 balance. The resulting mass measurements of the second set of laminates (N=7) before and after 13,221 shots are listed in Table 3. The post-test, fuel-fork mass was measured once. Although the pre-test laminate mass was only measured once, the very small variance given in column three of Table 3 lends confidence in the precision of the measurements. Column five of Table 3 gives the computed average recessions. From the data in Table 3, the combined Teflon laminate and HDPE laminate losses were 103.2 mg and 30.7 mg, respectively. The total Teflon loss including the fuel fork was computed to be 338 mg.

After only 13,221 shots, the laminates were beginning to show visible charring. Figures 8 and 9 are photographs of the Case 1b (N=3) and Case 2b (N=7) laminates immediately after 13,221 and 13,288 shots, respectively. Visual inspection of the Teflon laminates did not show recession below the HDPE laminates as in Case 2a after 67,560 shots. In these two figures, it appears that the clean region of the HDPE laminate nearest to the cathode shows charring patterns similar to Case 1b (Figure 5). Notice that with only 13,221 shots, the Case 1b fuel face char pattern did not develop into the pair of char-free regions of Case 1a. Recall that Cases 1a and 1b were subjected to 19,267 shots and 13,288 shots, respectively. Thus, if the Case 1b laminates had been subjected to further testing, it seems reasonable to hypothesize that the carbon charring would have continued to cover a larger portion of the fuel face area.

Using the mass loss data after 13,221 shots from Table 3 and the material geometry, values for recession rate and mass loss flux for the seven laminates and fuel fork are computed and displayed in Table 4.

ANALYSIS

A comparison of material properties in Appendix I, Table A.1 shows some important differences between the two polymers. For example, the heats of fusion of both Teflon and HDPE are nearly the same (≈6 kJ/mol for Teflon and ≈8 kJ/mol for HDPE), but Teflon's heat of depolymerization (155 kJ/mol) is 1.5 times that of HDPE (106 kJ/mol). Enthalpies for both materials were computed from temperature-dependent (experimental) specific heat data[8,10,13] using a fourth-order, numerical integration from 20° C to the vaporization temperature. As shown in Table A.1, the results for Teflon and HDPE are 50 kJ/mol and 26 kJ/mol, respectively. The sum of the enthalpy, heat of fusion, and heat of depolymerization yields the heat of vaporization, which for Teflon is 211 kJ/mol and for HDPE, 140 kJ/mol. However, because the C_2F_4 monomer molecular weight is ≈3.5 times that of C_2H_4, the heat of vaporization per unit mass of Teflon (2,110 J/g) is half that of HDPE (4,990 J/g).[8,11] Volumetrically, the heat of vaporization of Teflon (4,540 J/cm^3) is slightly *less* than that of HDPE (4,791 J/cm^3). The energies necessary to completely dissociate C_2F_4 and ${}_2C_4H$ monomers, based upon average bond energies, are 2,554 kJ/mol and 2,266 kJ/mol, respectively. Thus, the total energy required to ablate and dissociate Teflon and HDPE (beginning at 20°C) is 2,765 kJ/mol and 2,406 kJ/mol, respectively. It is interesting to note that these two energies differ by about 15%.

A photograph of the Case 1a laminates after 19,267 discharges is shown in Figure 4. In Figure 4, the top HDPE laminate is closest to the cathode and spark plugs. An extensive amount of charring has occurred on both HDPE laminates, but almost none occurs on the Teflon, except at the left edge. Case 1b laminates after 13,288 discharges are shown in Figure 5. Because Case 1b was performed after Case 2b experiments, the single 1/16" Teflon laminate shown in the photograph allows the use of three 1/8" laminates within the 7/16" fuel fork gap. Notice that there is virtually no charring of the Teflon, except near the left edge of the middle laminate. The current paths are symmetric about a vertical plane bisecting the fuel fork for both Case 1a and 1b.

Case 2a photographs before and after 67,560 discharges are shown in Figures 3 and 6, respectively. In Figure 6, the top HDPE laminate is closest to the cathode and spark plugs. Notice that the top two HDPE laminates near the cathode have carbon-free regions similar to Case 1a. The lowest two laminates have only one pronounced gouge off-center towards the right edge. This suggests that regions of high current-density exist directly in line with the lateral position of the spark plugs.

Figures 8 and 9 show both Case 1b and Case 2b after 13,288 and 13,221 discharges, respectively. A comparison indicates that in both cases the carbonization covers more surface area near the anode (top laminate in both figures) than near the cathode.

In Table 2, the sum of all the Case 1b Teflon mass loss rates (including fuel fork and spacer) is 22.4 µg/shot, whereas the LES 8/9 rate for pure Teflon is 28.5 μg/shot[4], a difference of 6.1 μg/shot (21%). From Table 4, Case 2b, the combined mass loss rate for Teflon fork and laminates is 25.6 μg/shot. This is 2.9 μg/shot (10%) less than the LES 8/9 pure Teflon result. These results are consistent with the fact that the multi-material cases have less exposed Teflon surface area than the pure Teflon case. The Teflon mass loss per unit area of exposed Teflon surface, however, is higher than for pure Teflon. This may result from the relatively lower absorption of energy by the carbonized HDPE surfaces.

Table 4 also shows that the Case 2b *average* mass ablation rates of the HDPE laminates are 0.5909±0.05 μg/shot. This value is about 2.2 times smaller (45%) than that of Case 1b HDPE result listed in Table 4 as 1.315 μg/shot. The Case 2b *average* Teflon laminate ablation rate is 2.615±0.0822 μg/shot, which is 1.8 times smaller (54%) than that of Case 1b (4.7093 μg/shot). Additionally, the Teflon fuel spacer used in Case 1b has an average ablation rate of 2.39 μg/shot, which is within 9% of the Case 2b Teflon laminate averages. Since the Case 2 areas are known to be half that of Case 1 (not including the fuel spacer), this result suggests reasonably that the ablation rates are proportional to the exposed areas. This motivates the use of the ablation mass flux to compare laminates of differing sizes and materials.

Tables 2 and 4 also give mass loss fluxes for Case 1b and Case 2b, respectively. Data from Table 2 all of the Teflon items (fuel fork, spacer, and laminate) have about the same *average* flux loss (4.71±0.22 μg/(shot-cm^2)), while the HDPE laminate flux is 1.32μg/(shot-cm^2). Notice that the *average* Teflon fuel fork flux is slightly lower than the Teflon laminates (~14%). Data in Table 2 and 4 show that Case 2b Teflon and HDPE laminate flux values have small deviations from their own respective averages of 5.286 ± 0.14 μg/(shot-cm^2) and 1.19 ± 0.10 μg/(shot-cm^2). These results are also consistent with the hypothesis that the ablation rate is proportional to the exposed surface area.

Average values for the laminate mass loss fluxes as a function of the number of laminates is given in Table 5. Note that the total areas of each material for both Case 1b and Case 2b are the same; 4.8888 cm^2 for Teflon (including the fuel fork and 1/16" fuel spacer) and 1.9788 cm^2 for HDPE. Observe that as the number of laminates increases with fixed total area, the Teflon loss flux tends to increase but HDPE flux tends to decrease. If HDPE does not absorb the available energy as well as Teflon because of insulating layers of carbonous deposition or because of material properties, then perhaps the Teflon laminates have a higher mass loss flux than the case of pure Teflon (LES 8/9) because the HDPE laminates do not absorb their areal share of the available electrical energy.

First-order measurements of the ablated areas on the HDPE for Case 1a, as shown in Figure 4, lead to an interesting result. Measurement of the carbon-free region on the HDPE laminate nearest to the cathode yields an area of 39 mm^2. Displacement of a small pin was used to estimate the depth of the eroded area. The pin measurement for this laminate was 0.83 mm deep, giving a volume (assuming a constant depth over the exposed area) of about 32 mm^3. Using the density of HDPE from Table A.1 ($9.6x10^{-4}$ g/mm^3), the mass corresponding to this volume is ~0.031 g. After 19,267 discharges, the ablation rate is ~1.6 μg/shot. The mass loss flux is ~4.1 μg/(shot-cm^2). Likewise, the area of the carbon-free region nearest the anode is about 26 mm^2. Measurement using a machinist's rule gave a depth of about 1/32" (0.79 mm). This corresponds to a volume of ~20 mm^3. Again, using the density of HDPE, the mass ablated after 19,267 discharges is about ~0.02 g, thus the rate is ~1.0 μg/shot. These rough ablation flux estimates are nearly equal suggesting that most of the (Case 1a) HDPE ablated mass comes from the areas free of carbonous deposits. It may be true that without carbonous deposits, HDPE would absorb the available energy at about the same rate as Teflon.

First-order area measurements of the carbon-free regions for Case 1b HDPE laminates were measured using a millimeter ruler. The carbon-free area of the laminate nearest the cathode is about 56 mm^2, and the one nearest the anode is 37 mm^2. (The area ratio for Case 1b laminates turns out to be ~1.5, the same value for the Case 1a laminates). Using the known measured mass losses, the flux loss was re-computed based upon the area of the carbon-free regions, yielding ~2.3 μg/(shot-cm^2) for the cathode HDPE laminate and ~3.5 μg/(shot-cm^2) for the anode laminate.

THRUST-STAND RESULTS

Measurements were made using a thrust stand that has recently been built and tested for the purpose of obtaining thrust data in the micro-newton range for the LES 8/9 and advanced PPTs[18]. The new thrust stand is a torsional design, it can be used to measure the thrust of single pulses or the average thrust during times of auto-mode operation. The thrust stand was placed in the vacuum facility Tank 8 and the LES 8/9 thruster was mounted onto it.

Thrust measurements were conducted using multi-material fuel and pure Teflon fuel. Both individual pulse data and average thrust data were obtained for both fuels. For the average thrust data, the thruster was run in the 2 Hz mode (actually 2.206 Hz) for ten minutes, after which time the thruster was turned off for one minute; this was done to minimize thrust-stand drift. For the multi-material fuel, a seven laminate fuel set was prepared. The laminates were weighed before testing individually and all together; in addition, the fuel fork was weighed with and without the laminates. After the completion of the test, another set of mass measurements was performed. Table 6 lists the resulting mass measurements along with the mass loss per shot.

For the multi-material fuel, ten runs of ten minutes each were performed. Between those runs single pulse thrust data were obtained (a total of 30 pulses). For the pure Teflon fuel, two runs of ten minutes each were performed and three single-pulse thrust data were obtained. For the multi-material propellant, the average thrust for the ten runs was 462.8 μN. By using the mass loss rate of 22.5 μg/shot (see Table 6), an average exhaust speed of 9323.6 m/s was found corresponding to an average specific impulse of 950.4 s. The average thrust efficiency (mu_e^2/CV^2) was 4.52%. For the pure Teflon a mass loss rate of 28.5 μg/shot was used[4]. The average thrust was 584.2 μN, so the average exhaust speed was 9292.8 m/s, and the average efficiency was 5.69%. These results indicate the thrust for the pure Teflon is 26% higher than that of the multi-material fuel. The exhaust speeds and specific-impulse values are almost equal.

CONCLUDING REMARKS

From the results of these first experiments with laminated propellant mixtures, several conclusions may be drawn. After only 1,488 discharges (12.5 minutes) carbon deposits were visually perceptible in Case 1a on the outer edges of the HDPE surfaces. It appears that the path of highest current density connects a region near each spark plug at the cathode, to a region near the anode center. The arc has sufficient power density to erode any carbonous deposition in its vicinity, but not at more distant locations, such as the outer edges of the HDPE laminates. In time, charring builds upon the HDPE laminates from the outer edges to the central regions, eventually covering the entire width of the HPDE laminate. This coating of carbonous material may behave as a thermal insulator preventing the HDPE from absorbing energy. The uncoated HDPE area decreases with time, and since mass ablation is believed to be proportional to the exposed surface area, the HDPE mass ablation rate probably also decreases in time. The mass loss measurements for the HPDE laminates (and also the Teflon to a lesser extent) are thus averaged over the time required to develop complete coating of the HDPE. The first-order measurements of the exposed HDPE laminate areas described above indicate that the mass loss flux for the uncoated HDPE has a value similar to the Teflon mass loss flux. This suggests that in the absence of charring, HDPE and Teflon may absorb energy equally well.

The thrust-stand measurements indicate that lower mass flow rates are obtained with the HDPE/Teflon laminates vs pure Teflon, at comparable speeds. These results are probably due to the protective layer of carbon forming on the HDPE during the tests, which reduces HDPE ablation. The slight increase in ablation rate on the remaining Teflon does not compensate for this deficit. Future experiments must address the variation of HDPE surface properties with time (number of shots). Additional candidate polymers, such as polystyrene, $(C_2H_2)_x$, will also be explored. Differences in thermal diffusivity and in the temperature for monomer production maybe critical factors in this exploration.

APPENDIX I

Polymer Fuel Material Properties

Teflon consists of long fluorocarbon chains of CF_2 molecules bonded as shown in Figure A.1a. Teflon gains the property of inertness from the fact that fluorine atoms, once bonded to carbon, are so unreactive that they repel almost all other substances.[7] The polymer chains are flexible, aligned, and unbranched.[7] Although most polymers typically do not have a precise melting point, at temperatures above 327° C, experiments conducted in vacuum (10^{-5} Torr)[7] show that Teflon degradation occurs through two mechanisms. The first and slowest mechanism is the breaking of single C-C bonds (347 kJ/mol) at random positions along the chains due to local thermal agitation.[8,9,10] This process results in two smaller chains with free radical ends, shown in Figure A.1a. The second process[9,10,11] is a decomposition of these chain fragments into C_2F_4 monomers by a reaction beginning at the ends and working towards the middle, as shown in Figure A.1b. This process is called "unzipping". Note in Figure A.1b that the C_2F_4 monomer has a double carbon bond (614 kJ/mol).[9] Of the two mechanisms, the first is the slowest and is, therefore, the rate-determining reaction.[15] Experiments show that chain fragments larger than the monomer have no chance of escaping into the gaseous phase.[10] The viscosity remains high (10^{12} poise) to at least 500°C, and there is no evident liquid phase, so Teflon tends to undergo sublimation.[8] Spectral measurements of a Teflon surface subjected to ablating conditions in vacuum shows the surface temperature to be about 427°C (700 K).[8] Equilibrium pyrolysis experiments of Teflon gas at 500°C show species mole-fraction proportions of 94% C_2F_4, 0.86% CF_4, 2.6% C_3F_6, 0.73% $_4C_8F$, and 0% C_2F_6.[8] Measured values of Teflon equilibrium vapor pressure at 500°C and 608°C are 28 mmHg and 760 mmHg, respectively.[8] Complete dissociation of a C_2F_4 monomer requires approximately 2,554 kJ/mol, based upon average bond energies.[9]

The structure of polyethylene is analogous to that of Teflon with hydrogen substituted for fluorine. Polyethylene consists of long hydrocarbon chains of CH_2 molecules as shown in Figure A.2a. High density polyethylene (HDPE) chains are flexible, aligned, and unbranched.[7] Experiments in vacuum show that at 330°C solid HDPE has been completely vaporized.[10,13]

Pyrolysis data suggests that for temperatures below 800° C in vacuum, degradation of HDPE occurs in three stages, where the final equilibrium vapor consists of chain fragments of various sizes, and of very few C_2H_4 monomers. The first stage, called "initiation", begins at a "melting" point temperature of about 115°C. In this process, C-C bonds are ruptured at random points due to thermal agitation to produce polymer chains of free radicals. This is analogous to the case of Teflon degradation.[10] The second stage, as shown in Figure A.2b, consists of a "free-radical transfer" process where a hydrogen atom is confiscated from another chain (intermolecular) or from its own chain (intramolecular). This results in the formation of chains with one saturated end, one unsaturated end (note the double carbon bond), and a new free radical.[10] The final stage, called "termination", occurs when two free radicals recombine into a *larger* chain fragment.[10] This is the reason why few monomers are observed at temperatures below 800°C in vacuum.[10]

At temperatures higher than 800°C, the predominant mechanism of degradation tends to be the "unzipping" of the chains into mostly C_2H_4 monomers, just as in the case of Teflon (see Figure A.1b).[10] From Table A.1, note that the C-F bonds are stronger (485 kJ/mol) than that polyethylene C-H bonds (413 kJ/mol), so the free-radical transfer mechanism is not likely to dominate in Teflon degradation.[9,10]

Table A.1 lists some physical properties of Teflon[1,7,8,11,12,16] and HDPE.[7,10-17] Significant differences in these two materials should be noted. First, Teflon has a density over twice that of HDPE. The molecular weight of HDPE is rather low (28.054 g/mol) as compared to Teflon (100.014 g/mol). Second, the heat required to vaporize one mole of Teflon (211 kJ/mol) is 1.5 times greater than that of HDPE (140 kJ/mol). The average energies to dissociate Teflon and HDPE monomers may be computed from the average bond strengths.[9] The result gives 2,554 kJ/mol for Teflon and 2,266 kJ/mol for HDPE. At room temperature, the thermal diffusivity of HDPE is twice that of Teflon. Finally, note that the dielectric strength of Teflon is about ≈20 kV/mm and that of HDPE is ≈40 kV/mm.[16]

REFERENCES

1. Guman, W. and Palumbo, D.J., *Effects of Propellant and Electrode Geometry on Pulsed Ablative Plasma Thruster Performance*, AIAA 75-409, 11th Electric Propulsion Conference, New Orleans, LA, March 19-21, 1975.

2. Yuan-Zhu, Kuang, *Effects of Propellant Geometry on Pulsed Plasma Thruster Performance*, IEPC 84-94, Tokyo, 1984.

3. Myers, R., *Electromagnetic Propulsion for Spacecraft*, AIAA 93-1086, Aerospace Design Conference, Irvine CA, February 15-19, 1993.

4. Thomassen, K.I. and Vondra, R.J., *Flight Qualified Pulsed Electric Thruster for Satellite Control*, J. Spacecraft, Vol. 2, No. 9, Sept. 1974, AIAA 73-1067, 10th Electric Propulsion Conference, Lake Tahoe, NV, Oct. 31-Nov. 2, 1973.

5. Thomassen, K.I. and Vondra, R.J., *Performance Improvements in Solid Fuel Microthrusters*, J. Spacecraft, Vol 9, No. 10, AIAA 72-210 10th Aerospace Sciences Meeting, San Diego, CA, 1972.

6. Guman, W.J., *Pulsed Plasma Technology in Microthrusters*,Fairchild Hiller Corp./Republic Aviation Division Technical Report AFAPL-TR-08-132, Nov. 1968.

7. Herman, M.F., *Giant Molecules*, Time Inc., Life Science Library, N.Y., 1966.

8. Wentink, T., *High Temperature Behavior of Teflon*, Report No. 55, Avco-Everett Research Lab for USAF Ballistic

Missle Division, AF 04(647)-278, Contract No. AFBMD-TN-59-15, July, 1959.

9. Zumdahl, S., *Chemistry*, D.C. Heath and Co., Lexington Mass., 1986.

10. Madorsky, S.L., *Thermal Degradation of Organic Polymers*, Interscience Publishers, John Wiley & Sons, N.Y., 1964.

11. Billmeyer, F.W., *Textbook of Polymer Science*, Interscience Publishers, John Wiley & Sons, N.Y., 1962.

12. *CRC Handbook of Chemistry and Physics, 75th Ed.*, CRC Press,Inc., 1995

13. Raff, R.A. and Allison, J.B., *Polyethylene*, Interscience Publishers Inc., New York, 1956.

14. Schmidt, A.X. and Marlies, C.A., *Principles of High-Polymer Theory And Practice*, McGraw-Hill Book Co., Inc., New York, 1948.

15. Simonds, Weith, Bigelow, *Handbook of Plastics*, 2nd Ed., D. Van Nostrand Co., Inc., New York, 1949.

16. *Handbook of Mathematical, Scientific, and Engineering Formulas, Tables, Functions, and Graphs*, Research and Education Association, New Jersey, 1991.

17. Cook, D.M., *The Theory of the Electromagnetic Field*, Prentice-Hall, Inc., Englewood Cliffs, New Jersey, 1975.

18. Haag, T., *PPT Thrust Stand*, AIAA-95-2917, Joint Propulsion Conference, San Diego, CA, July 10-12, 1995.

Table 1.
Case 1b Fuel Mass Loss Measurements and Average Recessions

Item	Mass Before g	Mass After g	Mass Loss mg	Computed Average Recession
HDPE 1 (anode)	1.44815	1.43069	17.46	0.18 mm
Teflon 1	3.05727	2.99365	63.62	0.29 mm
HDPE 2	1.12369	1.10622	17.47	0.18 mm
Teflon FuelFork Spacer (cathode)	1.71359	1.68187	31.72	0.29 mm
Laminate sum (arithmetic)	7.3427	7.2124	130.27	
Fuel Fork	97.172	96.970	202	0.27 mm
Grand Total	104.514	104.182	332	

Table 2.
Case 1b Average Laminate Recession and Flux Results

Item	Exposed Area cm^2	Mass Loss μg/shot	Rate μmm/shot	Loss "Flux" μg/shot-cm^2
HDPE 1 (near anode)	0.9894	1.3147	13.84	1.32
Teflon 1	0.9894	4.7903	22.01	4.84
HDPE 2 (near cathode)	0.9894	1.3154	13.85	1.32
Teflon Fuel Fork Spacer	0.4947	2.3871	21.94	4.83
Fuel Fork	3.4047	15.21	20.30	4.46
HDPE Laminates total avg.	1.9788 —	2.6301 1.3150	— 13.84	— 1.32
Teflon Laminate + Spacer total avg.	1.4841 —	7.1774 3.5887	— 21.97	— 4.71
Teflon Fork + Lam. + Spacer total avg.	4.8888 —	22.39 7.4624	— 21.42	— 4.71
LES 8/9[4]	6.8677	28.50	19.28	4.15

Table 3.
Case 2b Measured Mass Losses and Computed Average Recession

Item	Mass Before g	Mass After g	Mass Loss mg	Computed Average Recession
HDPE 1 (anode)	0.7294	0.7213 ±0.0001	8.1	0.19 mm
Teflon 1	1.6909	1.6579 ±0.0004	33.0	0.35 mm
HDPE 2	0.7086	0.7004 ±0.0001	8.1	0.19 mm
Teflon 2	1.5502	1.5151 ±0.0001	35.1	0.37 mm
HDPE 3	0.6414	0.6336 ±0.0001	7.8	0.17 mm
Teflon 3	1.4035	1.3684 ±0.0001	35.1	0.37 mm
HDPE 4 (cathode)	0.5514	0.5447 ±0.0001	6.7	0.14 mm
Laminate sum (arithmetic)	7.2754	7.1414 ±0.001	134	—
Laminate sum (measured)	7.2757	7.1414 ±0.0005	134	—
Fuel Fork	97.805	97.570	235	0.32 mm
Grand Total	105.080	104.198	369	—

Table 4.
Case 2b Average Laminate Recession and Flux Results

Item	Exposed Area cm^2	Mass Loss μg/shot	Rate μmm/shot	Loss "Flux" μg/shot-cm^2
HDPE 1	0.4947	0.6217	14.37	1.256
Teflon 1	0.4947	2.5187	26.47	5.091
HDPE 2	0.4947	0.6301	14.37	1.274
Teflon 2	0.4947	2.6662	27.99	5.389
HDPE 3	0.4947	0.5922	12.86	1.197
Teflon 3	0.4947	2.6602	27.99	5.377
HDPE 4	0.4947	0.5196	10.59	1.050
Fuel Fork	3.4047	17.774	24.2	5.220
HDPE Laminates total avg.	1.9788 —	2.364 0.591	— 13.05	— 1.194
Teflon Laminates total avg.	1.4841 —	7.845 2.615	— 27.48	— 5.286
Teflon Fork + Laminates total avg.	4.8888 —	25.619 20.389	— —	— 5.269
LES 8/9[4]	6.8677	28.5	19.86	4.15

Table 5.
Average Mass Flux Loss For Given Total Number Of Laminates (Note: N = 0 Case based upon the LES 8/9 PPT using pure Teflon[4])

# of laminates, N:	0	3	7
Avg. Teflon flux, μg/(cm²-shot)	4.15	4.84	5.27
Avg. HDPE flux, μg/(cm²-shot)	0	1.32	1.19

Table 6.
Measured Mass Losses for Laminated Propellant

Item	Mass Before g	Mass After g	Mass Loss mg	Mass Loss μg/shot
FUEL FORK W/O LAMINATES	95.8003	95.6210	0.1793	13.4964
FUEL FORK W/ LAMINATES	102.2685	101.9688	0.2997	22.5593
TOTAL LAMINTES WEIGHT	6.46755	6.34819	0.11936	8.98457
HPDE 1	0.46107	0.45456	0.00651	0.49003
Teflon 1	1.22504	1.19757	0.02747	2.06775
HPDE 2	0.56976	0.56235	0.00741	0.55777
Teflon 2	1.39976	1.37037	0.02939	2.21227
HPDE 3	0.64366	0.63589	0.00777	0.58487
Teflon 3	1.46999	1.43762	0.03237	2.43658
HPDE 4	0.69830	0.68984	0.00846	0.63681

Table A.1.[7-13]
Material Properties of Teflon and HDPE

9Property	Teflon $(C_2F_4)_x$	HDPE $(C_2H_4)_x$
Density, 10^3 kg/m³	2.152	0.960
Mol. Wt. g/mol	100.014	28.054
Dielectric Constant at 23°C	2.10	2.26
Dielectric Strength at 23°C, kV/mm	20	40
Melt Temp., °C	~327	~115
Vaporization Temp., °C	~487	~330
Enthalpy $C_p\Delta T$, kJ/mol	50	26
Heat of Fusion, kJ/mol	6	8
Heat of Depolymerization, kJ/mol	155	106
Heat of Vaporization, kJ/mol J/cm³ J/g	 211 4,540 2,110	 140 4,791 4,990
Avg. Energy to Dissociate Monomer, kJ/mol	2,554	2,266
Thermal Conduct. at 23°C, W/(m-K)	0.167	0.347
Thermal Diffusivity at 23°C, m²/s x 10^8	7.76	15.71
Specific Heat at 23°, J/(g-°C)	1.00	2.30
Specific Heat at Melt Temp., J/(g-°C)	1.21	8.37

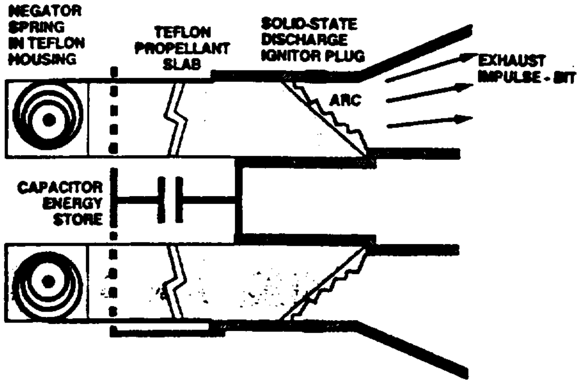

Figure 1: LES 8/9 Teflon fuel feed configuration[4]

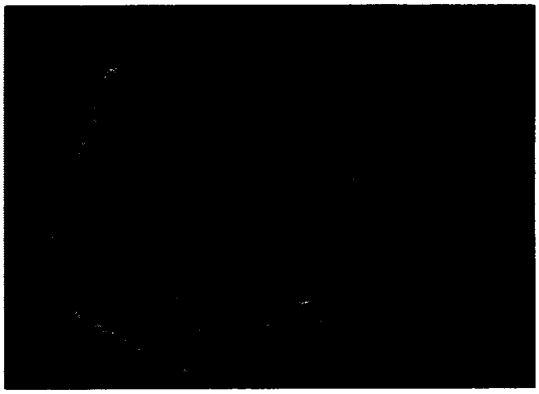

Figure 3: Typical laminate fuel configuration

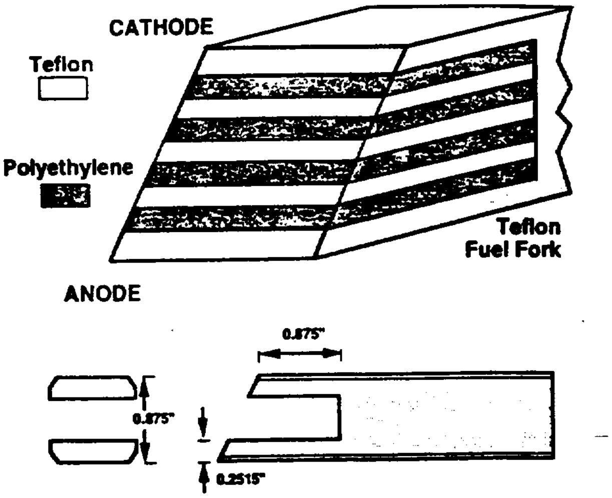

Figure 2: Teflon fuel fork geometry

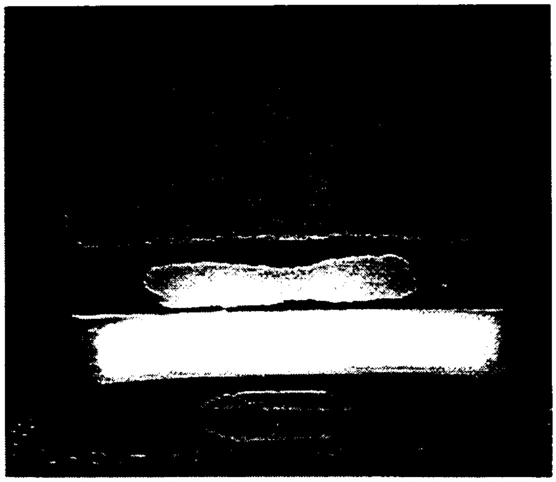

Figure 4: Case 1a laminates after 19,267 shots

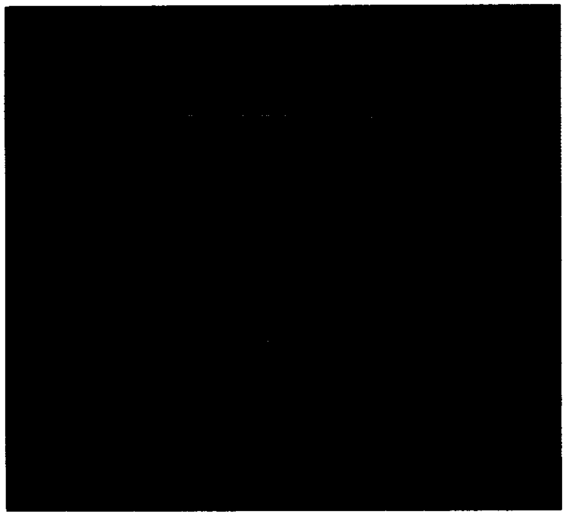

Figure 5: Case 1b laminates after 13,288 shots

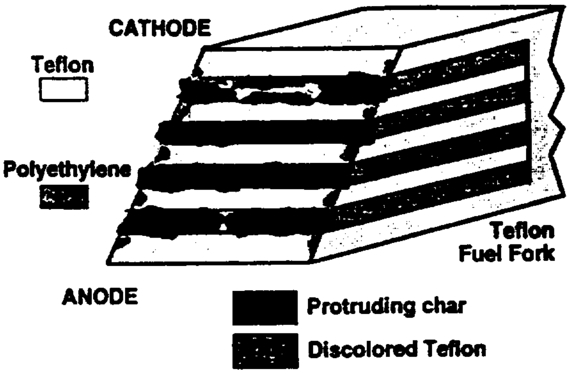

Figure 7: Case 2a laminate profile sketch

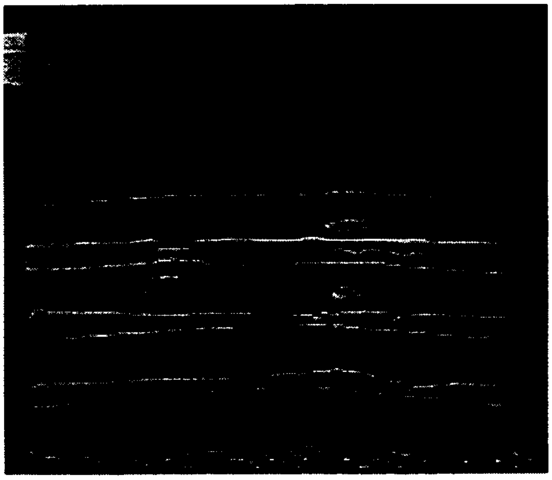

Figure 6: Case 2a laminates after 67,560 shots

Figure 8: Case 1b laminates in LES 8/9 after 13,288 shots

Figure 9:Case 2b laminates in LES 8/9 after 13,221 shots

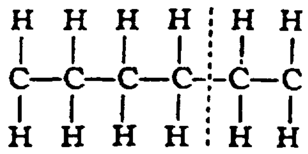

Figure A.1.b: Stage 1 HDPE degradation, "initiation"[10]

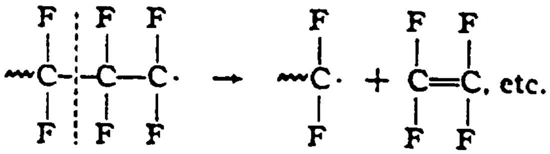

Figure A.2a: Stage 2 Teflon degradation, "un-zipping"[8,10]

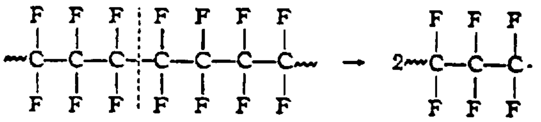

Figure A.1a: Stage 1 Teflon degradation, "initiation"[8,10]

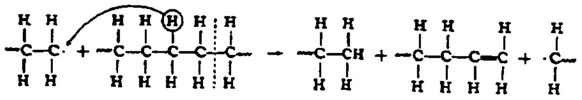

Figure A.2b: Stage 2 HPDE degradation, "free-radical transfer"[10]

AIAA 96-2731

DESIGN OF AN INDUCTIVELY-DRIVEN PULSED PLASMA THRUSTER

P.J. Turchi, R.J. Leiweke, and H. Kamhawi
The Ohio State University
Columbus, OH

32nd AIAA/ASME/SAE/ASEE
Joint Propulsion Conference and Exhibit
July 1-3, 1996/Lake Buena Vista, FL

DESIGN OF AN INDUCTIVELY-DRIVEN PULSED PLASMA THRUSTER

P.J. Turchi, R.J. Leiweke
and H. Kamhawi,
The Ohio State University
Columbus, OH

ABSTRACT

To improve the efficiency of pulsed plasma thrusters (e.g., PPTs) at low energy in either plasma-slug or quasi-steady modes, a new circuit has been devised. It consists of an initial current path, from a single capacitive element, through a PPT in series with an inductor, which results in transfer of the capacitive energy to energy stored in the inductor. Shortly after peak current, a second PPT, or other type of pulsed plasma thruster, is connected in a manner that crowbars the inductor, providing a new current path that circulates through the inductor and the two thrusters, all in series. By this approach, the capacitor can store energy at relatively high voltage and at high specific energy, but the thrusters do not have to absorb energy at equivalent voltage levels. The use of an inductive store to drive the plasma discharge can result in relatively high efficiency because the thruster discharges are the primary electrical loads, absorbing energy over the effective L/R-decay time of the inductive circuit. The present paper discusses the new circuit and provides results of numerical models with PPTs indicating improvements in both thrust efficiency and specific impulse.

INTRODUCTION

Higher efficiencies of transfer from electrical storage to kinetic energy in the exhaust of pulsed plasma thrusters would be possible if the power supply and plasma discharge impedances could be matched. Two major difficulties, however, prevent simple matching. The first is intrinsic to dynamic discharge behavior in pulsed plasma accelerators; the second is a practical engineering problem resulting from the confluence of constraints on the total system energy and mass, and the specific energy, inductance, voltage and lifetime of available capacitors.

Short pulse operation (~1 μsec vs ~100 μsec) of many pulsed plasma thrusters, such as the pulsed-plasma-microthruster (PPT) typically present the power source with time-varying impedances as the plasma discharge initiates and then accelerates in slug-fashion, driven by electromagnetic forces. The rate of change of inductance with time provides an effective resistance that is proportional to the speed of the plasma, and increases as electrical energy is tranferred to plasma kinetic energy. Thus, a power source characterized by a single value of impedance, such as a uniform pulseline, cannot match perfectly to a dynamic plasma discharge. Operation in quasi-steady mode represents a constant impedance situation, for which complete matching is possible. The engineering problem, however, remains to attain the relatively low values of impedance (~ 5 - 50 mΩ) found in pulsed plasma thrusters with circuits based on available capacitors. Such circuits can certainly achieve the necessary impedance values, but only at values of stored energy much higher than desired for small-satellite missions. Values of charging voltage, to obtain adequate specific energy, also tend to be much higher (~ 1 - 20 kV vs 100 - 200 V) than needed to power the relatively modest discharges for near-term satellite systems.

It is possible to store energy magnetically by discharging a capacitor through an inductor. The energy is then drained from this inductive store by the action of the load at a voltage that is determined by the load impedance, not the initial voltage of the capacitor. The behavior of a new kind of inductive-storage and switching circuit is examined in the context of PPTs in both plasma-slug and quasi-steady, ablation arc modes [1].

BACKGROUND

The pulsed-plasma-microthruster (PPT) has been used for satellite station-keeping for many years [2]. Traditionally, it operates by creating an arc discharge across the end of a Teflon propellant bar that is advanced between two electrodes by a negator spring. A single capacitor establishes a high voltage across the electrodes. This voltage is supported by the dielectric strength of the Teflon surface in vacuum. A separate spark-source in one electrode is triggered to provide ionized material near the Teflon surface, thereby igniting an arc over the surface. Ablation of the Teflon then supplies material to sustain the arc during the discharge of the capacitor. This material serves as the propellant reaction-mass for the thruster.

The basic circuit operation is similar to a standard LRC-circuit. Zero-dimensional calculations can model PPTs reasonably well, with single-loop circuit equations coupled to the dynamical equations for a magnetically-accelerated plasma-slug of assumed (and constant) mass. For example, the circuit and mass (per shot) values for the OSU/LeRC benchmark PPT [3] provide current and voltage waveforms that are essentially a damped sinusoids (Fig.1). The circuit voltage and current oscillate because the arc discharge impedance is less than the characteristic impedance of the LRC-circuit:

$$Z_{arc} < 0.5\,(L\,/\,C)^{1/2} \qquad (1)$$

where L and C are the values, respectively, of circuit inductance and capacitance, . This situation also implies that the energy of the circuit is not delivered efficiently to the plasma. Instead, it can be dissipated in the resistances of the circuit, including resistance associated with the capacitor. The thrust efficiency of the PPT has thus been rather modest (typically < 10%). Furthermore, voltage reversals at the electrodes and especially at the capacitor result in reduced lifetime for these components. (Within this reduced life, however, PPTs have nevertheless accumulated tens of millions of firings in the course of their orbital duties.)

The basic simplicity of the PPT has allowed it to enter the inventory of spaceflight-qualified thrusters for actual application. It is still useful, of course, to examine ways in which PPT performance can be improved and scaled to different mission needs, while retaining this simplicity. One avenue for such improvement is by means of better circuitry.

NEW CIRCUIT

The new circuit considered here is shown schematically in Fig. 2. It consists essentially of a single capacitor to store the initial electrical energy, an intermediate storage inductor, and two switches indicated with their respective resistances. The two switches are actually PPTs, so the circuit energy is dissipated in the PPTs to create thrust.

Figure 3 indicates the connection of the circuit to the PPTs.

The circuit operates by the following sequence of events. The capacitor is charged by an appropriate high voltage source to a value V_0 for which the specific energy of storage and the reliability of the capacitor are adequate for the thruster mission. The spark source in the first PPT is fired to initiate the PPT and allow the capacitor to discharge into the inductor. Shortly after peak current in the inductor, the capacitor becomes charged in the direction opposite to its initial charge, but with a magnitude $|V_1| << |V_0|$. While not unduly burdening the reliability of the capacitor, V_1 is still sufficient to allow breakdown across the propellant surface in the second PPT. This breakdown is triggered either by a spark source in the second PPT or by the plasma from the first PPT.

A typical set of waveforms calculated for the new circuit are shown in Fig. 4. To display the basic characteristics of the behavior of this circuit, the idealized form of Fig. 2 is used with constant values of the effective resistances of the PPTs; $L_t = 0.01$ L, and parasitic resistances and inductances are neglected. The voltage values are normalized to the capacitor voltage at the time of firing the second PPT (t=0). Current values are normalized to the inductor current at this time also. Elapsed time is measured in units of L/R, (where $R_1 = R_2 = R$). These calculations begin after the first PPT has fired and the capacitor has transferrred its energy to the inductor. The inductive store is then crow-barred by the firing of the second PPT. After a short transient, the capacitor voltage equals that necessary to sustain the voltage across the second PPT, and current circulates through the inductive store and the two PPTs in series. This circulation decreases exponentially with time in units of the (L / R)-time, which is much longer than the risetime of the initial current pulse to the inductor. The energy stored in the inductor is transferred to the PPTs during this exponential decay.

The new circuit arrangement allows the capacitor to be selected for high specific energy, which is associated with voltages that are much higher than needed by the PPT arc. High specific energy is also associated with limited tolerance for voltage reversal. The new circuit, while evidencing oscillatory and reversed voltage on the capacitor, limits the amplitude to small fractions of the initial charging voltage needed for high specific energy. Thus, the new circuit not only offers higher efficiency of transfer to the PPT flow, but also enhances the overall performance and reliability of the system.

PLASMA-SLUG CALCULATIONS

To understand the transfer from circuit energy to the directed kinetic energy of the thruster exhaust, zero-dimensional calculations are performed in which the plasma in each PPT is treated as a slug of constant mass, accelerated electromagnetically. The respective accelerating forces are given in terms of the inductance gradient, L' = dL/dz, in the exhaust direction (z) and the square of the instantaneous current, J, through the thruster:

$$F = L'J^2 / 2 \qquad (2)$$

The resistance of each plasma discharge may be estimated from reasonable values for the plasma resistivity and discharge dimensions, and comparisons with experiment:

$$R = \eta h / w\delta \qquad (3)$$

where η is the plasma resistivity ($\simeq 2 \times 10^{-4}$ Ω-m), and h, w and δ are the length, width and (streamwise) thickness of the discharge, respectively. Values from the OSU/LeRC benchmark PPT are 32 mΩ and 19.5 mΩ, for capacitor values of 10 and 30 µf, respectively [3]. These benchmark experiments also provide values for the mass per unit of initial energy of 1.43 µg/J and 1.28 µg/J for the lower and higher values of capacitance.

The principal difficulty in attempting to use zero-dimensional modeling (vs full numerical simulation techniques[4]) to evaluate PPT behavior over a range of operating parameters is that values of plasma mass obtained empirically do not predict the mass that would be accelerated under circuit conditions that are significantly different from the available experiments. In the initial calculations here, the mass for the first PPT is based on the energy stored originally in the capacitor, while the mass for the second PPT is based on the energy stored in the inductor just prior to switching, in both cases using the mass per unit energy values for the experiments with the respective capacitors.

An additional area of design uncertainty is the allowable length for acceleration of the plasma-slug. Ideal analysis of energy transfer from inductively-stored energy to the kinetic energy of a moving conductor yields an efficiency that is merely the change in circuit inductance divided by the instantaneous value of total circuit-inductance. Thus, the longer the acceleration distance for a given L', the higher the transfer efficiency. For plasma-slugs of finite dimensions, however, loss of plasma (mass, momentum and energy) to viscous drag and condensation on solid surfaces, and disruption of the plasma-slug integrity by instabilities should limit the practical electrode length for acceleration. Table I displays results from surveys of PPT performance with the inductive-drive circuit for a selection of electrode lengths. (The circuit has been burdened with the series resistances for the capacitor and plasma as discussed above. In the first two cases, the accelerated mass is based on the empirical data.)

It should be noted that the higher values of efficiency and speed indicated for the longer electrode lengths would be accessible at fixed proportions (h/w) for the plasma discharge, if the total energy (per pulse) of the system is increased. By increasing the plasma-slug mass in proportion to the energy, at fixed L', the same plasma acceleration is obtained, but the lateral dimensions of the plasma are larger, so the acceleration length can be increased.

The speed of the plasma, u(z,t), at any time or position would be the same. The dynamic impedance of the plasma-slug, L'u, would, therefore, also have the same history and value relative to the plasma resistance (assuming fixed discharge thickness, δ). The longer time and distance for plasma acceleration then allows the inductive store to be drained of energy more completely. Figures 5 and 6 display, respectively, the current and voltage behavior of the circuit and the dynamic behaviors of the plasma-slugs. The dimensions and energies for this calculation are h = w = 2.5 cm, and the initial energy is 20 J in a 30 µf capacitor; the storage inductor value is 1 µH, (with an additional 42 nH for the connection inductance to the first PPT in the benchmark system).

Recent numerical simulations [4], for example, suggest that as little as 10% of the mass loss per shot is actually accelerated electromagnetically; the remaining mass evolves over the time between thruster firings. Thus, the empirical scaling may be quite inaccurate. For the new circuit, furthermore, it is possible to operate each PPT with its own set of conditions. For example, the first PPT could be designed in conventional fashion with the ablating propellant surface filling the gap between the electrodes. The second PPT, however, could be arranged so that only a portion of the insulator readily ablates. In this way, the mass accelerated in the second PPT might be much less than in the first. Figures 7 and 8 provide results from a sample calculation in which the second PPT uses about one-tenth of the mass of the first (2.5 vs 25.6 µg). The other circuit parameters and the discharge dimensions are the same as for Figures 5 and 6. Table I indicates the variations of performance with electrode length, and suggests the complexity of design choices for relative masses and lengths.

QUASI-STEADY CALCULATIONS

It is possible to operate ablation-fed, pulsed plasma thrusters in quasi-steady mode, if the timescale for variation of the discharge current is long compared to flow transit-times and the electrode geometry is adjusted to force high current-density near the propellant surface. The latter condition recognizes the tendency for the discharge to propagate downstream along available (exposed) electrodes rather than remain adjacent to the propellant surface. (The discharge may stop at the ends of the electrodes and run off eroded material for the duration of the current pulse, but this is not usually an acceptable operating mode.) By restricting the exposed electrode extent (in the stream-

---

TABLE I
VARIATION OF PERFORMANCE WITH ELECTRODE LENGTH

(PPT1 / PPT2 Values for z and u)

C = 10 µf, E = 20 J, L = 1 µH

z [cm]	u [km/s]	ε [%]
2.5 / 1.3	4.5 / 4.2	2.1
5.0 /3.6	5.5 / 5.4	3.2
10 / 8.7	6.1 / 6.3	4.2
15 / 14	6.3 / 6.7	4.5

C = 30 µf, E = 20 J, L = 1 µH

z [cm]	u [km/s]	ε [%]
2.5 / .03	5.5 / .6	1.7
5.0 / 1.2	7.1 / 5.5	4.1
10 / 5.6	8.7 / 7.8	6.8
15 / 10.2	9.5 / 8.9	8.4

C = 10 µf, E = 20 J, L = 1 µH

[m1 = 28.6 µg , m2 = 2.5 µg]

z [cm]	u [km/s]	ε [%]
2.5 / 9.9	4.4 / 32.1	7.2
5.0 /28.3	5.2 / 39.4	10.6
10 / 68.2	5.6 / 45.5	13.9
15 / 109	5.7 / 47	14.8

C = 30 µf, E = 20 J, L = 1 µH

[m1 = 25.6 µg , m2 = 2.5 µg]

z [cm]	u [km/s]	ε [%]
2.5 / .23	5.5 / 4.0	1.9
5.0 / 7.5	7.1 / 31.8	8.8
10 / 33.9	8.3 / 46.7	16.6
15 / 62.9	8.8 / 52	20.1

wise direction) to less than the characteristic scale-size for current conduction, adequate heat transfer to the propellant surface can be maintained.

Based on previous analysis [1], the thickness of this conduction region is:

$$\Delta = 1 / \sigma\mu u_1 \qquad (4)$$

where σ is the electrical conductivity. The flow speed is that for the current-free, one-dimensional MHD channel immediately downstream of the conduction region:

$$u_1 = (2\,Q_a / m)^{1/2} \{1 + \gamma^2\theta / (\gamma-1)\}^{1/2} \qquad (5)$$

where Q_a is the energy absorbed in dissociation and ionization of a flow molecule of mass m, and

$$\theta = RT_1 / Q_a \qquad (6)$$

is the plasma temperature T_1 at sonic conditions in the MHD channel, normalized by Q_a; γ is the effective specific heat ratio for the frozen flow at this temperature. For a fully singly-ionized, single-temperature plasma, $R = 2k/m$, to account for the free electrons.

The voltage across the channel is merely the product of channel height, h, and the electric field in the current-free channel, $E = -u_1 B_1$, where the magnetic field in the channel:

$$B_1 = \mu\, J / 2w \qquad (7)$$

is proportional to the total discharge current, J, divided by the channel width, w. The effective impedance of the thruster discharge is then:

$$Z = \mu\, u_1\, h / 2w \qquad (8)$$

Note that this is constant, independent of the instantaneous value of the discharge current, (to the extent that the plasma properties remain constant). Operation in quasi-steady mode thus offers the possibility of improved performance by matching the power source to this impedance.

From the same analysis [1], the ultimate speed for the (frozen) flow from the thruster is:

$$u_f = (2\,Q_a / m)^{1/2} \{3 + \theta\, [(4\gamma^2 + 5\gamma + 1)/2(\gamma-1)]\}^{1/2} \qquad (9)$$

This result assumes that the necessary expansion of magnetized plasma to a field-free vacuum is carried out along electrodes that are shaped to result in axially-directed flow at the thruster exit, (analogous to the simple design of supersonic nozzles expanding flow from sonic conditions at a throat.)

With the directed kinetic energy of the exhaust flow determined by the same plasma properties that specify the internal energy of the flow, the ideal efficiency may be found:

$$\varepsilon_i = u_f^2 / [\, u_f^2 + 2\,(Q_a/m)(1 + \gamma\theta / (\gamma - 1))]$$

$$= \frac{\{3 + \theta\, [(4\gamma^2 + 5\gamma + 1)/2(\gamma-1)]\}}{\{4 + \theta\, [(4\gamma2 + 7\gamma + 1) / 2(\gamma-1)]\}} \qquad (10)$$

With T_1 = 2 eV and Q_a = 61.5 eV, ($\theta \ll 1$), the ideal efficiency of a quasi-steady plasma thruster can exceed 82%, for reasonable values of specific heat ratio ($\gamma \simeq 1.4$). The actual efficiency will depend on the total system behavior, especially the relative loss to circuit resistances outside the thrust chamber and to electrode falls.

With knowledge of the energy deposited per unit mass in the propellant, and the power delivered to the thrust chamber (as the product of voltage and current), the instantaneous mass flow rate can be computed. This rate may then be integrated over time to obtain the mass generated per pulse. The exhaust speed for the present model of quasi-steady operation is constant, so the impulse-bit per pulse is merely the product of this speed and the total mass ejected.

Figure 9 displays the current and voltage waveforms for the inductive circuit driving two identical PPTs with equal dimensions (h = w = 2.5 cm). For this calculation, the storage inductance is 1.042 μH, and the capacitor initially stored 20 J at 2000 V (C = 10 μf). The mass ejected by the first PPT is 15.1 μg, and the second PPT ejects 14.6 μg. (The difference is due to the mass ablated in the first PPT during the initial current-rise.) The exhaust speed for both PPTs is 31.9 km/s, providing a thrust efficiency of 75%. If the series resistance of the inductor is designed to be much lower than the sum of the thruster impedances, the only significant departures from the ideal efficiency value are due to the series resistance of the capacitor and the electrode fall voltages. In the present calculations, the impedance of each thruster (from Eqn. 6) is 11.1 mΩ, so their total load impedance is 22.2 mΩ. The series resistance of the inductive store is neglected compared to this value, but the series resistance of the capacitor is based on experimental values (16 mΩ). The loss due to resistance in the capacitive leg of the circuit occurs primarily during the initial current rise in the inductive store. (In the conventional LRC-circuit, the relatively high series-resistance of the capacitor compared to the PPT impedance seriously limits performance.)

Losses associated with electrode falls are important, but have not been included here in order to focus on the basic MHD and circuit behavior. For example, using a capacitor based on the OSU/LeRC benchmark PPT, the reversed-voltage is only about 10% of the rated-voltage of the capacitor (5 kV), thereby offering improved capacitor lifetime and reliability. Also, a survey of behavior over several values of voltage, energy and storage inductance indicates that (as expected) the mass evolved per unit of initial energy in the capacitor varies only slightly from 1.2 μg/J at L=100nH to 1.6 μg/J at L=2μH. (Curiously, these values for mass production are rather close to those found empirically, which include, however, substantial mass loss during the time between shots.)

CONCLUDING REMARKS

The new inductive-drive circuit offers the opportunity to match plasmadynamic processes, such as quasi-steady operation, that require longer timescales to evolve. This is accomplished by using an inductor to store energy, rather than demanding a capacitor capable of providing high energy per unit mass at the relative low total energies envisioned for small-satellite propulsion requirements. Quasi-steady operation of a PPT appears to provide much higher values of specific impulse and thrust efficiency than unsteady plasma-slug acceleration (with either LRC or inductive-storage circuits). Values of specific impulse of 3000 sec and thrust efficiencies in excess of 50% may be possible. Future calculational effort will examine the effects of electrode fall voltages, and will also attempt to incorporate the results of more detailed, numerical simulations of the PPT in order to utilize more appropriate values for plasma-slug mass. Experiments with the new inductive circuit are planned using the benchmark PPT system in its two-thruster configuration. Both plasma-slug and quasi-steady modes will be studied.

ACKNOWLEDGEMENTS

The authors would like gratefully to acknowledge the assistance of I.G. Mikellides and P.G. Mikellides in preparation of the manuscript, and the encouragement of Roger M. Myers.

Work supported by the NASA Lewis Research Center, Cleveland, OH, under NAG3-843, and The Ohio State University. One of the authors (RJL) was sponsored by the AFOSR Summer Research Program at Phillips Laboratory, Edwards AFB, during a portion of this work.

REFERENCES

1. P.J. Turchi and P.G. Mikellides, "Modeling of Ablation-Fed Pulsed Plasma Thrusters," AIAA Preprint 95-2915.

2. W.J. Guman and D.M. Nathanson, "Pulsed Plasma Microthruster Propulsion System," J. Spacecraft and Rockets, 7, 409 (1970).

3. H. Kamhawi, P.J. Turchi, R.J. Leiweke, R.M. Myers, "Design and Operation of a Laboratory Benchmark PPT," AIAA Preprint 96-2732.

4. P.G. Mikellides and P.J. Turchi, "Modeling of Late-time Ablation in Teflon Pulsed-Plasma-Thrusters," AIAA Preprint 96-2733.

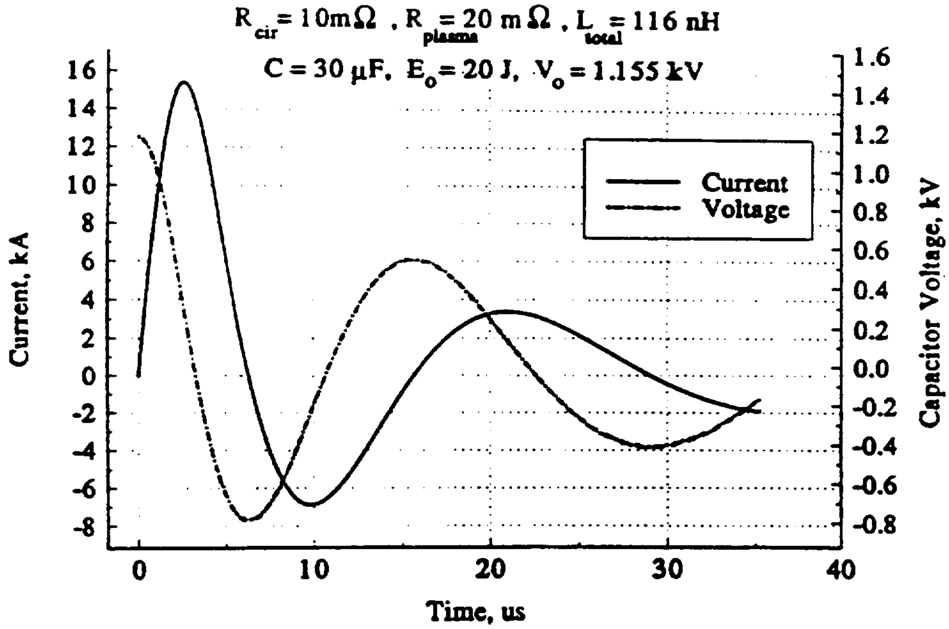

Figure 1: Current and voltage waveforms for PPT driven by LRC circuit.

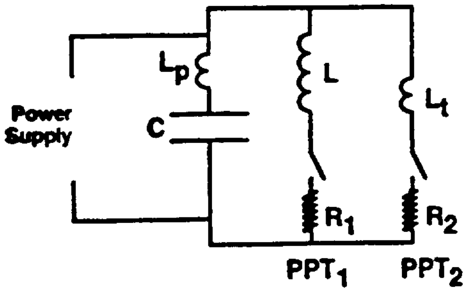

Figure 2: Schematic diagram of new inductive storage and switching circuit for driving pulsed plasma thrusters, indicated as resistors R$_1$ and R$_2$.

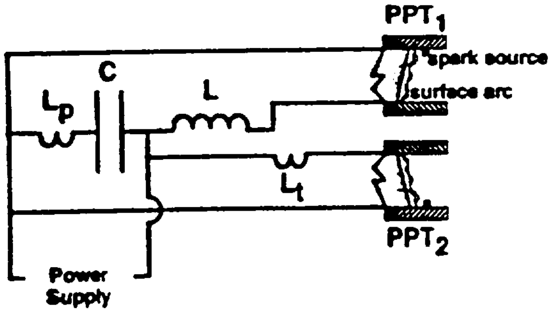

Figure 3: Schematic diagram depicting connection of new circuit to PPTs. Note PPT$_2$ does not carry current until triggered after the capacitor voltage reverses sign.

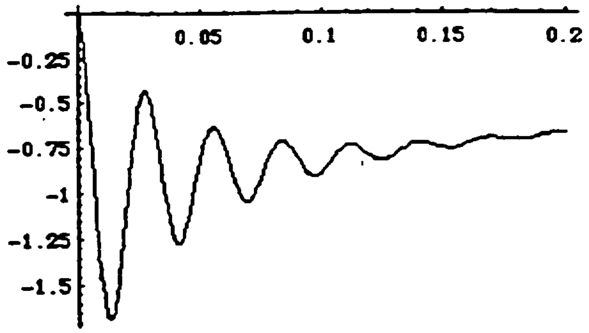

Figure 4a: Current vs time through PPT$_2$ for idealized calculation of circuit in Fig.2. Current in units of current in L at time of switching, time in units of L/R$_2$.

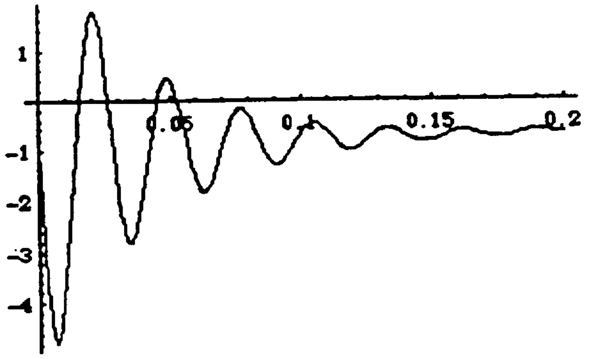

Figure 4b: Capacitor voltage vs time in units of voltage at time of switching (t=0).

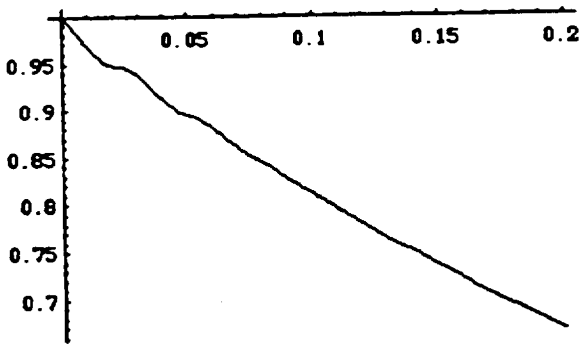

Figure 4c: Inductor current vs time in units of inductor current at t = 0.

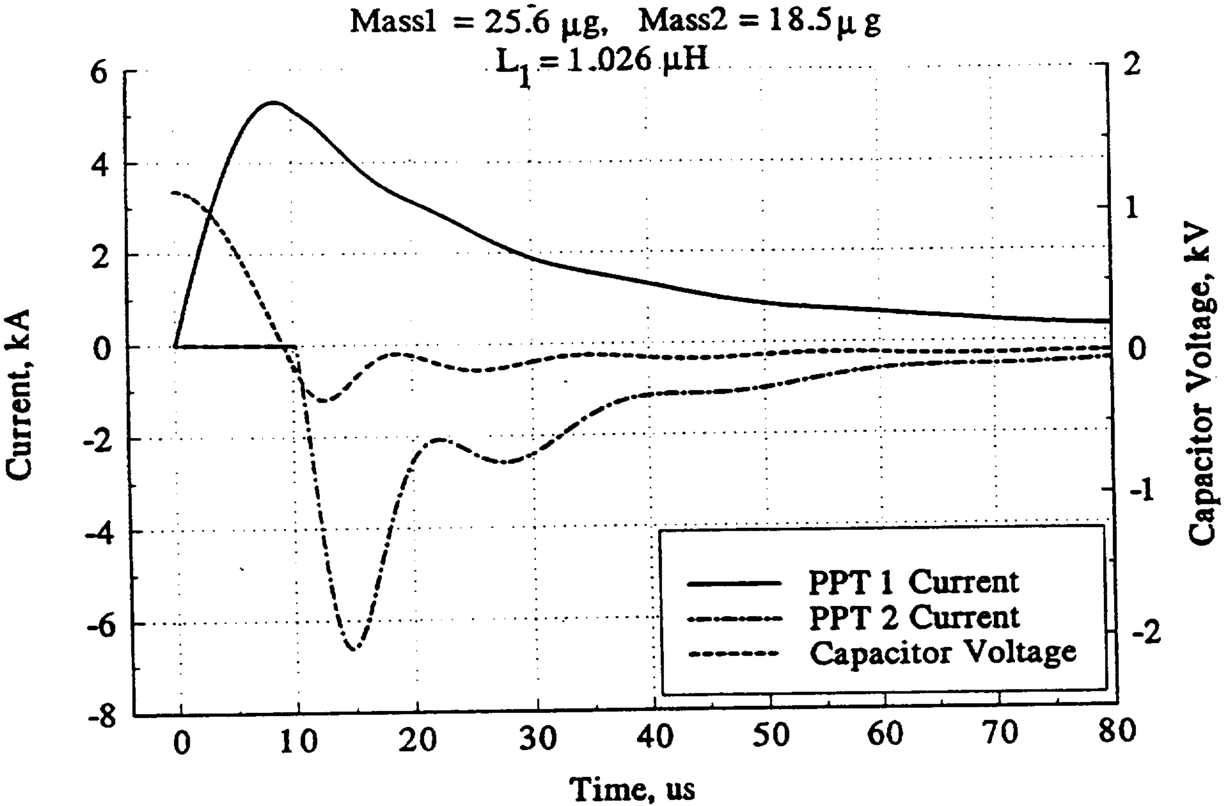

Figure 5: Currents and capacitor voltage vs time for inductively-driven PPTs, using energy-based, empirical scaling for plasma-slug masses.

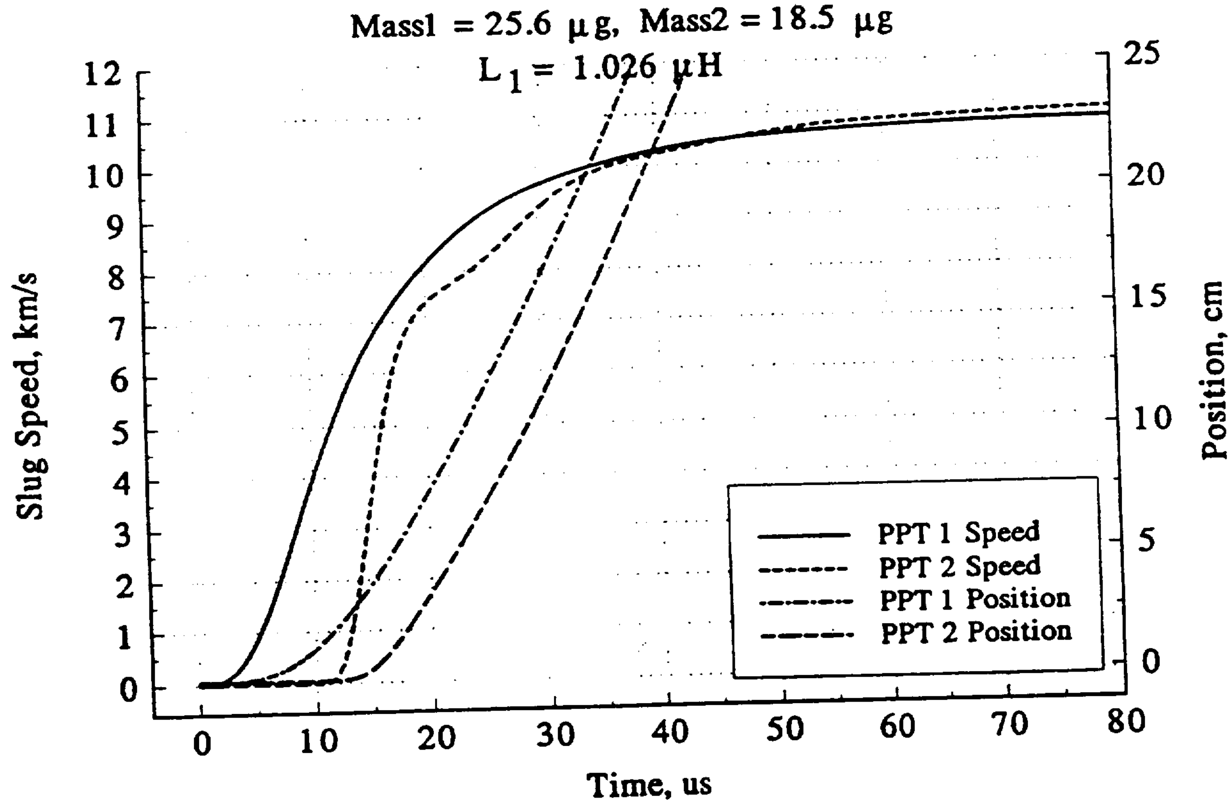

Figure 6: Speeds and positions of plasma-slugs for conditions of Fig. 5.

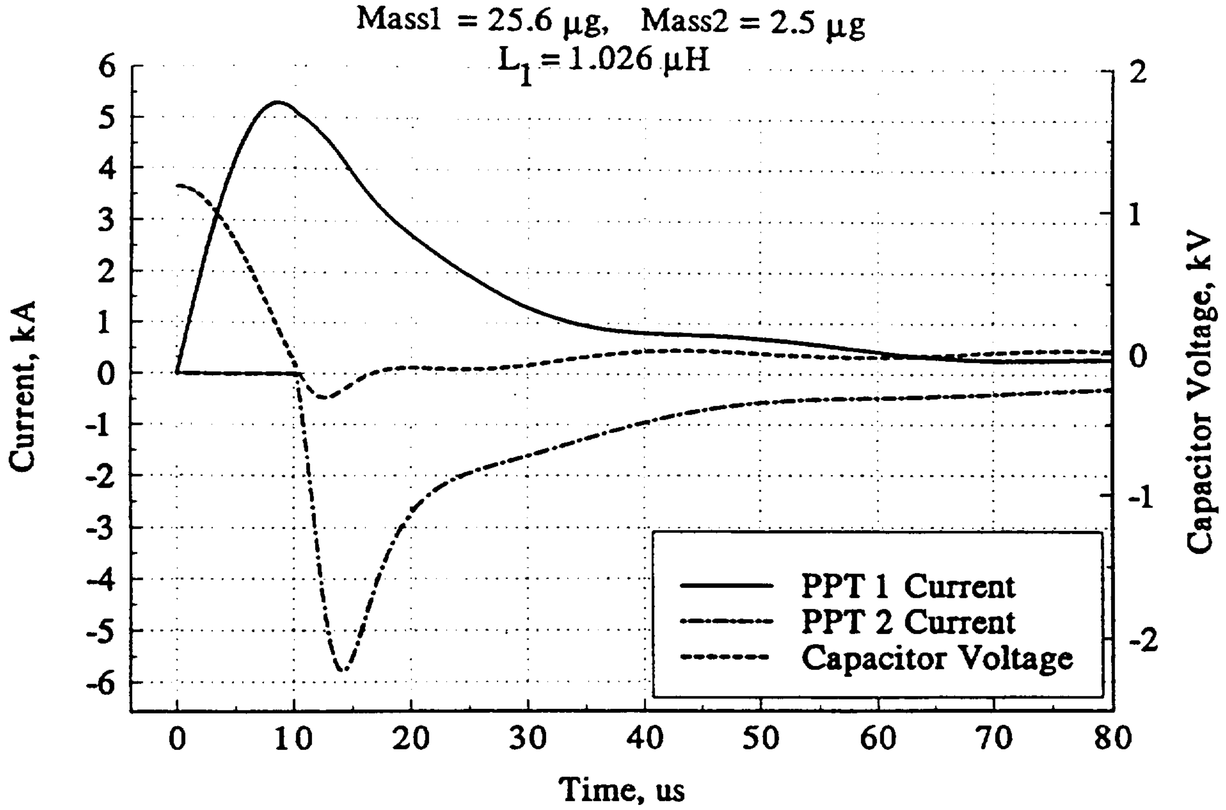

Figure 7: Currents and capacitor voltage vs time for inductively-driven PPTs, with mass in first PPT from empirical scaling, and mass in second PPT specified much smaller.

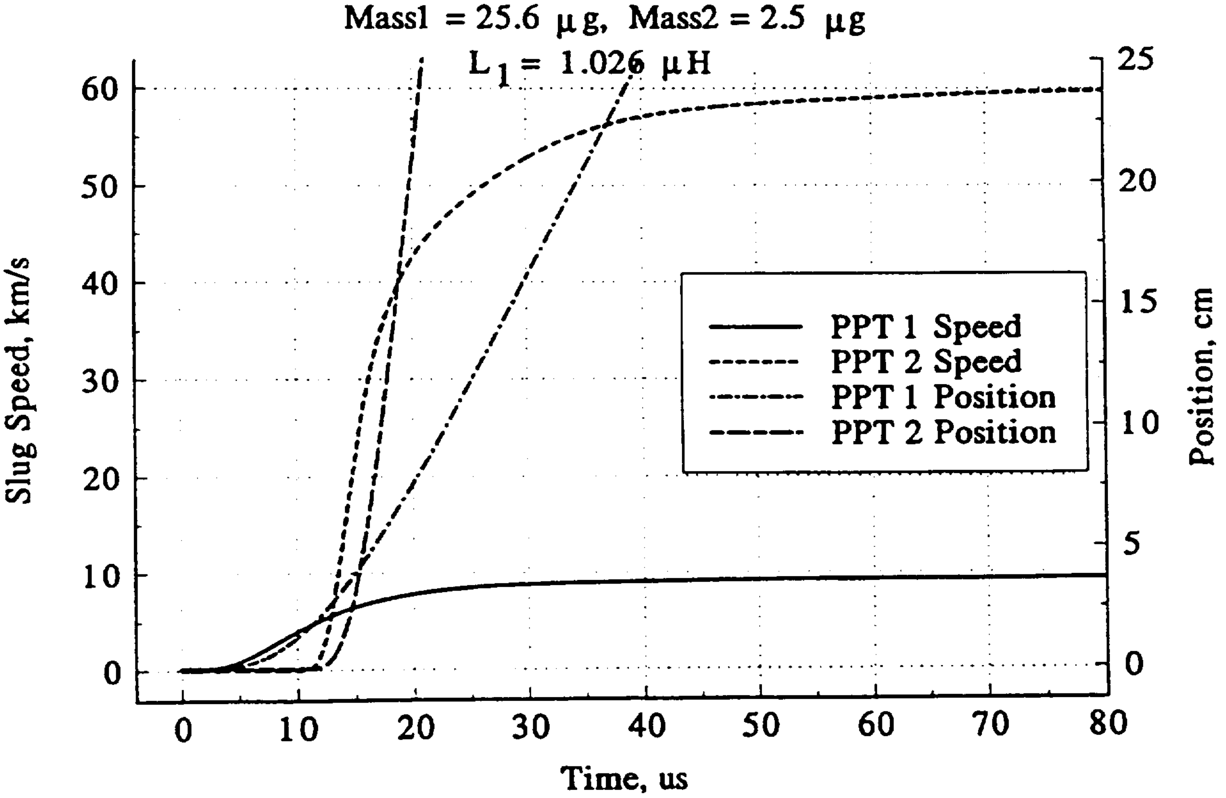

Figure 8: Speeds and positions of plasma-slugs vs time for conditions of Fig. 7.

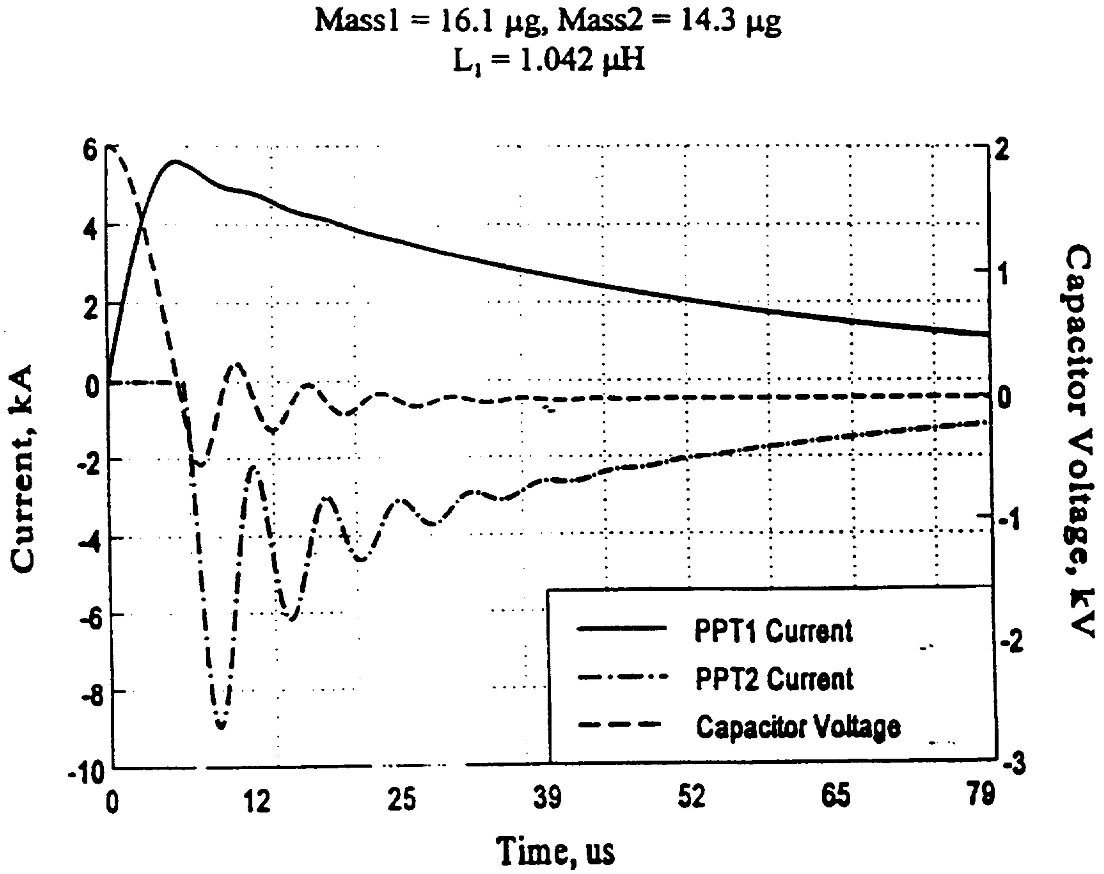

Figure 9: Currents and capacitor voltage vs time for PPTs operating in quasi-steady mode with new inductive-storage and switching circuit.

AIAA 96-2732

DESIGN AND OPERATION OF A LABORATORY BENCH-MARK PPT

H. Kamhawi, P.J. Turchi, and R.J. Leiweke
The Ohio State University
Columbus, OH

R.M. Myers
NYMA Inc.,
Cleveland, OH

32nd AIAA/ASME/SAE/ASEE
Joint Propulsion Conference and Exhibit
July 1-3, 1996/Lake Buena Vista, FL

DESIGN AND OPERATION OF A LABORATORY BENCHMARK PPT

H. Kamhawi, P.J. Turchi, R.J. Leiweke, The Ohio State University, Columbus, OH,
and R.M. Myers, NASA Lewis Research Center/NYMA, Cleveland, OH

ABSTRACT

The pulsed plasma microthruster (PPT) has been successfully employed in space for two decades. It has demonstrated satisfactory performance on low average-power satellites, and thus has become a candidate for future missions involving small satellites. While its specific impulse and efficiency are certainly adequate for present tasks, there is interest in achieving significant improvements through research. Many parameters determine PPT behavior, so it is useful to create a benchmark, laboratory device of sufficient simplicity and flexibility that many different research avenues may be followed within a reasonably common framework. Such a device has been designed, built and operated over a range of conditions, including variations of components (e.g., capacitors) and terminal properties (e.g., voltage). Diagnostic access is greatly improved compared to recent research using space-qualified devices that are largely sealed units. The design of the new benchmark system and experimental facility are discussed, and sample electrical and thrust-stand data are presented.

INTRODUCTION

Development of missions for small satellites has renewed interest[1] in the ablation-fed, pulsed plasma microthruster, (traditionally abbreviated simply as PPT). This interest is driven by the ability of the PPT to operate at very low average power levels (30 - 500 W), as demonstrated during two decades of successful use in station-keeping roles for the Nova and LES series satellites[2]. Several research groups have used the spacecraft-qualified PPT packages prepared, but not used, for the LES 8/9. Research has included a two-stage plasma propulsion scheme[3], in which the PPT provided a means for initiating a much higher energy, quasi-steady, plasma thruster. More recently[4] a LES 8/9 PPT was modified to permit substitution of multi-material laminates for the usual Teflon bar. The LES 8/9 package is relatively simple to use (requiring only a low voltage power supply and a modest vacuum system). While not employing modern electrical and electronic components, the PPTs still function at nominal values.

A major problem, however, is encountered in attempts to use the LES 8/9 PPTs for improving thruster performance. It is very difficult to access or change components, for example, to include a Rogowski coil for current monitoring or to alter the electrode dimensions. To achieve maximum flexibility for a research program, while retaining the basic characteristics of earlier PPTs, a new system has been designed, built and operated. It consists of a single capacitor (e.g., 10 µf, 5 kV) connected to two sets of electrodes, each of which has a semiconductor igniter. Solid propellant bars are provided between each electrode pair, in the same manner as the LES 8/9, thereby corresponding to the end-fed style of PPT. The capacitor can be housed inside a thin-walled, cylindrical container at

1 atm, in order to avoid de-pressurization of the insulating fluid. Full access to all parts of the system permits direct current and voltage measurements, variation of circuit electrical values (e.g., inductance), and alteration of electrode length and separation. Two thruster sets are combined on the same sytem to allow extension of the present design to a new, inductively-driven circuit[5]. The design is relatively trivial to build and modify, so it is reasonable to anticipate its use by several research groups. In this way a common or "benchmark" thruster can be developed for laboratory research and theoretical modeling. The present paper describes the benchmark thruster and experimental facility in detail, and provides a sample of electrical and thrust data obtained over a range of operating conditions and component choices.

EXPERIMENTAL FACILITIES

Vacuum Facility

PPT experiments were performed at NASA Lewis Research Center (LeRC) Electric Propulsion Laboratory, Cleveland, Ohio. Current and voltage measurements and mass loss data measurements were performed in the bell shaped vacuum facility 54 (VACFAC 54). VACFAC 54 has an interior diameter of 20 in. and is 39.4 in. long. A 10 in. diameter recess that is 6 in. deep allows the pumps to evacuate the chamber. VACFAC 54 is evacuated using an oil diffusion pump in conjunction with a roughing pump. The facility pressure was monitored with a RG-1002 ionization gauge and a capacitance monitor. The facility is equipped with a number of feedthrough flanges that can be used for thermocouple, BNC, and high voltage connections. In addition, the facility had Plexiglas windows that permit visual inspection of thruster assembly.

Screen Room and Grounding Plane

To eliminate and minimize EMI and RFI noise pick-up the oscilloscope and the ignition circuit power supply were placed inside a screen room. The screen room dimensions are 19W X 19D X 48L in. A Corcom high frequency power filter was used to filter the power input into the screen room. A 6 in. wide, 6 in. long copper ground plane extends from the screen room side wall to the vacuum facility BNC feed through flange. The PPT is placed on the grounding plane inside VACFAC 54. The PPT's ground transmission line attaches to the ground plane. The coaxial cable leads from the Rogowski coils and the voltage lead were traced and taped along the grounding plane so that EMI pickup is minimized.

High Voltage Power Supply

A Kepco BHK 2000 V- 0.10 Amp high voltage power supply was used to charge the capacitors to the desired operating voltages. Two high-frequency filters were built to protect the high voltage power supply from any high frequency oscillations that occur when the PPT is fired. In addition, high voltage diodes were used to protect the power supply from the voltage reversal that occurs when the PPT is fired.

BENCHMARK PPT THRUSTER

The basic layout of the benchmark PPT is depicted in Figure 1 which shows a schematic of the thrust chamber and connecting plates. Figure 2 shows an overall view of the actual thrust chamber.

Electrodes

Two sets of oxygen-free-copper electrodes were made. Each set consists of an anode and a cathode. For the first electrode set, the anode is 1.5 in. long and the cathode is 1.75 in. long. For the second electrode set the anode is 2.5 in. long and the cathode is 2.75 in. long, both sets are 1 in. wide. The anode electrode has a 0.035 in. deep shoulder at a distance of 0.5 in. from the anode bottom surface, while the cathode has a 0.5 in. hole for the ignition spark plug location, centered at 1.065 in. from the cathode bottom surface.

Transmission Line

The PPT transmission line was made from 0.25 in. thick aluminum. The ground line is 12.6 in. long and is 3.6 in. wide. The hot line is 8.5 in. long and is 1 in. wide. The ground line has two 2.6 in. X 2.6 in. square openings to allow for the insertion of the hot electrodes and a Plexiglas assembly insulating the region of Teflon feed. The hot line is wrapped with 3 layers of 0.010 in. thick Teflon for electrical insulation.

Propellant Feed Assembly

The Teflon feed assembly was made of Plexiglas. A spring, ty-wrapped to the end piece of Plexiglas pushes the Teflon fuel bar against the shoulder in the anode. The side Plexiglas pieces guide the Teflon fuel bar. In addition, the Plexiglas assembly insulates the anode from the ground transmission line, this is necessary to prevent any voltage breakdowns.

Capacitors

Two pulse discharge, oil-filled capacitors from Maxwell Laboratories Inc., were used, with capacitance values of 10 μf and a 30 μf (actual 31.3 μf)[7]. The 10 μf capacitor has a metal drawn can with double rolled seams. It has a 5 kV voltage rating with a maximum peak current rating of 25 kA. It is 3.5 in. wide, 1.75 in. deep, 7.25 in. long, and weighs 2.7 lbs. As for the 30 μf capacitor, it has a cylindrical metal case. It has a 2 kV voltage rating with a maximum peak current rating of 25 kA. It has a 3.3 in. diameter, 3.5 in. long, and weighs 2.2 lbs.

Spark Plug and Exciter Ignition Circuit

The arc discharge is initiated via a spark plug. The spark plug, ignition exciter circuit, and the ignition lead are manufactured by Unison Industries Inc. The ignition exciter circuit is capable of firing the spark plug at different frequencies by controlling the input voltage to the circuit. The circuit has an input voltage range between 10 to 30 Vdc and an input current range up to 3.5 amps[8]. The total ignition exciter stored energy is approximately 4.7 J and the spark plug energy is 1.3 J which is 28% of the ignition exciter circuit[8]. A Kepco JQE 36V-3A power supply was used to power the ignition circuit. Tests were performed to confirm that the exciter ignition circuit and spark plug do operate in a vacuum environment. The tests were conducted at a pressure of 4 X 10^{-6} Torr. The results indicated that the circuit and spark plug fire successfully for extended periods of time. Voltage across the spark plug terminals was measured, breakdown voltages varied between 400 to 1200 volts. An input voltage of 10 Vdc was used to fire the spark plug at a rate of 1pps.

Capacitor Housing

The 10μF capacitor is housed inside a thin-walled cylindrical container at 1 atm to avoid de-pressurization of the insulating fluid inside the capacitor can. Figure 3 shows an overall view of the benchmark PPT with the 10 μf capacitor inside the pressurized enclosure. The container has an I.D. and O.D. of 4.75 and 5.0 in., respectively and is 7.5 in. long. At one end, the cylindrical shell is welded via a vacuum tight weld to a circular aluminum plate that serves as the base for the entire assembly. On the other end, an aluminum adaptor piece that has an O-ring groove is also welded via a vacuum tight weld to the cylindrical shell. A Plexiglas plate, cap, which has two holes to allow for the aluminum studs coming out of the capacitor, is bolted to the aluminum adaptor piece. Aluminum collar-pieces screw into the capacitor brass studs and make contact with the steel windings which are around the base of the capacitor studs. The middle section of the aluminum collar pieces is threaded to permit mechanical pressure to compress the O-rings around the flat portion of the aluminum collar pieces. The PPT transmission line is placed onto the collar pieces and screws are used to hold it in place.

As for the 30 μF capacitor, it is not housed inside a de-presurrized chamber because tests at Olin Aerospace showed that there was no evidence of leakage. But as a precaution Varian Torr Seal® was epoxied around the base of the hot stud. Figure 4 shows an overall view of the benchmark PPT with the 30 μf capacitor.

EXPERIMENTAL RESULTS

Voltage and Current Waveforms

Two Rogowski coils were constructed, one was placed around the hot aluminum collar piece (Rogowskil A) and the other around the ground aluminum collar piece (Rogowski B). Rogowski A has 45 turns of 20 gauge wire wrapped around a toroidal plexiglass piece that has an I.D. of 0.82 in., O.D. of 1.22 in., and is 0.210 in. thick. Rogowski B has 36 turns of 20 gauge wire wrapped around a toroidal Plexiglas piece that has an I.D. of 0.82 in., O.D. of 1.10 in., and is 0.140 in. thick. Both Rogowski coils were calibrated using an LRC circuit. The calibration circuit consisted of a single turn inductor made by wrapping square wire around a 2 in. O.D. PVC pipe. A 0.15 μf 2000 Vdc capacitor was used in conjunction with an inductor made in-house to provide the desired period for the corresponding voltage and current waveforms. The output of both Rogowski coils exceeded the range allowed on the oscilloscope used , therefore, two 50Ω voltage dividers were made. For Rogowski A the signal was measured across a 1.5 Ω resistor, while for Rogowski B the voltage was measured across a 0.8 Ω resistor. The output of the Rogowski signals was integrated numerically. A model 101 Pearson wide band current monitor was used to measure the current in the circuit, it has an output of 0.01 volt/amp with a 1% accuracy[9]. In addition, since the circuit parameters were known a code was written to predict the current and voltage waveforms of the calibration LRC circuit. The LRC circuit was triggered by the closing of a hand knife switch. Fifteen calibration shots were taken for each Rogowski coil, for Rogowski A an average calibration number of 1.75×10^9 volt/amp was computed with a discrepancy of ±3%, while for Rogowski B a calibration number of 1.82×10^9 volt/amp was computed with a discrepancy of ±3.5%.

Two Tektronix voltage probes were used to measure the voltage across the capacitors output terminals. A P5100 100X 2500V 100 MHZ voltage probe[10] and a P6015A 1000X high voltage probe[10]. Prior to data acquisition the voltage probes were compensated and calibrated.

Several PPT firings were performed to determine the circuit external parameters (i.e, the resistance and inductance of the transmission line and the parasitic resistance and inductance of the capacitor), the PPT was fired across a 0.125 in. gap and across a 0.047 in. gap for the 30 µf capacitor and only across a 0.047 in. gap for the 10 µf capacitor. Current and voltage measurements were taken at different capacitor voltages ranging from 700 to 1300 volts for the 30 µf capacitor and ranging from 700 to 1880 volts for the 10 µf capacitor. Results showed that for the 30 µf capacitor setup $R_{ext}=0.01\ \Omega$ and $L_{ext}=0.093\ \mu H$, while for the 10 µf capacitor setup $R_{ext}=0.016\ \Omega$ and $L_{ext}=0.116\ \mu H$.

Current and voltage waveforms were obtained for the one-inch electrode set at 10 and 20J for the 10 µf capacitor and at 20 J for the 30 µf capacitor. The measured voltage waveform had to be corrected to account for the effect of inductive pickup due to the existence of mutual inductance across the leads of the voltage probe. The value of mutual inductance was found by theoretically predicting the voltage waveform from the circuit parameters predicted from the current waveform. Then, at the peak negative voltage the value of mutual inductance was computed according to

$$M=\frac{(V_{predicted}-V_{measured})}{(\frac{dI}{dt})}$$

where M is the mutual inductance in Henrys and dI/dt is in amps/sec. In addition, the discrepancy between the ground and hot current waveforms was found to be 5% due to different current return paths of the ground side.

Figures 5, 6 and 7 present the experimental current and voltage waveforms for the 10 µf and 30 µf capacitors. From Figure 5, for the 10 µf capacitor at 10 J, the computed circuit parameters are L=0.13 µH and R=0.051 Ω with a peak current of 10 kA. In Figure 6, for the 10 µf capacitor at 20 J, the computed circuit parameters are L=0.13 µH and R=0.044 Ω with a peak current of 14.8 kA. In Figure 7, for the 30 µf capacitor at 20 J, the computed circuit parameters are L=0.11 µH and R=0.031 Ω with a peak current of 16.8 kA.

Mass Loss Data

Mass loss data were obtained for the one-inch electrode set at 10 and 20 J for the 10 µf capacitor and at 20 J for the 30 µf capacitor. To determine the number of pulses required to reach the steady state mass loss rate, the PPT with the 10 µf capacitor was fired for approximately 10,000 and 20,000 pulses. The mass loss rate per shot for 10,584 pulses was 29.6 µg/shot (1.48 µg/J), while for 19,946 pulses the mass loss rate was 28.57 µg/shot (1.43 µg/J). Since the discrepancy between the two mass loss rates was less than 4% it was decided that the remainder of the mass loss data for the different electrode configurations and energy levels would be obtained at approximately 10,000 pulses. For the 10 µf capacitor at an energy level of 10 J the mass loss rate was 11.6 µg/shot (1.16 µg/J). For the 30 µf capacitor at an energy 20 J the mass loss rate was 26.5 µg/pulse (1.325 µg/J). The mass loss rates obtained for the 10 µf and 30 µf capacitors at 20 J were found to be comparable to earlier results for a similar configuration and energy level[4,11].

Impulse-Bit and Average-Thrust Measurements

Impulse-bit and average-thrust measurements were performed in Tank 8 vacuum facility at NASA LeRC. The thrust stand used is a torsional-type capable of measuring thrust of PPT's in single shot or repetitive firing modes[12]. The thrust stand was calibrated using three weights of approximately 25 mg each. The PPT was mounted onto the thrust stand via specially made Plexiglas mounting plate. The ignition exciter circuit was mounted on the thrust stand's torsional arm. Figure 8 shows the benchmark PPT mounted on the thrust stand.

Impulse-bit and average-thrust measurements were obtained for the 30 µf capacitor for two different electrode configurations. For the first configuration the electrode length was 1 in. while for the second configuration the electrode length was 2 in. For both configurations the electrode width and the spacing between the electrodes was 1 in. For both configurations, data were obtained at energy levels of 10, 20, 30, 40, 50, and 60 J. At each energy level, the thruster was fired 5 times in a single shot mode and was run for 2 minutes at a rate of 1 pps for the average thrust data. Figures 9 and 10 present impulse-bit and average-thrust data for the one-inch electrode set, while Figures 11 and 12 present the results for the two-inch electrode set. Figures 9, 10, 11, and 12 show that the impulse-bit and average-thrust increase linearly with the energy level. Comparisons of Figures 9 and 11 show that the impulse bit values are 24% higher for the one-inch long electrodes when compared to the two-inch electrode for all the energy levels that were investigated.

CONCLUDING REMARKS

The present benchmark system has already provided useful data for theoretical modeling efforts, including zero-dimensional[4] and numerical simulation[5] techniques. It has also helped to identify sources of experimental error (e.g., induced voltage pickup) that are difficult to evaluate long after experiments are completed and published. To date, basic PPT scaling of mass loss and impulse-bit with stored energy has been observed. It will soon be possible to make close comparisons of theoretical predictions for improved performance and the results of experiments based on such predictions. In particular, the relationship of mass loss per shot and the thermal environment of the PPT will be examined; demonstration of inductively-driven PPTs will be attempted, and quasi-steady operation will also be investigated, all within the same basic apparatus.

ACKNOWLEDGMENTS

The authors would like gratefully acknowledge the assistance of Tom Haag in obtaining the impulse-bit and average-thrust measurements.

Work supported by the NASA Lewis Research Center, Cleveland, OH, under NAG3-843, and the Ohio State University.

REFERENCES

1. Myers, R., Electromagnetic Propulsion for Spacecraft, AIAA 93-1086, Aerospace Design Conference, Irvine CA, Feb. 15-19, 1993.

2. W.J. Guman and D.M. Nathanson, "Pulsed Plasma Microthruster Propulsion System", J. Spacecraft and Rockets, No. 7, Pg. 409 (1970).

3. P.J. Turchi, J.F. Davis, C.N. Boyer, "Multi-stage Plasma Propulsion", Proc. Of 17th International Electric Propulsion Conference, Tokyo (1984). Pg. 356.

4. R.J. Leiweke, P.J. Turchi, H. Kamhawi, R.M. Myers, Experiments with Multi-Material Propellants in Ablation-Fed Pulsed Plasma Thrusters, AIAA-95-2916, Joint Propulsion Conference, San Diego, CA, July 10-12, 1995.

5. P.J. Turchi, R.J. Leiweke, H. Kamhawi, and R.M. Myers, "Experiments with Multi-material Propellants in ablation-fed, Pulsed Plasma Thrusters", AIAA Preprint 96-2731.

6. P.G. Mikellides and P.J. Turchi, "Modeling of late time ablation in Teflon Pulsed-plasma-Thrusters", AIAA Preprint 96-2733.

7. High Voltage Products Catalog, Maxwell Laboratories Inc., San Diego, CA.

8. Components Maintenance Manual, Unison Industries, Jacksonville, FL.

9. Standard Current Monitors Data Sheet, Pearson Electronics, Inc., Palo Alto, CA.

10. Instruction Manuals for P5100 and P6015A High Voltage Probes, Tektronix Inc., Beaverton, OR.

11. Thomassen, K.I. and Vondra, R.J., Flight Qualified Pulsed Plasma Electric Thrtuster for Satelite Control, J. Spacecraft, Vol. 2, No. 9, Sept 1974, AIAA 73-1067, 10th Electric Propulsion Conference, Lake Tahoe, NV, Oct. 31-Nov. 2, 1973.

12. Haag, T., "PPT Thrust Stand", AIAA-95-2917, Joint Propulsion Conference, San Diego, CA, July 10-12, 1995.

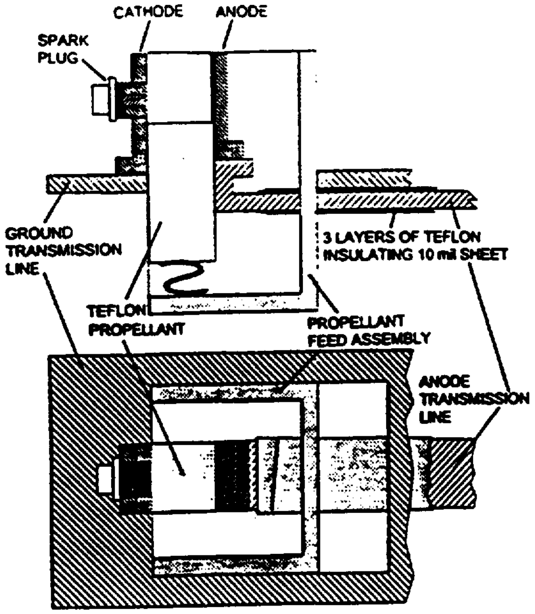

Figure 1. Schematic of thrust chamber and connecting plates.

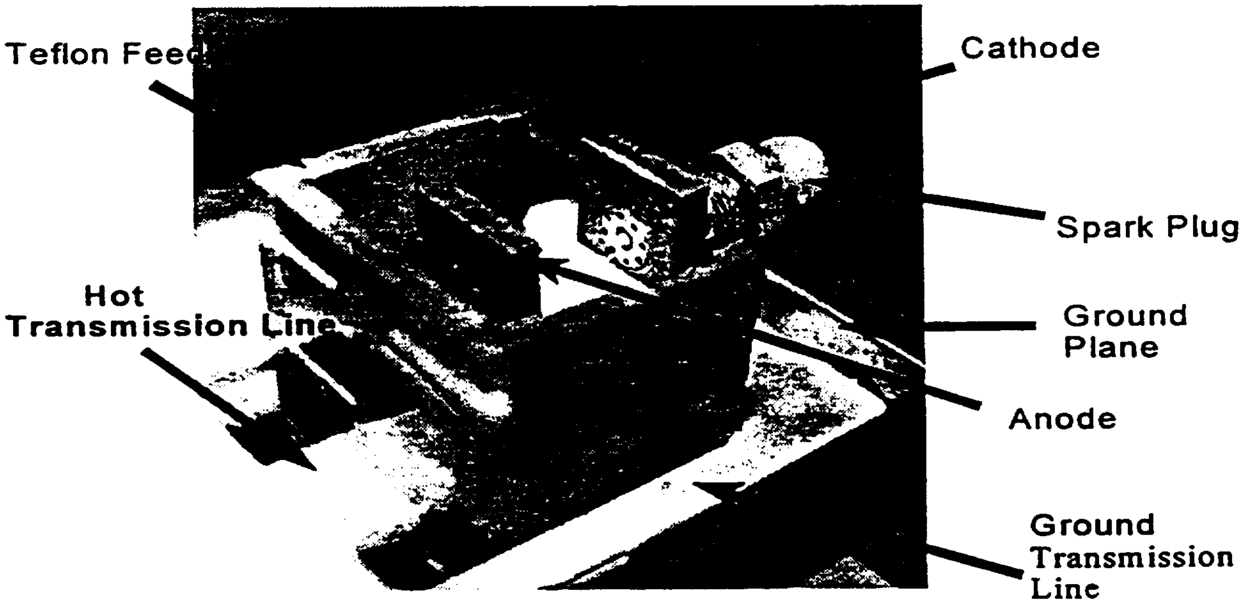

Figure 2. Overall view of the actual thrust chamber.

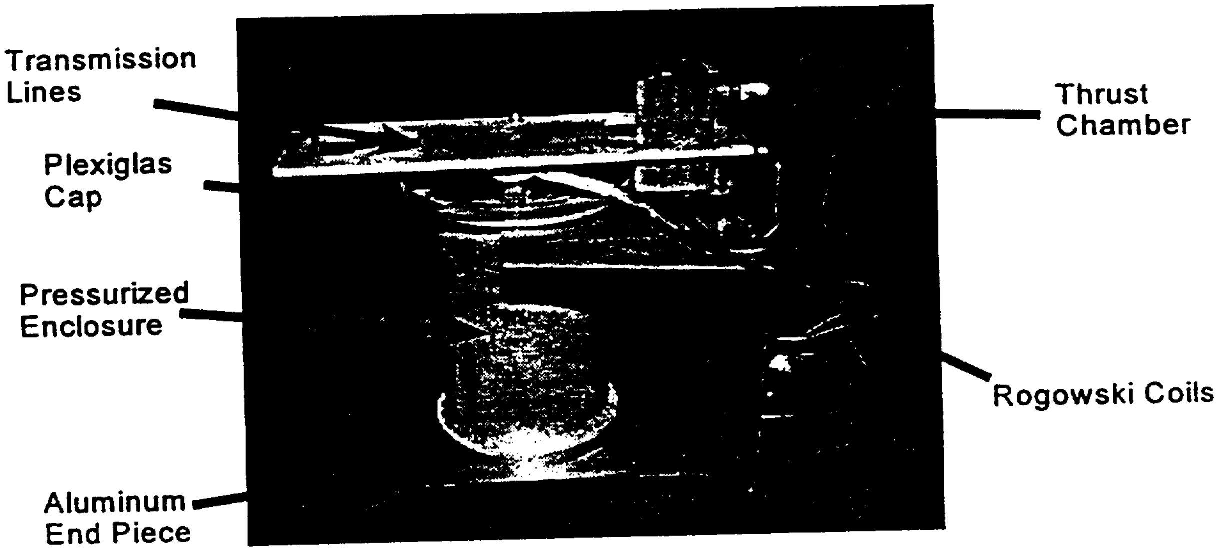

Figure 3. Overall view of the benchmark PPT with the 10 μf capacitor inside the pressurized enclosure.

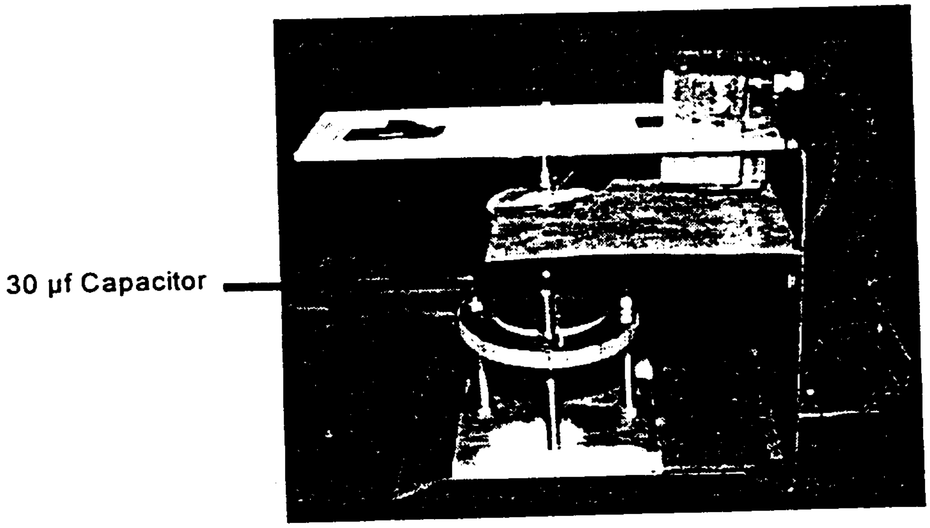

Figure 4. Overall view of the benchmark PPT with the 30 μf capacitor.

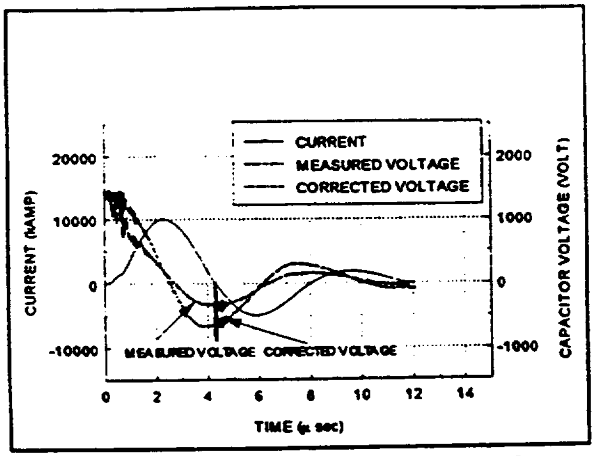

Figure 5. Current and voltage waveforms for the 10 μf capacitor at 10J.

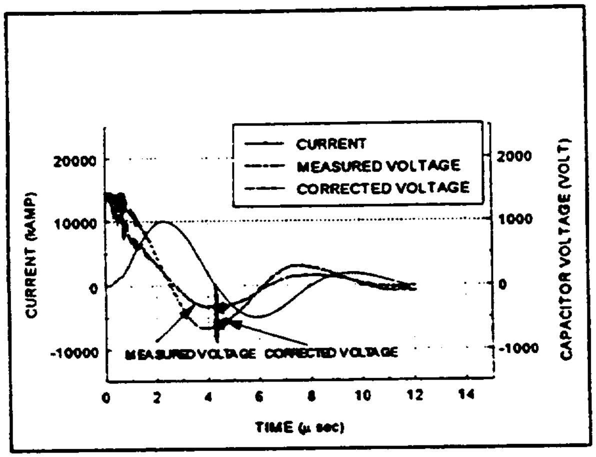

Figure 6. Current and voltage waveforms for the 10 μf capacitor and 20J.

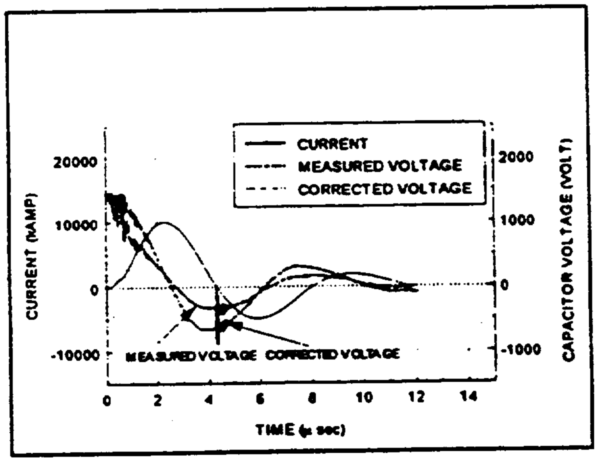

Figure 7. Current and voltage waveforms for the 30 μf capacitor at 20J.

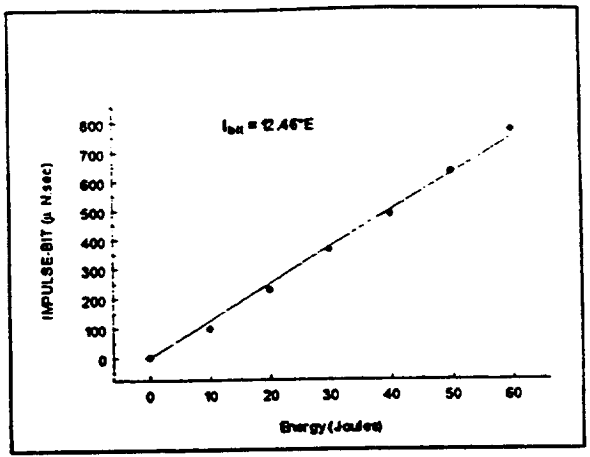

Figure 9. Impulse-bit vs energy for 30 μf capacitor, 1 in. electrodes.

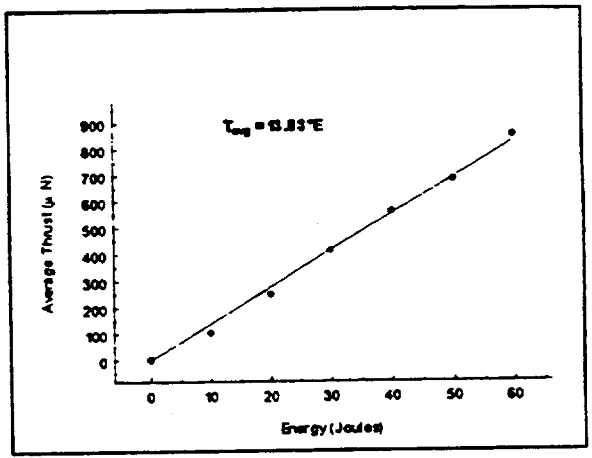

Figure 10. Average-thrust vs energy for the 30 μf capacitor,1 in. electrodes.

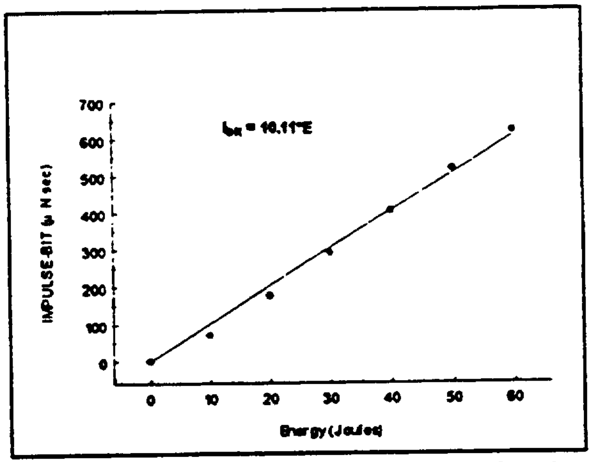

Figure 11. Impulse-bit vs energy for the 30 μf capacitor, 2 in. electrodes.

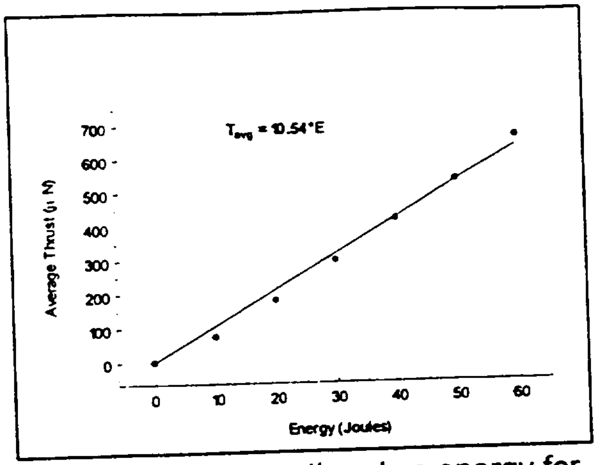

Figure 12. Average thrust vs energy for the 30 μf capacitor, 2 in electrodes.

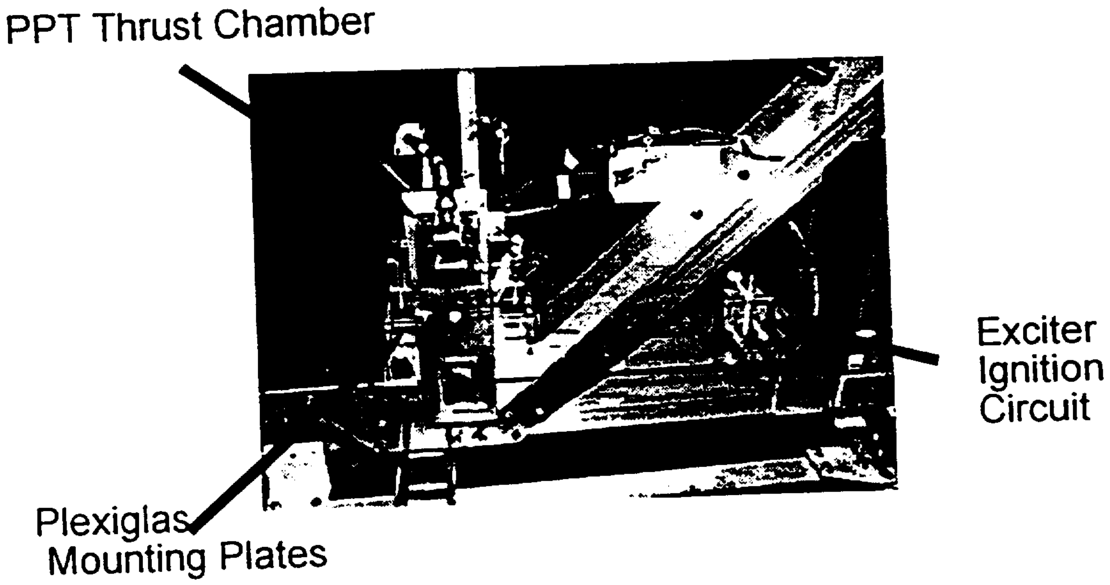

Figure 8. Benchmark PPT mounted on thrust stand.

REPORT DOCUMENTATION PAGE

Form Approved
OMB No. 0704-0188

1. AGENCY USE ONLY *(Leave blank)*

2. REPORT DATE
May 1997

3. REPORT TYPE AND DATES COVERED
Final Contractor Report

4. TITLE AND SUBTITLE
The Effects of Magnetic Nozzle Configurations on Plasma Thrusters

5. FUNDING NUMBERS
WU–242–70–01
G–NAG3–843

6. AUTHOR(S)
P.J. Turchi

7. PERFORMING ORGANIZATION NAME(S) AND ADDRESS(ES)
Ohio State University
Department of Aerospace Engineering, Applied Mechanics and Aviation
2036 Neil Ave, 328 Bolz Hall
Columbus, Ohio 43210–1276

8. PERFORMING ORGANIZATION REPORT NUMBER
E–10721

9. SPONSORING/MONITORING AGENCY NAME(S) AND ADDRESS(ES)
National Aeronautics and Space Administration
Lewis Research Center
Cleveland, Ohio 44135–3191

10. SPONSORING/MONITORING AGENCY REPORT NUMBER
NASA CR–202341

11. SUPPLEMENTARY NOTES
Project Manager, Maris A. Mantenieks, Power & On-Board Propulsion Technology Division, NASA Lewis Research Center, organization code 5430, (216) 977–7460.

12a. DISTRIBUTION/AVAILABILITY STATEMENT
Unclassified - Unlimited
Subject Category 20

This publication is available from the NASA Center for AeroSpace Information, (301) 621–0390.

12b. DISTRIBUTION CODE

13. ABSTRACT ***(Maximum 200 words)***

Over the course of eight years, The Ohio State University has performed research in support of electric propulsion development efforts at the NASA Lewis Research Center, Cleveland, OH. This research has been largely devoted to plasma propulsion systems including magnetoplasmadynamic (MPD) thrusters with externally-applied, solenoidal magnetic fields, hollow cathodes, and pulsed plasma microthrusters (PPTs). Both experimental and theoretical work has been performed, as documented in four master's theses, two doctoral dissertations, and numerous technical papers. The present document is the final report for the grant period 5 December 1987 to 31 December 1995, and summarizes all activities. Detailed discussions of each area of activity are provided in appendices: Appendix I - Experimental studies of magnetic nozzle effects on plasma thrusters; Appendix II - Numerical modeling of applied-field MPD thrusters; Appendix III - Theoretical and experimental studies of hollow cathodes; and Appendix IV - Theoretical, numerical and experimental studies of pulsed plasma thrusters. Especially notable results include the efficacy of using a solenoidal magnetic field downstream of a plasma thruster to collimate the exhaust flow, the development of a new understanding of applied-field MPD thrusters (based on experimentally-validated results from state-of-the art, numerical simulation) leading to predictions of improved performance, an experimentally-validated, first-principles model for orificed, hollow-cathode behavior, and the first time-dependent, two-dimensional calculations of ablation-fed, pulsed plasma thrusters.

14. SUBJECT TERMS
Electric propulsion; Magneto-hydrodynamic pulsed thrusters; Pulsed plasma thrusters; Hollow cathodes

15. NUMBER OF PAGES
214

16. PRICE CODE
A10

17. SECURITY CLASSIFICATION OF REPORT
Unclassified

18. SECURITY CLASSIFICATION OF THIS PAGE
Unclassified

19. SECURITY CLASSIFICATION OF ABSTRACT
Unclassified

20. LIMITATION OF ABSTRACT

NSN 7540-01-280-5500

Standard Form 298 (Rev. 2-89)
Prescribed by ANSI Std. Z39-18
298-102